

Marte Jørstad Uthus

U-Pb geochronological and whole-rock geochemical analysis of the augen gneiss of the Dagsvolsjøen Nappe, central Norwegian Caledonides

Master's thesis in Geology

Supervisor: Bjørn Eske Sørensen

Co-supervisor: Bernard Bingen and Johannes Jakob

May 2023

Marte Jørstad Uthus

U-Pb geochronological and whole-rock geochemical analysis of the augen gneiss of the Dagsvolsjøen Nappe, central Norwegian Caledonides

Master's thesis in Geology

Supervisor: Bjørn Eske Sørensen

Co-supervisor: Bernard Bingen and Johannes Jakob

May 2023

Norwegian University of Science and Technology

Faculty of Engineering

Department of Geoscience and Petroleum



Norwegian University of
Science and Technology

Abstract

The augen gneiss of the Dagvolsjøen Nappe in the central Norwegian Caledonides is poorly mapped, and modern geochronology and geochemistry is lacking at its type locality near Brekken, Røros municipality. This study aimed to enhance the understanding of the augen gneiss assigned to the Dagvolsjøen Nappe through two weeks of mapping and targeted sampling. Additionally, reference samples of the Tännäs augen gneiss Nappe (TAG) from its type locality in Sweden and from the basement exposed in the Skardøra antiform (the Vigelen granite) were collected for comparison with the Dagvolsjøen augen gneiss.

Field work revealed that there are possibly three variations within the augen gneiss of the Dagvolsjøen Nappe: (1) quartz striped K-feldspar augen gneiss, (2) unstriped augen gneiss with fine-grained matrix and (3) strongly quartz striped K-feldspar augen gneiss. Due to the mineralogy, texture and the geochemical analyses, all of these variants are interpreted as the Dagvolsjøen augen gneiss, however, further investigations are necessary to provide conclusive evidence for the unstriped augen gneiss. The three variants are observed in the Dagvolsjøen Nappe and the TAG, but the unstriped augen gneiss with fine-grained matrix is less abundant in the TAG in the field area. Even though the augen gneiss is non-continuous in the field, structural observations implies that the augen gneiss is a single tectonostratigraphic unit.

The U-Pb geochronological data obtained using LA-ICP-MS provide an average $^{207}\text{Pb}/^{206}\text{Pb}$ zircon age of 1655 ± 5 Ma for the Dagvolsjøen augen gneiss. This age overlaps within error with the Tännäs augen gneiss, which yields a $^{207}\text{Pb}/^{206}\text{Pb}$ age of 1654 ± 5 Ma. Both are interpreted to be the magmatic crystallisation age of the protolith of the augen gneisses. In addition, ages of the Vigelen granite and a granitic sheet in the TAG have been obtained: 1657 ± 6 Ma (Vigelen granite, $^{207}\text{Pb}/^{206}\text{Pb}$ age) and 436 ± 43 Ma to 351 ± 38 Ma (granitic sheet, lower intercept age), respectively. The augen formation in the augen gneiss occurred after ~ 1655 Ma, but before the emplacement of the granitic sheet. The age group of 1190-1180 Ma reported by Handke et al. (1995) and Lamminen et al. (2011) has not been provided in this study.

The Dagvolsjøen Nappe can be correlated with the TAG, but it is still unclear whether there is a correlation between the Dagvolsjøen Nappe and the Risberget Nappe. There is a possible affinity between the Western Gneiss Region and the Dagvolsjøen Nappe/TAG. However, there is no or little affinity between the Dagvolsjøen augen gneiss and the Vigelen granite. It has been proposed that the Dagvolsjøen Nappe and the TAG share a common I-type granitic protolith. The augen gneiss of the Dagvolsjøen Nappe and the TAG is enriched in LREE compared to the HREE and has negative anomalies for Nb, P and Ti and a positive anomaly for Pb. These characteristics suggest that the protolith was formed in a volcanic arc setting in a supra-subduction zone environment.

Sammendrag

Øyegneisen i Dagvolsjødekket i de sentrale, norske Kaledonidene er dårlig kartlagt, og moderne geokronologi og geokjemi mangler fra typelokaliteten nær Brekken i Røros kommune. For å få en bedre forståelse av øyegneisen som tilhører Dagvolsjødekket, er det i denne studien gjennomført to uker med kartlegging og målrettet prøvetaking. I tillegg ble referanseprøver fra typelokaliteten til Tännäs øyegneisdekket (TAG) i Sverige fra grunnfjellet (Vigelen-granitten) som er eksponert i Skardøra antiformalen prøvetatt. Disse prøvene ble prøvetatt for å kunne sammenlignes med Dagvolsjø-øyegneisen.

Feltarbeidet avdekket at det er muligens tre forskjellige variasjoner innenfor øyegneisen i Dagvolsjødekket: (1) kvartsstripet alkalifeltspat øyegneis, (2) ikke-stripet øyegneis med finkornet matriks og (3) sterkt deformert kvartsstripete alkalifeltspat øyegneis. På grunn av mineralogien, teksturen og de geokjemiske analysene er det tolket at de tre variantene er alle Dagvolsjø-øyegneis. Det er derimot nødvendig med videre undersøkelser for å konkludere for den ustripede øyegneisen. Alle variantene er observert i Dagvolsjødekket og i TAG, men den ikke-stripete øyegneisen med finkornet matriks er mindre utbredt i TAG i feltområdet. Selv om øyegneisen ikke er kontinuerlig i felt, antyder strukturelle observasjoner at øyegneisen er en tektonostratigrafisk enhet.

Geokronologiske analyser med LA-ICP-MS gir en gjennomsnittlig U-Pb zirkonalder på 1655 ± 5 Ma ($^{207}\text{Pb}/^{206}\text{Pb}$ alder) for Dagvolsjø øyegneisen. Denne alderen overlapper innenfor feilmarginen med alderen til Tännäs øyegneisen, som er datert til 1654 ± 5 Ma ($^{207}\text{Pb}/^{206}\text{Pb}$ alder). Begge er tolket til å være den magmatiske krystalliseringsalderen til protolitten til øyegneisene. I tillegg ble Vigelen-granitten fra grunnfjellet i Skardøra antiformalen og en granittisk intrusjon i TAG datert til henholdsvis 1657 ± 6 Ma (Vigelen-granitten, $^{207}\text{Pb}/^{206}\text{Pb}$ alder) og 436 ± 43 Ma til 351 ± 38 Ma (granittisk intrusjon, nedre skjæringspunkt). Dannelsen av øynene i øyegneisen skjedde etter ~ 1655 Ma, men før intrusjonen av den granittiske gangen. Aldersgruppen 1190-1180 Ma som er rapportert av Handke et al. (1995) og Lamminen et al. (2011) ble ikke funnet i denne studien.

Dagvolsjødekket kan korreleres med TAG, men det er fortsatt uklart om det er en korrelasjon mellom Dagvolsjødekket og Risbergdekket. Det er en mulig korrelasjon mellom den Vestre Gneisregionen og Dagvolsjødekket/TAG. I tillegg er det ingen likhet eller liten likhet mellom Dagvolsjø-øyegneisen og Vigelen-granitten. Det er foreslått at Dagvolsjødekket og TAG har en felles I-type granittisk protolitt. Øyegneisen er anriket på LREE sammenlignet mot HREE og har negative anomalier for Nb, P og Ti og en positiv anomali for Pb. Dette antyder at protolitten ble dannet i en vulkansk øybuesetting over en subduksjonssone.

Acknowledgement

This Master's Thesis was carried out at the Norwegian University of Science and Technology (NTNU) in collaboration with the Geological Survey of Norway (NGU), with the guidance from Bjørn Eske Sørensen (NTNU), Bernard Bingen (NGU) and Johannes Jakob (NGU).

First and foremost, I would like to express my gratitude to my supervisors. Thank you for the support and guidance throughout this project. I would like to give a special thank you to Bernard and Johannes for introducing me to the world of augen gneisses, your dedicated commitment to this project, countless hours of support and the valuable discussions we have had over the past two years.

I would also like to say thank you to the people who have helped me at NGU, especially the section for laboratories and the section for bedrock geology. Thank you for welcoming me with open arms, the discussions and the coffee breaks. Particularly thank you to Håvard, Frida and Raghubansh for the help in the lab during the last years. Thank you to Magdalena for the help with the LA-ICP-MS. Additionally, thank you to the MiMaC laboratory at NTNU and Stephanie for the help with the SEM.

In the end would I like to say thank you and give a big hug to my family and friends for the endless support you have given me through the years of study. Thank you!



Marte Jørstad Uthus

Trondheim, May 2023

Table of content

List of figures	i
List of tables	iii
List of abbreviations	iv
1 Introduction	1
1.1 <i>Background of the study</i>	1
1.2 <i>The study area</i>	1
2 Geological setting	3
2.1 <i>The Caledonian orogeny</i>	3
2.2 <i>The Scandinavian Caledonides</i>	5
2.3 <i>Regional tectonostratigraphy</i>	6
2.3.1 <i>The Baltican basement and cover</i>	9
2.3.2 <i>The Osen-Røa Nappe Complex</i>	9
2.3.3 <i>The Remslikleppen Nappe Complex</i>	10
2.3.4 <i>Tännäs Augen Gneiss Nappe</i>	11
2.3.5 <i>The Esandsjøen Nappe</i>	11
2.3.6 <i>The Røragen detachment</i>	11
3 Theoretical background	13
3.1 <i>U-Pb geochronology</i>	13
3.1.1 <i>U-Th-Pb decay</i>	13
3.1.2 <i>Interpretation of U-Pb zircon ages</i>	14
3.1.3 <i>Concordant data</i>	16
3.1.4 <i>Causes of discordance</i>	16
3.2 <i>Geochemistry</i>	18
3.2.1 <i>Major and trace elements</i>	18
3.2.2 <i>Rare earth elements</i>	18
3.2.3 <i>Tectonic discrimination diagrams</i>	19
4 Method	21
4.1 <i>Field work</i>	21
4.2 <i>Construction of maps and structural interpretation</i>	22
4.3 <i>Geochronology</i>	22
4.4 <i>Geochemistry</i>	25
5 Results	27
5.1 <i>Lithological descriptions</i>	27
5.1.1 <i>Quartz striped K-feldspar augen gneiss</i>	29
5.1.2 <i>Unstriped augen gneiss with fine-grained matrix</i>	33
5.1.3 <i>Strongly quartz striped K-feldspar augen gneiss</i>	35
5.1.4 <i>Fine-grained and muscovite-rich rock</i>	37
5.1.5 <i>The Tännäs augen gneiss</i>	38
5.1.6 <i>Mylonite</i>	39
5.1.7 <i>Granitic intrusion</i>	40
5.2 <i>Structural descriptions</i>	42

5.2.1 Foliation	43
5.2.2 Lineations	45
5.2.3 Kinematic indicators	46
5.2.4 Dynamic recrystallisation of quartz and feldspar	48
<i>5.3 U-Pb geochronology</i>	<i>55</i>
5.3.1 Sample BB20_20	57
5.3.2 Sample MU126	60
5.3.3 Sample MU021	62
5.3.4 Sample BB20_19	64
5.3.5 Sample JJ23	65
5.3.6 Sample JJ29	67
<i>5.4 Geochemistry</i>	<i>69</i>
5.4.1 Geochemical classification	70
5.4.2 Major elements	77
5.4.3 Rare earth elements in spider diagrams	79
5.4.4 Tectonic discrimination diagrams	81
6 Discussion	83
<i>6.1 The Dagvolsjøen Nappe</i>	<i>83</i>
<i>6.2 Correlation between the Dagvolsjøen Nappe and other tectonic units in the central Scandinavian Caledonides</i>	<i>87</i>
6.2.1 The Vigelen granite	87
6.2.2 The Tännäs Augen Gneiss Nappe	90
6.2.3 The Risberget Nappe	94
6.2.4 The Western Gneiss Region	94
<i>6.3 The pre-Caledonian history of the Dagvolsjøen Nappe</i>	<i>94</i>
<i>6.4 Further work</i>	<i>99</i>
7 Conclusion	100
References	101
Appendices	109

List of figures

Figure 1. Overview map with the location of this study	2
Figure 2. Overview over where remnants of the Caledonian Orogen	3
Figure 3. A paleogeographic reconstruction	4
Figure 4. The possible palaeogeographical position of continents on the southern hemisphere during Cambrian-Silurian	5
Figure 5. Map over the main subdivisions of the Baltic Shield	6
Figure 6. Geological overview map	7
Figure 7. Geological overview map over the study area	8
Figure 8. Simplified tectonostratigraphic model of the study area	9
Figure 9. Profile over the Skardøra antiform	12
Figure 10. The three decay chains for ^{238}U , ^{235}U and ^{232}Th	14
Figure 11. A Wetherill concordia diagram demonstrating different distributions of data relative to the concordia curve	15
Figure 12. Wetherill concordia diagram and cathodoluminescence (CL) image of a polished zircon crystal	17
Figure 13. Tectonic discrimination diagram for granitoid rocks from Pearce et al. (1984)	20
Figure 14. Concordia diagrams for the standard Plesovice	25
Figure 15. Geological map over the study area with my observation points	27
Figure 16. The different variants of the augen gneiss in the Dagvolsjøen Nappe	28
Figure 17. The quartz striped K-feldspar augen gneiss	30
Figure 18. Matrix and augens of the quartz striped K-feldspar augen gneiss	31
Figure 19. The locality MU016	32
Figure 20. Micrographs of thin section from MU016	33
Figure 21. The unstriped augen gneiss with homogenized fine-grained matrix	34
Figure 22. Strongly quartz striped K-feldspar augen gneiss	36
Figure 23. Fine-grained and muscovite-rich rock	37
Figure 24. The Tännäs augen gneiss	38
Figure 25. Mylonites	40
Figure 26. The granitic intrusion	41
Figure 27. The contact between the augen gneiss and the granitic sheet	42
Figure 28. The augen gneiss is a L>S tectonite	43
Figure 29. Foliation in the western limb of the Skardøra antiform	44
Figure 30. Foliation in the eastern limb of the Skardøra antiform	45
Figure 31. Mineral lineations	46
Figure 32. Symmetrical sigma-clasts at the locality MU021	47
Figure 33. Micro-scale kinematic indicators	47
Figure 34. Dynamic recrystallisation of quartz and feldspar in quartz striped K-feldspar augen gneiss	49
Figure 35. Dynamic recrystallisation of quartz and feldspar in the unstriped augen gneiss with homogenized fine-grained matrix	50
Figure 36. Dynamic recrystallisation of quartz and feldspar the strongly quartz striped augen gneiss	51
Figure 37. Dynamic recrystallisation of quartz and feldspar in the fine-grained and muscovite-rich rock	52
Figure 38. Dynamic recrystallisation of quartz and feldspar in the Tännäs augen gneiss	53
Figure 39. Dynamic recrystallisation of quartz and feldspar in the protomylonite	54
Figure 40. Dynamic recrystallisation of quartz and feldspar in the granitic intrusion	55
Figure 41. Geological overview map over the study area with the sample localities for geochronology	56
Figure 42. Undeformed and coarse-grained granite	58
Figure 43. Wetherill concordia diagrams for the Vigelen granite	59

Figure 44. Sample MU126 (Tännäs augen gneiss)	60
Figure 45. Wetherill concordia diagrams for the Tännäs augen gneiss	61
Figure 46. Sample MU021	62
Figure 47. Wetherill concordia diagrams for MU021	63
Figure 48. Wetherill concordia diagrams for BB20_19	64
Figure 49. Wetherill concordia diagrams for JJ23	66
Figure 50. Sample JJ29	68
Figure 51. Concordia diagrams for sample JJ29	68
Figure 52. Geological overview map over the study area with the sample localities for geochemistry	69
Figure 53. Classification of igneous rocks from Middlemost (1994)	72
Figure 54. Classification of igneous rocks from Debon and Le Fort (1983)	73
Figure 55. Classification of metaluminous, peraluminous and peralkaline rocks of Shand (1943)	74
Figure 56. Feldspar triangle diagram with anorthite (An), albite (Ab) and orthoclase (Or) of O'Connor (1965)	75
Figure 57. Tectonic discrimination diagrams for granite from Frost and Frost (2008)	76
Figure 58. Classification of granites from Whalen et al. (1987)	77
Figure 59. Harker diagrams	78
Figure 60. Chondrite-normalized trace element diagrams after Boynton (1984)	80
Figure 61. MORB-normalized trace element diagrams	81
Figure 62. Tectonic discrimination diagrams for granites from Pearce et al. (1984)	82
Figure 63. Major element classifications of sediments after Herron (1988)	83
Figure 64. Feldspathic igneous rocks' classification scheme from Frost et al. (2001)	86
Figure 65. Trends of I- and S-type granites proposed by Chappell and White (1992)	86
Figure 66. Age distribution of the magmatic crystallization age	88
Figure 67. Spider diagrams	90
Figure 68. Field photos from the Dagvolsjøen Nappe and the TAG	91
Figure 69. Micrographs of augen gneisses from the Dagvolsjøen Nappe and the TAG	92
Figure 70. Global paleogeographic reconstruction at 1650 Ma according to Pisarevsky et al. (2014)	95
Figure 71. A simplified model over Fennoscandinavia	96
Figure 72. Simplified map over the western part of Fennoscandinavia	97
Figure 73. Simplified model for the western part of Baltica	98

List of tables

Table 1. The atomic symbols, names and atomic numbers of the rare earth elements	18
Table 2. Information about the samples	21
Table 3. The settings used for the LA-ICP-MS analysis	24
Table 4. The standards with the respective ages	24
Table 5. Summary of the zircon U-Pb geochronological data	56
Table 6. Summary of the geochemical classification	71

List of abbreviations

α	Alpha particle
β	Beta particle
Λ	Decay constant
An	Anorthite
Ab	Albite
Afs	K-feldspar
BLG	Bulging
BSE	Back-scattered electron
Bt	Biotite
Chl	Chlorite
CL	Cathodoluminescence
DIM	Diiodomethane
Ep	Epidote
Fsp	Feldspar
Ga	Billions of years
GBM	Grain boundary migration
GCDkit	The Geochemical Data Toolkit
Gyr	Gigayear
HIC	Hustad Igneous Complex
HFSE	High field strength elements
HREE	Heavy rare earth element
LA-ICP-MS	Laser ablation-inductively coupled plasma-mass spectrometry
LILE	Large ion lithophile elements
LREE	Light rare earth element
Ma	Millions of years
MiMac	Norwegian Laboratory of Minerals and Materials
MORB	Mid-ocean ridge basalt
Ms	Muscovite
MSWD	Mean squared weighted deviation
N	Concentration of the parent isotopes (in moles)
N/A	Not applicable
NGU	Norwegian Geological Survey
NMORB	Normal mid-ocean ridge basalt
NTNU	Norwegian University of Science and Technology
Or	Orthoclase
Pb	Lead
Pl	Plagioclase
PPL	Plain polarized light image
Ppm	Part pr. Million
Q	Energy released during decay
Qz	Quartz
REE	Rare Earth Elements
RDB	Røragen detachment basin
SEM	Scanning electron microscope
SGR	Sub grain rotation
t	Time

TAG	Tännäs Augen Gneiss Nappe
TIB	Transscandinavian Igneous Belt
Ttn	Titanite
U-Pb	Uranium-lead
UHP	Ultra-high-pressure
WGR	Western Gneiss Region
Wt. %	Weight percent
XPL	Crossed polarized light image
XRF	X-Ray fluorescence

1 Introduction

1.1 Background of the study

The bedrock underlying Norway consists of different bedrock windows and nappes transported several hundreds of kilometres from their origin before they were thrust onto Baltica (the Fennoscandian Shield). The thrust succession is composed of igneous and metasedimentary rocks of wide-ranging metamorphic grade and age (Roberts and Wolff, 1981, Gee et al., 1985). In the Brekken area in Røros municipality, Trøndelag, a persistent, but discontinuous sheet of augen gneiss is present. In the field area, the augen gneiss is assigned to the Dagvolsjøen Nappe.

This Master's Thesis studies the augen gneiss of the Dagvolsjøen Nappe in the Brekken area. The thesis is conducted jointly between Norwegian University of Science and Technology (NTNU) and Norwegian Geological Survey (NGU), and the aim was to collect new field data to acquire information regarding the lithological, structural, geochronological and geochemical aspects of the augen gneiss of the Dagvolsjøen Nappe. The augen gneiss of the Dagvolsjøen Nappe is poorly mapped in places and modern geochronology and geochemistry is lacking from its type locality near Brekken. Therefore, the main emphasis has been the field mapping as well as geochronological and geochemical investigations. The objective is to gain a better understanding of the Dagvolsjøen augen gneiss in addition to a comparative analysis with other units with augen gneiss in the central Scandinavian Caledonides.

The Dagvolsjøen Nappe is part of the Remslikleppen Nappe Complex of Middle Allochthon according to the traditional tectonostratigraphic division in Norway. West of the Trondheim Nappe Complex, the Dagvolsjøen Nappe is correlated with the Risberget Nappe, which is also part of the Remslikleppen Nappe Complex. In Sweden, the Dagvolsjøen Nappe is correlated with the Tännäs Augen Gneiss Nappe. The protolith of the Tännäs augen gneiss has been dated by Claesson (1980) to 1685 ± 20 Ma (U-Pb on four zircon fractions). Handke et al. (1995) dated three samples of augen gneiss of the Risberget Nappe at the same structural level as the Dagvolsjøen Nappe, and they dated the protolith to ~1190-1180 Ma. They also dated the protolith of gneisses from the WGR to ~1650-1540 Ma. Lamminen et al. (2011) has dated a sheared granite 1183 ± 7 Ma, while Røhr et al. (2013) dated a granodioritic augen gneiss of the Risberget Nappe to 1676 ± 18 Ma.

This study will commence with a presentation of the Scandinavian Caledonides before the regional geology is presented. Subsequently, a chapter with the theoretical background for U-Pb geochronology and whole-rock geochemistry followed by the methods used to collect and produce results are presented. The result chapter is divided into four: (1) lithological descriptions, (2) structural observations, (3) U-Pb geochronological analysis and (4) geochemical analysis. Succeeding the results is the discussion before a conclusion is given. The appendices are at the end.

1.2 The study area

The study area is situated near Brekken in Røros municipality, Trøndelag. The field area is located near to the border with Sweden, and in terms of bedrock geology, is it part of

the Caledonian nappe stack (Fig. 1a). The elevation in the area ranges from appr. 900 meters above sea level to 1036 meters above sea level at Kvitmannen (Fig. 1b). The area of interest is focused on hiking trails in each rectangle in Fig. 1b. The hiking trails are directly on bedrock and follow ridges. There are vegetation and swamps with just a few and small outcrops between the ridges. The field area is situated on the limbs of a large-scale antiform, the Skardøra antiform. In addition, one location near Tännäs, Sweden was visited and sampled. The sampling locality is along the river Tännån (Fig. 1c).

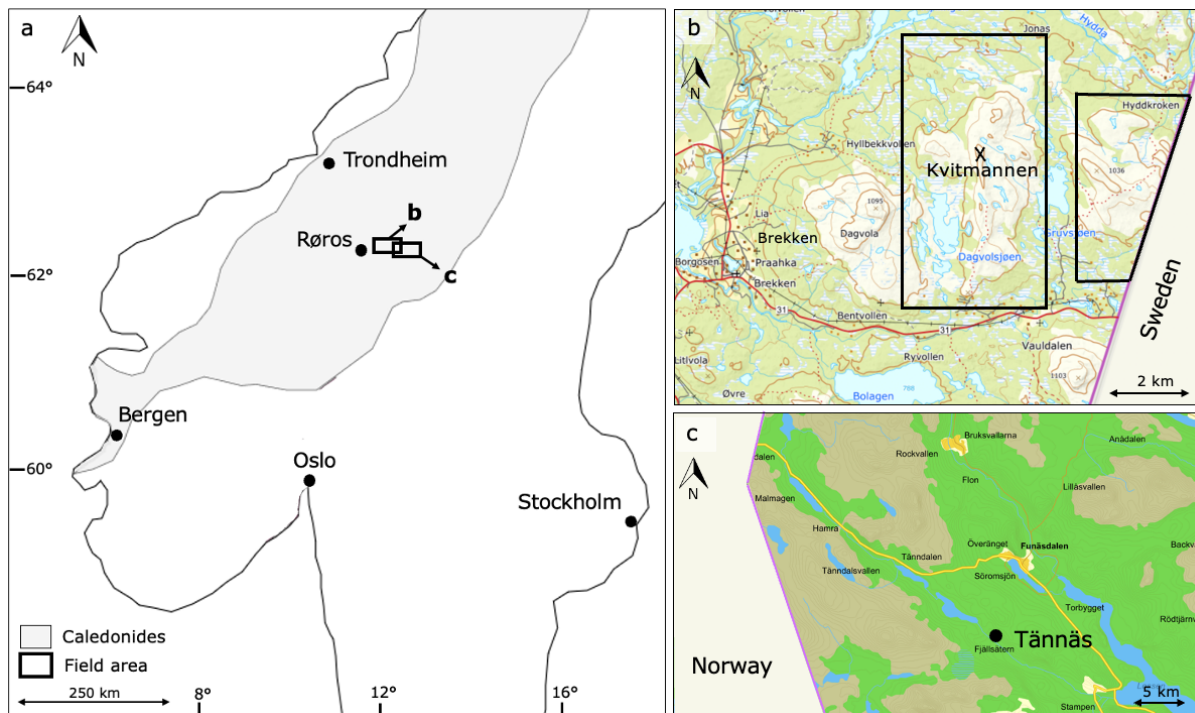


Figure 1. Overview map with the location of this study. a) Simplified map over the southern and central Scandinavian Caledonides after Corfu et al. (2014a). The black rectangles show the field area and the locations of Figs. 1b and 1c. b) The study area for this thesis is located a few kilometers east of the village Brekken in Røros municipality, close to the Swedish border. The map is from Kartverket (2022). c) The sampling location near Tännäs, Sweden, marked with a black circle. The map is from Gulesider (2022).

2 Geological setting

2.1 The Caledonian orogeny

The Wilson cycle is fundamental to the theory of plate tectonics. The opening and closing of oceans is a key process of break-ups of continents and assembling them, and the Atlantic margin is a classic example of ancient and present Wilson cycles (Wilson et al., 2019). Observations along the North Atlantic margin led to the theory that the present-day Atlantic ocean was formed along the remnants of an older ocean, called the proto Atlantic Ocean, now commonly referred as the Iapetus Ocean (Wilson, 1966, McKerrow et al., 2000). These observations led to the concept of the Wilson cycle, which shortly states that ocean basins open after continental rifting before they are closed by subduction and collisional orogenesis (Dewey and Burke, 1974, Wilson et al., 2019). The remnants of a complete Wilson cycle are preserved in the Caledonian Orogen; from rifting to continent-continent collision and orogenic collapse (Warvik et al., 2022). This orogen affected the continental margins of Baltica, Laurentia and Avalonia. Vestiges of the Caledonian Orogen can be found on the British islands, in Ireland, North America and Scandinavia (Fig. 2) (Suess, 1906, McKerrow et al., 2000).



Figure 2. Overview over where remnants of the Caledonian Orogen can be found in present day (dark grey). The study area is marked with a red X. The figure is from Grenne et al. (1999).

Around 1000 Ma, most of the continents were assembled as the supercontinent Rodinia before it broke apart (Powell et al., 1993). The initial break-up of Rodinia is still debated, with estimates around 750-550 Ma (Robert et al., 2021). During the initial break-up, the continent Laurentia was located around the equator and Baltica was at the southern hemisphere (Fig. 3) (Li et al., 2008). According to Torsvik et al. (1996), the initial break-up of Rodinia was initiated along a rifted margin between the eastern part of Gondwana and the western margin of Laurentia. On the contrary, Robert et al. (2021) argue that the break-up of Rodinia was a three-way break-up of Amazonia, Baltica and Laurentia.

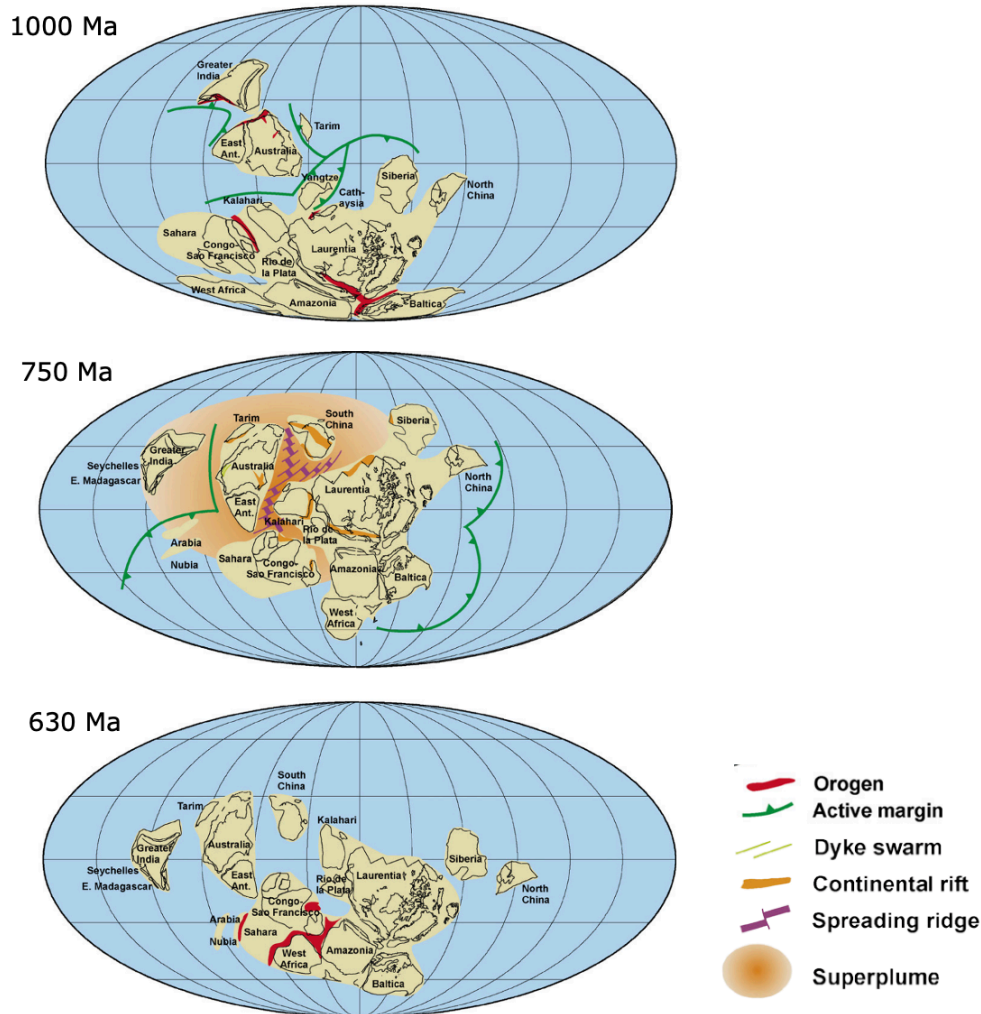


Figure 3. A paleogeographic reconstruction at 1000 Ma, 750 Ma and 630 Ma. The figure is from Li et al. (2008).

During the Ordovician, Baltica started to rotate counter-clockwise (Fig. 4), and the Iapetus Ocean reached its widest c. 480 Ma (Torsvik and Cocks, 2005). In the same time frame, the Caledonian orogeny commenced with subduction of the Iapetus Ocean along the continental margin of Laurentia (Gee et al., 2008). This convergence culminated in the continent-continent collision between Baltica and Laurentia at c. 430 Ma, forming the Scandian Orogen (Fig. 4) (Torsvik et al., 1996). In the traditional models, the Baltican margin is passive, however, the occurrence of high-pressure eclogites in the Seve Nappe Complex derived from the Baltoscandian margin indicate tectonic activity on the Baltic side (Roberts, 2003, Root and Corfu, 2012). The closure of the Iapetus Ocean resulted in southeastward thrusting of nappes onto Baltica until c. 415 Ma (Roberts, 2003, Tucker et al., 2004, DesOrmeau et al., 2015).

After the continent-continent collision, orogenic collapse occurred in early Devonian (Braathen et al., 2000). The southeast-directed nappe translation caused by the Caledonian contractional deformation was replaced by extensional deformation (Fossen, 1992, Fossen and Hurich, 2005). The orogenic collapse was associated with the formation of large-scale detachment faults, such as the Røragen detachment in the central segment of the Scandinavian Caledonides (Gee et al., 1994).

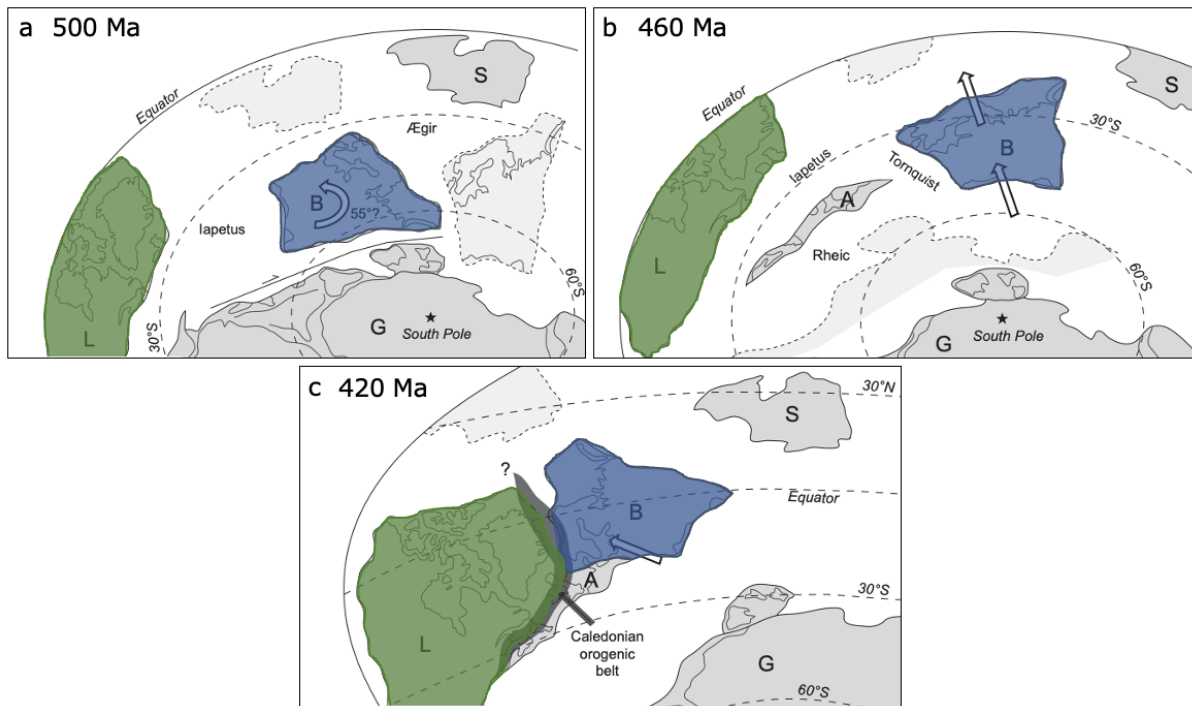


Figure 4. The possible palaeogeographical position of continents on the southern hemisphere during Cambrian-Silurian. Baltica is marked with a "B" and blue, Laurentia is marked with a "L" and green, Siberia is marked with a "S", Gondwana is marked with a "G" and Avalonia is marked with a "A". a) The palaeogeographical positions at 500 Ma. The light grey and stippled polygons are alternative positions of Baltica and Siberia. b) The palaeogeographical positions at 460 Ma. Alternative positions of Siberia and Gondwana are marked in light grey and stippled lines. The alternative position of Siberia aligns more with the interpretations of Torsvik et al. (1996)c) The palaeogeographical positions at 420 Ma. The alternative position of Siberia is in light grey with stippled lines, and this position fits better with the interpretations of Torsvik et al. (1996). The Caledonian Orogen is marked with dark grey and dark blue and green between Baltica and Laurentia. The figure is modified after Corfu et al. (2014a).

2.2 The Scandinavian Caledonides

The Scandinavian Caledonides in Norway extended from the Stavanger area and up to the Barents sea region, which is approximately 1500 km and up to 300 km in width (Roberts and Gee, 1985, Corfu et al., 2014a). The western part of Scandinavia is underlain autochthonous and (par-)autochthonous caledonized bedrock. The nappes within the Caledonian nappe sheet were transported hundreds of kilometres (Törnebohm, 1888, Gee et al., 1985, Roberts and Gee, 1985, Gee et al., 2010, Jakob et al., 2022). The metamorphic grade in the different nappes increases from sub-greenschist to greenschist facies in the lowest allochthonous units in the foreland to amphibolite and ultra-high-pressure (UHP) metamorphism in the hinterland. However, the metamorphic grade also varies within the nappe stack from greenschist facies to amphibolite facies and (U)HP metamorphism across structural levels (Gee et al., 1985, Gee et al., 2020).

As a consequence of the extension in Devonian, basement was locally exhumed, such as the Western Gneiss Region (WGR) in west of Norway and the Vigelen window in the Skardøra antiform in the study area (Fig. 5) (Gee et al., 1994, Osmundsen et al., 2005). The WGR appears as a basement window at the base of the nappe stack consisting of Middle Proterozoic Baltican basement (Roberts and Gee, 1985, Austrheim et al., 2003, Ganzhorn et al., 2014).

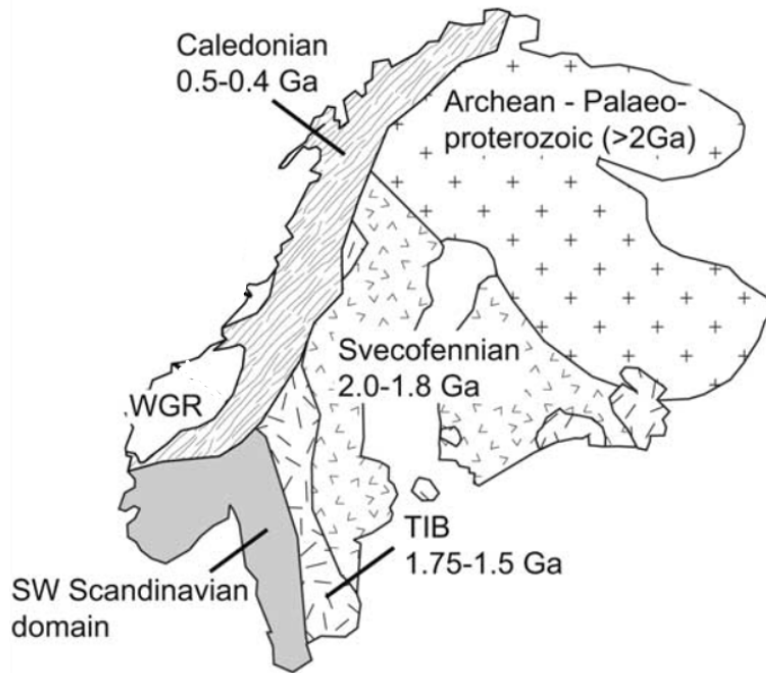


Figure 5. Map over the main subdivisions of the Baltic Shield: the Archean core (>2 Ga), the Svecofennian Province (2-1.8 Ga), the Transscandinavian Igneous Belt (TIB, 1.75-1.5 Ga), the Sveconorwegian SW-Scandinavian domain and the Western Gneiss Region (WGR). The figure is from Austrheim et al. (2003).

2.3 Regional tectonostratigraphy

The tectonic units in the study area and the surroundings will briefly be described in the following sections (Figs. 6, 7 and 8). The regional overview map is divided into three segments: the *Western Segment* (western part of the Trondheim Nappe Complex and westward), the *Central Segment* (eastern part of the Trondheim Nappe Complex and to the border between Norway and Sweden) and the *Eastern Segment* (from the border between Norway and Sweden and eastward) (Fig. 7). The study area is assigned to the Central Segment, and it is linking the Eastern- and Central Segment.

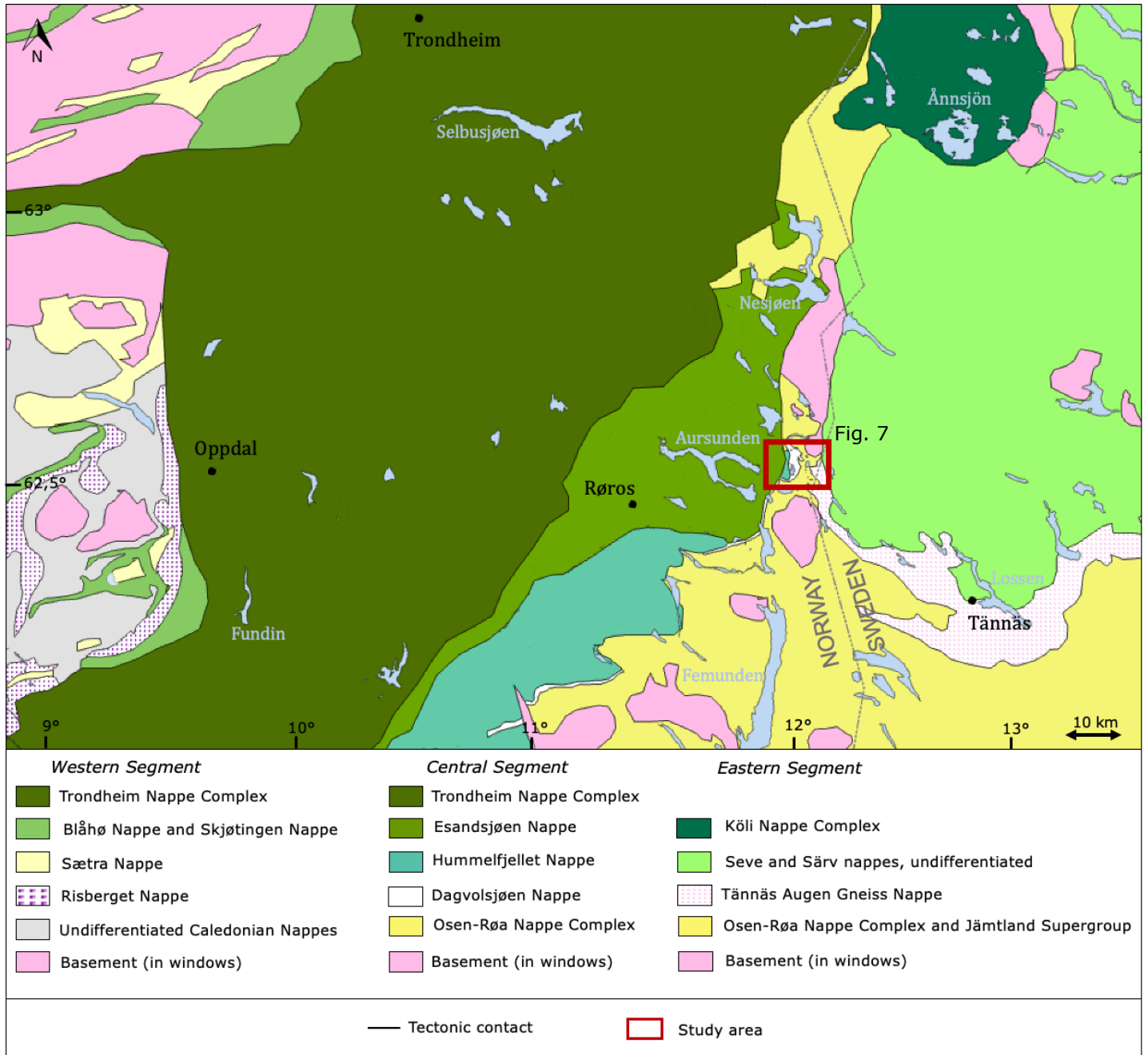


Figure 6. Geological overview map. The map is divided into a Western Segment, a Central Segment and an Eastern Segment. The Western Segment is the Trondheim Nappe Complex and westward, the Eastern Segment is the Swedish part of the map while the Central Segment is between Sweden and the Western Segment. The study area is marked with a red box. The map is after NGU (2022a), NGU (2022b) and Bergman et al. (2012). The coordinate system is WGS84 UTM Zone 32N and 33N.

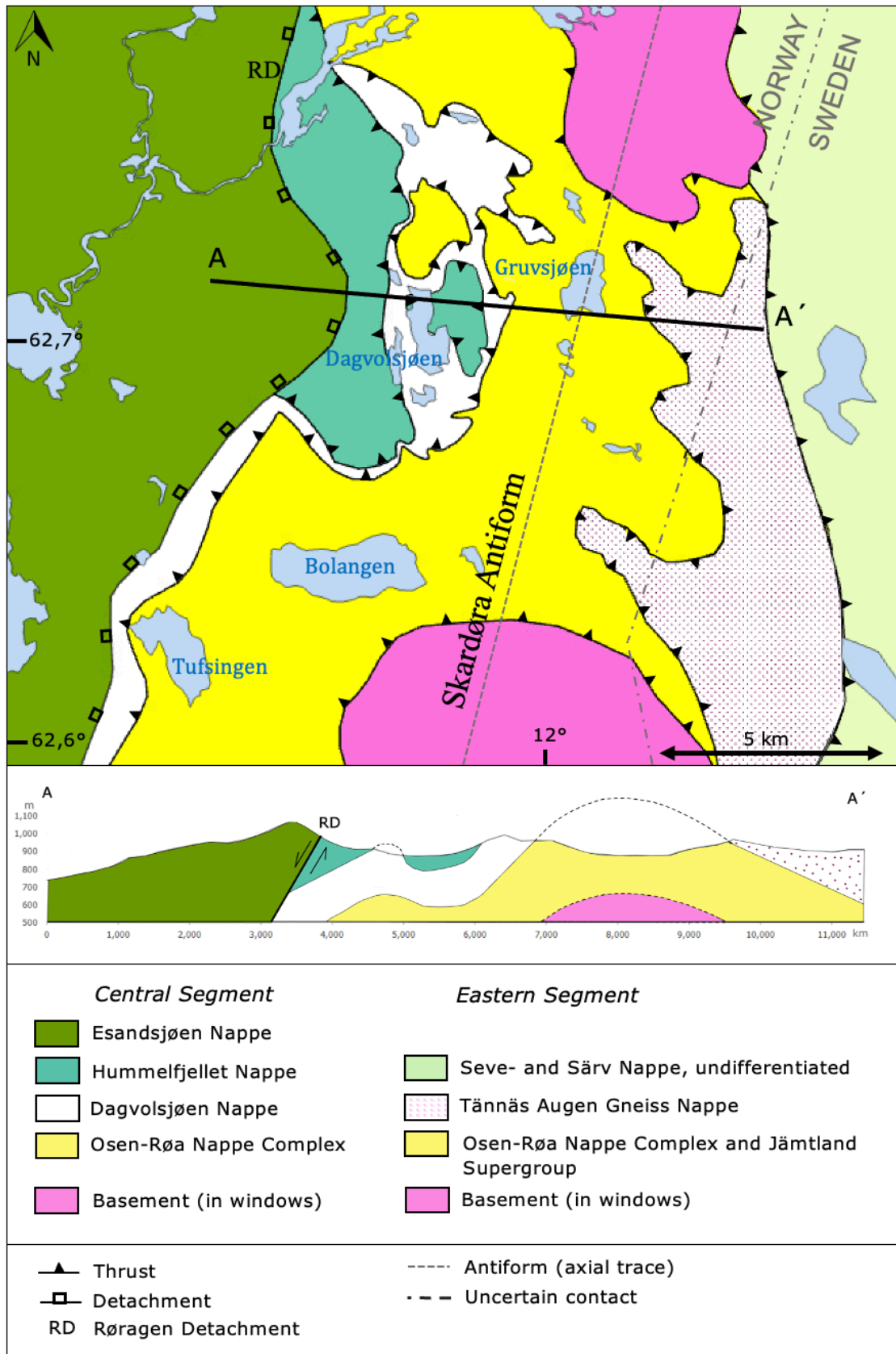


Figure 7. Geological overview map over the study area (the red box in Fig. 6). The field work was done east of the lake Dagvolsjøen in the Dagvolsjøen Nappe and in the Tännäs Augen Gneiss Nappe (the Norwegian part). The profile shows a cross-section between A and A' in the map. The map is based on Nilsen and Wolff (1989), NGU (2023), Bergman et al. (2012) and observations in the field. The coordinate system is WGS84 UTM Zone 32N and 33N.

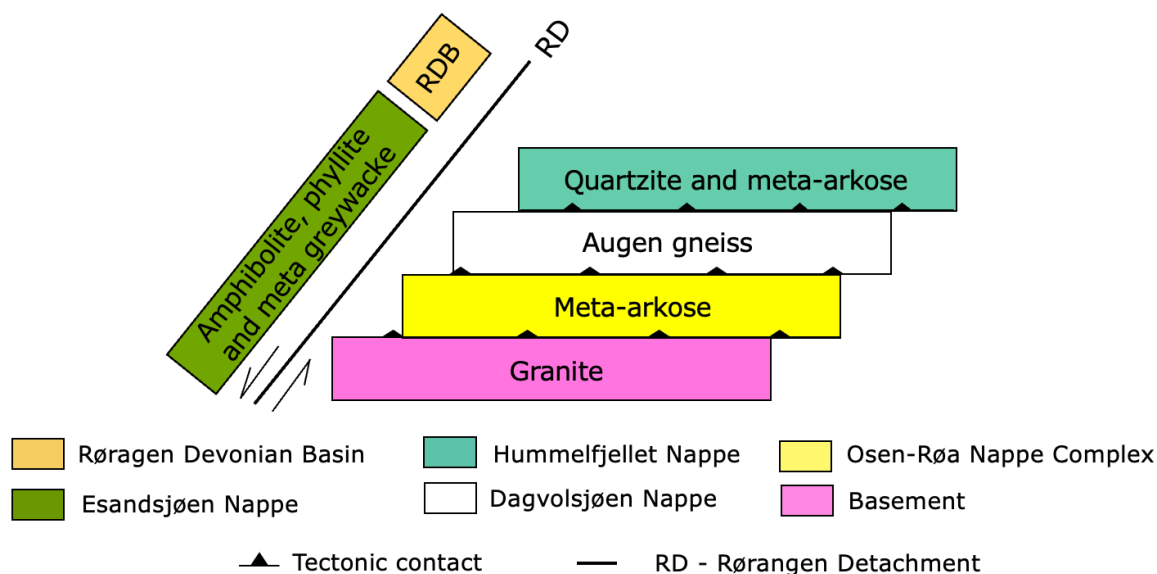


Figure 8. Simplified tectonostratigraphic model of the study area.

2.3.1 The Baltican basement and cover

The crystalline basement of Baltica is a part of the Fennoscandian Shield (Tucker et al., 2004). At the southwestern part of the Fennoscandian margin is the Sveconorwegian orogenic belt, and there is an ongoing debate on the origin of the Sveconorwegian orogeny. Several models are proposed: (1) a four-phase model proposed by Bingen et al. (2008b) and (2) an accretionary model proposed by Slagstad et al. (2013). The four-phase model suggests that the Sveconorwegian orogeny was a continent-continent collision between c. 1065 and 920 Ma (Bingen et al., 2008b, Bingen et al., 2021). The accretionary model suggests that there was a non-collisional accretionary orogeny with extensive magmatism (Slagstad et al., 2013, Granseth et al., 2020). The Fennoscandian Shield near the study area and east of the Caledonian erosional front is dominated by granites of the Transscandinavian Igneous Belt (TIB) with ages ranging from c. 1850 to 1650 Ma (Gorbatshev, 2004, Högdahl et al., 2004, Gee et al., 2014). The basement in the field area is exposed in antiformal windows, such as the Vigelen window in the Skardøra antiform. The Skardøra antiform exposes Proterozoic granite and rhyolite (Gee et al., 1994, Hurich and Roberts, 2018).

2.3.2 The Osen-Røa Nappe Complex

The lowest allochthonous unit in the field area consists of quartzite and meta-arkose. These rocks have been correlated with the Proterozoic metasediments of the Rendalen Formation of the Hedmark Group in the Osen-Røa Nappe Complex, in addition to mid-Proterozoic sheets of crystalline basement rocks (Nystuen, 1983). The Hedmark Group is approx. 4 km thick and weakly deformed, and the Rendalen Formation belongs to the lowermost part of the Hedmark Group. The Rendalen Formation is more than two km thick, and it is characterized by fluvial arkose and conglomerate (Nystuen, 1982). Detrital zircon dating of the Rendalen Formation has recorded a Proterozoic age of 1500-1800 Ma, and the youngest zircons are <620 Ma (Bingen et al., 2005). In the field area, the rocks of the Rendalen Formation are heavily deformed and locally mylonitic. In central Sweden, the lower thrust units are referred to as the Jämtlandian nappes. The sedimentary successions are referred to as the Jämtland Supergroup (Gee and Stephens, 2020).

2.3.3 The Remslikleppen Nappe Complex

The Remslikleppen Nappe Complex is divided into a western and an eastern part. The western part is west of the Trondheim Nappe Complex and consists of the Risberget Nappe and the Sætra Nappe. The eastern part is on the eastern side of the Trondheim Nappe Complex and comprises the Dagvolsjøen Nappe and the Hummelfjellet Nappe (Fig. 6). The following sections will briefly describe the different parts of the Remslikleppen Nappe Complex and the correlated units.

2.3.3.1 The Dagvolsjøen Nappe and the Risberget Nappe

The area that was studied for this thesis is assigned to the Dagvolsjøen Nappe. In the field area, the Dagvolsjøen nappe consists of augen gneiss. According to Nilsen and Wolff (1989), the Dagvolsjøen Nappe also includes anorthosite and amphibolite, which have not been observed in the field area. However, a comprehensive description of the Dagvolsjøen Nappe from its type locality is missing.

The Risberget Nappe is characterized by augen gneiss that is coarse-grained with fine-grained biotite-rich matrix (Walsh and Hacker, 2004). Similar rocks have been interpreted to be Proterozoic orthogneisses that have been deformed (Röshoff, 1978, Krill, 1980). In addition to the augen gneiss, rapakivi granite, meta-gabbro and meta-anorthosite are described in the nappe (Krill, 1980, Tucker et al., 2004). U-Pb zircon analysis of the Risberget Nappe have yielded two age groups for the protolith: c. 1674 Ma and c. 1190 Ma (Handke et al., 1995, Røhr et al., 2013). According to Handke et al. (1995), the ~1190 Ma augen gneiss may represent a granitoid that was emplaced into the Svecoscandian basement of Baltoscandian origin. Previous studies correlates the Risberget Nappe with the Tännäs Augen Gneiss Nappe in Sweden (Krill, 1980).

2.3.3.2 The Hummelfjellet Nappe and correlated units

The Hummelfjellet Nappe comprises of meta-arkose and quartzite, in addition to phyllite and slate in the upper part (Nilsen and Wolff, 1989). The nappe has bodies of amphibolites and subordinate carbonates, however, the mafic rocks in the Hummelfjellet Nappe are as of today undated. The Hummelfjellet Nappe is commonly correlated with the Särvi Nappe or the Seve nappes in Sweden (Gee et al., 1985, Jakob et al., 2022).

The Sætra Nappe

The Sætra Nappe is structurally above the Risberget Nappe and consists of felspathic metasandstone and thin sheets of amphibolites, locally eclogitic. Dolerite dikes are observed in the Sætra Nappe. The sandstone and dykes typical of the Särvi Nappe in Sweden correlates with the Sætra Nappe (Krill, 1980, Robinson, 1995).

The Särvi Nappe and the Seve Nappe Complex

The Särvi Nappe consists of sandstone sequences, dolomite and tilite from the late Proterozoic, and the succession is intruded by the Ottfjället dolerite (Holmquist, 1894, Strömberg, 1961, Gee et al., 1985). U-Pb dating of baddeleyite gives an emplacement age of 596.3 ± 1.5 Ma for a dolerite dyke in Härjedalen, Sweden (Kumpulainen et al., 2021). The Särvi Nappe is greenschist metamorphic, and it is the metamorphic grade that mainly differentiate between the Särvi and Seve nappes.

The Seve Nappe Complex is metamorphosed in amphibolite or eclogite facies (Arnbom, 1980, Li et al., 2020). The Seve Nappe Complex's main lithologies are amphibolite,

psammitic schist and gneiss/migmatite, and locally it contains eclogite (Gee et al., 1985). Compared to the nappes structurally below and above, the nappe complex exhibits a higher metamorphic grade. The Köli Nappe Complex overlies the Seve Nappe Complex (Corfu et al., 2014a). According to Stephens et al. (1985), the Köli Nappe Complex consists of fine-grained siliciclastic, sedimentary rocks with volcanic sequences affected by greenschist to lower amphibolite facies metamorphism. Units of the Köli Nappe Complex are correlated with the Trondheim Nappe Complex.

2.3.4 Tännäs Augen Gneiss Nappe

In Sweden, the nappe composed of augen gneiss is called the Tännäs Augen Gneiss Nappe (TAG). The TAG is underlying the Särvi Nappe and overlying the Jämtland Supergroup. According to Claesson (1980), the TAG is more than 100 km long, up to ten km wide and two km thick. In the field area, the nappe extends into Norway in the eastern limb of the Skardøra antiform (Claesson, 1980, Gee et al., 2020). It is suggested that the TAG is metamorphosed Precambrian basement-derived granites and gneissic granodiorites (Röshoff, 1978, Gee et al., 2020). According to Claesson (1980), the TAG consists of grey to greenish matrix with pink K-feldspar porphyroclasts/augen. Besides the K-feldspar, the rock is also composed of quartz, plagioclase, biotite, hornblende and some epidote. Claesson (1980) dated the protolith of the augen gneiss to 1685 ± 20 Ma (U-Pb on four zircon fractions).

The degree of deformation varies in the TAG, and the strain has been heterogeneous (Röshoff, 1978). Towards the thrust contacts, the augen gneiss is mylonitic. These mylonites are greenish in colour. The increase of deformation has reduced the grain size of the matrix, however, the K-feldspar augens have retained their shape and size better (Claesson, 1980).

2.3.5 The Esandsjøen Nappe

The Esandsjøen Nappe contains of amphibolite, phyllite and meta greywacke (Wolff, 1979). The Esandsjøen Nappe exhibits a similar lithological assemblage, depositional ages, and metamorphic grade as the lower Köli Nappe in Sweden. Therefore, a correlation of the Esandsjøen Nappe with the lower Köli Nappe in Sweden has been suggested (Grenne et al., 1999, McClellan, 2004, Jakob et al., 2022).

2.3.6 The Røragen detachment

In the field area, the Røragen detachment cuts through all tectonostratigraphic units. The Devonian strata in the Røragen detachment basin (RDB) dips towards southeast with 45-50°. The RDB consists of sediment, sandstone, shale and conglomerate. The succession is c. 1.5 km thick, and the sediments were deposited in an intercontinental basin (Holmsen, 1963). According to Gee et al. (1994), the displacement of the Røragen detachment might be as large as 10 km. A shear zone juxtaposes rocks from the Esandsjøen Nappe against the rocks from the basement, Osen-Røa Nappe Complex, Dagvolsjøen Nappe and the Hummelfjellet Nappe (Figs.7, 8 and 9). These nappes are excised laterally along the length of the Røragen detachment (Norton et al., 1987).

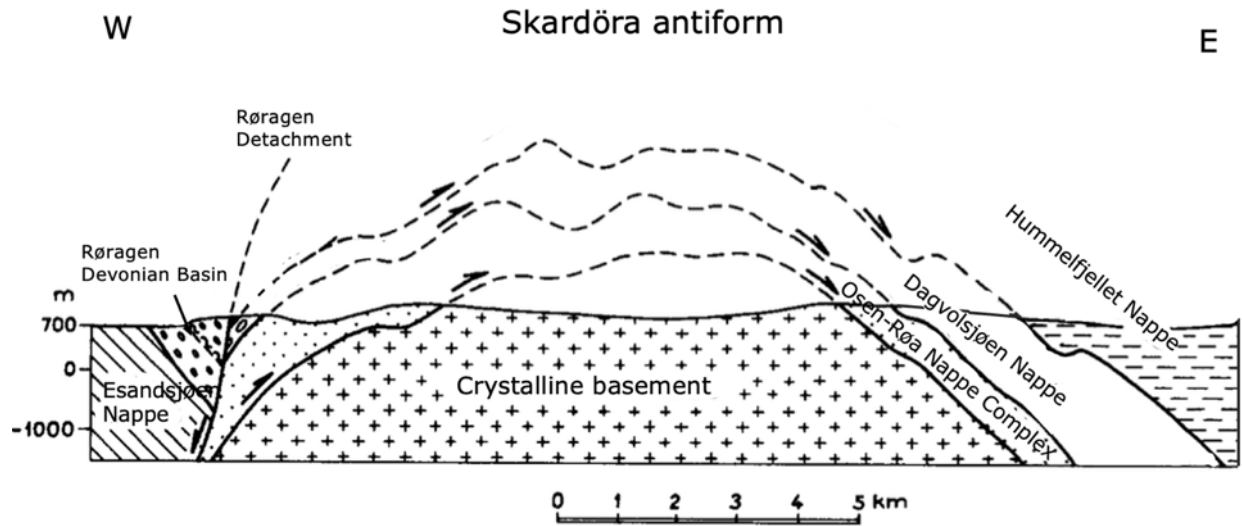


Figure 9. Profile over the Skardøra antiform. It is a generalized profile indicating the relationships between the different tectonic units, and it is not to scale. The Norwegian names have been used for all units. The figure is modified after Gee et al. (1994).

3 Theoretical background

3.1 U-Pb geochronology

One of the most important isotopic dating methods is the U-Th-Pb system, and it permits to date rocks that are up to appr. 4.57 Ga (Schoene, 2014). A common mineral used for U-Pb geochronology is zircon due to its ability to survive magmatic, metamorphic and erosional processes that normally destroy other minerals (Corfu et al., 2003). In addition, zircon incorporate uranium (U) at crystallization while lead (Pb) is being rejected. Therefore, lead hosted in zircons are radiogenic lead and not initial or common lead. Zircon is therefore near a "perfect" geochronological mineral or "clock" (Dickin, 2005). However, some complications do exist, and they will be explained later.

3.1.1 U-Th-Pb decay

The Pb content in a mineral comprises two components: (1) the non-radiogenic (the initial) Pb that is inherited from the environment during the crystallization and (2) the radiogenic Pb that is accumulated after crystallization due to decay of U and Th (thorium). The first one contains all Pb stable isotopes, which are ^{204}Pb , ^{206}Pb , ^{207}Pb and ^{208}Pb , whereas the second one only contains the last three isotopes (Vermeesch, 2020). The principle of U-Th-Pb geochronology is the decay of the unstable parent isotopes ^{238}U , ^{235}U and ^{232}Th to their stable daughter isotopes ^{206}Pb , ^{207}Pb and ^{208}Pb , respectively. None of the parent isotopes decay directly to the daughter isotope, but instead follows a chain of alpha and beta decay (Fig. 10) (Schoene, 2014). In an uranium-bearing mineral, such as zircon, the radiogenic isotopes ^{206}Pb , ^{207}Pb and ^{208}Pb will accumulate over time due to decay (Andersen, 2002).

While the half-lives of the intermediate daughter isotopes range from microseconds to hundreds of thousands of years, the three parent isotopes in the decay chain have a long half-life ($t_{1/2} \gg 0.7$ Gyr) (Bourdon et al., 2003). The final isotopes for the chains, ^{206}Pb , ^{207}Pb and ^{208}Pb , are stable. The decay chains are unique, i.e., no isotope occurs in more than one chain (White, 2014). In order to achieve secular equilibrium, the parent isotope's decay constant (λ) must be greater than that of the intermediate daughter isotope (White, 2014). Secular equilibrium is an important concept for geochronology. A decay chain is in secular equilibrium when the product of an isotope abundance and its decay constant are equal among all the intermediate isotopes that are in the decay chain. It can also be called steady state, and is given by:

$$N_1\lambda_1 = N_2\lambda_2 = N_3\lambda_3 = \dots \quad [1]$$

where N is the concentration of the parent isotopes (in moles) and λ is the decay constant.

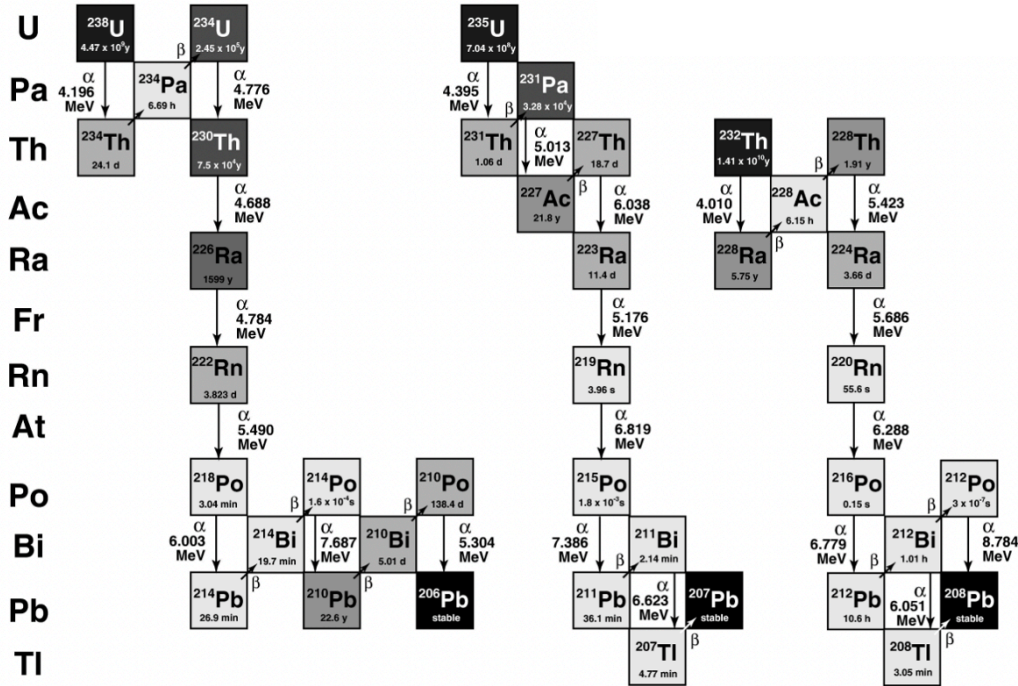


Figure 10. The three decay chains for ^{238}U , ^{235}U and ^{232}Th and their stable daughter products: ^{206}Pb , ^{207}Pb and ^{208}Pb respectively. The different nuances of grey represent half-life, with the darker the grey, the longer the half-life. The figure is from Bourdon et al. (2003).

The reaction equations for ^{238}U , ^{235}U and ^{232}Th are as following:

$$^{238}\text{U} \rightarrow ^{206}\text{Pb} + 8\alpha + 6\beta + Q; \lambda_{238} = 1.55125e^{-10} \text{ year}^{-1} \quad [2]$$

$$^{235}\text{U} \rightarrow ^{207}\text{Pb} + 7\alpha + 4\beta + Q; \lambda_{235} = 9.8485e^{-10} \text{ year}^{-1} \quad [3]$$

$$^{232}\text{Th} \rightarrow ^{208}\text{Pb} + 6\alpha + 4\beta + Q; \lambda_{232} = 4.9475e^{-11} \text{ year}^{-1} \quad [4]$$

where ^{238}U , ^{235}U and ^{232}Th are the parent isotopes, ^xPb is the stable daughter isotope, α is the alpha particle, β is the beta particle, Q is the energy released during the decay and λ_x is the decay constant.

If there is a closed system, the decay chain will reach secular equilibrium in a time that is proportional to the longest half-life amongst the daughter isotopes in the decay chain. However, the secular equilibrium or the decay chain can be disturbed if one of the isotopes is fractionated from the others. This can occur e.g. by low-temperature fractionation during chemical weathering or chemical partitioning in a magmatic system (Schoene, 2014).

3.1.2 Interpretation of U-Pb zircon ages

Three different equations can be derived if these assumptions are made: (1) independence between the three decay chains, (2) secular equilibrium and (3) no initial lead:

$$^{206}\text{Pb}/^{238}\text{U} = (e^{\lambda_{238}t} - 1) \quad [5]$$

$$^{207}\text{Pb}/^{235}\text{U} = (e^{\lambda_{235}t} - 1) \quad [6]$$

$$^{208}\text{Pb}/^{232}\text{Th} = (e^{\lambda_{232}t} - 1) \quad [7]$$

where λ is the decay constant and t is the time. These equations can be used to plot the data into diagrams, namely the Wetherill concordia diagram (plots $^{207}\text{Pb}/^{235}\text{U}$ vs $^{206}\text{Pb}/^{238}\text{U}$) and the Tera-Wasserburg diagram (plots $^{238}\text{U}/^{206}\text{Pb}$ vs $^{208}\text{Pb}/^{206}\text{Pb}$). In this thesis, the Wetherill concordia diagram is used, providing a clear representation of data.

2.1.1.1 The Wetherill concordia diagram

In 1956, Wetherill introduced the concordia diagram. The concordia diagram plots $^{206}\text{Pb}/^{238}\text{U}$ against $^{207}\text{Pb}/^{235}\text{U}$, and the concordia curve can be drawn by using the equations [5] and [6] with equal values for t (Wetherill, 1956, Schoene, 2014). This line will be non-linear due to the different half-life of ^{238}U and ^{235}U . It represents the points that have the same age for both $^{235}\text{U}/^{207}\text{Pb}$ and $^{238}\text{U}/^{206}\text{Pb}$ decay systems (Schoene, 2014).

If the sample behaved in a closed system from the time of initial crystallization, the sample would plot on the concordia curve and be concordant. However, if the system was open at some point, the sample would not plot on the concordia curve and will therefore be discordant (Schoene, 2014). The age of a concordant sample can be provided by the calculated $^{238}\text{U}/^{206}\text{Pb}$ age or by the $^{235}\text{U}/^{207}\text{Pb}$ age. Generally, it will be interpreted as a crystallization or recrystallization age. Estimation of the age of discordant analyses requires a projection onto the concordia curve, and three ways of projecting the data are demonstrated in Fig. 11 (Corfu, 2013).

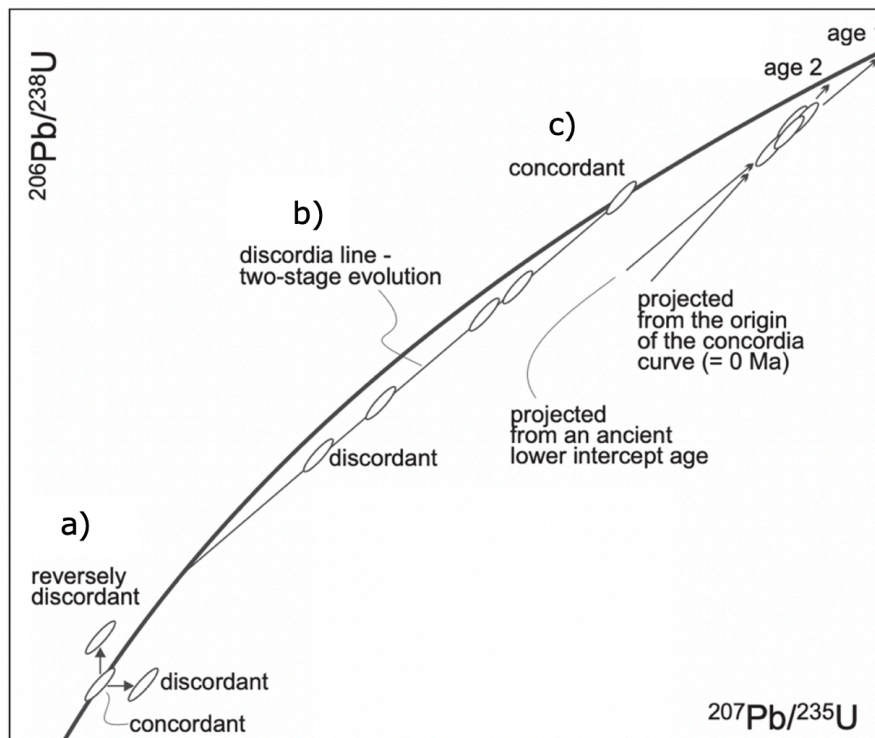


Figure 11. A Wetherill concordia diagram demonstrating different distributions of data relative to the concordia line/curve. The concordia line is curved since ^{235}U and ^{238}U have different half-lives. a) The difference between concordant samples that plot on the concordia curve and discordant samples that do not plot on the concordia curve. b) Illustration of a discordia line when different

analyses are concordant to discordant. They define a discordia line below the concordia line. The two intersections of this line with the concordia curve are called upper intercept and lower intercept where the upper intercept normally records initial crystallization of the mineral and the lower intercept records episodic Pb loss or recrystallization. c) The data is almost concordant, and the figure demonstrates two ways of projecting the analyses towards the concordia curve: (1) projecting either from a lower intercept or (2) projecting from the origin of the diagram (0 Ma). This is equivalent to the $^{207}\text{Pb}/^{206}\text{Pb}$ age. The figure is from Corfu (2013).

3.1.3 Concordant data

An analysis can be considered concordant if the 2 sigma uncertainty ellipse intersect the concordia line. The centroid can be positioned either above or below the concordia line. There are three methods to calculate the age estimate from a set of concordant analyses: (1) the weighted average $^{206}\text{Pb}/^{238}\text{U}$, (2) the weighted average $^{207}\text{Pb}/^{206}\text{Pb}$ and (3) the concordia age. The concordia age is the shortest projection of an analysis or the weighted mean for multiple analyses onto the concordia curve (Ludwig, 1998). The choice of method depends on the rock being analysed, with the weighted average $^{206}\text{Pb}/^{238}\text{U}$ generally more precise for rocks young rocks, while the weighted average $^{207}\text{Pb}/^{206}\text{Pb}$ is often more precise for older rocks (Gehrels, 2011).

3.1.4 Causes of discordance

Analyses used for U-Pb geochronology are regularly discordant (Petrus and Kamber, 2012). There are multiple known causes of discordance:

(1) Mixing of different age domains

The simplest reason for discordance is the growth of new zircon around an old core, namely rim and core. The analysis can reflect a mixture of different zones if the analytical method is not small enough to analyse different zones of a zircon. If this is the case, the analyses will be discordant and distributed along a discordia line. In this case, the upper intercept is corresponding to the primary crystallization of the core, while the lower intercept is recording the age of the formation of the overgrowth (Mezger and Krogstad, 1997, Schoene, 2014, Villa and Hanchar, 2017). Imaging of zircon with cathodoluminescence (CL) and backscattered electron (BSE) detectors in a scanning electron microscope (SEM) allows to visualize the different zones in a zircon crystal. SEM imaging provides an opportunity to target individual growth zones during analysis, making it a tool to as best as possible to avoid discordance (Fig. 12).

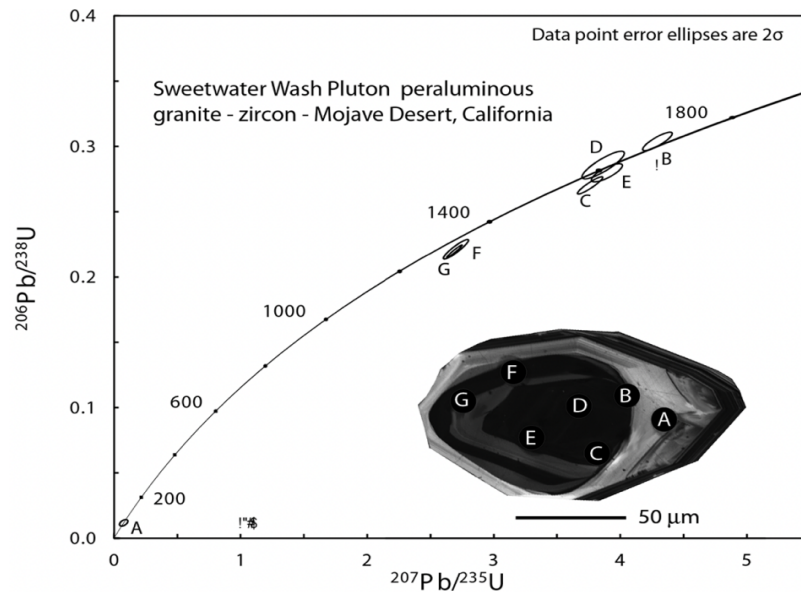


Figure 12. Wetherill concordia diagram and cathodoluminescence (CL) image of a zircon crystal. Seven analyses of a zircon were performed in the core, in the rim-core boundary and in the rim. The results are plotted in the concordia diagram. The data show that analysis A is younger than analyses B, C, D and E (the core). The figure is from Villa and Hanchar (2017).

(2) Loss of Pb

Lead loss should not occur in zircons (Schoene, 2014). Zircons do not contain Pb at crystallization, meaning that there is no good crystallographic site in zircon's lattice to incorporate Pb, and in particular radiogenic Pb. Hence, Pb is more mobile in zircon than other elements bounded in the lattice (Gehrels, 2011). Another reason for Pb mobility is the progressive destruction, or metamictization, of the lattice due to U and Th decay. Metamict zircon is prone to alteration and interaction with fluids. Therefore, metamict zircon can incorporate common lead from the surroundings (Cherniak, 2010). If a metamict zircon is in contact with fluids, loss of radiogenic Pb can take place under low-grade conditions (Villa and Hanchar, 2017). However, if the temperature is above the annealing temperature for zircon, the lattice will be repaired and the loss of radiogenic Pb will therefore be limited (Mezger and Krogstad, 1997).

(3) Intermediate daughter product disequilibrium or secular equilibrium

As mentioned earlier, secular equilibrium is an important concept in geochronology, and it is crucial for simplifying the U-Pb decay chain (Schoene, 2014). If an open system behavior occurs in the decay chain, the secular equilibrium is disturbed. During melting and metamorphism, a daughter product can be incorporated in the crystal lattice, and the analysed age will be increased due to an excess amount of radiogenic Pb. Alternatively, if the intermediate product is portioned into the melt, will there be an undersupply in radiogenic Pb and the calculated age will be too young (Schoene, 2014).

(4) The initial Pb and correction

Zircon generally does not contain any Pb at crystallization, but some common Pb can be present. This is detected by a significant signal of ^{204}Pb (Schoene, 2014). In the Wetherill concordia diagram, the presence of common lead creates a discordia line. Consequently, the data are usually corrected for common lead before being plotted based on the ^{204}Pb signal (Schoene, 2014).

(5) *Analytical*

The use of well characterized primary and secondary standards of zircons is important to calibrate the U/Pb ratio correctly. To obtain concordant analyses, correct calibration of the U/Pb ratio is vital.

3.2 Geochemistry

Whole-rock geochemical data can be used to classify rocks. They can in addition be used to identify and interpret geological processes that involve the mobility and partitioning of elements.

3.2.1 Major and trace elements

The elements that predominate in any rock analysis are known as the major elements. Major elements have a concentration greater than 1.0 wt. %, and the concentration is expressed as oxides in wt. %, such as SiO₂, FeO, MgO and Al₂O₃. In silicate rocks, the major elements are normally Si, Ti, Al, Fe, Mn, Mg, Ca, Na and K (Winter, 2014, Rollinson and Pease, 2021). The elements with a concentration in the interval between 0.1-1.0 wt. % are called minor elements. Trace elements constitute less than 0.1 wt. %, and are normally expressed as elements in ppm (parts pr. Million) (Winter, 2014, Rollinson and Pease, 2021).

The elements can be used to show relationships between elements in a rock, and these relationships can be used to interpret geochemical processes. The major elements can be used in different ways: (1) for rock classification, (2) to construct variation diagrams and (3) for comparison with known processes (Rollinson and Pease, 2021). The trace elements are more sensitive to geochemical processes than the major elements. This makes the trace elements better for petrological process discrimination (Rollinson and Pease, 2021).

3.2.2 Rare earth elements

The rare earth elements (REE) are amongst the most useful trace elements for geochemistry (Rollinson and Pease, 2021). The REE comprise a series of elements with atomic numbers 57-71, in addition to scandium (Sc) with the atomic number 21 and yttrium (Y) with the atomic number 39 (Table 1). The elements with the lowest atomic numbers are called light rare earth elements (LREE) while the ones with the higher atomic numbers are termed heavy rare earth elements (HREE) (Rollinson and Pease, 2021). REE have large ionic radiuses and they are incompatible elements. Therefore, they tend to concentrate in the melt during partial melting or fractional crystallisation (Voncken, 2016). Due to differences in size and behaviour, the REE tend to become fractionated relative to each other when exploited by different petrological processes. This makes it possible to interpret geological processes based on the pattern and shape of the REE anomalies (Rollinson and Pease, 2021).

Table 1. The atomic symbols, names and atomic numbers of the rare earth elements (REE). The table is after Voncken (2016) and Van Gosen et al. (2017).

Symbol	Name	Atomic number
Sc	Scandium	21

Y	Yttrium	39
La	Lanthanum	57
Ce	Cerium	58
Pr	Praseodymium	59
Nd	Neodymium	60
Pm	Promethium	61
Sm	Samarium	62
Eu	Europium	63
Gd	Gadolinium	64
Tb	Terbium	65
Dy	Dysprosium	66
Ho	Holmium	67
Tm	Thulium	68
Er	Erbium	69
Yb	Ytterbium	70
Lu	Lutetium	71

The REE and the trace elements can be visualised in spider diagrams. There are different types of spider diagrams with different types of elements on the x-axis and different normalization schemes (Winter, 2014). The objective is to illustrate the relative abundance of elements relative to a geochemical reservoir. One example of a geochemical reservoir is a chondritic reservoir (Rock, 1987). Often, the more incompatible elements are on the left side of the diagram. The trends on the REE diagrams are referred to as REE patterns, and it is the shape of the REE pattern that is of particular petrological interest (Rollinson et al., 2021). If the slope is negative, the more incompatible elements are more enriched (Winter, 2014). Europium may plot off the general trend of the other REE, defining a europium anomaly. If the anomaly lies below the trend, the anomaly is described as a negative anomaly. If the anomaly is above the general trend, the anomaly is described as a positive anomaly (Rollinson and Pease, 2021). Under reducing conditions, Eu^{2+} tend to substitute for Ca^{2+} in plagioclase, and it will partition into plagioclase and behave less incompatible than other REEs. Therefore, existence of an europium anomaly in a magmatic rock indicate a relatively shallow igneous partial melting in the presence of plagioclase or fractional crystallisation of plagioclase (Sverjensky, 1984, McLennan and Ross Taylor, 2011).

3.2.3 Tectonic discrimination diagrams

Tectonic discrimination diagrams attempt to link the geochemical signatures of a rock with their geotectonic setting (Fig. 13). The method uses rock suites of known geotectonic setting to study the setting of unknown rocks. The link between geotectonic environment and geochemical properties is rarely unique, so discrimination diagrams should be used with caution (Pearce, 2014). Winter (2014) advocates to use several discrimination parameters. If the same tectonic setting is proposed by different schemes, the tectonic setting can be interpreted with slightly more confidence even though the discrimination diagrams are empirical.

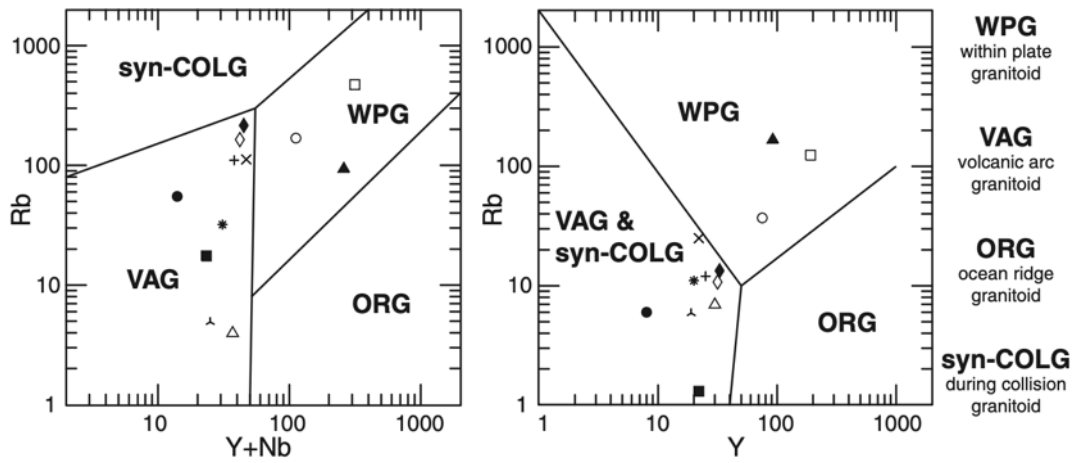


Figure 13. Tectonic discrimination diagram for granitoid rocks from Pearce et al. (1984). The diagram is using concentrations in Rb, Y and Nb. The figure is from Winter (2014).

4 Method

4.1 Field work

Fieldwork was carried out in the end of August 2022 and lasted for 12 days between 22nd of August and 2nd of September. However, during the summer 2021 when I was working at NGU, a couple of days were spent in the same area. There was no direct working with this thesis during the summer of 2021, but samples that were analysed and discussed in this thesis were collected by NGU in the framework of an ongoing mapping project.

The bedrock mapping was carried out by using *Fieldmaps*. During the fieldwork, a tablet from *Android* was used. Therefore, the tablet's GPS was used to find the accurate coordinates for the localities that were visited (Appendix A). A geological compass from *Silva* with a circular spirit level was used to measure dip direction and dip for planar features and plunge and azimuth for linear features. In addition to the tablet, a waterproof field book was used to take notes, make sketches and write down the structural measurements. All the field pictures were taken with an *iPhone 13 mini*, and they were annotated in the field to get the right spatial orientations. In the photos, different tools were used as a scale:

- My index finger on the left hand
- A sledgehammer that is 60 cm long
- A piece of waterproof paper with a north arrow that is 14 cm x 6 cm
- A Silva compass where the compass house is 10 cm x 6,5 cm
- A field notebook with the measurements 18 cm x 12 cm

In total, ten samples were collected in the field (Table 2). Eight of them are augen gneisses, in addition to one protomylonite and one granitic intrusion. The sampling was targeted, and samples from both the western (Dagvolsjøen Nappe) and eastern (TAG) limb of the Skardøra antiform were sampled to be able to compare and possibly correlate the nappes. One day was spent near Tännäs in Sweden to get a targeted sample of the TAG from its type locality to compare with the Dagvolsjøen augen gneiss. Three samples were selected specifically for geochronological analysis: (1) an augen gneiss located in the western limb of the Skardøra antiform (the Dagvolsjøen Nappe), (2) the Tännäs augen gneiss and (3) the granitic sheet emplaced in the TAG. In addition to these three samples, eight others were chosen for geochemical analysis. All these samples were also prepared as thin sections for microscopic examination. In addition, three samples (two augen gneisses and one granite exposed in the Skardøra antiform) collected by Bernard Bingen and Johannes Jakob were analysed for U-Pb geochronology and whole-rock geochemistry. The granite exposed in the Skardøra antiform was collected to test a possible resemblance in age and geochemical composition between the basement and the Dagvolsjøen augen gneiss.

Table 2. Information about the samples. Gch: Whole-rock geochemistry, U-Pb: U-Pb geochronology, Ts: Thin sections. The coordinate system is WGS84 UTM Zone 32N and 33N.

Sample	Lat.	Lon.	Rock type	Conducted analyses	Sampled by and when
BB20_20	62.60031	12.04446	Granite	Gch, U-Pb	Bernard Bingen, 2020
BB20_19	62.63592	11.90435	Augen gneiss	Gch, U-pb	Bernard Bingen, 2020
JJ23	62.63549	11.98209	Augen gneiss	Gch, U-Pb	Johannes Jakob, 2021

JJ29	62.67009	12.06386	Granite	Gch, U-Pb, Ts	Johannes Jakob, 2022
MU010	62.68408	11.99885	Protomylonite	Gch, Ts	Marte Uthus, 2022
MU016	62.68781	12.00609	Augen gneiss	Ch, Ts	Marte Uthus, 2022
MU021	62.65663	12.00072	Augen gneiss	Gch, U-Pb, Ts	Marte Uthus, 2022
MU052	62.66149	12.00290	Augen gneiss	Ts	Marte Uthus, 2022
MU108	62.65541	11.99913	Augen gneiss	Gch, Ts	Marte Uthus, 2022
MU124	62.65021	12.07077	Augen gneiss	Gch, Ts	Marte Uthus, 2022
MU126	62.48818	12.47844	Augen gneiss	Gch, U-Pb, Ts	Marte Uthus, 2022
MU168	62.67651	12.05413	Augen gneiss	Gch, Ts	Marte Uthus, 2022

4.2 Construction of maps and structural interpretation

For constructing the maps, *ArcGIS Pro* from ESRI was used. The observation points and information from Fieldmove were intergrated into ArcGIS Pro, alongside with pre-existing data from NGU. To analyse the structural data gathered in the field, the program *Stereonet v. 11.4.5* was used. In addition, structural data in the microscopic scale was obtained by examination thin sections.

4.3 Geochronology

Nine primary operations were preformed to obtain U-Pb geochronological data on the zircon: (1) preparation and cutting, (2) crushing and splitting, (3) mineral separation, (4) picking and mounting, (5) polishing, (6) SEM imaging, (7) LA-ICP-MS U-Pb analysis, (8) data reduction and (9) visualizing and interpretation of the data. Throughout these steps, the unused material got stored and labeled to ensure proper identification. In the fear of contamination, all equipment was carefully cleaned in between the different samples. In the following chapters will the steps be described in more detail.

(1) Preparation and cutting

The selected samples were cut with a diamond saw at NGU to discard weathered surfaces, prepare slabs for thin sections and reference pieces. In addition, the samples were cut for the rock crusher. The rock slabs for thin sections were forwarded to NTNU for further preparation.

(2) Crushing and splitting

To preform mineral separation and geochemical analysis, the samples were crushed in a jaw crusher. Material for mineral separation was sieved to less than 250 μm . These procedures were performed at NGU by Raghubansh Strøm Singh.

(3) Mineral separation

The mineral separation was done using the sieved fraction. Firstly, the water table was used (Wilfley water table). This step is done to separate the light minerals from the heavy ones. The light minerals flow faster down the water table than the heavy minerals. The heavy minerals were collected in one container while the light ones were collected in another. With a specific gravity of 4.6, zircon is one of the heavy minerals (Pirkle and Podmeyer, 1993). The heaviest fraction, with zircons, was then dried and used for the next mineral separation step.

The next mineral separation step was vertical magnetic separation by using the *Frantz isodynamic magnetic separator*. In this step, the heavy fraction was sent through a separator with two electromagnets. The Frantz induces a magnetic field, and minerals with higher magnetic susceptibility get attached to the paper, meaning they are separated from the less magnetic minerals. The zircons are in the category of less magnetic minerals, and this fraction was used in the heavy liquid separation.

During heavy liquid mineral separation, the aim is to get a pure fraction of heavy minerals with zircons that is separated from the lighter minerals. The heavy fraction will sink in the heavy liquid whereas the lighter ones will float. *DIM* (diiodomethane) was used as the heavy liquid, and it has a density of 3.33 g/cm³. To speed up the sinking process, the separation funnel was shaken carefully and sat to rest to let the minerals sink. This operation was repeated 3-4 times for each sample. When the heavy fraction had settled in the bottom of the separation funnel, the funnel was opened and closed quickly to move the heavy fraction from the light fraction. The minerals were then cleaned and dried.

Once again, a magnetic separator was used to separate the minerals with higher magnetic susceptibility and leave fewer, unmagnetic minerals in the fraction containing zircons. A horizontal Frantz was used after the heavy liquid separation. The horizontal Frantz was used multiple times on each sample, but with different ampere and dip angle to separate increasingly less-magnetic minerals. After these steps were done, the heavier, less-magnetic fraction with zircons were put in a petri dish.

(4) *Picking and mounting*

The picking of zircons was done with a binocular microscope, tweezer and a pipette. The microscope and the area around were cleaned, and new paper sheets were used to cover the workspace to minimize the chance of contamination. The number of zircons in the different samples varied: from thousands to only 13 in JJ29. If possible, around 30 zircons were picked and mounted for each sample. The most clear and transparent zircons were picked, ranging from rounded to prismatic. The coloured zircons were avoided, as well as the ones with inclusions and fractures. However, since some of the samples had fewer zircons, the less transparent ones with possible inclusions were also picked and mounted with the idea that they might be inherited zircons. Depending on the quantity of zircons in the samples, between 13 and 33 zircons from each sample were mounted on the same double-sided tape before the mount was cast in a 25 mm mold. *Struers EpoFix* epoxy resin was used. The mount was cured at room temperature for four days.

(5) *Polishing*

The mount was polished with 6 µm diamond pasta to expose the interior of the zircons. To make sure that the smallest zircons were not polished away, the polishing was monitored with an optical microscope in transmitted and reflected light.

(6) *SEM*

CL imaging and BSE imaging are essential aids for selecting the crystals or crystal domains for further analysis. CL images gives information about the internal structure of the zircon, while BSE imaging can be used to locate fractures and inclusions in the zircon (Schaltegger et al., 2015). The SEM work was done at NTNU by Stephanie Lode, using a ZEISS Sigma 300VP FE scanning electron microscope.

(7) LA-ICP-MS

LA-ICP-MS (laser ablation-inductively coupled plasma-mass spectrometry) analysis was done at the MiMaC laboratory at NGU under the guidance of Magdalena Huyskens. The samples were analyzed in one analytical session on the 15th of November 2022 (session 13275). The mounted zircons were ablated with a *Teledyne- Photon Machines Analyte Excite 193 nm* excimer laser. A spot analyses of 15 μm in diameter was used, and the laser was feeding a *NU Plasma 3 multicollector ICP-MS*. Daly detectors measured ^{206}Pb and ^{207}Pb , giving high sensitivity. The settings that were used are summarized in Table 3.

Table 3. The settings used for the LA-ICP-MS analysis at the MiMaC laboratory at NGU.

Setting	
Laser spot size	15 μm diameter
Shot count	120
Repetition rate	6 Hz
Fluence	2 J/cm ²
Laser output	41,3 %
Actions at Start of Ablation Pass (Pause)	30.0 seconds
Actions at Start of Each Pattern (Pause)	15.0 seconds
Actions at End of Each Pattern (Pause)	5.0 seconds

Calibration of the Pb isotopic composition and the U/Pb ratio of the zircons were performed with characterized standards of zircons (Table 4). In the analytical protocol used in this study, *GJ1* and *91500* were used as the primary standards. These were analysed at regular intervals with one analysis of each standard every fifth analyses of unknown. In addition, the reference zircons *Plesovice*, *Z-6412* and *Kara* were used as secondary standards. The secondary standards were also analysed at regular intervals, but with a lower frequency than the primary standards. The standards were used to evaluate the quality of calibration and the quality of data.

The CL and BSE images were used to select the locations of the laser ablation spots in the zircons. The CL images of zircon suggest that most crystals grew during a single magmatic event. However, some of the crystals exhibit a core that might represent inherited zircon, patchy zones that could represent zircon recrystallization or a thin rim. The rim could represent metamorphic overgrowth. Different zones with different CL intensity were targeted, trying to avoid analysis locations between two zones. Five of the zircon crystals were analysed in two locations: one in the centre and one in the rim/outer zonation.

Table 4. The standards with the respective ages that were used when analysing the zircons with LA-ICP-MS at NGU.

Standard	Age
GJ1	607 \pm 0.4 Ma (Jackson et al., 2004)
91500	1065 Ma (Wiedenbeck et al., 1995)
Plesovice	337 \pm 0.7 Ma (Sláma et al., 2008)
Z-6412	Age c. 1160 \pm 1.6 Ma
Kara	Age c. 2625 Ma

(8) Data reduction

Data reduction was done with the software *iolite v. 4*. This program reduces vast arrays of data in a short time frame (Petrus and Kamber, 2012). *iolite* calculates the signals of the baseline, samples and the standards. Two levels of propagation errors are performed in the program: (1) internal uncertainty, which is the baseline and standard interpolation and (2) external uncertainty, which is the uncertainty on the standards and decay constants. For this study, the uncertainties are at the 2 sigma level. Analyses that showed common Pb (^{204}Pb), poor counting statistics, widely discordant ratios or widely distinct ages were filtered away. The data reduction was done on both the GJ1 and 91500 as the primary standard.

(9) Visualizing and interpretation of the data

The program *IsoplotR v. 5.1* was used to interpret and visualize the data (Vermeesch, 2018). This program makes the plots and calculate the ages for a set of selected analyses. With this program is it possible to remove discordant analyses for plotting and age calculations. Both GJ1 and 91500 standards were plotted in *IsoplotR* to see which primary standard that should be selected. The data sets were very consistent with using both primary standards, and could therefore be used. However, the standard Plesovice plots marginally differently using GJ1 or 91500 as primary standard (Fig. 14). By using 91500, the analyses are slightly more concordant and grouped. Consequently, the primary standard 91500 is used for all samples.

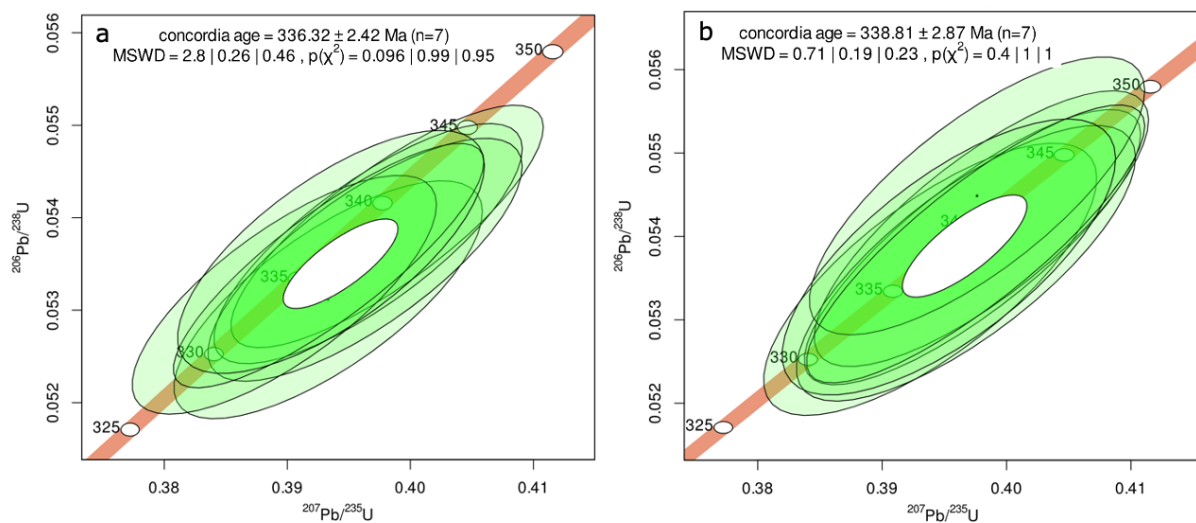


Figure 14. Concordia diagrams for the standard Plesovice with known age off 337 Ma (Sláma et al., 2008). Each analysis ($n=7$) is represented by a 2 sigma error ellipse. The concordia curve is represented by a brown band, and it is encompassing the uncertainty in the decay constants. The concordia age is the shortest and most probable projection of the white ellipse (the average ellipse of the n analyses) on the concordia curve (Ludwig, 1998). A concordia age can only be provided for a set of concordant analyses, meaning analyses with a green ellipse intersecting the concordia curve. The concordia age is provided with a 2 sigma error. The 2 sigma includes the error on decay constants. a) Concordia age of 336 ± 2 Ma for using GJ1 as primary standard. b) Concordia age of 339 ± 3 Ma using 91500 as primary standard.

4.4 Geochemistry

The first two steps described under section 4.3 *Geochronology* were also done for the geochemical analysis. For the whole-rock geochemical analysis, appr. 40 grams of crushed material was split and powdered in a disk mortar of agate before further

analysis. Furthermore, three methods were done to obtain the whole-rock geochemical data: (1) XRF (X-Ray Fluorescence) spectrometry at NGU, (2) LA-ICP-MS at NGU and (3) ICP-MS at NTNU at the Department of Geology and Mineral Resources Engineering.

To determinate the concentration of the major elements, XRF at NGU was done. This was done on all the samples. LA-ICP-MS at NGU was exclusively done on the samples BB20_19 and BB20_20 since they were sampled prior to the field work for this study. The sample JJ23 was only analysed with XRF at NGU. ICP-MS at NTNU was done by Laurentius Tjihuis for the samples sampled by me, and two different methods were used: (1) flux method and (2) hot acid digestion (HNO_3). The flux method was done first, but due to several of the REE being below the detection limit, the other dissolution procedure was done. At NTNU, only the trace elements were analysed.

Since different methods were used to obtain the geochemical data, a consolidation of the data was done for the best outcome. Which method that was used is in Appendix D. The elements analyzed using multiple techniques were carefully evaluated, taking into consideration the obtained results and detection limits. If the result for an element were under the detection limit, the corresponding method was not used for that specific element. The same applied if one sample was below the detection limit for the method. In cases where the results were above the detection limit for all samples, the method with the results furthest away from the detection limit was chosen. For elements suspected to reside in minerals resistant to acid digestion, analysis was conducted using XRF or the flux method, despite the higher detection limits.

For the plotting and visualizing the geochemical data, the statistical programming language *R* version 4.1.3 was used with the package *The GeoChemical Data ToolKIT* version 6.1, GCDkit for short, by Janoušek et al. (2006). GCDkit is a software tool used to handle and recalculate geochemical whole-rock data for igneous and metamorphic rocks (Janoušek et al., 2006).

5 Results

During the field work, a total of 198 observation points were collected (Fig. 15). The coordinates of each observation point alongside with the rock type observed can be found in Appendix A.

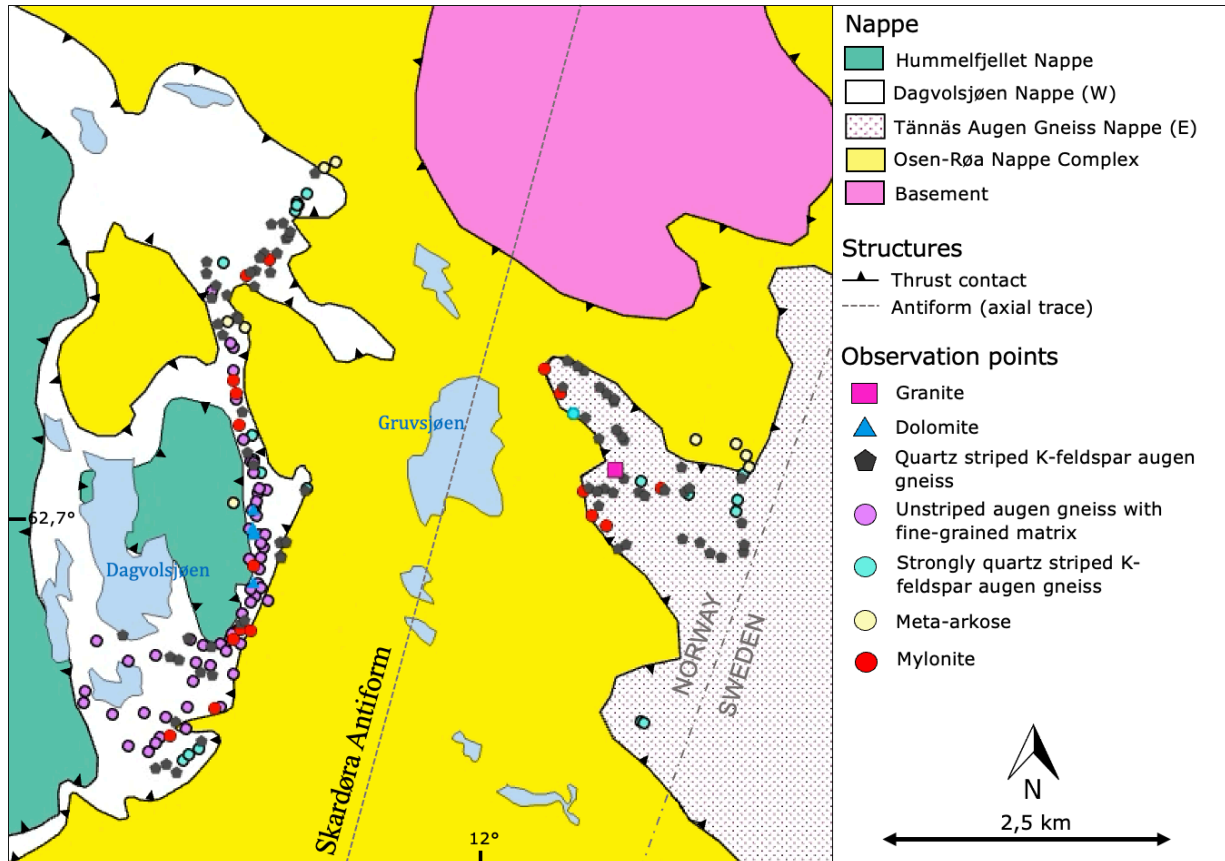


Figure 15. Geological map over the study area with my observation points from the field work in 2022. The coordinate system is WGS84 UTM Zone 32N and 33N.

5.1 Lithological descriptions

In this study, the augen gneiss assigned to the Dagvolsjøen Nappe is mapped and divided into three different variants based on the matrix characteristics: (1) quartz striped K-feldspar augen gneiss, (2) unstriped augen gneiss with homogenized fine-grained matrix and (3) strongly quartz striped K-feldspar augen gneiss (Fig. 16). Even though the matrix is different for the different variants of the Dagvolsjøen augen gneiss, all of them exhibit a greenish colour and the matrix flows around the ovoidal porphyroclasts, commonly referred to as augens. The augens of K-feldspar are in the size range of ~0.5-15 cm. The augens are heterogeneously distributed, and the rocks are leucocratic. Subsequently, the different augen gneiss variations will be described from the most abundant to the least abundant, alongside the fine-grained and muscovite-rich rock, the Tännäs augen gneiss, the mylonites and the granitic intrusion.

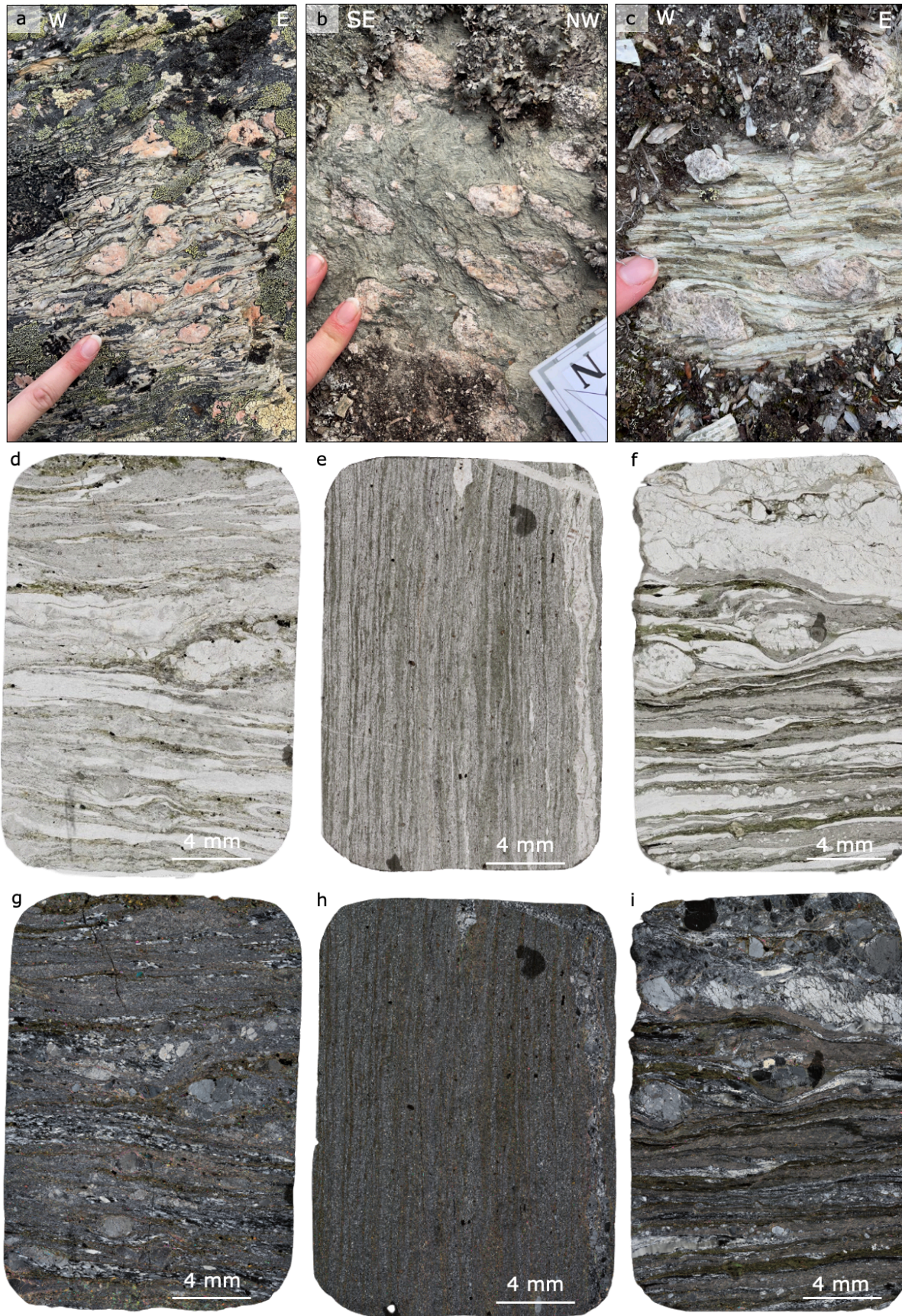


Figure 16. The different variants of the augen gneiss in the Døgvolsjøen Nappe. a) Field photo of the quartz striped K-feldspar augen gneiss at MU021. b) Field photo of the unstriped augen gneiss with homogenized fine-grained matrix at MU052. c) Field photo of the strongly quartz striped K-feldspar augen gneiss at MU124. d) Scan photo of the thin section from MU021 (PPL with

magnification 5x). e) Scan photo of the thin section from MU052 (PPL with magnification 5x). f) Scan photo of the thin section from MU124 with 5x magnification (PPL). g) XPL of d). h) XPL of e). i) XPL of f).

5.1.1 Quartz striped K-feldspar augen gneiss

The quartz striped K-feldspar augen gneiss is abundant in both the eastern and western limb of the Skardøra antiform (Fig. 15). When the surface is weathered, the augen gneiss has a pale greenish or a rusty-orange coloured matrix (Figs. 17a-b and 18a). The matrix is greyer and darker green in colour where the surface is fresher (Fig. 17c and 18e). The matrix is medium to coarse grained and consist of bands of quartz- and feldspar-rich domains and mica-rich domains, hence the appearance of a stripy matrix. Colours of the bands vary slightly from a more transparent colour to milk-white and a more greyish colour, and the bands are in the mm-scale. The thickness of the bands is between 1-3 mm. The matrix consists of quartz, feldspar (K-feldspar and minor plagioclase) and different types of micas, where biotite is dominating. There is minor muscovite and chlorite, in addition to minor epidote and titanite. There is mineral segregation between mica-rich and quartz-rich domains.

The augen gneiss has pink augens of K-feldspar (Figs. 17 and 18). The size of the augens ranging from mm-scale to cm-scale, and the biggest is 13 cm in diameter while the smallest is ~0.5 cm in the field. On average, the augens have a diameter of 3-4 cm, with very few being smaller than 1 cm. This is consistent in the whole field area. The augens exhibit diverse shapes, depending on the plane of observation, as the augen gneiss is a L-S tectonite. The shape of the feldspars varies from stretched too angular and circular. It was also observed augens that are boudinaged (Fig. 18c). By measuring the aspect ratio of the augens, only a few augen appear angular, and most of the augens are stretched with a lensoid shape.

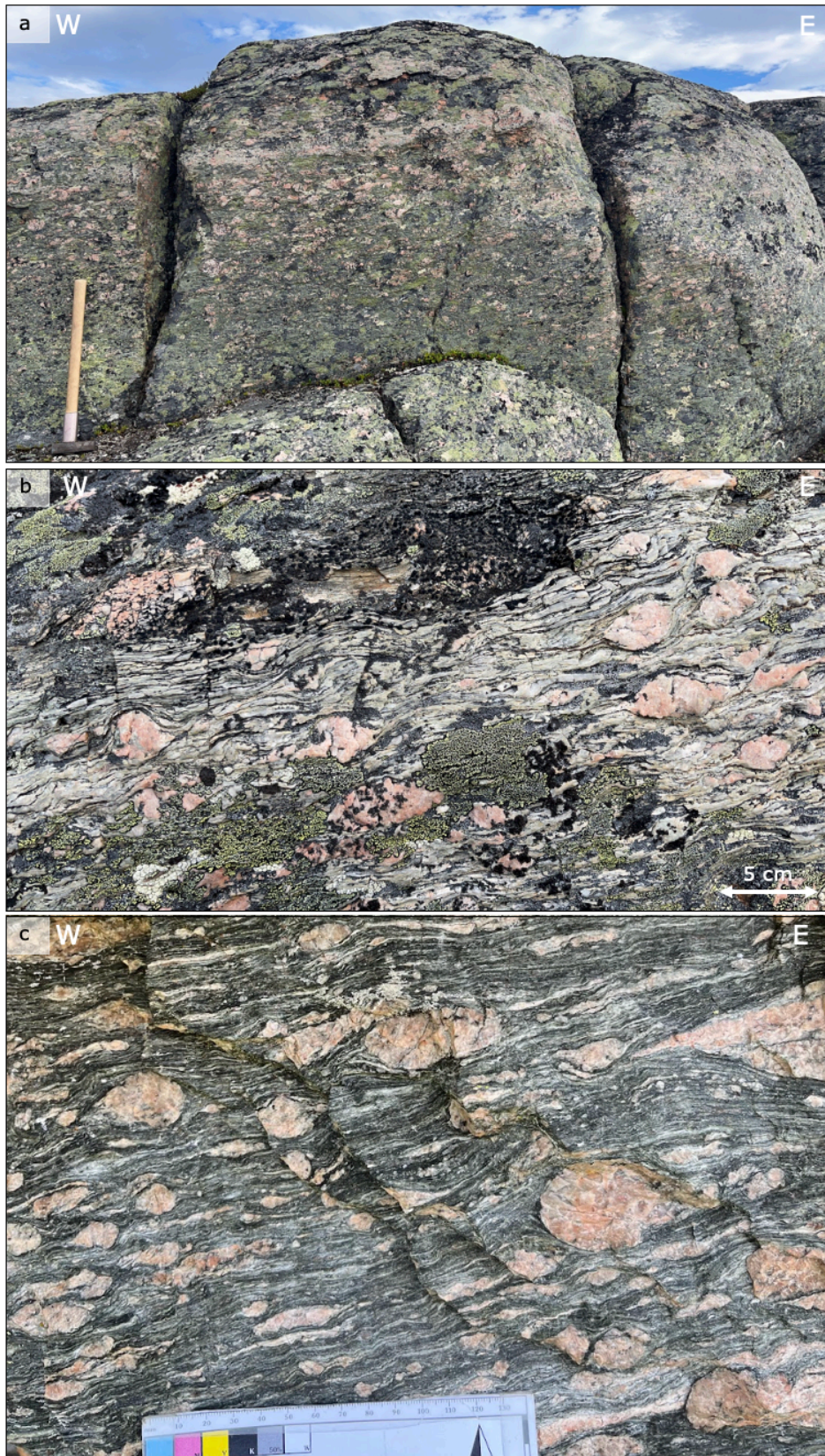


Figure 17. The quartz striped K-feldspar augen gneiss. a) Overview picture over locality MU021. b) Close-up of the wall in a). The picture shows the pink K-feldspar augen and the quartz bands. The surface has a light green colour due to weathering. c) A fresher surface with a darker grey and greenish colour compared to a weathered surface. This is from the locality MU193.

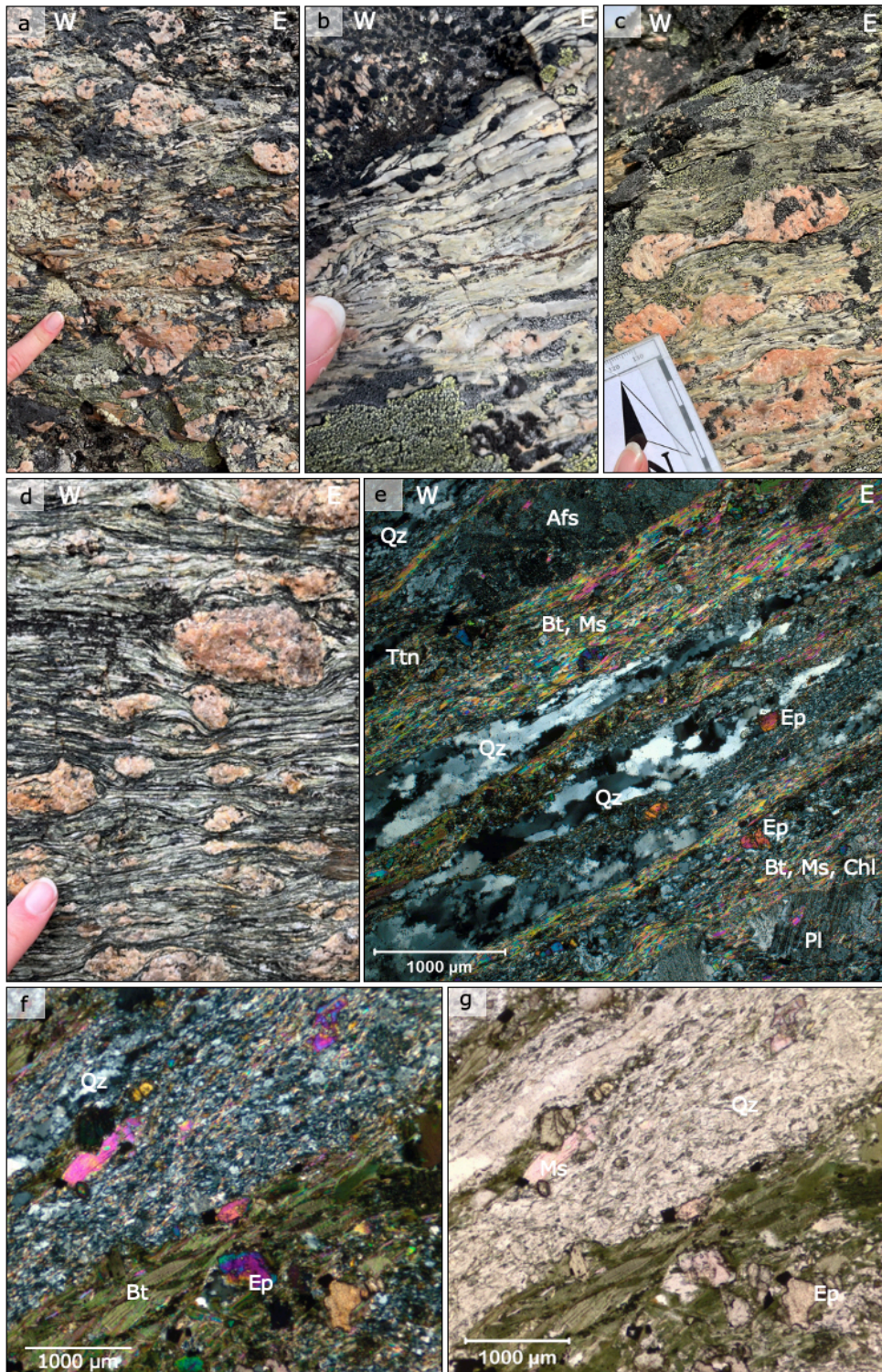


Figure 18. Matrix and augens of the quartz striped K-feldspar augen gneiss. a) Multiple localities have a rusty appearance. This is from MU133. b) When the surface is weathered, the matrix has a light greenish colour, in addition to the white quartz bands. c) A boudinage-augen of K-feldspar at locality MU021. d) Different sizes and shapes of K-feldspar augens in a dark grey and green matrix. This is at locality MU137. e) Thin section micrograph of MU021 indicating that there are mineral segregation between quartz- and feldspar-rich and mica-rich domains (XPL, 2.5x magnifying). f) Zoom-in micrograph of biotite, muscovite and epidote (XPL, 5x magnification). g) PPL image of f).

One locality has a coarser grained quartz striped K-feldspar augen gneiss, known as locality MU016 (Fig. 19). The augens of K-feldspar are more equidimensional. Dark

inclusions of biotite in some K-feldspars were observed, and they could have been caught under the growth of the feldspar (Fig. 19d). This locality has more epidote and plagioclase than the other localities with quartz striped K-feldspar augen gneiss (Fig. 20c-f), in addition to larger grains of K-feldspar than the other localities with sizes up to 15 cm. The quartz bands that are in a milky-white colour and they are in the mm-scale.

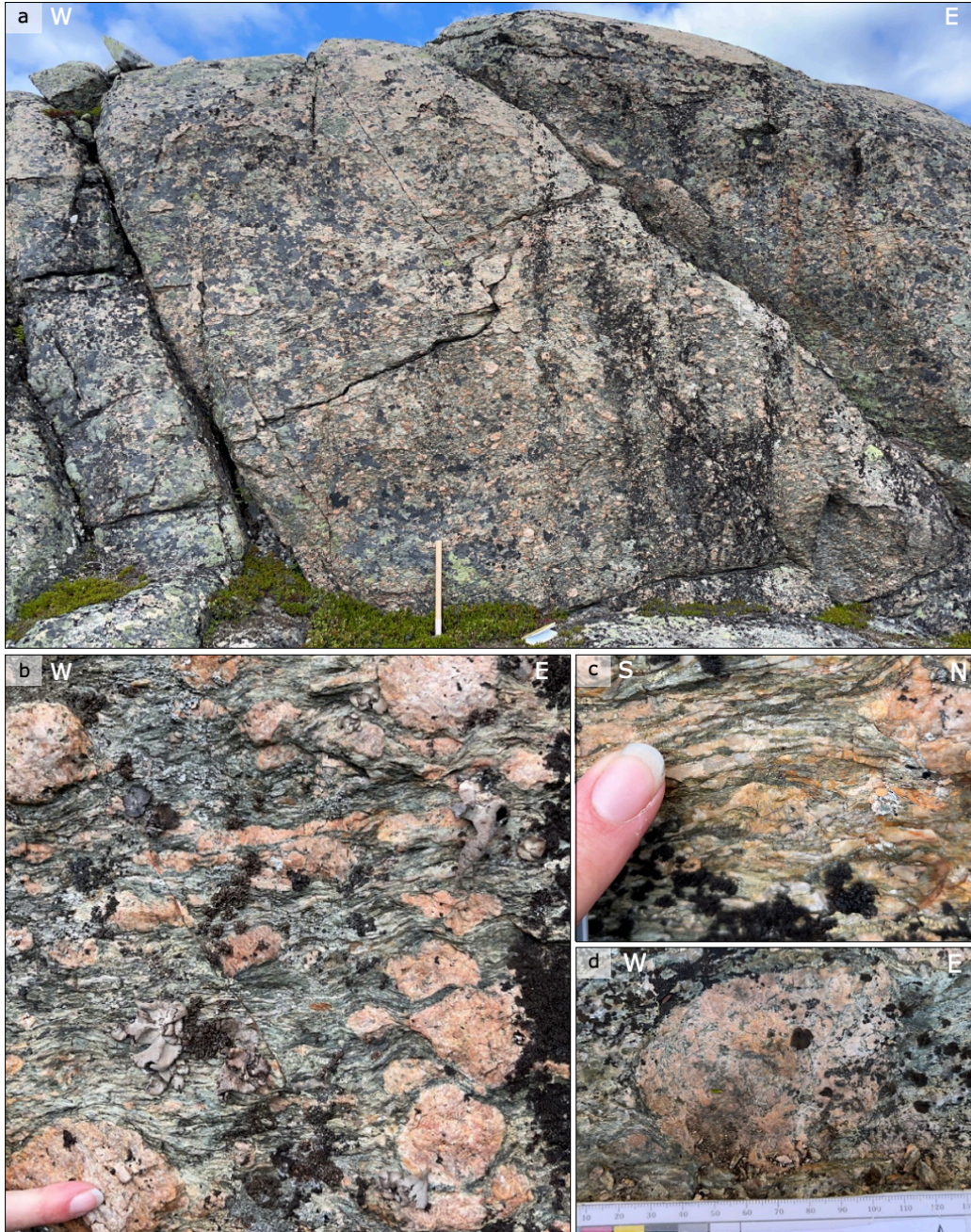


Figure 19. The locality MU016 is a coarser grained quartz striped K-feldspar augen gneiss. a) Field photo over the locality. b) Close-up of the K-feldspar augens in a quartz banded matrix. c) Close-up of mm thick quartz band. d) K-feldspar augen with inclusion of biotite.

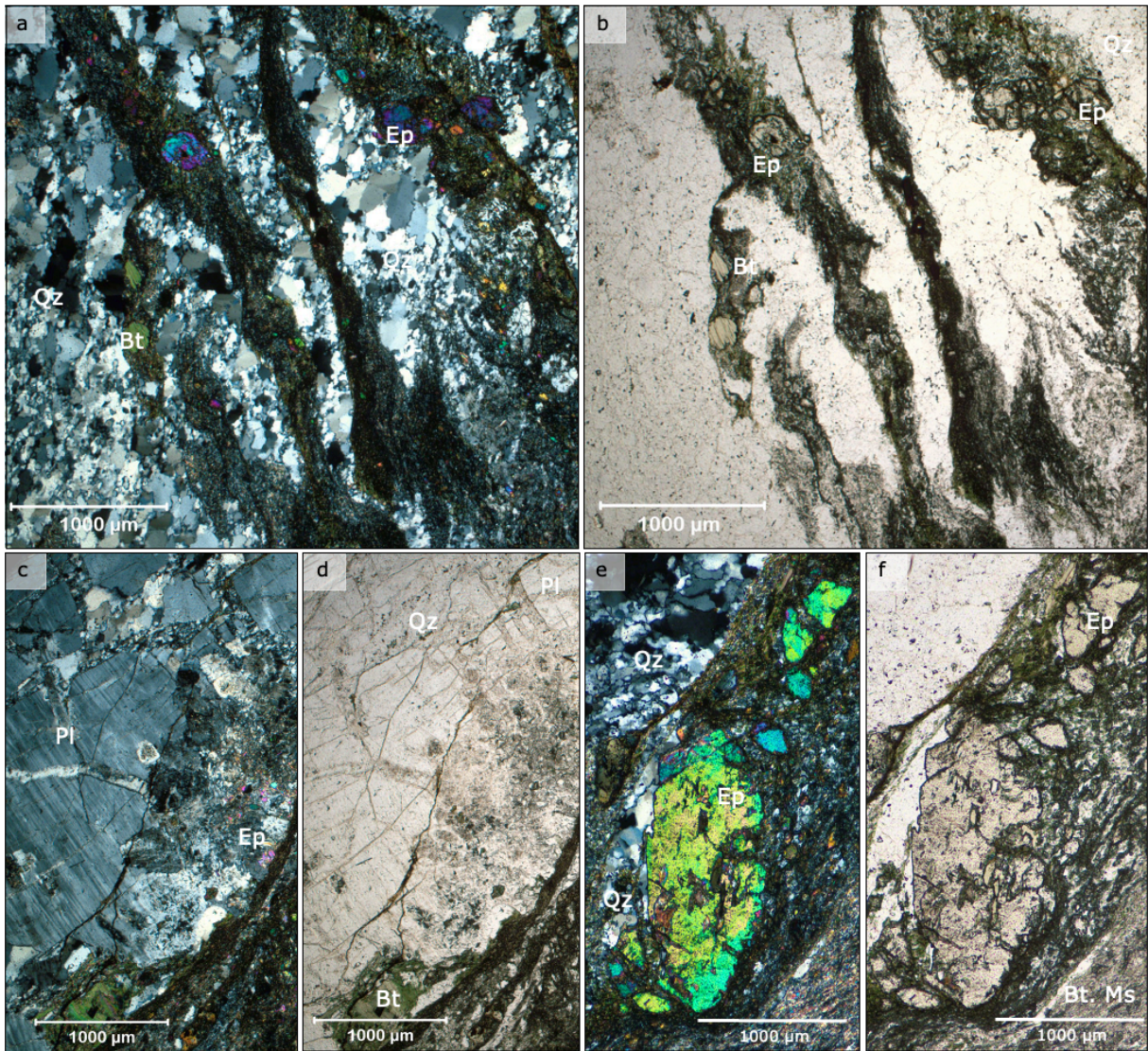
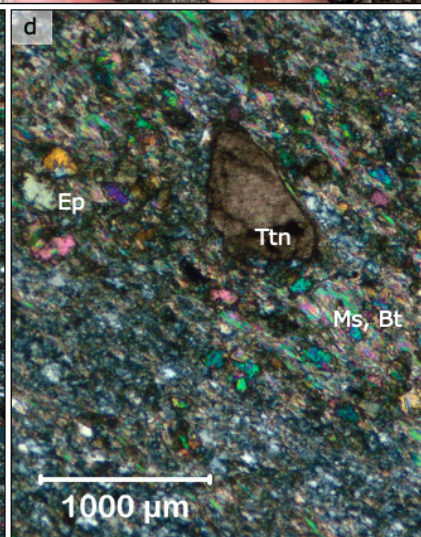
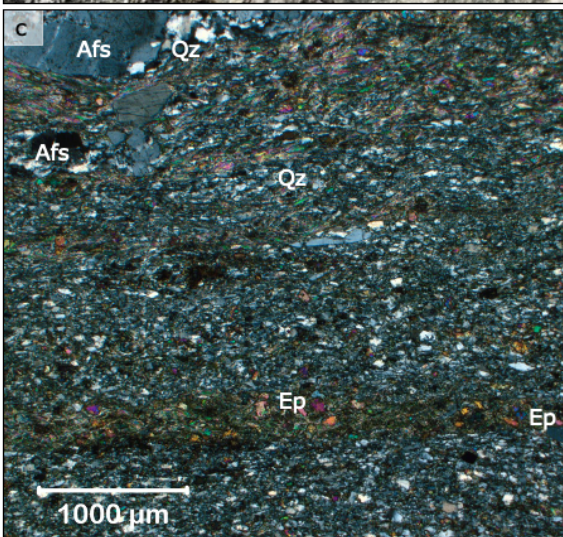


Figure 20. Micrographs of the thin section from MU016. a) XPL micrograph with 2.5x magnification. There is mineral segregation between quartz-rich and mica-rich domains where biotite is the dominant type of mica. Epidote is also present. b) PPL of a). c) XPL micrograph with 2.5x magnification. The thin section micrograph shows that this rock contains plagioclase, quartz, mica and epidote. d) PPL of c). e) XPL zoom-in micrograph of epidote (5x magnification). f) PPL of e).

5.1.2 Unstriped augen gneiss with fine-grained matrix

The unstriped augen gneiss with fine-grained matrix is characterized by K-feldspar augens in a fine-grained matrix lacking the quartz bands of the quartz striped K-feldspar augen gneiss. The unstriped augen gneiss has matrix that is light grey to light green in colour (Fig. 21a). This variant of the augen gneiss has faint segregation between quartz-rich and biotite-rich domains. The biotite is both green and brown in colour, and the rock also contains K-feldspar and minor muscovite, epidote, titanite and chlorite (Fig. 21).

The pink/salmon pink to white augens of K-feldspar are present. The different outcrops have augens of different sizes and shapes, ranging from mm to cm where the biggest is 8 cm. The feldspar augens covers the spectra from angular to subrounded, to stretched. However, almost all of the outcrops only have one plane to investigate.



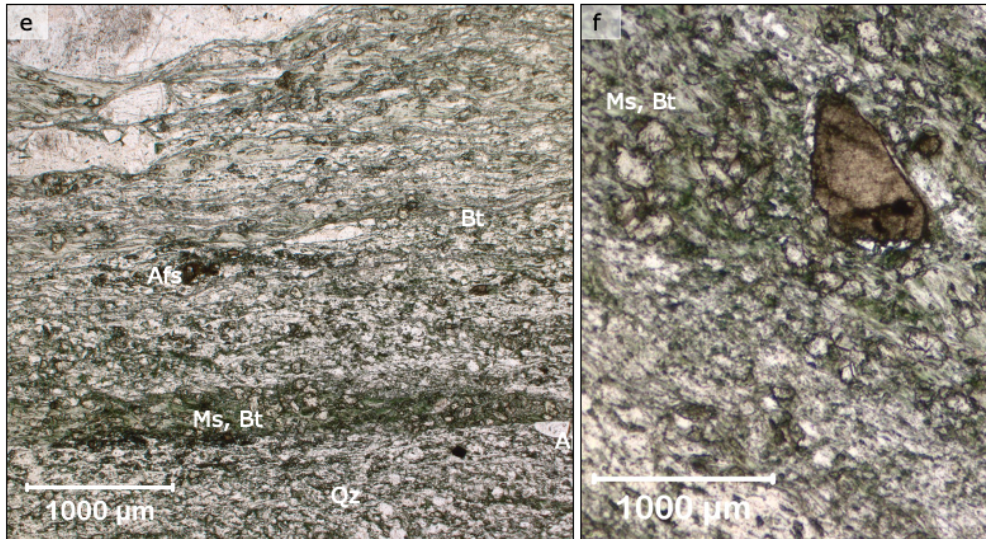


Figure 21. The unstriped augen gneiss with fine-grained matrix. a) Field photo of locality MU026. The matrix is fine-grained, and it is green-grey in colour. There are augens of K-feldspar. b) Field photo from locality MU052. c) Thin section micrograph showing that the matrix contains quartz, micas (biotite, muscovite and minor chlorite) and epidote. There is a faint segregation between the quartz-rich and the biotite-rich domains (XPL, 5x magnifying). d) 5x magnification micrograph in XPL of titanite, biotite, muscovite and epidote. e) PPL image of c). f) PPL image of e).

5.1.3 Strongly quartz striped K-feldspar augen gneiss

The last variation of the augen gneiss is the strongly quartz striped K-feldspar augen gneiss (Fig. 22). This variant of the augen gneiss has quartz banded, and the bands are milk-white in colour. A distinct contrast can be observed between the white quartz bands and the military green-coloured matrix (Fig. 2a-b). This is due to a significant mineral segregation between quartz-rich and the mica-rich domains. The darker bands are dominated by biotite (both green and brown in colour), but there are minor muscovite and chlorite. The bands are in the mm-scale and are up to 1 cm thick. In addition, the matrix also consists of minor epidote and ilmenite. Both plagioclase and K-feldspar are in the matrix, but K-feldspar is the dominating feldspar (Fig. 22c-e).

All the outcrops studied consist of the light pink/salmon pink K-feldspar augens that vary in shape and size. The largest augen is 10 cm in diameter, but the average size is ~5 cm. The shape of the augens vary from circular to angular, depending on the plane of observation.

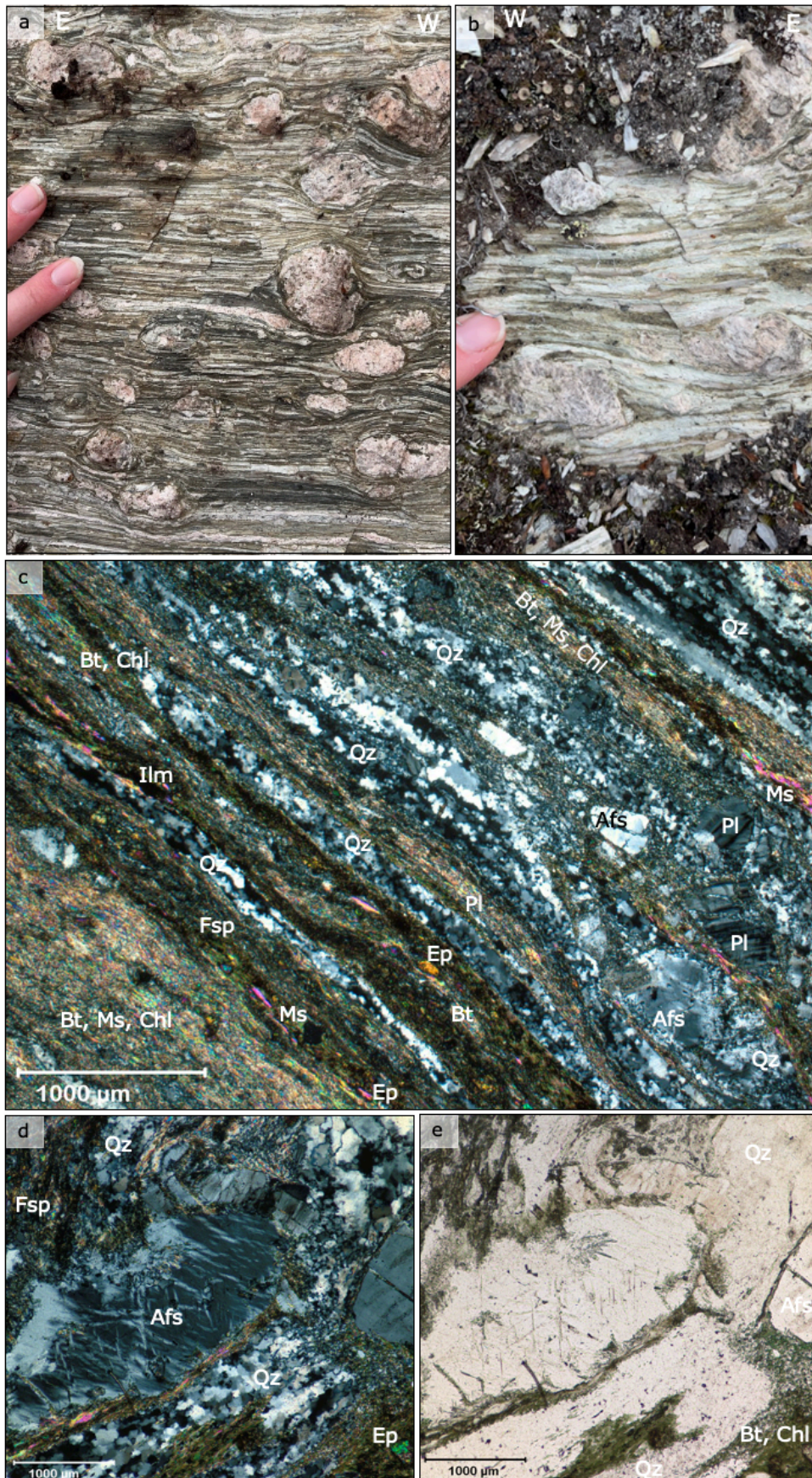


Figure 22. Strongly quartz striped K-feldspar augen gneiss. a) Field photo of the locality MU045. The matrix has quartz bands and in addition to augens of light pink K-feldspar in the cm-scale. b) Field photo from locality MU124. c) XPL thin section micrograph of MU124 with the magnification

2.5x. The micrograph shows that the matrix consists of bands of quartz and mica, in addition to K-feldspar, plagioclase and epidote. The stripy appearance is due to significant mineral segregation.

d) XPL micrograph of MU124 with magnification 5x. The rock consists of K-feldspar (here: perthite), micas (biotite and minor muscovite and chlorite) and minor epidote. e) PPL micrograph of d).

5.1.4 Fine-grained and muscovite-rich rock

In the field, a fine-grained and muscovite-rich rock was observed. When observed in the field, it looked like the unstriped augen gneiss with fine-grained matrix, but with smaller K-feldspar augens in the mm-cm scale. Therefore, this rock was interpreted to be an augen gneiss. However, further investigations indicate that it is not an augen gneiss, but rather a metasediment (section 5.4 Geochemistry).

The matrix is light grey (Fig. 23a). It does not have quartz bands, however, the matrix is quartz-rich (Fig. 23b). The matrix also consists of muscovite, K-feldspar and minor epidote and opaque minerals where the muscovite defines a continuous foliation (Fig. 23b-c). The K-feldspar augens are up to 2 cm in size, but the majority are c. 1 cm in size, both in the field and in thin section.

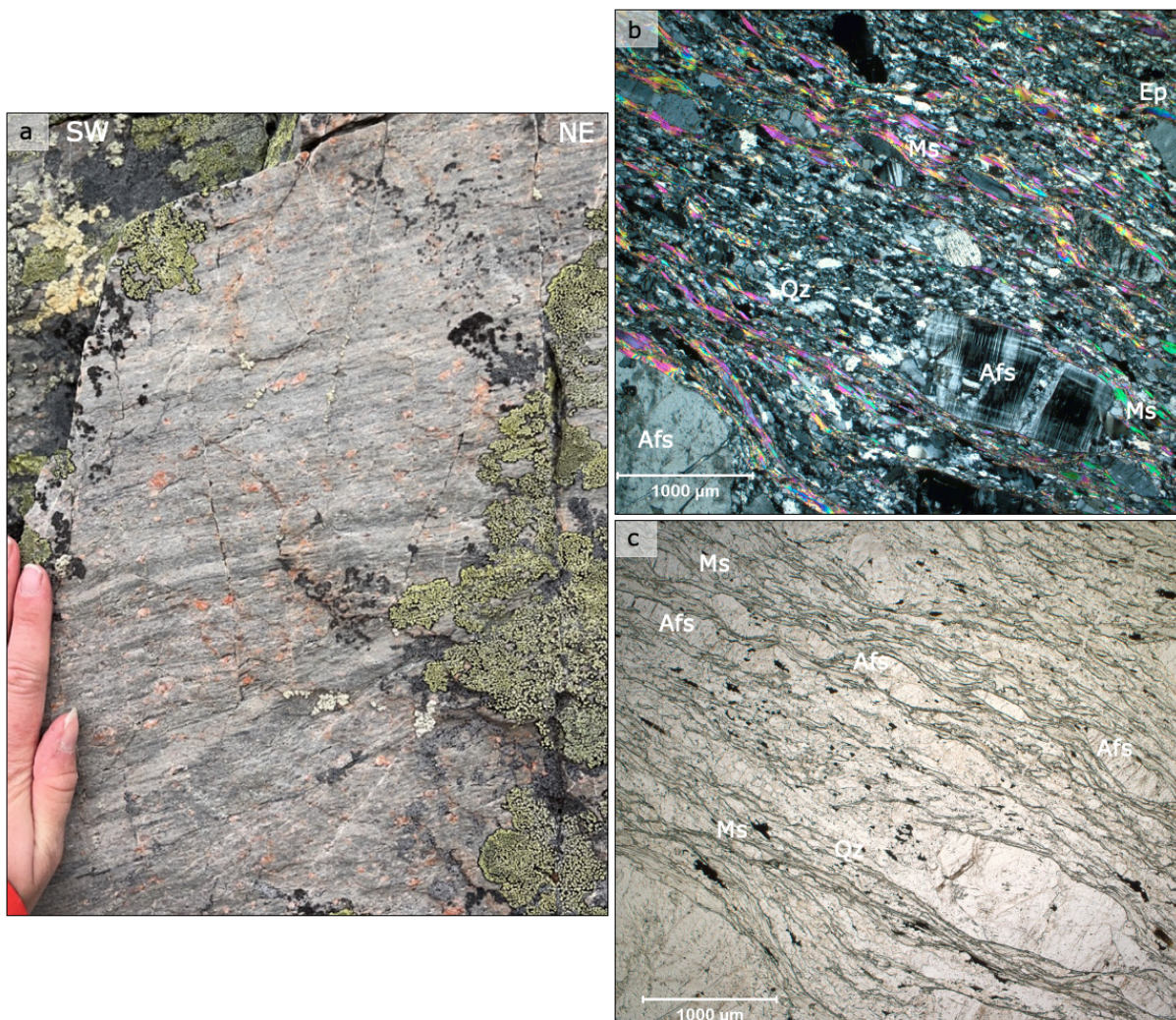
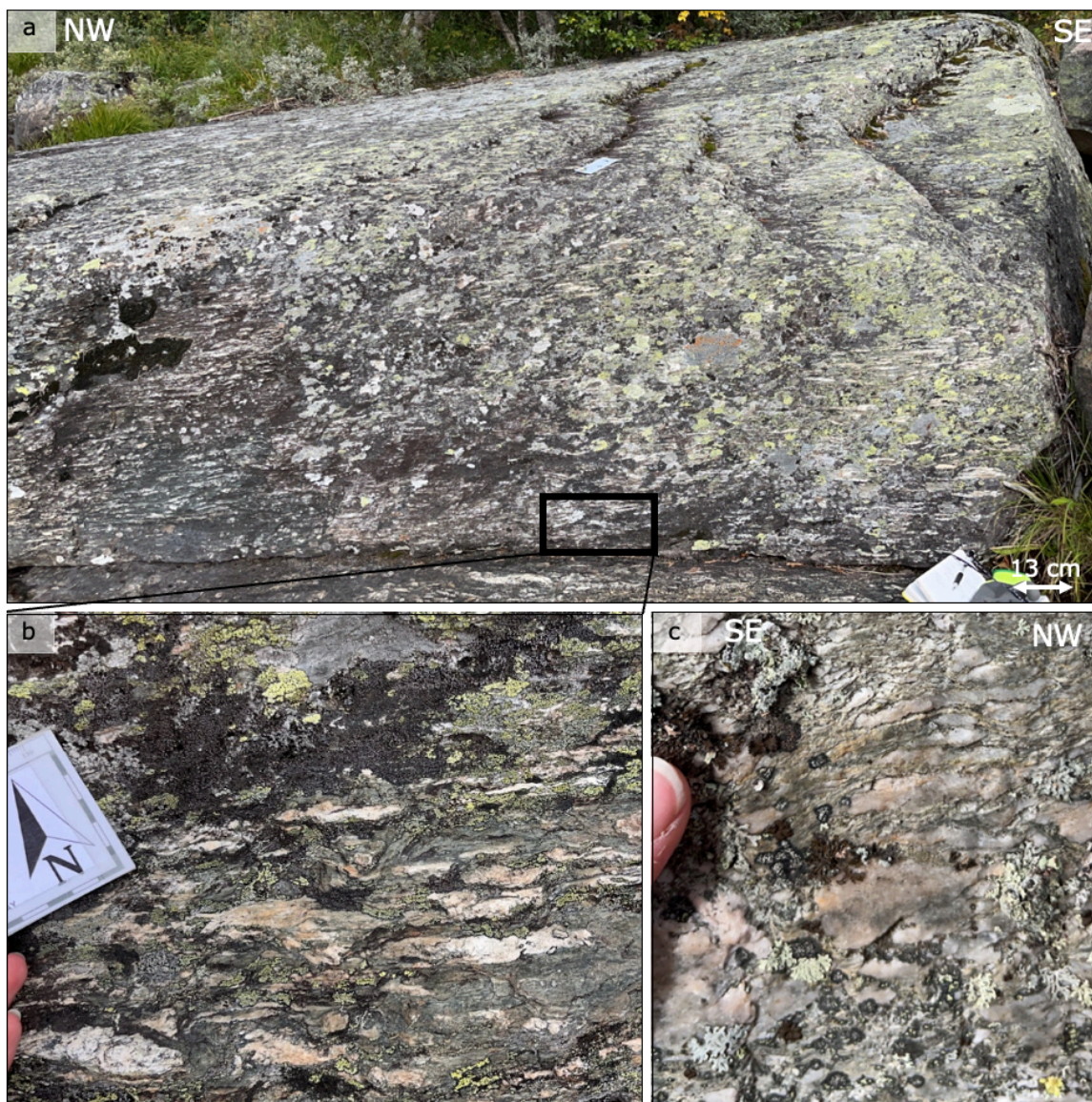


Figure 23. The fine-grained and muscovite-rich rock at the locality MU108. a) Field photo. The matrix is very fine-grained and has a light grey colour with augens of K-feldspar up to 2 cm in size.

b) Thin section micrograph with 5x magnification (XPL). The thin section consists of quartz, K-feldspar, muscovite and minor epidote and opaque mineral(s). c) PPL images of b).

5.1.5 The Tännäs augen gneiss

Two localities located close to the Swedish village Tännäs were investigated (MU125 and MU126). The Tännäs augen gneiss has matrix that is grey in colour and it has quartz bands, categorizing it as the quartz striped K-feldspar augen gneiss variant (Fig. 24a-b). However, the quartz bands are not very abundant. On fresh surfaces, micas could be observed. Both biotite, muscovite and minor chlorite are identified. In addition, K-feldspar, epidote and minor plagioclase are in the matrix. The Tännäs augen gneiss has mineral segregation between quartz-rich and mica-rich domains (Fig. 24c-d). The K-feldspar augens range in colour from light pink to white, and they are elongated. The longest K-feldspar augen was measured to be 8 cm in length and 2 cm thick.



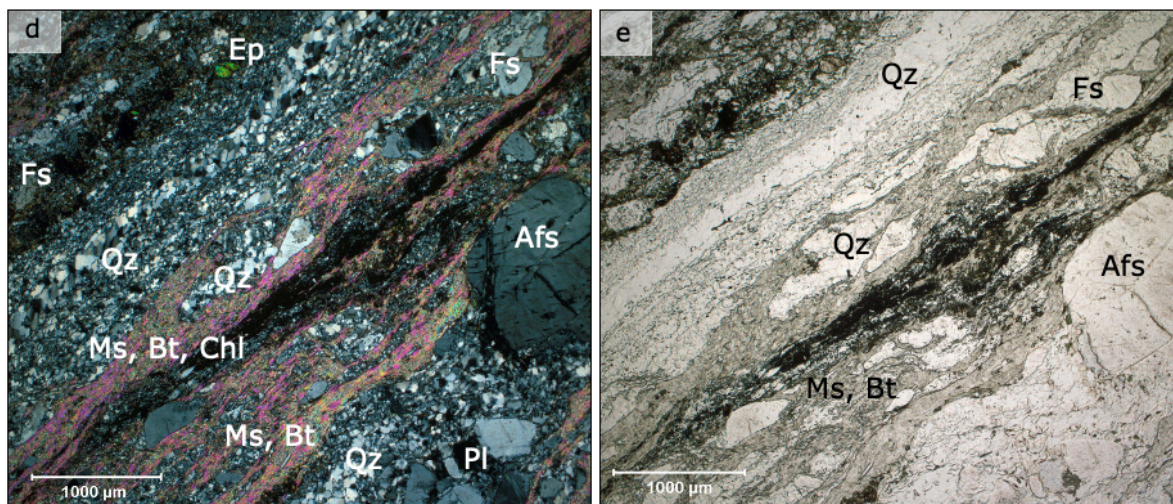


Figure 24. The Tännäs augen gneiss. The Tännäs augen gneiss has matrix that is fine-grained and grey in colour. The K-feldspar augens are elongated and the rock has a few quartz bands. a) Overview picture of the locality MU125. This rock is foliated, and the foliation is 241/06 (dip-direction/dip). The K-feldspar augens are elongated, and they give a lineation, which is 285-06 (plunge-azimuth). b) Close-up inside the black rectangle in a). The close-up shows the light pink to white K-feldspar augens that are elongated in a grey matrix. c) Close-up picture of quartz bands in the mm-size. d) XPL micrograph from MU126 with magnification 2.5x. The matrix has mineral segregation between quartz-rich and mica-rich domains. K-feldspar, plagioclase and epidote are present. e) PPL of d).

5.1.6 Mylonite

Mylonites are widespread throughout the study area, occurring on both limbs of the Skardøra antiform. This includes protomylonites, mylonites and ultramylonites are observed. All the mylonites are fine-grained and grey-greenish in colour (Fig. 25). The protomylonites contain pink K-feldspar porphyroclasts that are elongated, and they are up to 1 cm thick. In the mylonites, the K-feldspar porphyroclasts are light pink to pink and elongated, although they are less abundant compared to the protomylonites (Fig. 25a-b). The ultramylonites are very fine-grained, and some of them lack porphyroclasts. If the ultramylonites have porphyroclasts, the porphyroclasts are pink in colour and in the mm-scale, up to 0.7 mm (Fig. 25c).

One protomylonite was sampled. By examination of the thin section, this protomylonite has matrix consisting of K-feldspar, quartz, chlorite, biotite, muscovite and minor plagioclase. However, a large portion of the matrix consists of very fine-grained feldspar that is broken up to determine the mineralogical composition.

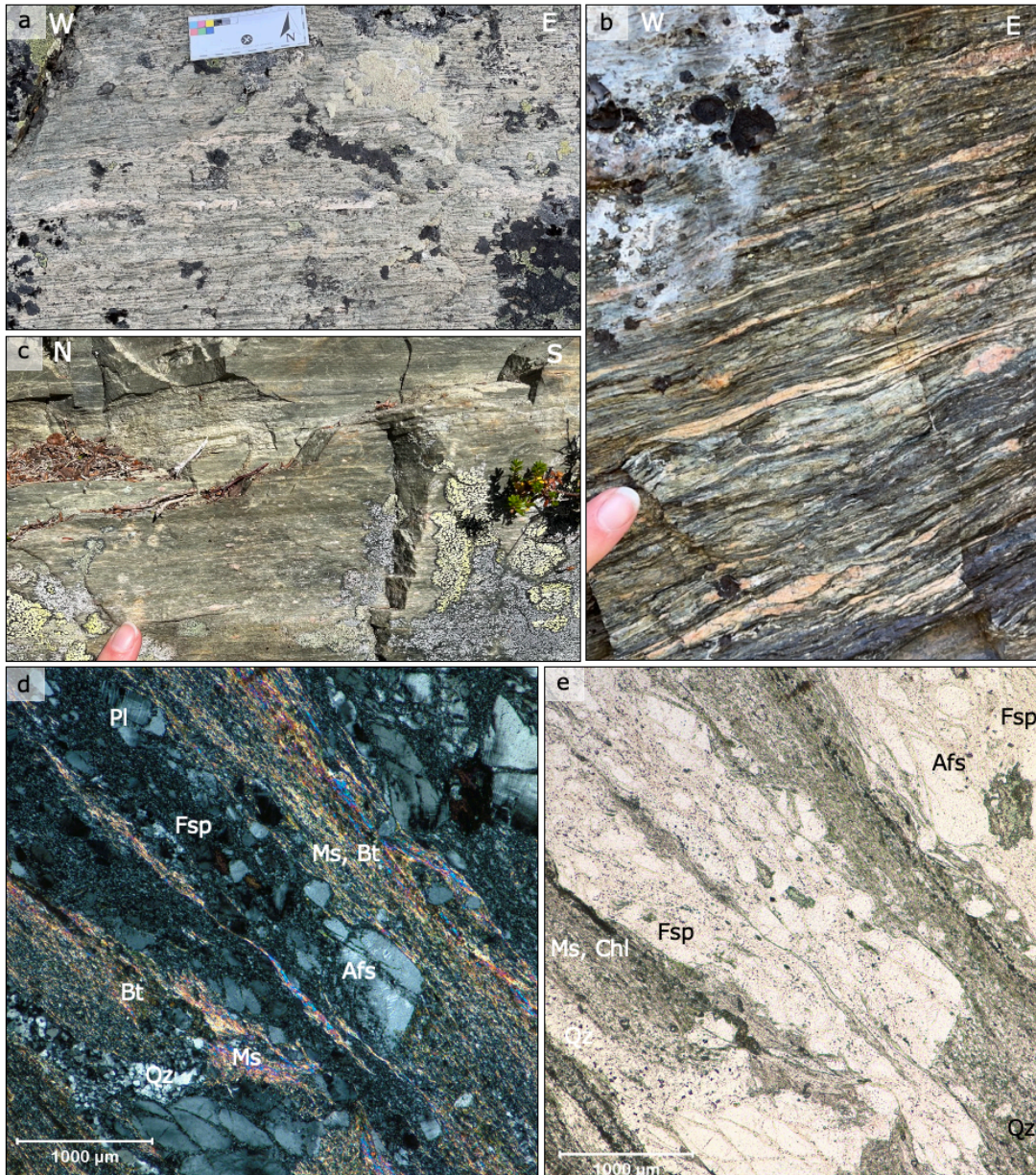


Figure 25. Mylonites. a) Mylonite at locality MU080. This mylonite is fine-grained and with elongated light pink K-feldspar porphyroclasts. b) Protomylonite with elongated pink K-feldspar porphyroclasts at locality MU010. c) Ultramylonite at MU177. The ultramylonite is very fine-grained with a few mm-sized light pink K-feldspar porphyroclasts. d) XPL micrograph of MU010 with 5x magnification. The matrix of this protomylonite consists mostly of feldspar and quartz, but also minor amounts of muscovite and biotite. Most of the feldspar is very fine-grained. e) PPL of d).

5.1.7 Granitic intrusion

One granitic intrusion/sheet was observed in the eastern limb of the Skardøra antiform (in the TAG). The intrusion is pink in colour, although some areas are more enriched in epidote, resulting in a greener colour (Fig. 26). The rock is medium-grained and primarily composed of K-feldspar, plagioclase, quartz and minor biotite, muscovite and epidote, however; feldspar and quartz are the rock forming minerals. A magmatic (phaneritic) texture is present. The intrusion occurs like a sheet, cutting the foliation in the augen gneiss. Precisely determining the size of the intrusion is challenging, however, it has been estimated to be at least 2-3 meters wide and 9-10 meters long. No other outcrops that were studied have intrusions. The contact between the intrusion and the augen

gneiss is sharp, and the augen gneiss is not affected by the emplacement of the sheet (Fig. 27).

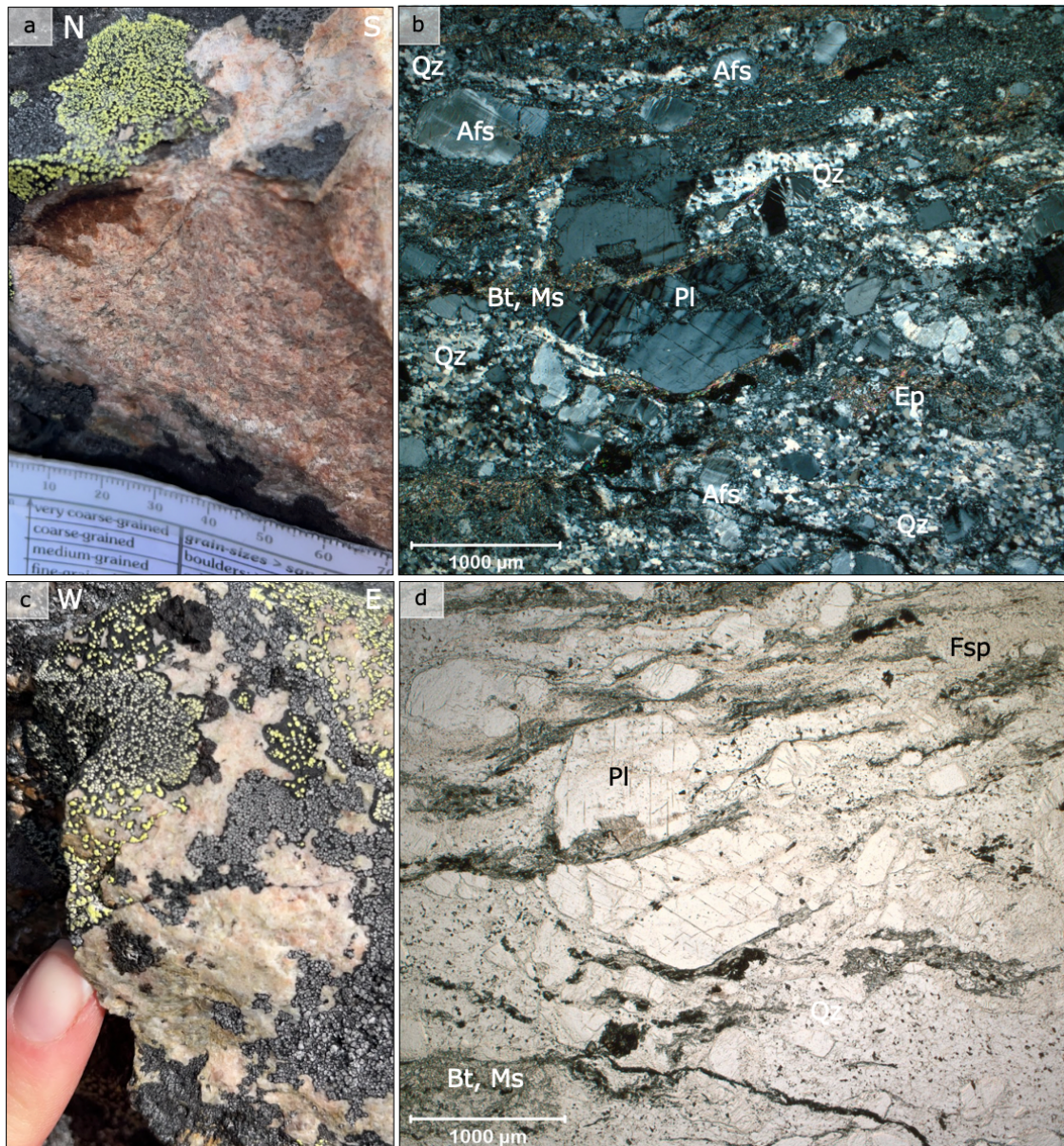


Figure 26. The granitic intrusion in the eastern limb of the Skardøra antiform. a) The intrusion is medium-grained and pink in colour. b) XPL micrograph with 2.5 x magnification. The rock forming minerals are feldspar and quartz, but biotite, muscovite and epidote are also present. c) Close-up field photo of the granite where it is greener in colour. d) PPL micrograph of Fig. b.

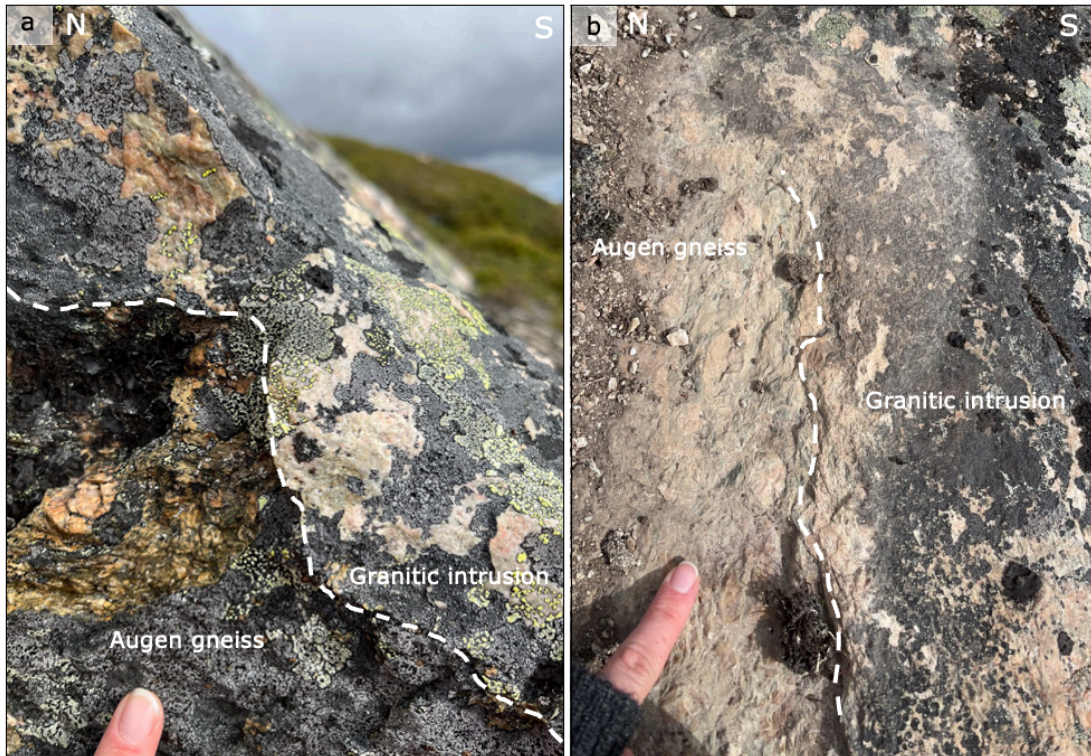


Figure 27. The contact between the augen gneiss and the granitic sheet is marked with a white, stippled line. The contact between these rocks is sharp, and the augen gneiss has not been affected by the intrusion.

5.2 Structural descriptions

During the field work, structural measurements were conducted. The structural measurements taken in the field include foliation and mineral lineation. The foliation measurements are consistently written as dip/dip direction, and the lineations are written as plunge-trend. The augen gneiss is a L>S tectonite where the augens often are prolate spheroids (Fig. 28). The prolate spheroids often have their longest axes aligned parallel to the lineation.

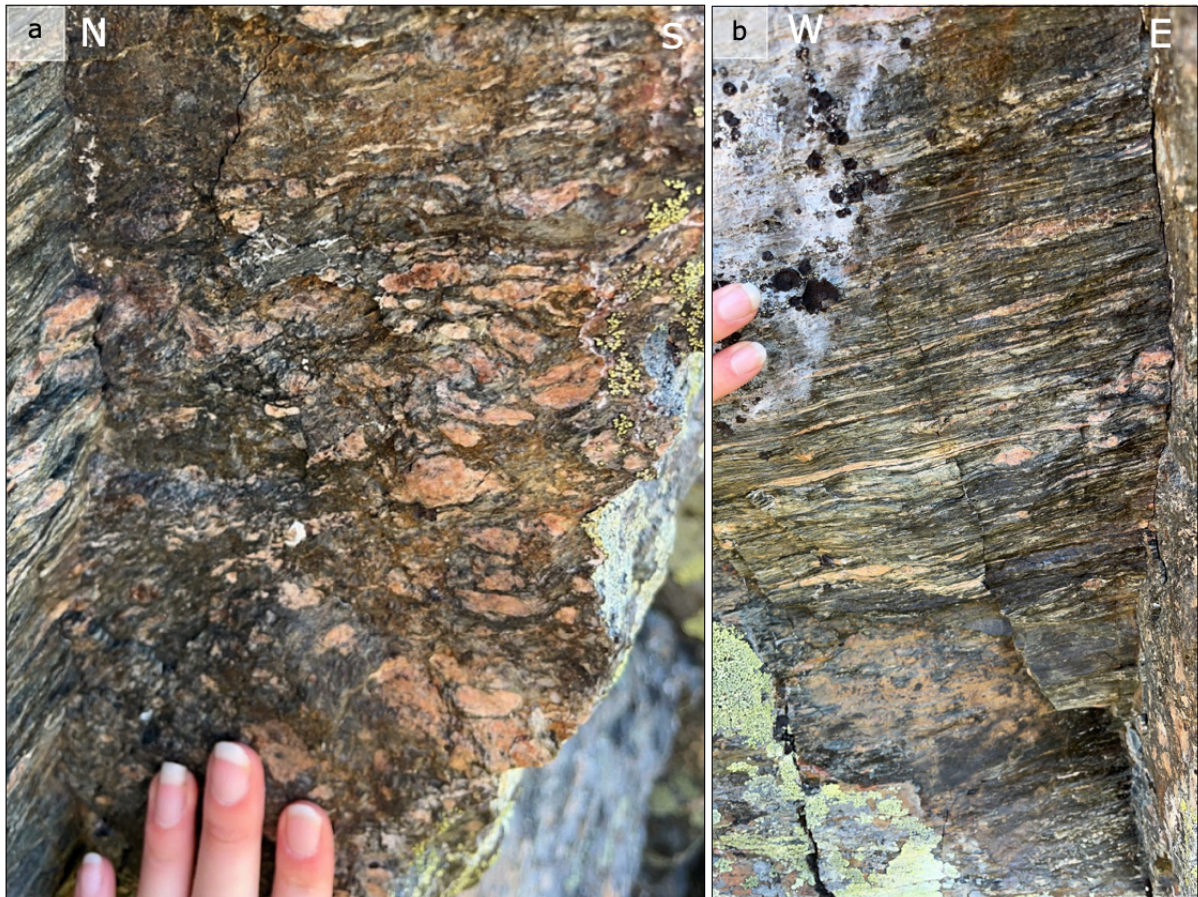


Figure 28. The augen gneiss is a L>S tectonite. Protomylonite at locality MU010 seen from different planes. a) The K-feldspar porphyroclasts appears spherical. b) The K-feldspar porphyroclasts appear as prolate spheroids.

5.2.1 Foliation

A tectonic foliation is developed in all the lithologies. The foliation varies from gently west dipping to gently east/northeast dipping with mineral lineations on the foliation planes. Foliation measurements were taken on both limbs of the Skardøra antiform.

5.2.1.1 Western limb of the Skardøra antiform

The foliation in the western limb of the Skardøra antiform dips gently towards the west (Fig. 29). Most of the measurements of the foliation are coherent, but eleven dips more steeply towards southwest and three dips steeply towards north/northeast. The mean dip direction/dip of the foliation in the western limb of the Skardøra antiform is 238/31.

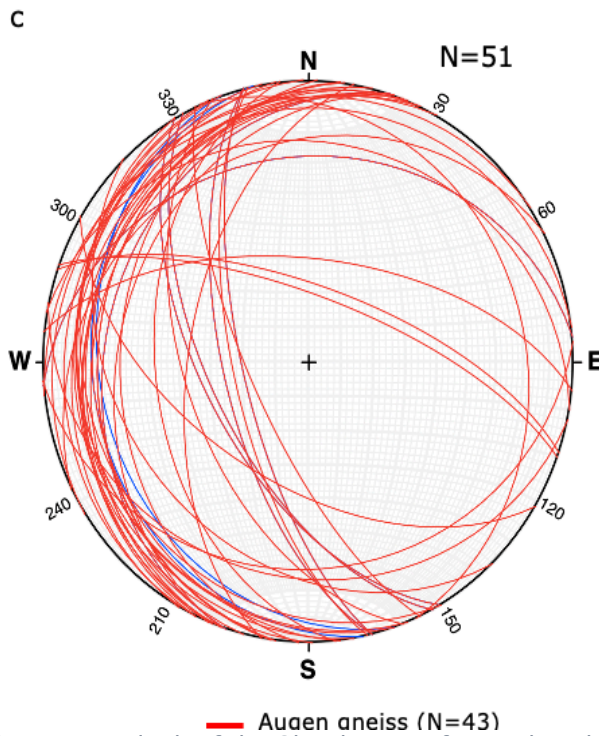
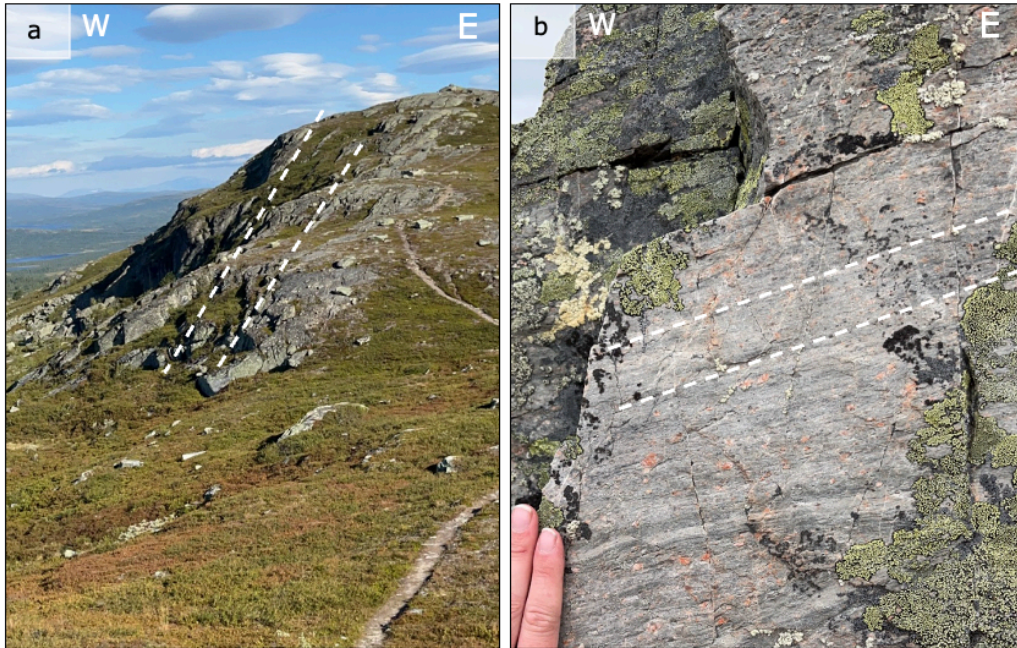


Figure 29. Foliation in the western limb of the Skardøra antiform. The white dashed lines indicate the foliation. a) Foliation in augen gneiss dipping steeply to the west. The picture is taken from the locality MU027 towards north. b) Foliation measured to 195/18 at MU108. c) Stereoplot of the measured foliations in the western limb of the Skardøra antiform ($n=51$).

5.2.1.2 Eastern limb of the Skardøra antiform

On the eastern limb of the Skardøra antiform, the foliation dips gently towards east/northeast (Fig. 30). All measurements of the foliation except one is coherent, and this foliation dips towards south. The mean dip direction/dip of the foliation in the eastern limb is 061/27.

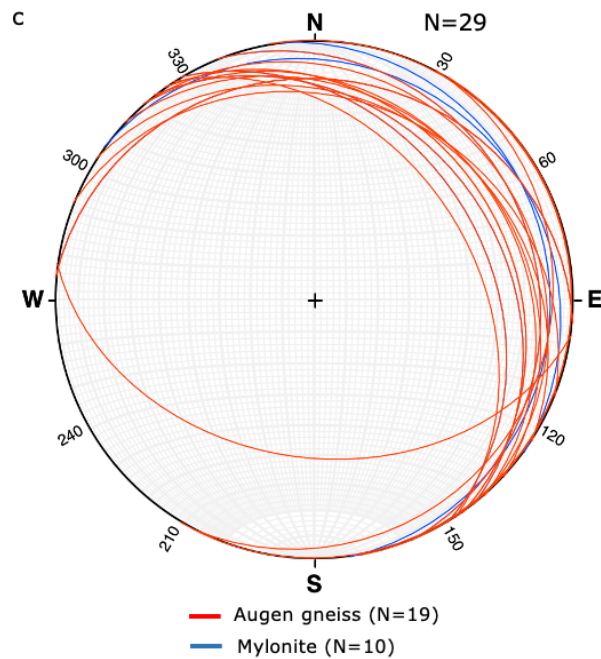
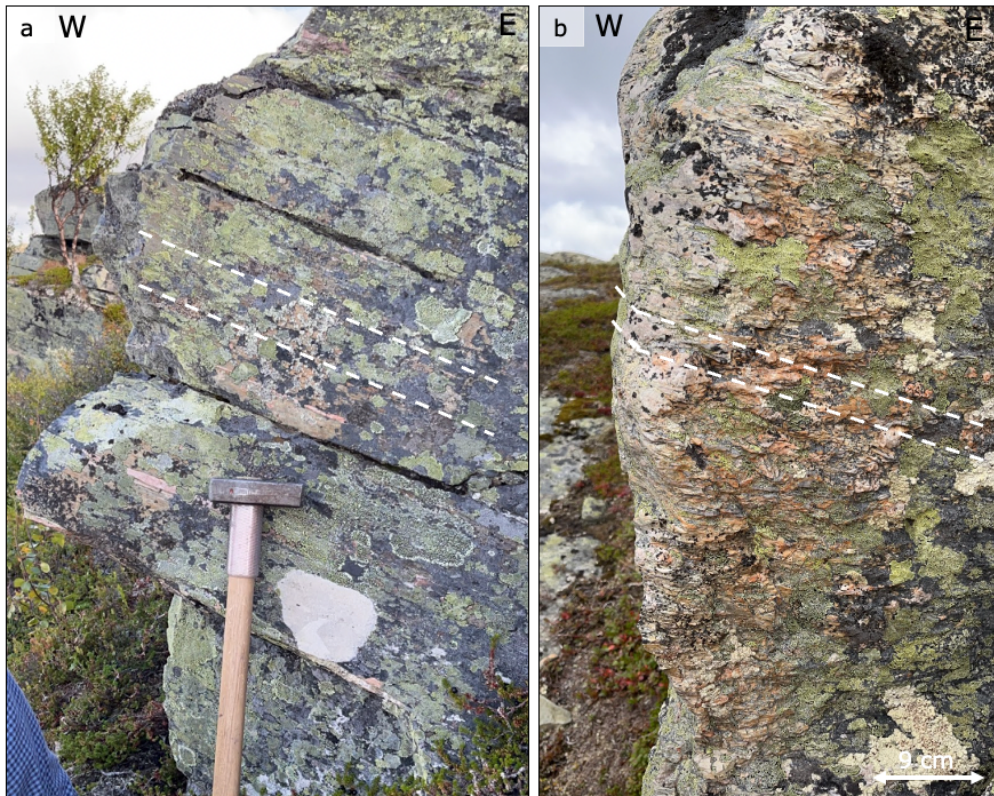


Figure 30. Foliation in the eastern limb of the Skardøra antiform. White dashed lines indicate the foliation. a) Foliation in a mylonite measured to be 052/28 at locality MU129. b) Locality MU147 with foliation 055/25. c) Stereoplot of the measured foliations in the eastern limb of the Skardøra antiform ($n=29$).

5.2.2 Lineations

The lineations are represented as elongated K-feldspar and quartz grains (Fig. 31). In total, 29 measurements were taken in the field, however, there is a bias towards the eastern limb with 26 measurements compared with three on the western limb of the

Skardøra antiform. The lineations on the western limb plunge gently towards west/northwest with a mean mineral lineation of 294-11. For the eastern limb, the lineations plunge gently towards east with a mean mineral lineation of 087-04.

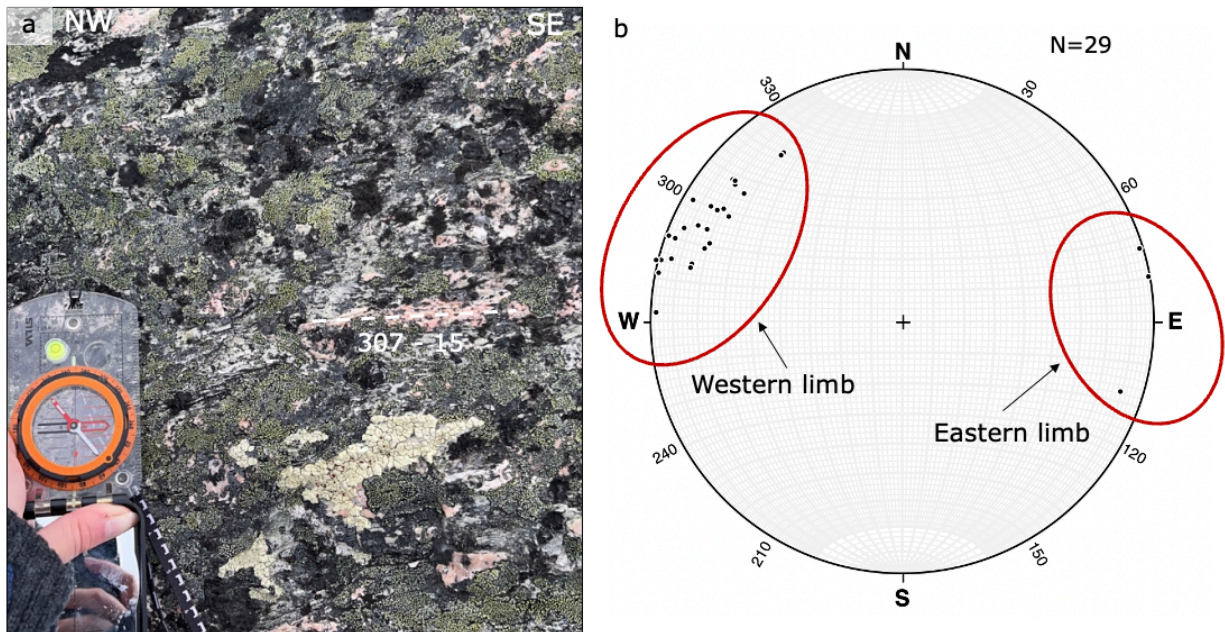


Figure 31. a) Mineral lineation along an elongated pink K-feldspar at MU021 (marked with a white dashed line). The mineral lineation is 307-15. b) A stereonet with the measured lineations. There are two populations: the eastern limb of the Skardøra antiform dipping gently towards west/northwest and the western limb of the antiform dipping gently towards east. There are 26 measurements from the eastern limb, and three measurements from the western limb.

5.2.3 Kinematic indicators

Only symmetrical augens were observed in the field (Fig. 32). Since they are symmetrical, can they not be used as kinematic indicators. However, the thin sections showed several kinematic indicators. Fig. 33 shows a selection of micro-scale kinematic indicators, and mostly top-to-the east sense of shear is observed in the augen gneiss of the Dagvolsjøen Nappe. The protomylonite (MU010) indicates top-to-the west movement.

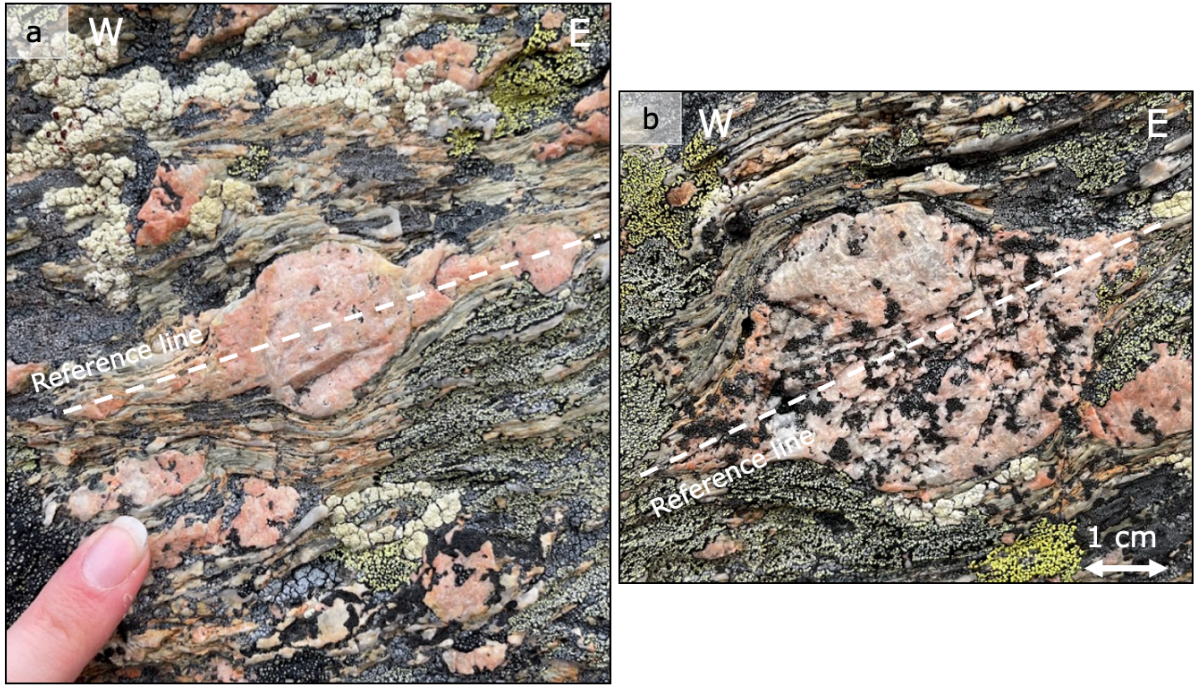
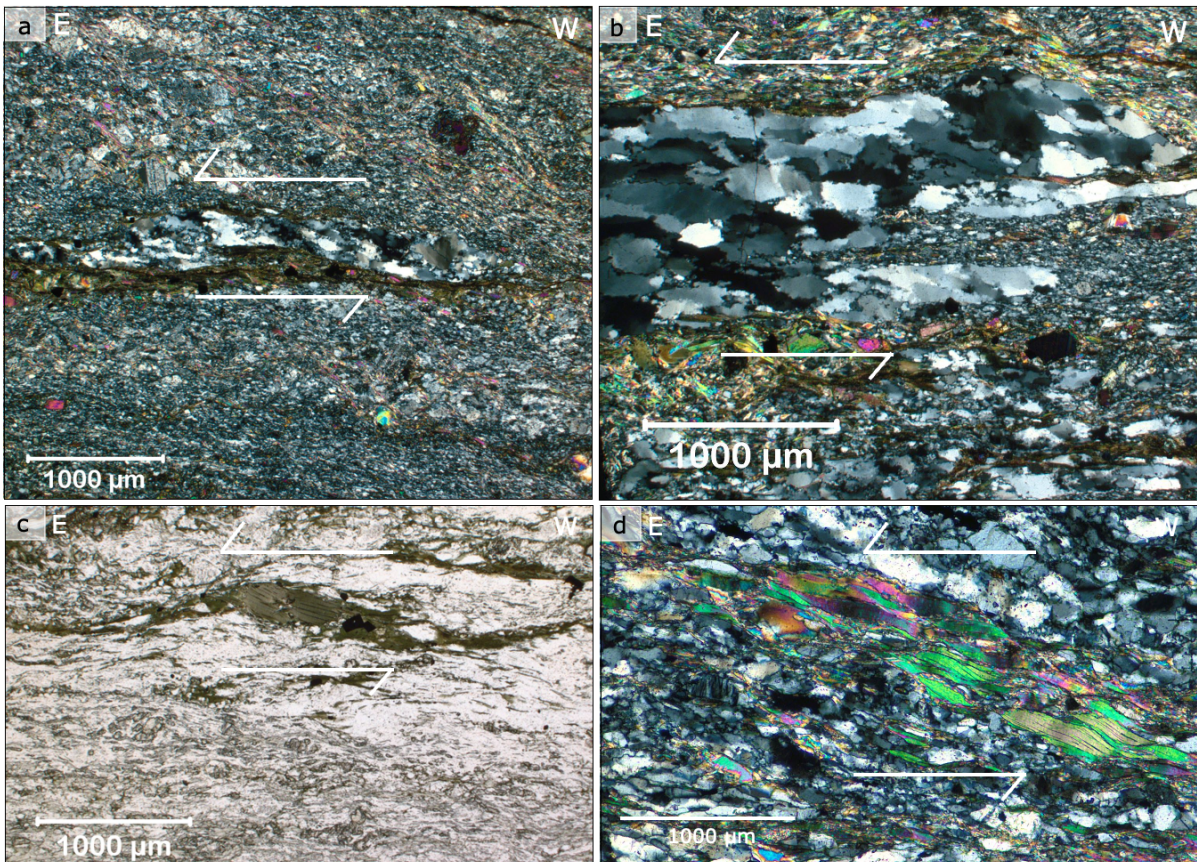


Figure 32. Symmetrical sigma-augens at the locality MU021. The reference plane is parallel to the foliation (marked with a white, dotted line). Since they are symmetrical, they cannot determine the sense of shear.



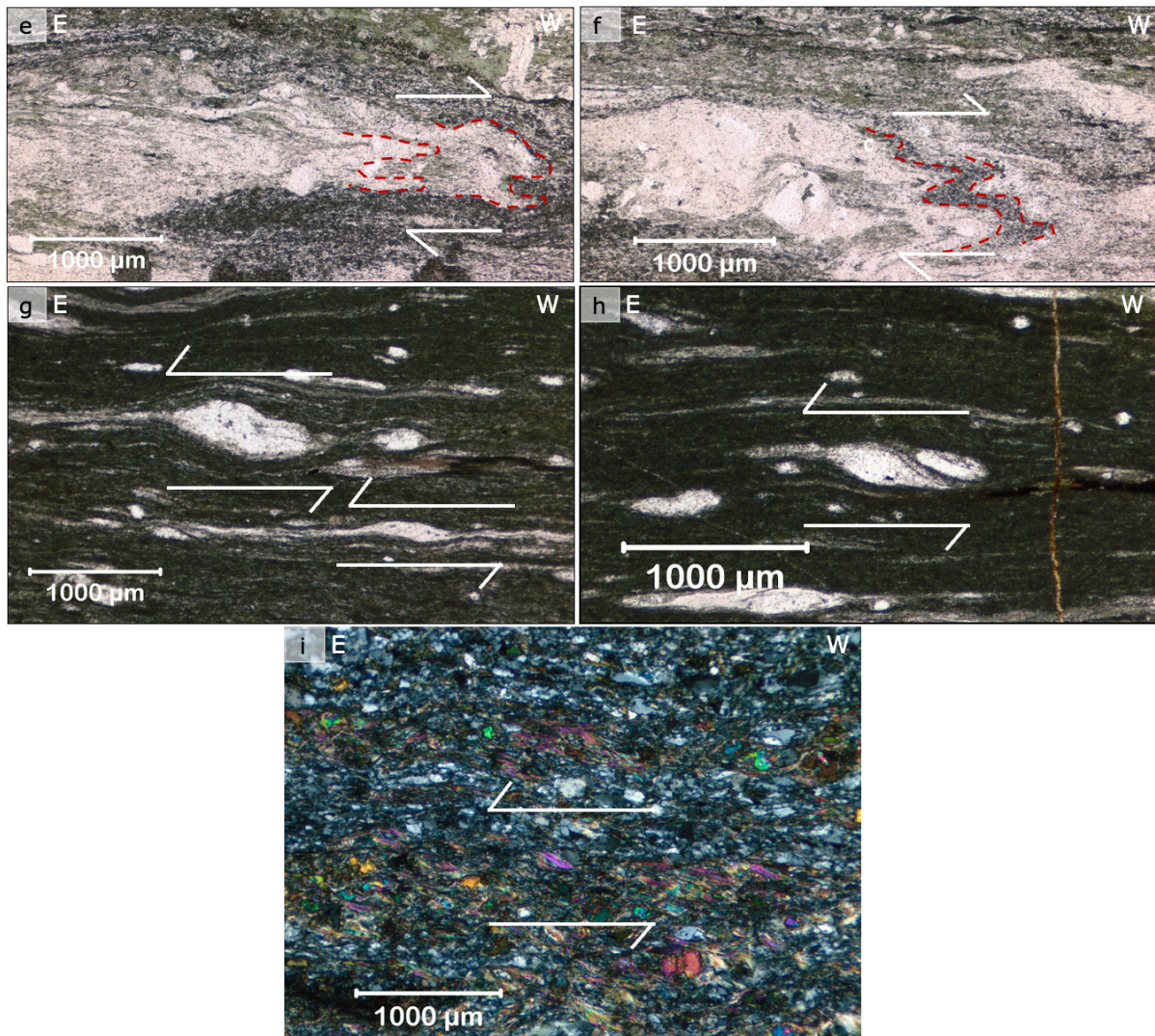


Figure 33. Micro-scale kinematic indicators. a) Oblique fabric in quartz in the quartz striped K-feldspar augen gneiss (MU021) indicating sinistral sense of shear (2.5x magnification). b) Oblique fabric in MU021 with sinistral sense of shear (5x magnification). c) Mica fish of biotite in MU021 (5x magnification). The sense of shear is sinistral. d) S-C fabric in the fine-grained and muscovite-rich rock (MU108) with sinistral sense of shear (5x magnification). e) Folds in the mylonite (MU010) (5x magnification) indicating dextral sense of shear. f) Folds in MU010 with dextral sense of shear (5x magnification). g) Sigma clasts of K-feldspar in a quartz striped K-feldspar augen gneiss (MU032) indicating sinistral sense of shear. The magnification is 5x. h) Sigma clast in MU032. The sense of shear is sinistral (5x magnification). i) S-C fabric in MU108 with magnification 2.5x.

5.2.4 Dynamic recrystallisation of quartz and feldspar

The following sections will describe the dynamic recrystallisation observed in quartz and feldspar in the different variations of the augen gneiss, the fine-grained muscovite-rich rock, the mylonite and in the granitic intrusion.

5.2.4.1 Quartz striped K-feldspar augen gneiss

The quartz in the quartz striped K-feldspar augen gneiss is primarily recrystallized by sub-grain rotation (SGR) (Fig. 34a-b), but it also shows sign of grain boundary migration (GBM) (Fig. 34c). Along the grain boundaries of the quartz are there smaller, recrystallized grains, indicating bulging (BLG) mechanisms. The BLG overprints the SGR and the GBM. The quartz has patchy, undulatory extinction and the grain size is up to ~1 mm. The feldspar porphyroclasts have undulose extinction, in addition to fractures and

flame perthite (Fig. 34d). These recrystallization mechanisms correspond to a recrystallization temperature of appr. 500-600 degrees (Passchier and Trouw, 2005).

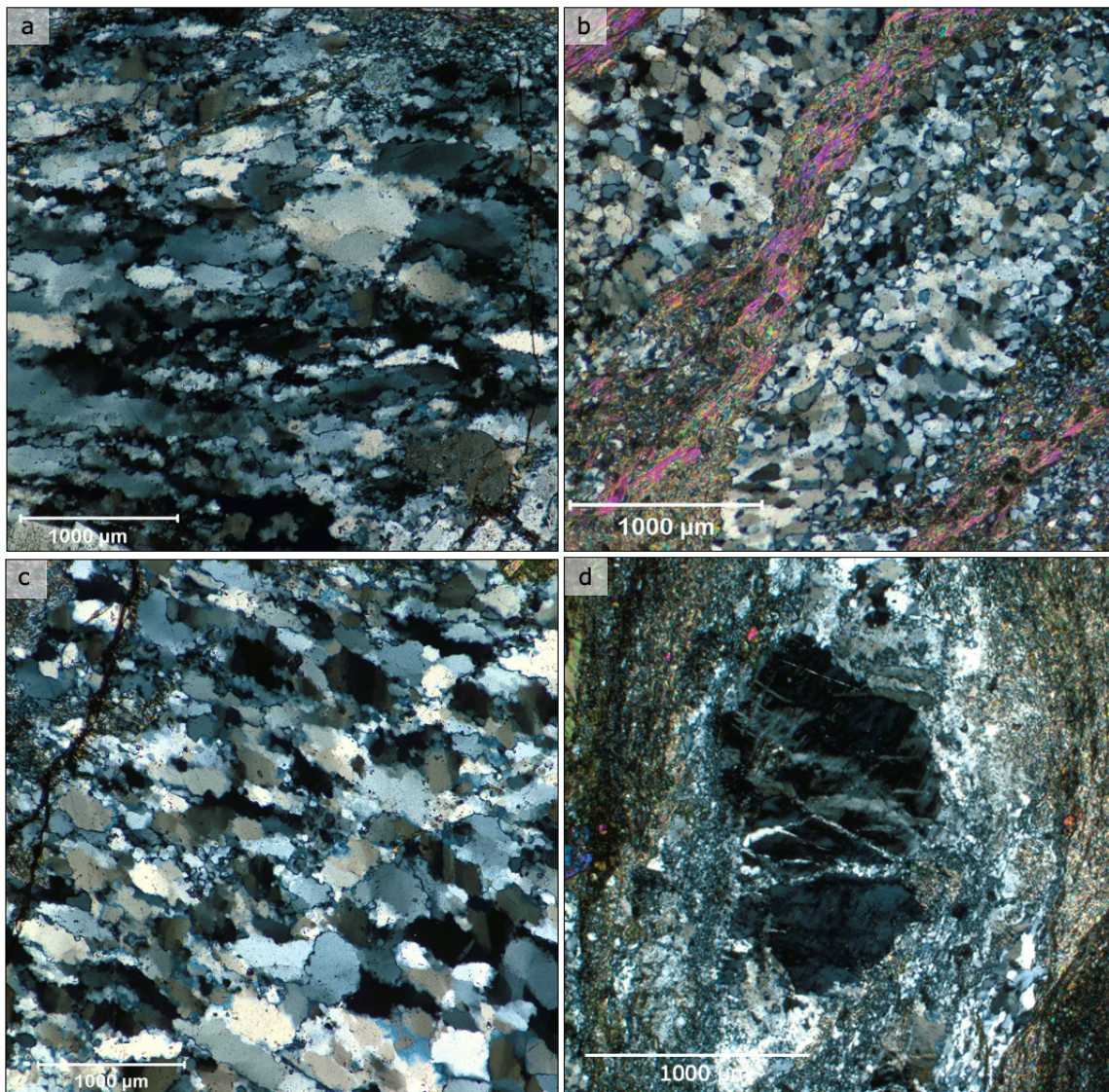


Figure 34. Dynamic recrystallisation of quartz and feldspar in quartz striped K-feldspar augen gneiss. a) Thin section micrograph with 2.5x magnification of MU021 showing BLG and SGR in quartz. The quartz has fine, recrystallized grains along the grain boundaries and patchy undulatory extinction. b) Thin section micrograph of MU168 (magnification is 5x). The quartz indicates SGR with sub grains and recrystallized grains with the same size. c) Thin section micrograph of MU016 with 2.5x magnification. d) An c. 1.5 mm K-feldspar porphyroblast with undulose extinction, fractures and flame perthite in MU016 (magnification is 2.5x).

5.2.4.2 Unstriped augen gneiss with fine-grained matrix

The unstriped augen gneiss with fine-grained matrix has quartz up to ~0.5 mm in size. The quartz has undulose extinction (Fig. 35a). The main recrystallisation mechanism is SGR with some indications for GBM. Additionally, the SGR is overprinted by BLG. The K-feldspars are up to c. 2 mm, and they have deformation bands and fractures. In the fractures and along the grain boundaries, recrystallisation has started (Fig. 35b). In addition, some feldspars have a thin mantle of fine-grained grains. According to Passchier and Trouw (2005), the conditions described correspond with a recrystallisation temperature of 500-600 °C.

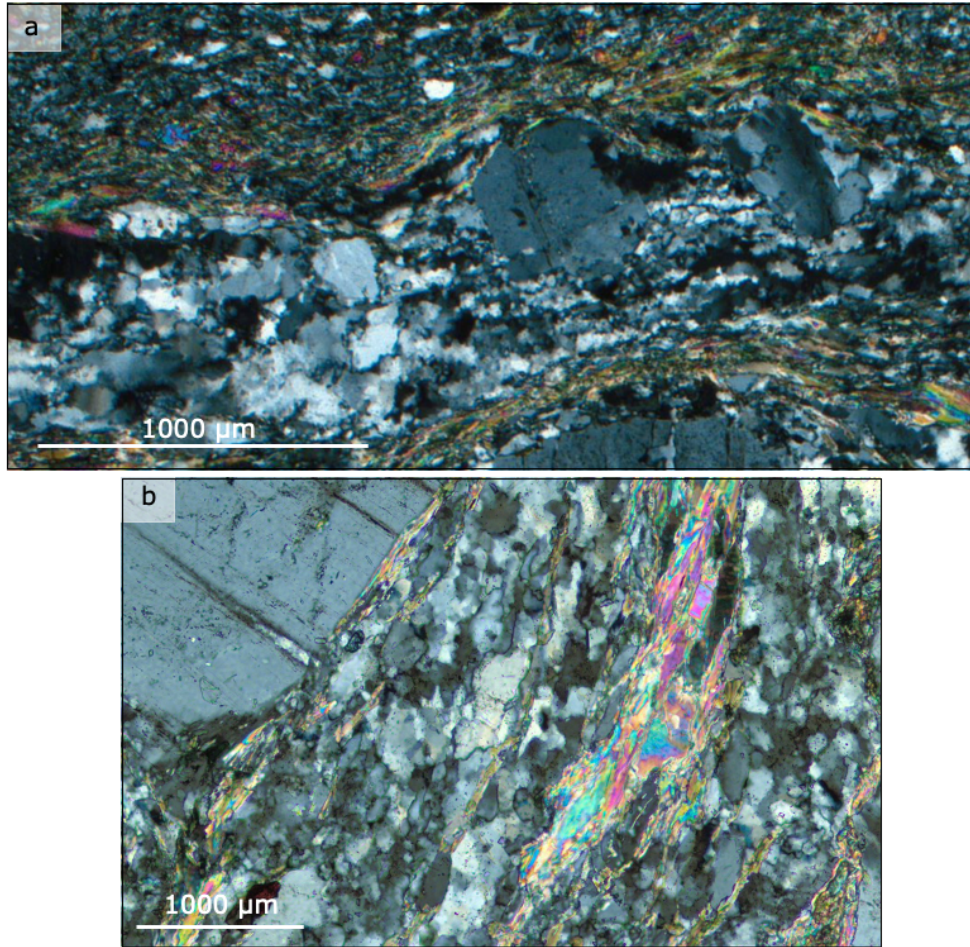


Figure 35. Dynamic recrystallisation of quartz and feldspar in the unstriped augen gneiss with fine-grained matrix. a) Micrograph of a quartz band in MU052 with magnification 10x. The main recrystallization mechanism is SGR, but with indication of GBM. b) K-feldspar in MU052 (5x magnification). The feldspar is fractured, and recrystallisation is observed in the fractured zones and along the grain boundary.

5.2.4.3 Strongly quartz striped K-feldspar augen gneiss

The strongly quartz striped K-feldspar augen gneiss is dominated by BLG and SGR recrystallization where BLG is overprinting SGR (Fig. 36a-b). The quartz has undulose extinction, and core-and-mantle structure where the ribbon grains are surrounded by finer, recrystallized grains (Fig. 36b). The feldspars are fractured, and recrystallization is observed in the fractured zones (Fig. 36c). In addition, undulous extinction, flame-shaped albite lamellae (flame perthite) and deformation bands are observed in the feldspars. Hence the recrystallization mechanisms correspond to a recrystallization temperature of appr. 500 °C (Passchier and Trouw, 2005)

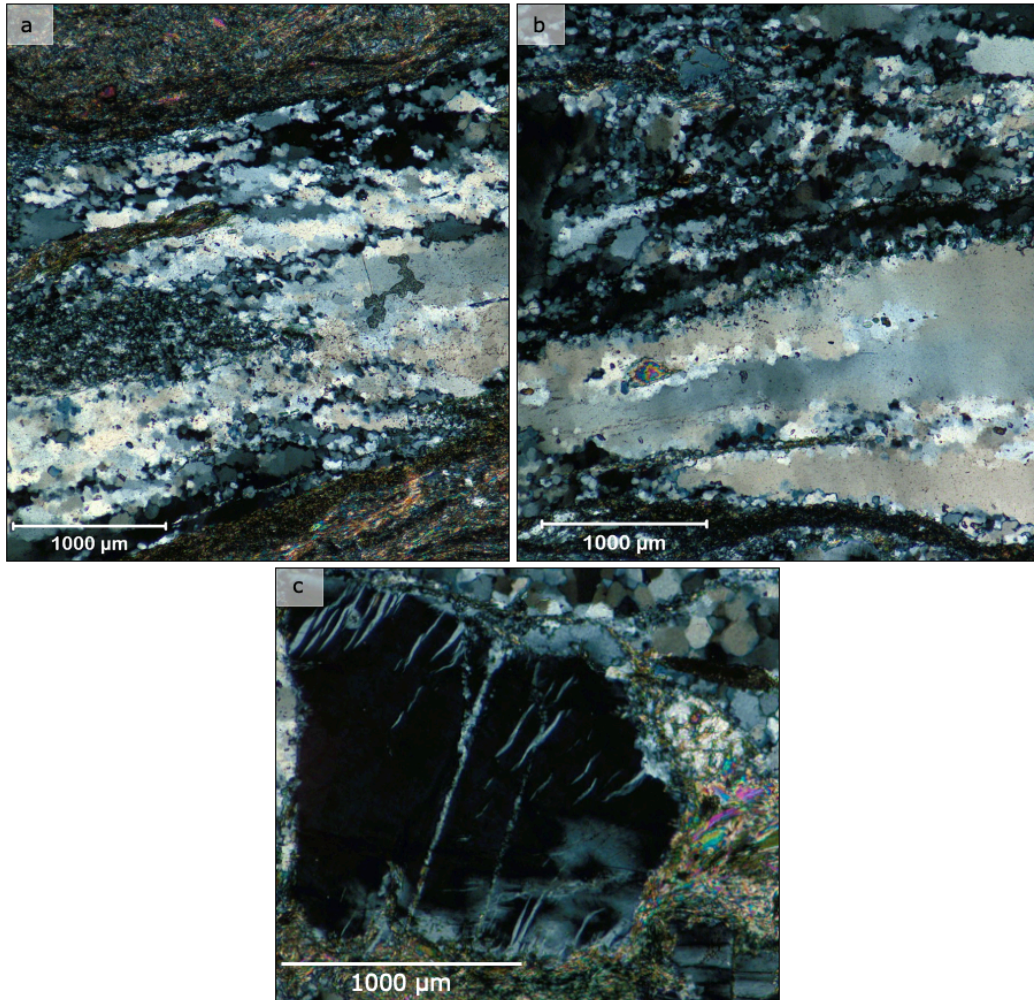


Figure 36. Dynamic recrystallisation of quartz and feldspar the strongly quartz striped augen gneiss from locality MU124. a) BLG and SGR in quartz. The magnification is 2.5x. b) Core-and-mantle structure with recrystallised mantle grains (magnification 5x). c) K-feldspar with perthite flames, and undulose extinction in addition to be fractured (5x magnification).

5.2.4.4 The fine-grained and muscovite-rich rock

The quartz in the fine-grained and muscovite-rich rock is up to ~0.5 mm in size. Fig. 37a shows that the quartz has undulose extinction. SGR is the primary recrystallisation mechanism in the quartz. BLG has overprinted the SGR. K-feldspars are up to ~2.5 mm in size and have fractures and recrystallisation along the edges, in addition to flame perthite (Fig. 37b). Recrystallisation has begun in the fractures. Some feldspars also have a thin mantle of fine-grained grains. According to Passchier and Trouw (2005), the conditions described correspond with a recrystallisation temperature of 400-500 °C.

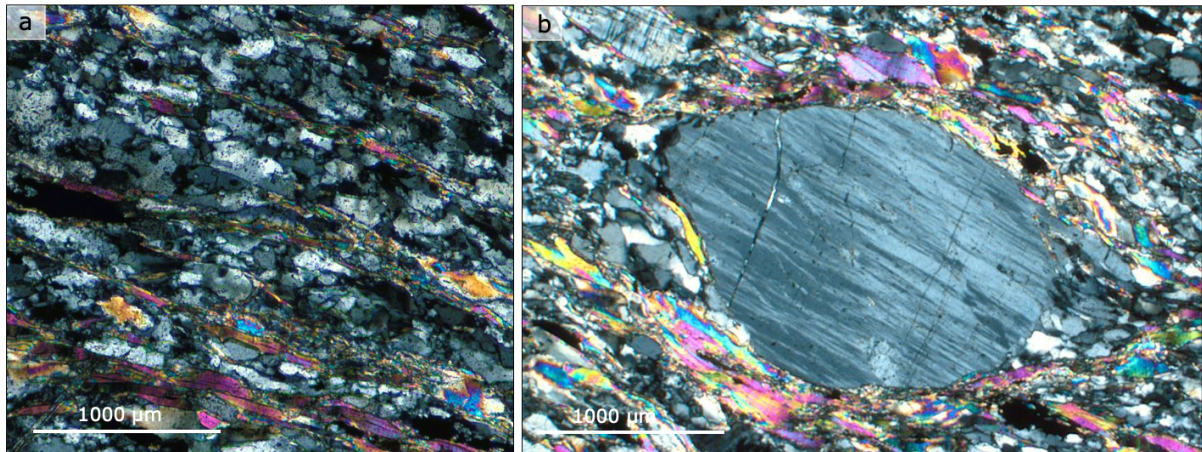


Figure 37. Dynamic recrystallisation of quartz and feldspar in the fine-grained and muscovite-rich rock (MU108). a) SGR is the main recrystallisation mechanism in quartz. BLG has overprinted the SGR (10x magnification). b) K-feldspar porphyroblast with magnification 2.5x. The clast has fractures, recrystallisation at the edges and flame perthite.

5.2.4.4 Tännäs augen gneiss

The Tännäs augen gneiss has quartz that is up to c. 1 mm in size. The main recrystallization mechanisms are SGR and GBM (Fig. 38a-b). There are some indications of BLG (Fig. 38b). The porphyroclasts of K-feldspar are up to ~2.5 mm in size (Fig. 38c). The grains are fractured with indication of recrystallization in the fractures. There is also recrystallisation along the grain boundaries. In addition, multiple grains have undulose extinction. According to Cocks and Torsvik (2005), the conditions described correspond to a recrystallisation temperature of c. 600 °C.

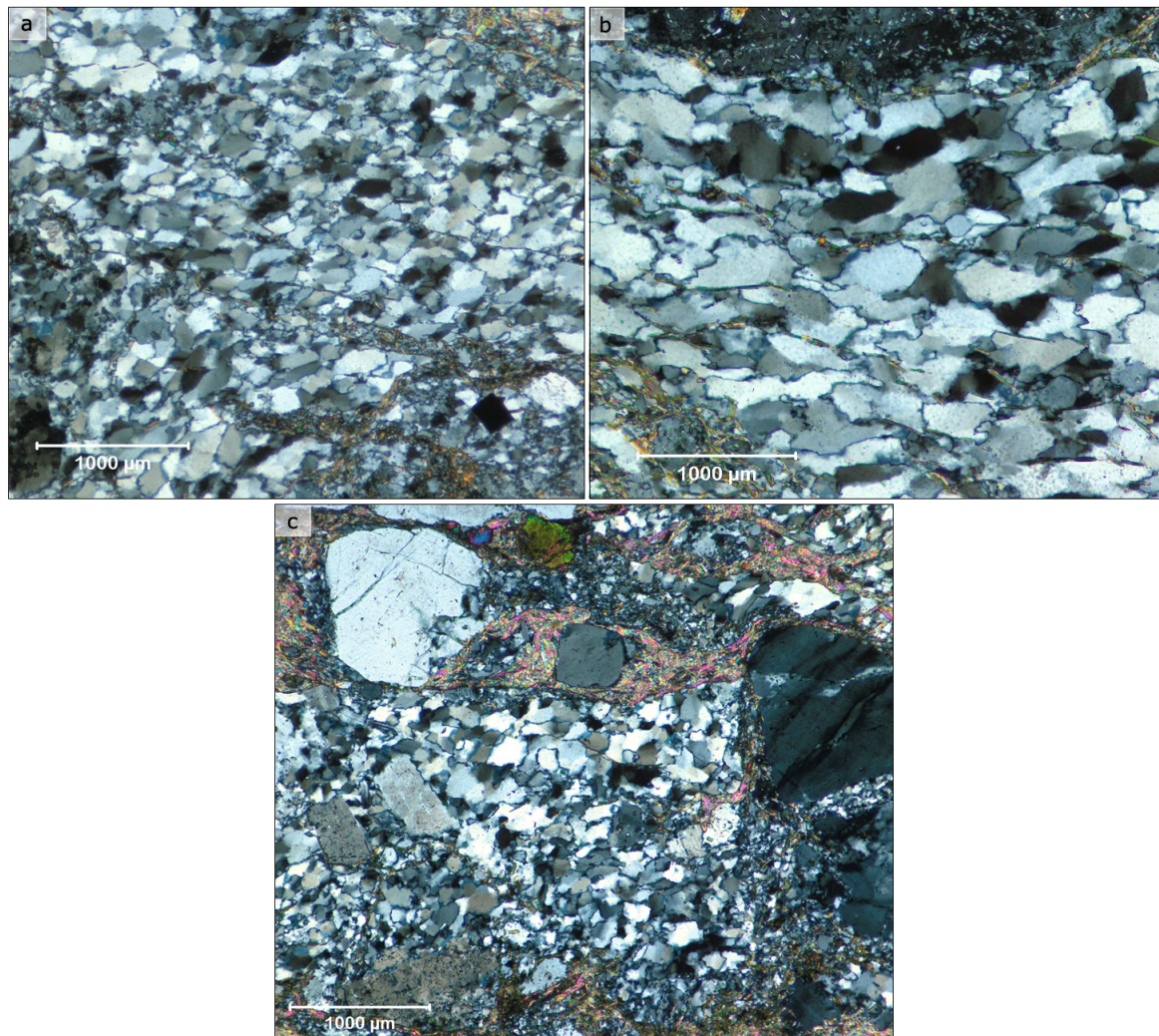


Figure 38. Dynamic recrystallisation of quartz and feldspar in the Tännäs augen gneiss (MU126). a) Micrograph of quartz with magnification 5x. The quartz is interpreted to have SGR and GBM recrystallization mechanisms. b) Micrograph of quartz with 10x magnification showing SGR and GBM that is weakly overprinted by BLG. c) Thin section micrograph with 2.5x magnification showing quartz, feldspar, micas and epidote. The feldspars are fractured and recrystallisation has begun in the fractures and along the grain boundaries.

5.2.4.5 Mylonite

In the protomylonite, most of the quartz is in the quartz bands (Fig. 39a). The average quartz grain size is appr. 0.5 mm, and the dominant recrystallisation mechanism is SGR (Fig. 39). Most of the quartz has undulose extinction. Core-and-mantle structures where the ribbon grains are surrounded by finer, recrystallized grains were observed (Fig. 39c). The K-feldspars are fractured, and the size of the grains vary from <0.01mm to c. 0.5 mm. In the fractures, smaller, recrystallised grains are observed. Due to its fragmentation and the wide range of grain size, the feldspars appear cataclastic. The recrystallisation temperature corresponds with a temperature of 400-500 degrees according to the quartz. However, the cataclastic description of the feldspars, the temperature of the recrystallisation is <400 °C (Passchier and Trouw, 2005).

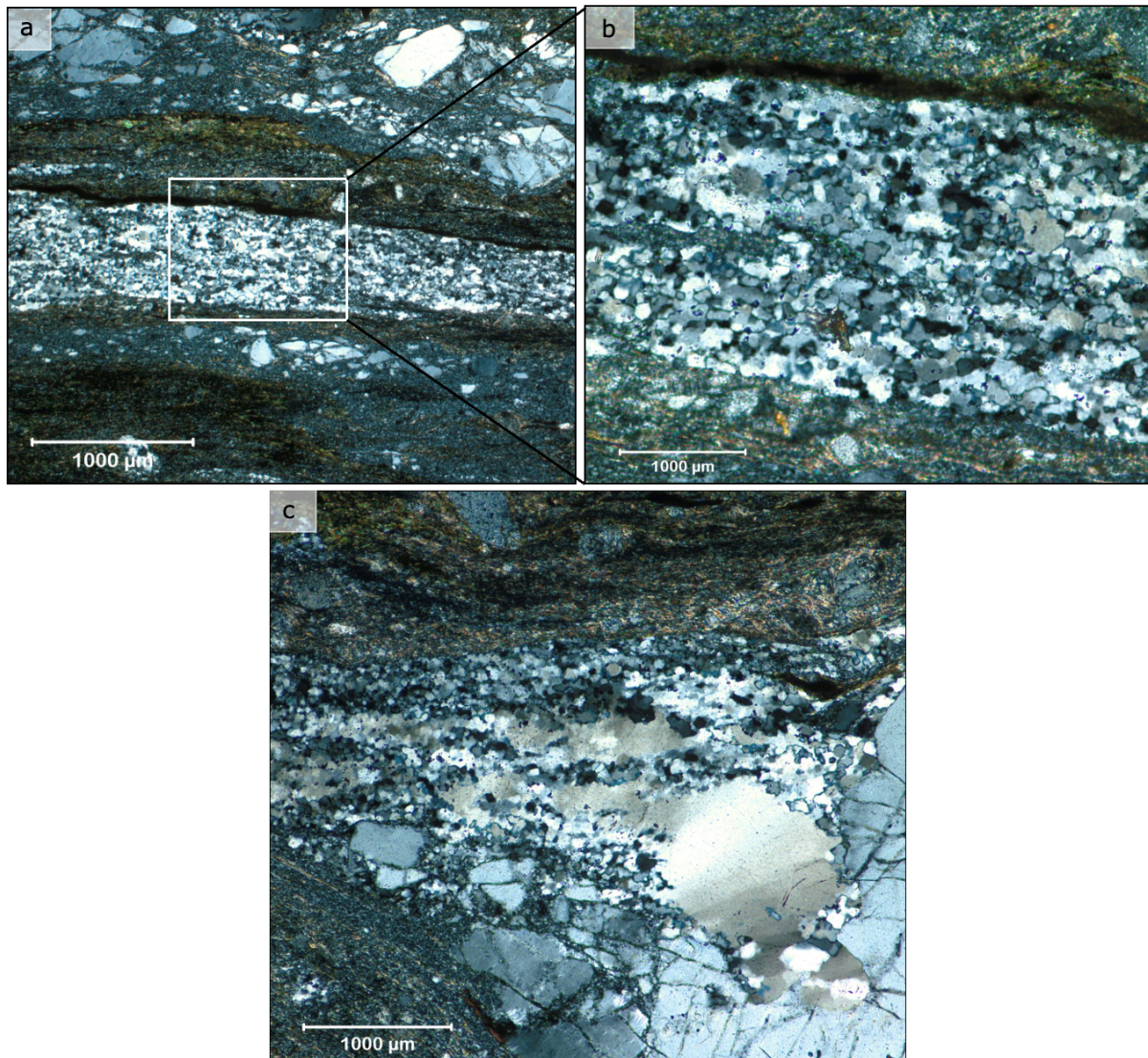


Figure 39. Dynamic recrystallisation of quartz and feldspar in the protomylonite (MU010). a) Micrograph with magnification 2.5x. A quartz ribbon, surrounded by very fine fragments and feldspars. The feldspars are heavily fractured and are in a wide range of size. b) Close-up of the white rectangle in a) with 10x magnification. The picture is a zoom-in of the quartz showing that SGR is the dominant recrystallization mechanism. c) Core-and-mantle structure in quartz with magnification of 5x.

5.2.4.6 The granitic intrusion

The quartz has an average size of ~0.3 mm in the granitic sheet, and it has undulatory extinction. The main recrystallization mechanism in the intrusion is SGR with some indications for BLG (Fig. 40). The K-feldspars are fractured, in addition to having undulose extinction and deformation bands (Fig. 40b). Some of the feldspars have a thin mantle of fine-grained grains. These recrystallization mechanisms correspond to a recrystallization temperature of appr. 500 °C (Passchier and Trouw, 2005).

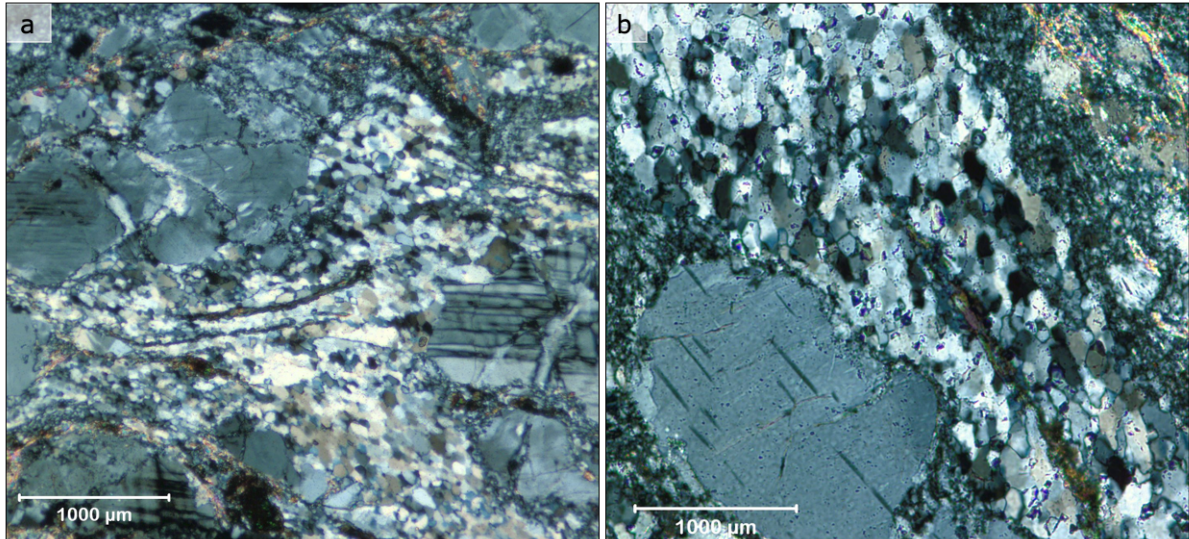


Figure 40. Dynamic recrystallisation of quartz and feldspar in the granitic intrusion (JJ29). a) Micrograph over the intrusion showing quartz and feldspar. The main recrystallization mechanism in the quartz is SGR. The feldspars have experienced fracturing and recrystallisation in the fractures. The magnification is 5x. b) Zoom-in micrograph with magnification of 10x. The quartz shows SGR and the feldspar has deformation lamella. There is a thin mantle of fine-grained grains around the feldspar.

5.3 U-Pb geochronology

Table 5 provides a summary of the U-Pb geochronological data. Fig. 41 shows where the samples were collected, except the sample from Tännäs (MU126). Detailed analyses of the samples are described in the following sections. The dataset is in Appendix B.

Table 5. Summary of the zircon U-Pb geochronological data. The coordinate system is WGS84 UTM Zone 32N and 33N. ¹Inherited zircons with the same age as the augen gneiss. ²Interpreted as an older population. ³Interpreted as the intrusion age.

Sample	Lat.	Long.	Rock description	Zircon description	Age
BB20_20	62.60031	12.04446	Unfoliated granite from the crystalline basement in the Skardøra antiform	300-600 µm in length (Sub)euohedral, prismatic, anhedral and subrounded grains	²⁰⁷ Pb/ ²⁰⁶ Pb: 1657 ± 6 Ma Concordia: 1656 ± 6 Ma
BB20_19	62.63592	11.90435	Augen gneiss with a mylonitic and finely laminated matrix	Length of c. 250 µm Subrounded to rounded grains	²⁰⁷ Pb/ ²⁰⁶ Pb: 1649 ± 5 Ma Concordia: 1648 ± 6 Ma
JJ23	62.63549	11.98209	Augen gneiss sheet in meta-arkose near the top of the the Osen-Røa Nappe Complex	200-500 µm in length Metamict and euohedral with remnants of the prismatic feature	²⁰⁷ Pb/ ²⁰⁶ Pb: 1659 ± 5 Ma Concordia: 1655 ± 6 Ma
JJ29	62.67009	12.06386	Granitic, medium grained intrusion with mostly feldspar and quartz	Length of c. 250 µm Several of the zircons are metamict	²⁰⁷ Pb/ ²⁰⁶ Pb: 1658 ± 6 Ma ¹ ²⁰⁷ Pb/ ²⁰⁶ Pb: 1711 ± 14 Ma ² ²⁰⁷ Pb/ ²⁰⁶ Pb: 436 ± 43 Ma ³ and 351 ± 38 ³
MU021	62.65663	12.00072	Quartz striped K-feldspar augen gneiss	300-600 µm in length. (Sub)anhedral grains	²⁰⁷ Pb/ ²⁰⁶ Pb: 1658 ± 5 Ma ²⁰⁷ Pb/ ²⁰⁶ Pb: 1698 ± 13 Ma ²
MU126	62.48818	12.47844	Tännäs augen gneiss	250-300 µm in length. Metamict and euohedral grains	²⁰⁷ Pb/ ²⁰⁶ Pb: 1654 ± 5 Ma Concordia: 1649 ± 6 Ma

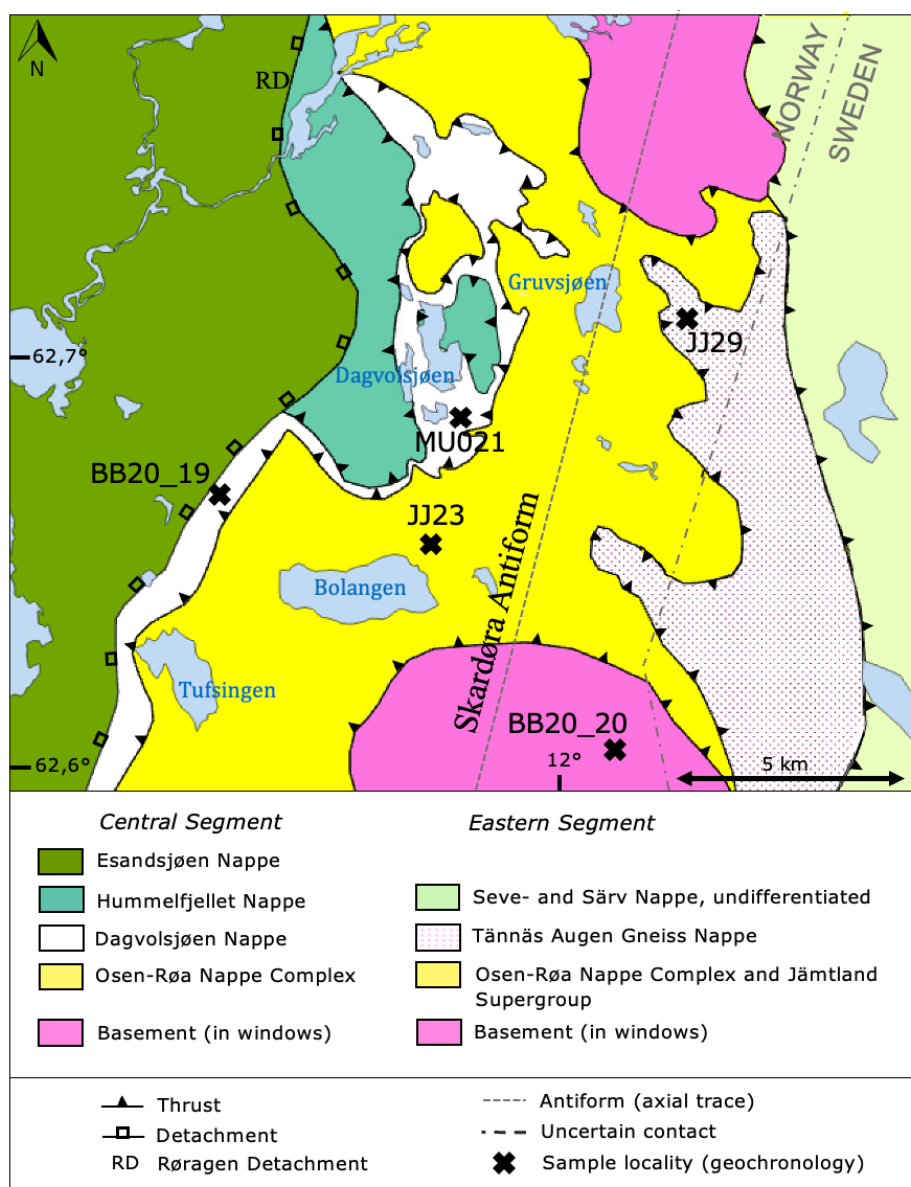


Figure 41. Geological overview map over the study area with the sample localities for geochronology. The map is based on Nilsen and Wolff (1989), NGU (2023), Bergman et al. (2012) and observations in the field. The coordinate system is WGS84 UTM Zone 32N and 33N.

5.3.1 Sample BB20_20

BB20_20 was collected by Bernard Bingen. It is an unfoliated, coarse-grained granite from the crystalline basement exposed in the Skardøra antiform (Fig. 42). It will from hereon be referred to as the Vigelen (basement) granite. This sample was sampled to test for a possible resemblance in geochemical signature and age between the basement and the augen gneiss in the field area.

The zircons vary in size between 200 μm to 600 μm in length, and the zircon population is comprised of clear, almost colourless grains with a hint of a light brown colour. A few of the zircons have inclusions, but these were avoided during the LA-ICP-MS analysis. The zircons occur as (sub)euhedral grains with a typical prismatic as well as anhedral and subrounded grains. A few zircons show fractures, and most of the zircons have oscillatory

zoning. Five grains appear too bright in the CL image to characterize their zoning. 18 spots were analysed on 16 grains.

U-Pb analysis gives a well grouped cluster of analysis that are concordant with a $^{207}\text{Pb}/^{206}\text{Pb}$ age of 1657 ± 6 Ma with a mean square weighted deviates (MSWD)=0.45 and a concordia age of 1656 ± 6 (Fig. 43). Two zircons were analysed twice, and they indicate that there is no metamorphic zone around the magmatic core. Analyses no. 1 and 15 targeted the oscillatory centre while analyses no. 2 and 16 targeted the margin of the crystals. They gave respectively $^{207}\text{Pb}/^{206}\text{Pb}$ ages of 1664 ± 16 Ma, 1653 ± 11 Ma, 1642 ± 45 Ma and 1656 ± 8 Ma. The average of 1657 ± 6 Ma is interpreted to be magmatic crystallisation of the zircon. One outlying analysis is discordant and yields a $^{207}\text{Pb}/^{206}\text{Pb}$ age of 1848 ± 23 Ma. This zircon could be inherited, and the analysis is discarded in the average calculation. There are no fractures or inclusions in this zircon according to the BSE-image (Appendix C).



Figure 42. Undeformed and coarse-grained granite collected in a window of Baltican crystalline basement exposed in the Skardøra antiform. The picture is taken by Bernard Bingen.

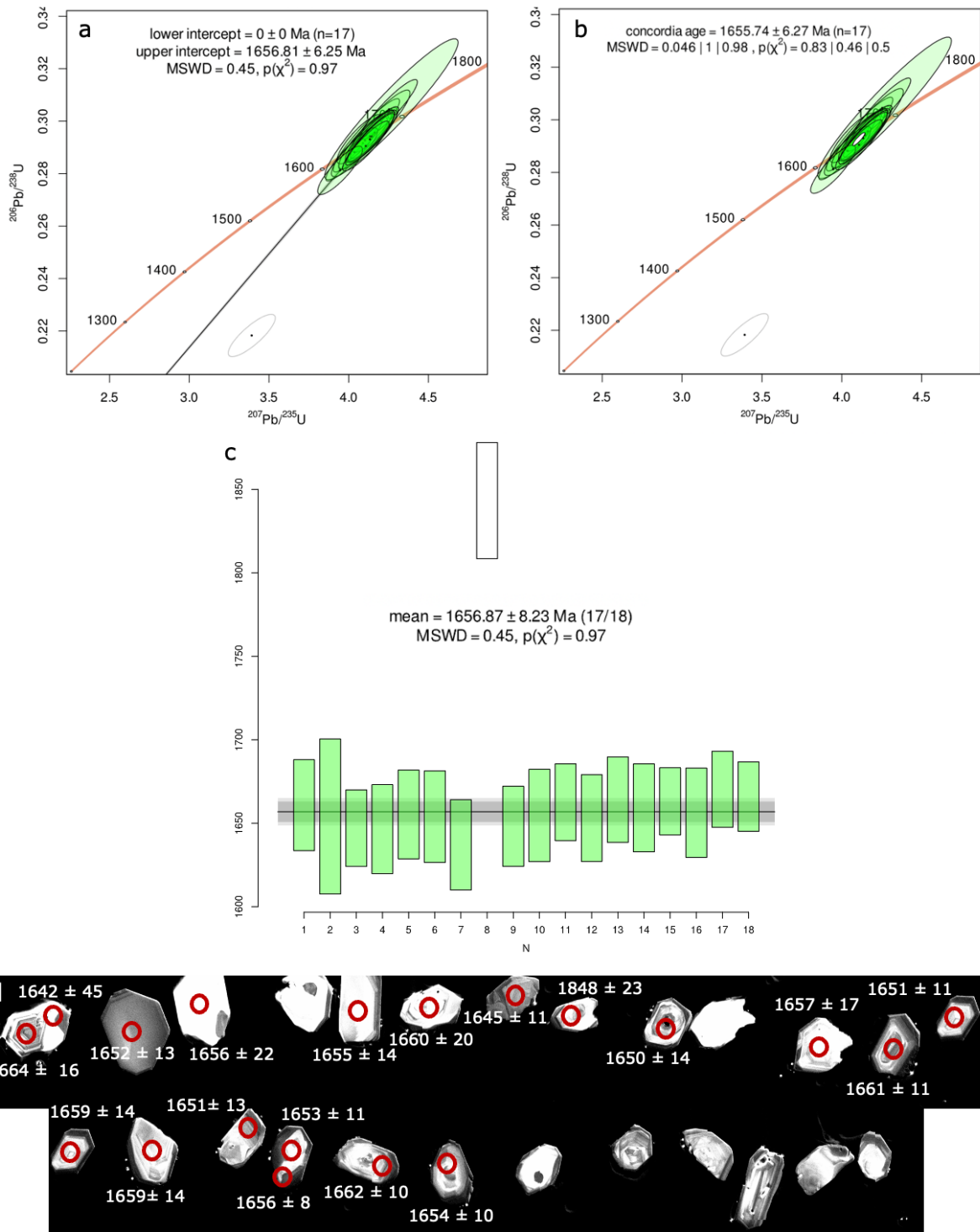


Figure 43. Wetherill concordia diagrams for the Vigelen granite collected in a basement window (BB20_20). a) Concordia diagram indicating an average $^{207}\text{Pb}/^{206}\text{Pb}$ age of 1657 ± 6 Ma. The $^{207}\text{Pb}/^{206}\text{Pb}$ age corresponds to the upper intercept of the discordia line forced through 0 ± 0 Ma. One analysis is discordant (the white ellipse with grey contour). Due to this, the analysis is discarded for the calculation. b) Concordia diagram indicating a concordia age of 1655 ± 6 Ma for the 17 concordant analyses. c) Weighted mean $^{207}\text{Pb}/^{206}\text{Pb}$ age of 1657 ± 8 Ma. Analysis no. 8 is rejected (the white with grey contour). d) CL image of the zircons with the respective $^{207}\text{Pb}/^{206}\text{Pb}$ ages. The red circles indicate where the laser appr. ablated the zircon.

5.3.2 Sample MU126

The sample MU126 is a reference sample of the Tännäs augen gneiss from the TAG. It was sampled along the river Tännän near the village Tännäs in Sweden (Fig. 44). The Tännäs augen gneiss has a grey coloured matrix with a few quartz bands and light pink K-feldspar augen that are elongated.

There is an abundance of zircons in the sample. The zircons have an average length of c. 250-300 μm . The zircon population comprises of clear, almost colourless, rounded to prismatic crystals with a hint of a brown colour. Almost all the grains have oscillatory zoning. There are metamict grains. Some of the fractured zircons have several fractures, in addition to inclusions (Appendix C). The analyses were done on 18 zircons.

All the analyses are concordant and cluster around c. 1650 Ma. The zircons yield a $^{207}\text{Pb}/^{206}\text{Pb}$ age of 1654 ± 5 Ma (MSWD=0.51) (Fig. 44a) and a concordia age of 1649 ± 6 Ma (Fig. 45b). The average age of 1651 ± 4 Ma is interpreted to be the magmatic crystallisation of the zircon. This new estimate is improving the upper intercept age of 1685 ± 20 Ma obtained by Claesson (1980).



Figure 44. Sample MU126 (Tännäs augen gneiss). a) The sample locality. The white, dotted circle marks where the sample was collected. b) Hand specimen of the sample.

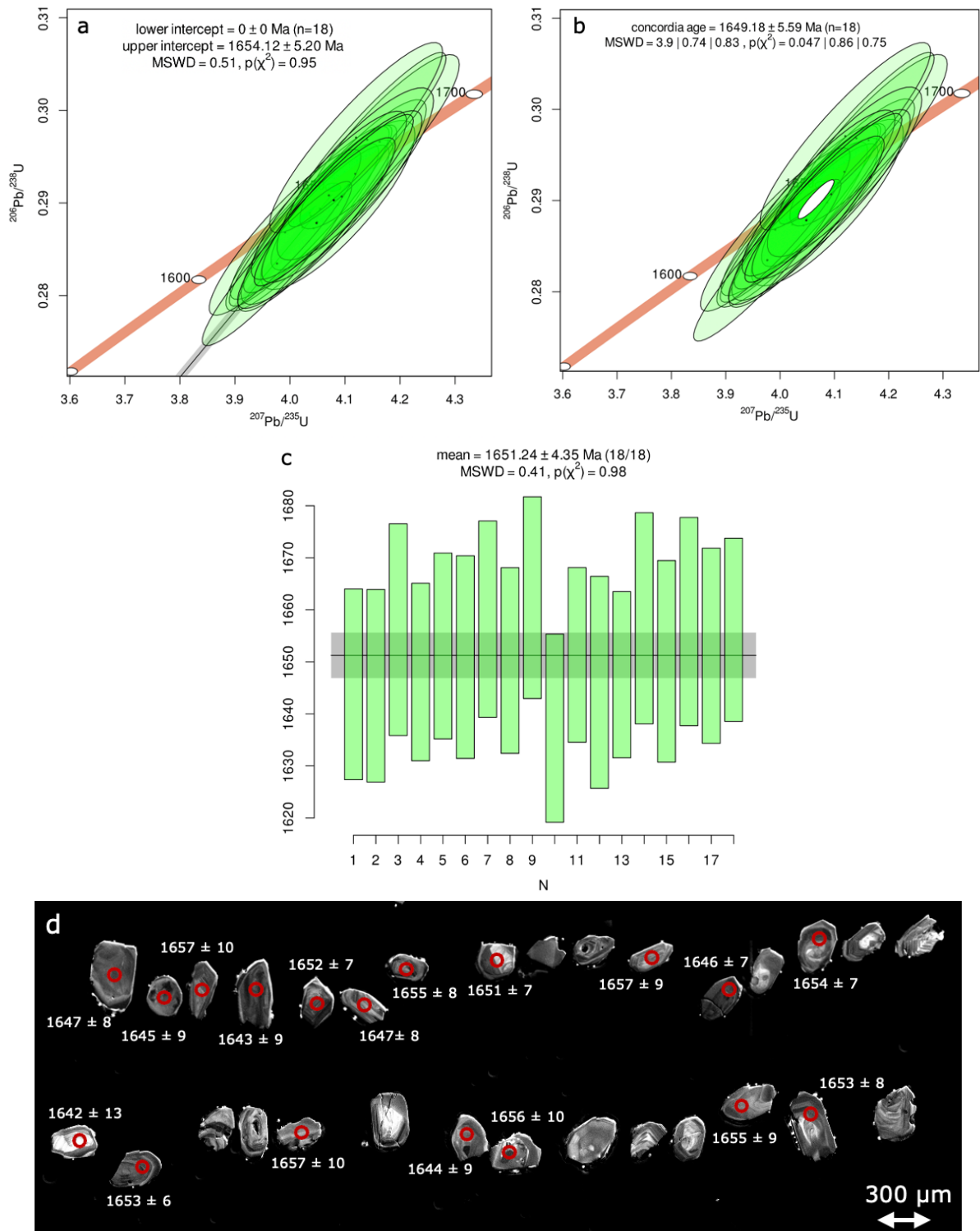


Figure 45. Wetherill concordia diagrams for the Tännäs augen gneiss (MU126). a) Concordia diagram indicating an age of 1654 ± 5 Ma ($^{207}\text{Pb}/^{206}\text{Pb}$ age). The $^{207}\text{Pb}/^{206}\text{Pb}$ age corresponds to the upper intercept of the discordia line forced through 0 ± 0 Ma. b) Concordia diagram indicating a concordia age of 1649 ± 6 Ma. c) Weighted mean $^{207}\text{Pb}/^{206}\text{Pb}$ age of 1651 ± 4 Ma. d) CL image of the zircons with the respective $^{207}\text{Pb}/^{206}\text{Pb}$ ages. The red circles indicate where the laser app. ablated the zircon.

5.3.3 Sample MU021

This sample represents the quartz striped K-feldspar augen gneiss collected in the Dagvolsjøen Nappe (Fig. 46). It has grey-green matrix with bands of quartz and light pink augens of K-feldspar up to 13 cm in size.

Zircons are abundant in this sample. The size of the zircons varies from c. 300 μm to around 600 μm in length. The zircons are almost colourless with a brownish hint. The crystals are anhedral to subhedral due to the lack of the prismatic look. The zoning varies from distinctly oscillatory zoning to more weak zoning. Two of the zircons look metamict, and several of them have inclusions and/or fractures (Appendix C). In total, 18 spot analyses were done on 16 zircons to target central and more marginal zones.

All but three analyses are concordant, one of the discordant is above the concordia line and the other two are under. The main population of zircon defines a $^{207}\text{Pb}/^{206}\text{Pb}$ age of 1658 ± 5 Ma with a MSWD of 0.71 (Fig. 47a). The two analyses under the concordia line yield a $^{207}\text{Pb}/^{206}\text{Pb}$ age of 1698 ± 13 Ma (MSWD=2.6) (Fig. 47b). The main population of analyses is interpreted to be the age of the magmatic crystallization of the protolith of the augen gneiss with an age of 1658 ± 5 Ma. The zircons with the older age of 1698 ± 13 Ma are interpreted to be inherited zircons. According to the BSE image, these two zircons were not ablated where there are inclusions or fractures (Appendix C).

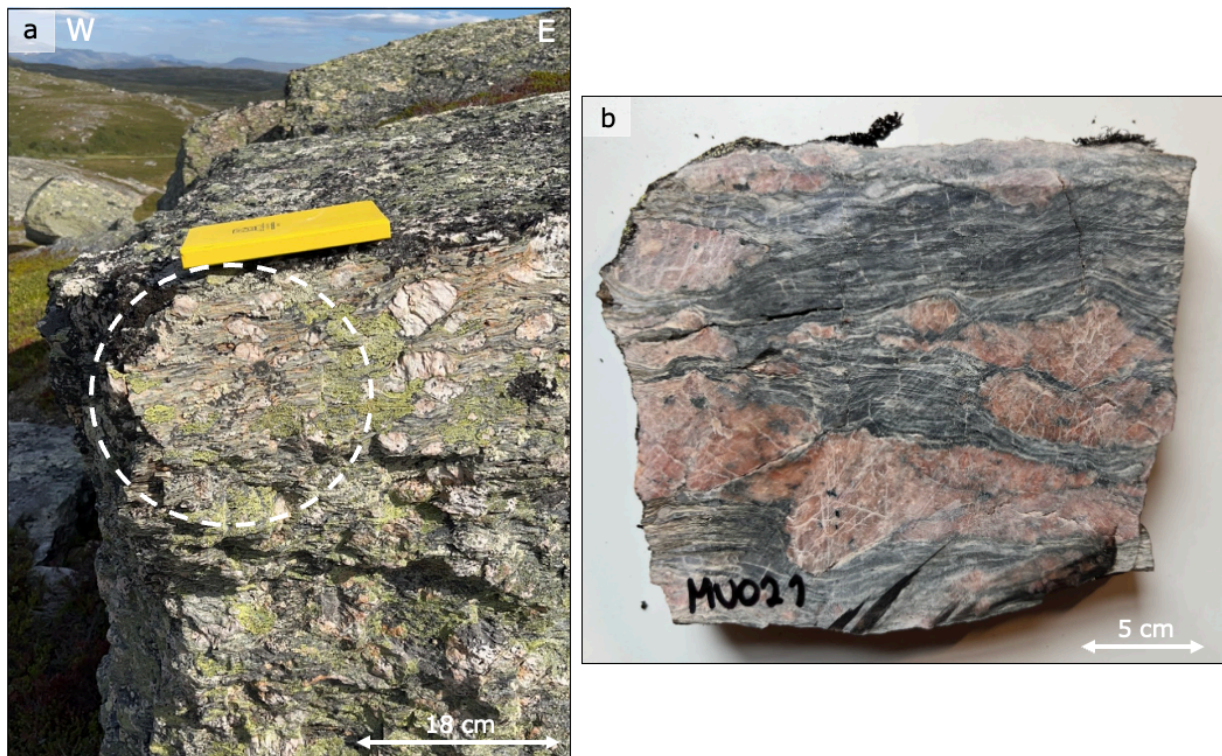


Figure 46. Sample MU021. a) The sample locality. The white, dotted circle marks where the sample was collected. b) Hand specimen cut parallel to the mineral lineation.

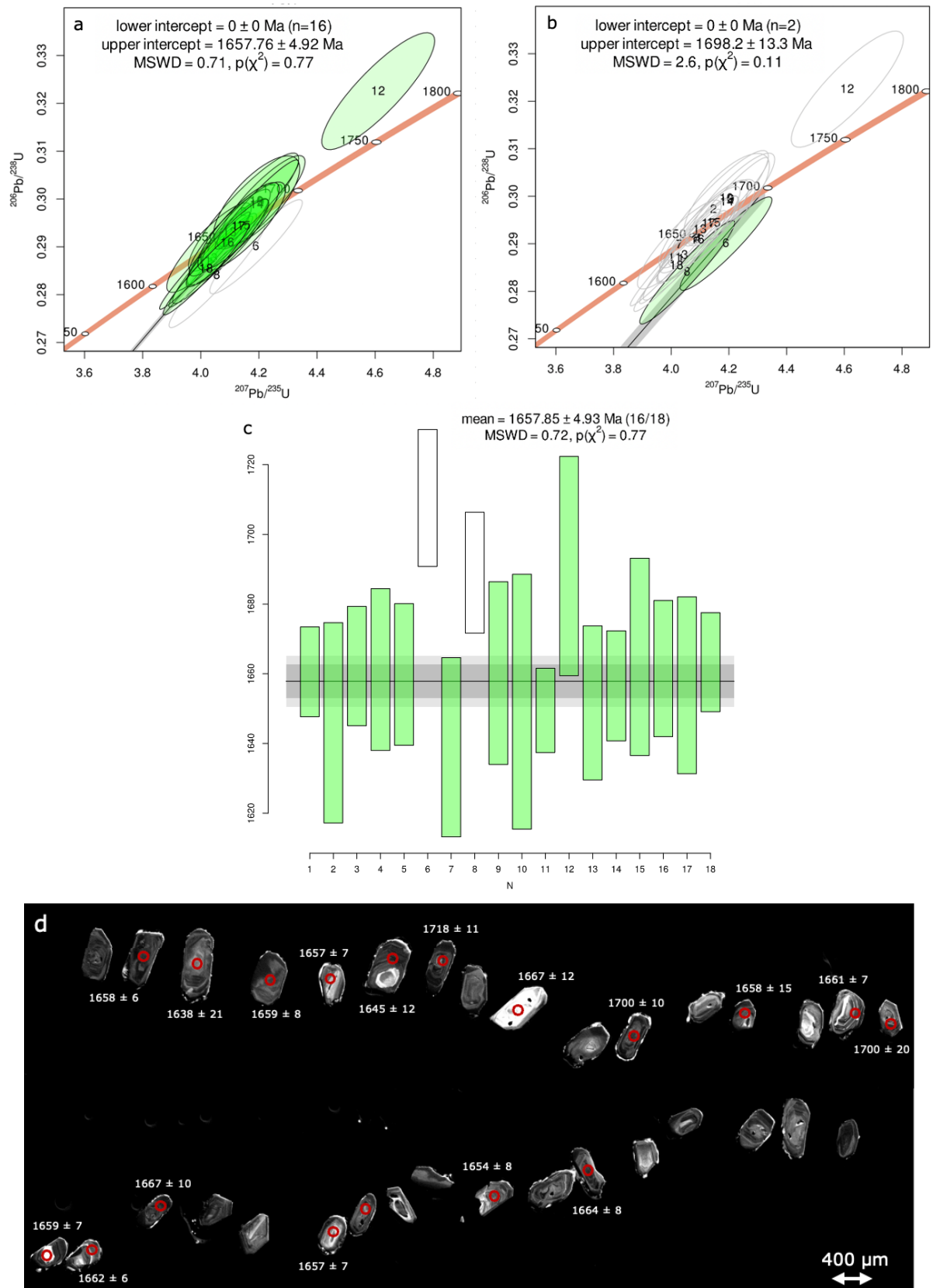


Figure 47. Wetherill concordia diagrams for MU021 from the Dagsvolsjøen Nappe. The $^{207}\text{Pb}/^{206}\text{Pb}$ age corresponds to the upper intercept of the discordia line forced through 0 ± 0 Ma. a) Concordia diagram indicating an age of 1658 ± 5 Ma ($^{207}\text{Pb}/^{206}\text{Pb}$ age) for the main population of zircons. The outliers (n=2) are white ellipses with grey contour and they are not included in the calculation. In the corner, the age calculation of the weighted mean of $^{207}\text{Pb}/^{206}\text{Pb}$ is presented. b) Concordia diagram indicating a $^{207}\text{Pb}/^{206}\text{Pb}$ age of 1698 ± 13 Ma for the two analyses that are discordant. c)

Weighted mean $^{207}\text{Pb}/^{206}\text{Pb}$ age of 1657 ± 5 Ma. Two analyses are rejected. d) CL-image of the zircons with the respective $^{207}\text{Pb}/^{206}\text{Pb}$ ages. The red circles indicate where the laser appr. ablated the zircon.

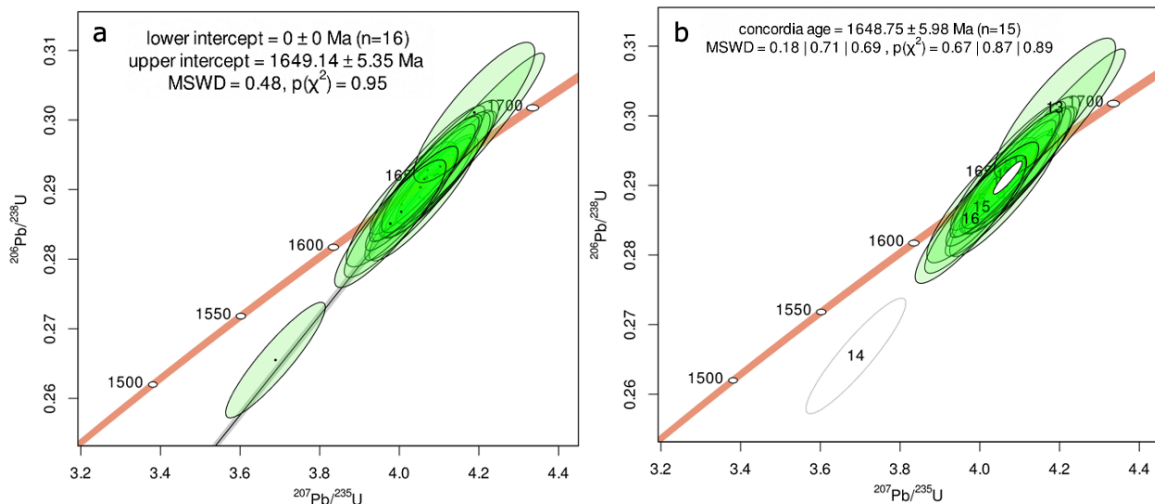
5.3.4 Sample BB20_19

Sample BB20_19 was sampled by Bernard Bingen. This sample is an augen gneiss from the Dagvolsjøen Nappe, and it was collected in the footwall of the Røragen detachment. The sampling outcrop is located at the Ryfossen waterfall. It has a mylonitic and finely laminated matrix which is green in colour with large, rose-red K-feldspar augens up to several cm in size. Quartz augens are also present. The rock is extremely deformed.

The sample is rich in zircon. The zircons have an average length of c. 250 μm . The population is comprised of clear zircons with a slightly light brown colour with just a few of them containing inclusions. There are no euhedral grains, and the distinct prismatic look is missing in almost all the grains. The zoning varies from oscillatory to more patchy, weak to broad zoning. There are a few fractures and inclusions according to the BSE image in Appendix C. In total, 16 spots were analysed on 16 grains.

15 of the analyses are concordant and overlapping. One analysis is discordant. All 16 analysis yields a $^{207}\text{Pb}/^{206}\text{Pb}$ age of 1649 ± 5 Ma with a MSWD of 0.48 (Fig. 48a) and the 15 concordant analysis yields a concordia age of 1648 ± 6 Ma (Fig. 48b). The discordant analysis is analysis no. 14 and has a $^{207}\text{Pb}/^{206}\text{Pb}$ age of 1645 ± 7 Ma (Fig. 48d).

According to the BSE image is there no fractures or inclusions where the laser ablated (Appendix C). Even though both cores and rims of the zircons were selected for analysis, all the analysis in BB20_19 yield a consistent age. The average age of this sample is interpreted to date the intrusion of the granite protolith of the augen gneiss.



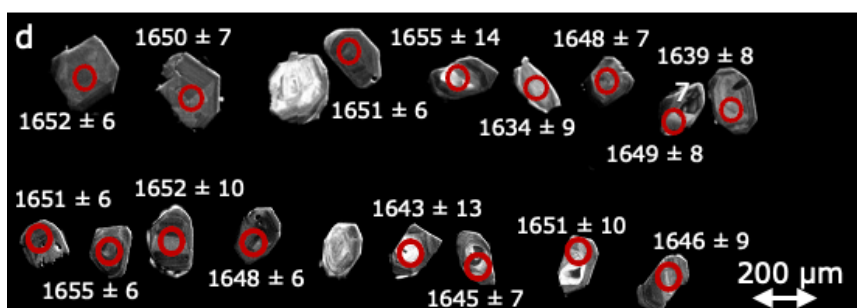
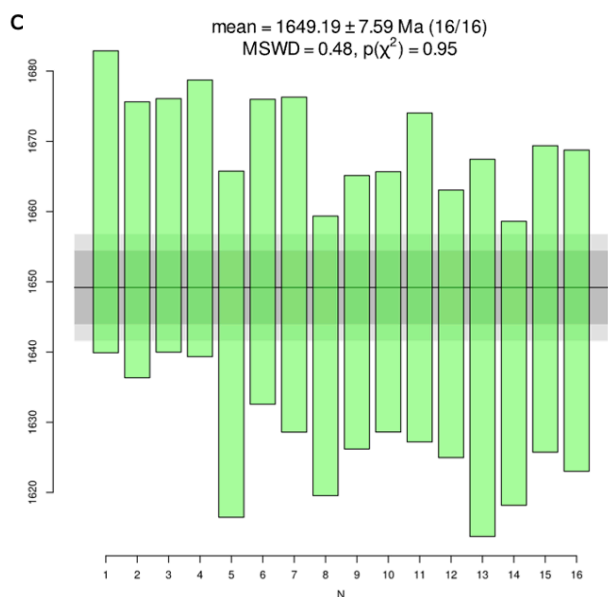


Figure 48. Wetherill concordia diagrams for BB20_19 from the Dagsvolsjøen Nappe. a) Concordia diagram for sample indicating an average age of 1649 ± 5 Ma ($^{207}\text{Pb}/^{206}\text{Pb}$ age). The $^{207}\text{Pb}/^{206}\text{Pb}$ age corresponds to the upper intercept of the discordia line forced through 0 ± 0 Ma. b) Concordia diagram indicating a concordia age of 1649 ± 6 Ma. One analysis is discordant (white ellipse with grey contour) and therefore rejected for the calculation. c) Weighted mean $^{207}\text{Pb}/^{206}\text{Pb}$ age of 1649 ± 8 Ma. d) CL image of the zircons with the respective $^{207}\text{Pb}/^{206}\text{Pb}$ ages. The red circles indicate where the laser appr. ablated the zircon.

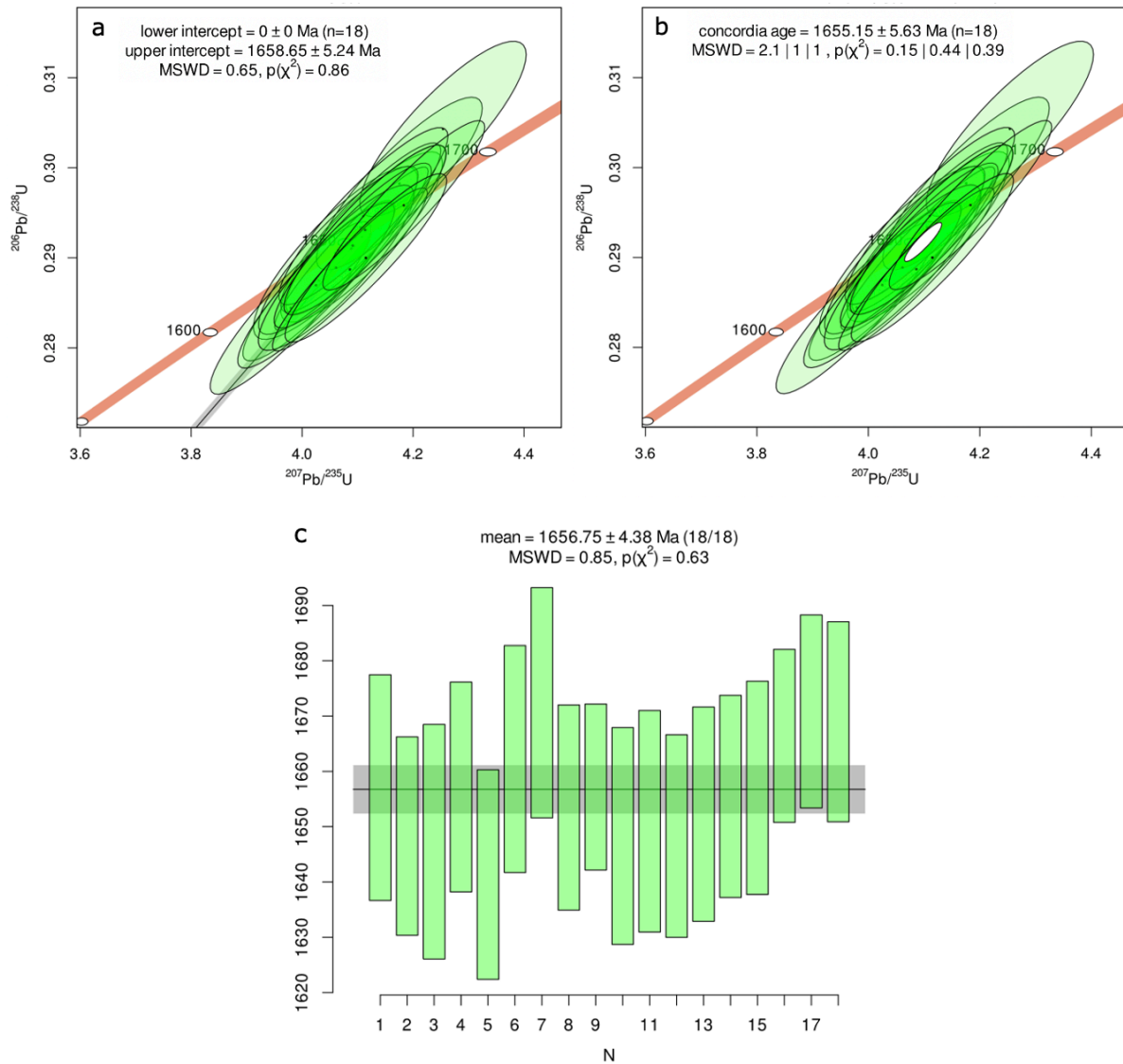
5.3.5 Sample JJ23

Sample JJ29 was collected by Johannes Jakob. This sample was collected for testing four hypotheses: (1) the conglomerate or meta-arkose in the Osen-Røa Nappe Complex can be misidentified in the field for augen gneiss, (2) sheets of augen gneiss from the Dagsvolsjøen Nappe are present in the underlying Osen-Røa Nappe Complex, (3) another rock is interlayered in the Osen-Røa Nappe Complex or (4) sheets of the basement of Skardøra antiform are interlayered in the overlying Osen-Røa Nappe Complex. JJ23 represents a thin sheet with unknown thickness of augen gneiss hosted in meta-arkose near the top of the Osen-Røa Nappe Complex. It was sampled along the river Vaula, and it is a foliated and deformed augen gneiss with blue quartz up to 3 mm in size. The augen gneiss is sheared and foliated with K-feldspar augen up to appr. 4 cm in size that forms little knolls on the outcrop surface in a dark, coarse-grained matrix that is chlorite-rich.

The size of the zircons varies from c. 200 μm to c. 500 μm in length, and the grains are (sub)euhedral. The zircons are almost colourless with a slightly light brown colour. Some of the crystals are metamict. The zircons are subhedral to euhedral, and a few of them have fractures. In the CL image, the zoning varies from distinct oscillatory zoning to

more weak zoning. There are almost no inclusions and fractures according to the BSE image (Appendix C). 16 spots were analysed on 16 different crystals.

The analyses are well grouped and concordant. They yield a $^{207}\text{Pb}/^{206}\text{Pb}$ age of 1659 ± 5 Ma with a MSWD of 0.65 (Fig. 49a) and an equivalent concordia age of 1655 ± 6 Ma (Fig. 49b). The obtained age is interpreted to be the age of magmatic crystallization of the granitic protolith of the augen gneiss.



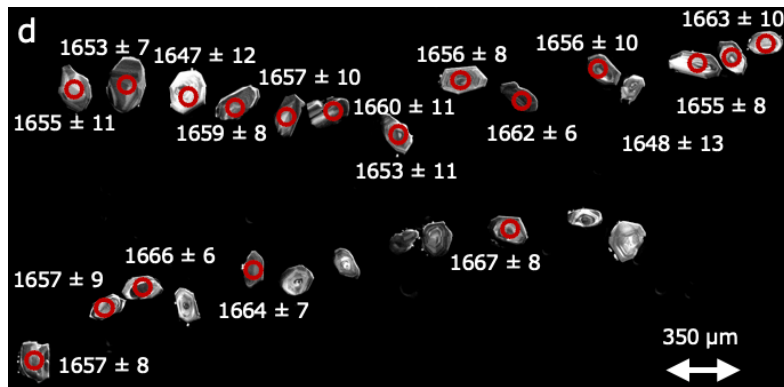


Figure 49. Wetherill concordia diagrams for JJ23. a) Concordia diagram indicating a $^{207}\text{Pb}/^{206}\text{Pb}$ age of 1659 ± 5 Ma. The $^{207}\text{Pb}/^{206}\text{Pb}$ age corresponds to the upper intercept of the discordia line forced through 0 ± 0 Ma. b) Concordia diagram indicating a concordia age of 1655 ± 6 Ma. c) Weighted mean $^{207}\text{Pb}/^{206}\text{Pb}$ age of 1657 ± 4 Ma. d) CL image of the zircons with the respective $^{207}\text{Pb}/^{206}\text{Pb}$ ages. The red circles indicate where the laser appr. ablated the zircon.

5.3.6 Sample JJ29

The granite JJ29 was sampled by Johannes Jakob when we were in the field together (Fig. 50). The sample JJ29 represents a pink coloured granitic intrusion that has intruded the augen gneiss of the TAG on the eastern limb of the Skardøra antiform. The rock cuts the foliation in the augen gneiss.

Only 13 zircons were recovered for this sample due to the low abundance of the mineral. The zircons have an average length of c. 250 μm and the population is comprised of clear zircons with a slightly light brown colour. Several of the zircons may be metamict. The zircons have zoning, both distinct and weak oscillatory and faint zoning. There are almost no fractures and just a few inclusions according to the BSE image (Appendix C). In total, 16 analyses were performed on 12 crystals where four of the zircons were analysed twice.

This sample has analyses that are scattered, and there are discordant analyses. Consequently, no concordia age was calculated. In Fig. 51, several combinations of analyses are proposed for extracting ages. In Fig. 51a-b, a $^{207}\text{Pb}/^{206}\text{Pb}$ age of 1658 ± 6 Ma is yield from eleven well aligned analyses with a MSWD=1.5. Under these analyses, a group of three analyses is plotting. They are plotting under the regression line defined by the eleven analyses and yield a $^{207}\text{Pb}/^{206}\text{Pb}$ age of 1711 ± 14 Ma (MSWD=0.78) (Fig. 51c). Analysis no. 4 is discordant and plots alone. This analysis is performed on a rim, and it yields a $^{207}\text{Pb}/^{206}\text{Pb}$ age of 1490 ± 11 Ma. The rim is too thin to be analysed separately. A lower intercept age can be calculated through the oldest analyses. Two calculations were performed, and they yield a lower intercept age of 436 ± 43 Ma with a MSWD=2.2 (Fig. 51d) and 351 ± 38 Ma with a MSWD=1.1 (Fig. 51e). The zircons with older age are interpreted to be inherited, while the lower intercept ages of 436 ± 43 Ma and 351 ± 38 Ma can be interpreted to be the time frame of the emplacement of the granite.

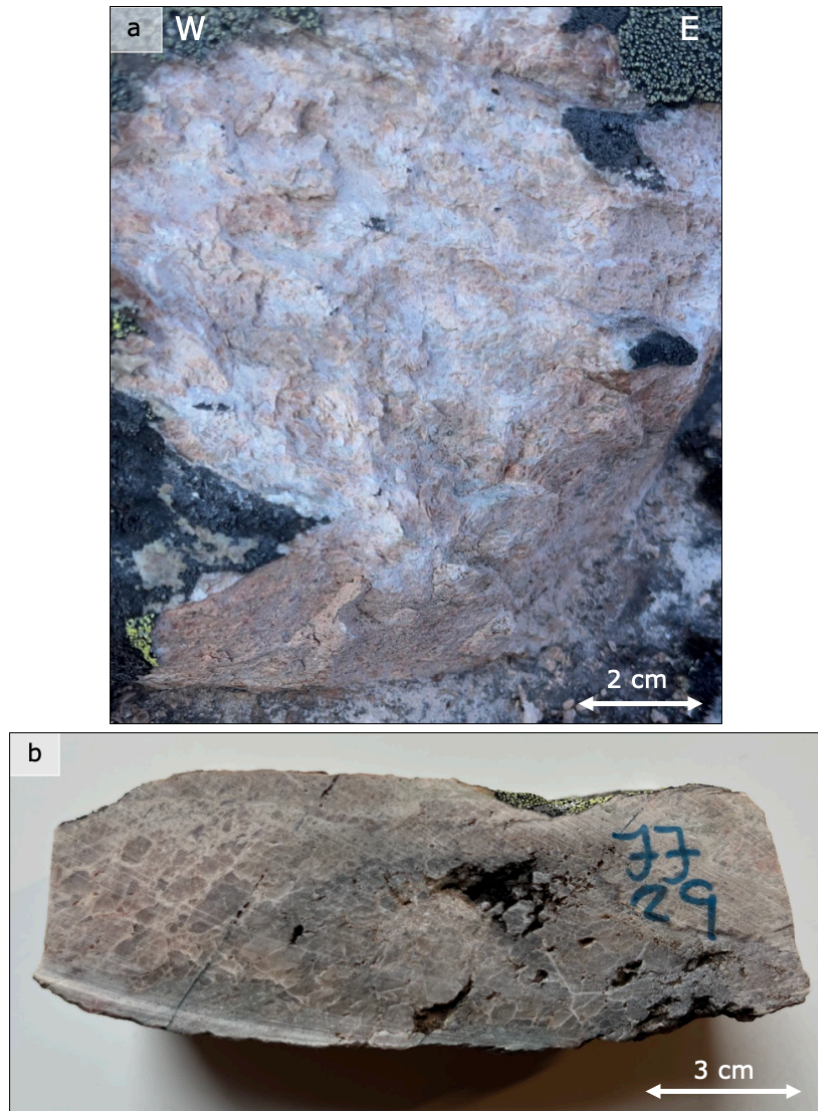
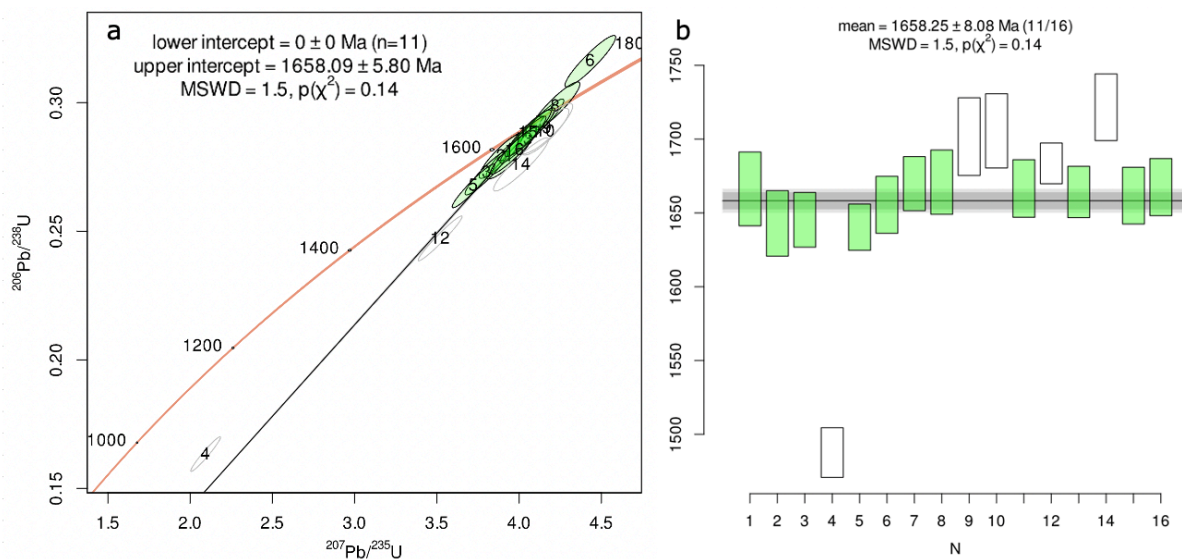


Figure 50. Sample JJ29. a) The sample locality. I was not present when the sample was taken, however, this is where Johannes Jakob sampled it. b) Hand specimen of the sample.



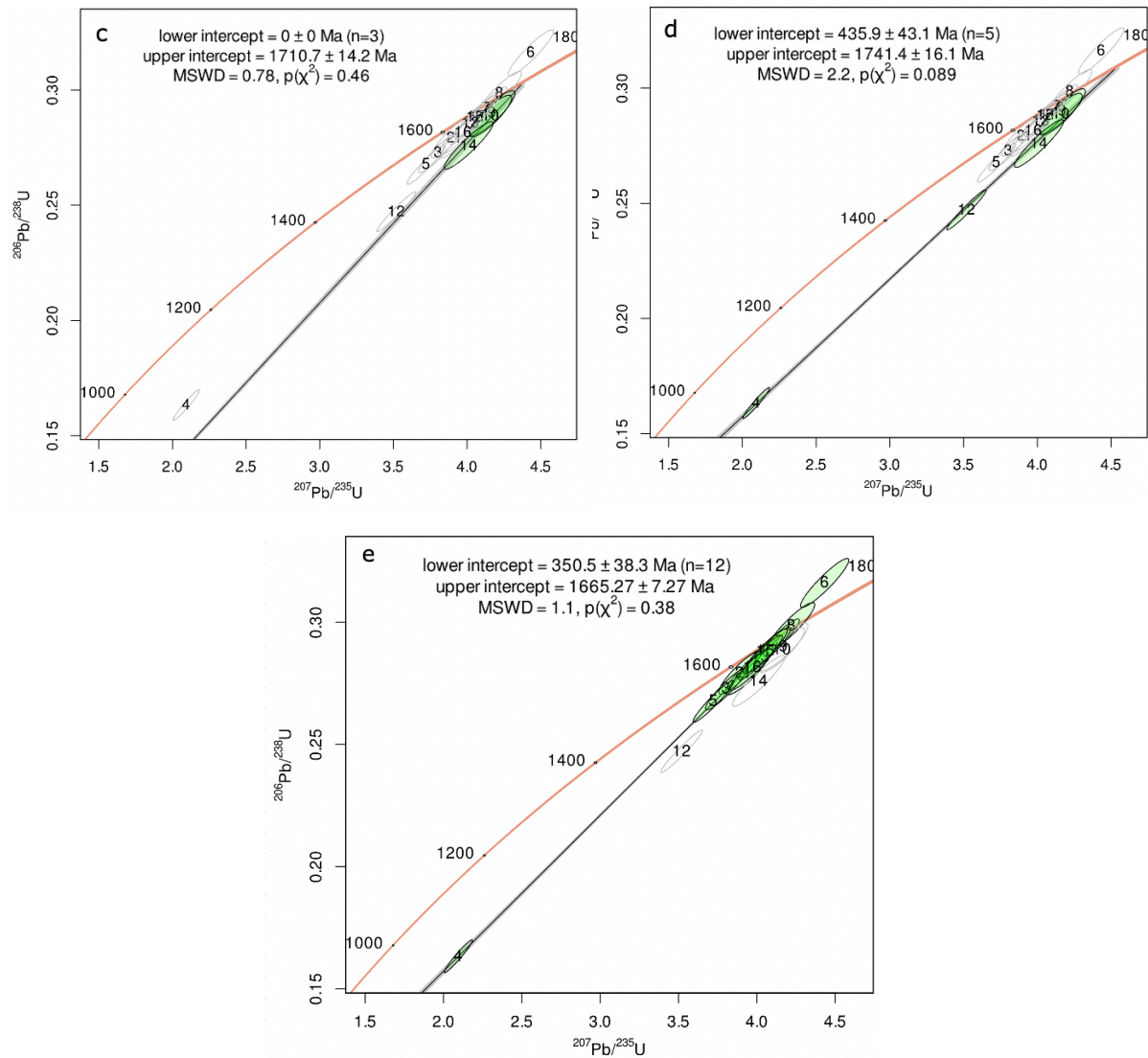


Figure 51. Concordia diagrams for sample JJ29 (the granitic sheet). In each of the diagrams, the green ellipses are selected for the calculation and the white ellipses with grey contour are discarded for the calculation. The $^{207}\text{Pb}/^{206}\text{Pb}$ age corresponds to the upper intercept of the discordia line forced through 0 ± 0 Ma. a) Concordia diagram of the main eleven analyses that are grouped together. They indicate a $^{207}\text{Pb}/^{206}\text{Pb}$ age of 1658 ± 6 Ma. b) Weighted mean plot for the concordia plot in Fig. a with a $^{207}\text{Pb}/^{206}\text{Pb}$ age of 1658 ± 8 Ma. c) Concordia diagram for three analyses plotting under the group of the eleven analyses indicating an upper intercept age of 1711 ± 14 Ma ($^{207}\text{Pb}/^{206}\text{Pb}$ age). d) Concordia diagram indicating a lower intercept age of 435 ± 43 Ma ($^{207}\text{Pb}/^{206}\text{Pb}$ age). e) Concordia diagram indicating a lower intercept age of 351 ± 38 Ma ($^{207}\text{Pb}/^{206}\text{Pb}$ age). f) CL image of the zircons with the respective $^{207}\text{Pb}/^{206}\text{Pb}$ ages. The red circles indicate where the laser appr. ablated the zircon.

5.4 Geochemistry

Whole-rock geochemical analyses were performed on ten samples from this study, including five of the samples for geochronology. Fig. 52 shows the location of the samples, except MU126 from Tännäs. Appendix D has the data set of the samples collected for this thesis. In addition to the samples from this study, published analyses

from Austrheim et al. (2003), Røhr et al. (2013) and Bjerkan (2020) have been plotted for comparison. The data sets are in Appendix E-G. The analyses are of a diversity of orthogneisses of 1700–1600 Ma from the WGR. There are eleven samples from Austrheim et al. (2003) from the Hustad Igneous Complex (HIC), seven from Røhr et al. (2013) from the Molde area and 28 samples from Bjerkan (2020), mainly from the Eidsvåg area.

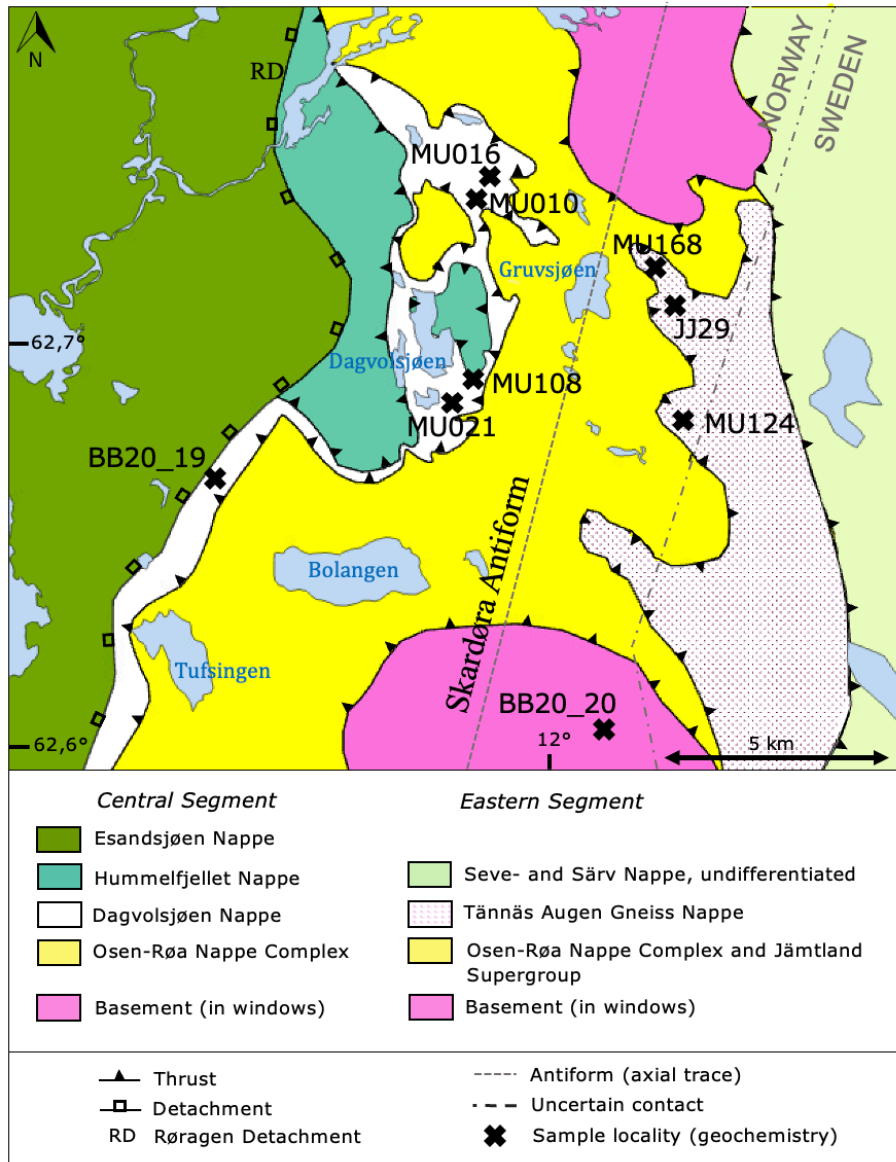


Figure 52. Geological overview map over the study area with the sample localities for geochemistry. The map is based on Nilsen and Wolff (1989), NGU (2023), Bergman et al. (2012) and observations in the field. The coordinate system is WGS84 UTM Zone 32N and 33N.

5.4.1 Geochemical classification

Table 6 summarizes the geochemical classification. The sections below will describe the results from the different classifications schemes.

Table 6. Summary of the geochemical classification after Middlemost (1994), Debon and Le Fort (1983), Shand (1943), O'Connor (1965) and Frost and Frost (2008). If the sample is on the boundary between two field, but more in one field, the classification is marked with *. If the sample is outside of the classification range, N/A is used.

Sample	Middlemost (1994) TAS	Debon and Le Fort (1983) Q-P	Shand (1943) A/CNK-A/NK	O`Connor (1965) Ab-Or-An	Frost and Frost (2008) MG#-SiO₂	Frost and Frost (2008) SiO₂-MALI
BB20_20	Granite	Granite*	Metaluminous	Granite	Magnesian	Alkali-calcic
BB20_19	Granodiorite	Adamellite	Peraluminous	Quartz monzonite	Magnesian	Alkali-calcic
JJ29	Granite	Granodiorite	Metaluminous	Granite	Magnesian	Calcic
JJ23	Granite*	Granite	Peraluminous	Granite	Magnesian	Alkali-calcic
MU010	Granite*	Granite	Peraluminous	Quartz monzonite	Magnesian	Calc-alkalic
MU016	Granodiorite	Adamellite	Boundary	Quartz monzonite	Magnesian	Boundary
MU021	Granite	Adamellite	Peraluminous	Granite	Magnesian	Calc-alkalic
MU108	Granite	N/A	Peraluminous	N/A	Ferroan	Alkalic
MU124	Granodiorite	Granite	Peraluminous	N/A	Magnesian	Alkali-calcic
MU126	Quartz monzonite	Adamellite	Metaluminous	Granite	Magnesian	Alkali-calcic
MU168	Granite*	Granite	Peraluminous	Quartz monzonite*	Magnesian	Alkali-calcic

Fig. 53 shows an igneous classification after Middlemost (1994), known as the TAS diagram. The SiO_2 - $\text{Na}_2+\text{K}_2\text{O}$ diagram is a geochemical classification diagram for magmatic rocks. The rocks from this study are clustered at the boundary between the fields of granite (BB20_20, JJ29, MU010, MU021, MU108, and MU168), quartz monzonite (MU126) and granodiorite (BB20_19, MU016 and MU124). The samples from the WGR are more scattered and show more variability in the fields of granite, quartz monzonite, granodiorite, monzonite, diorite, monzodiorite and gabbroic diorite. Three samples from the HIC (Austrheim et al., 2003) plot in the monzodiorite and the gabbroic diorite fields.

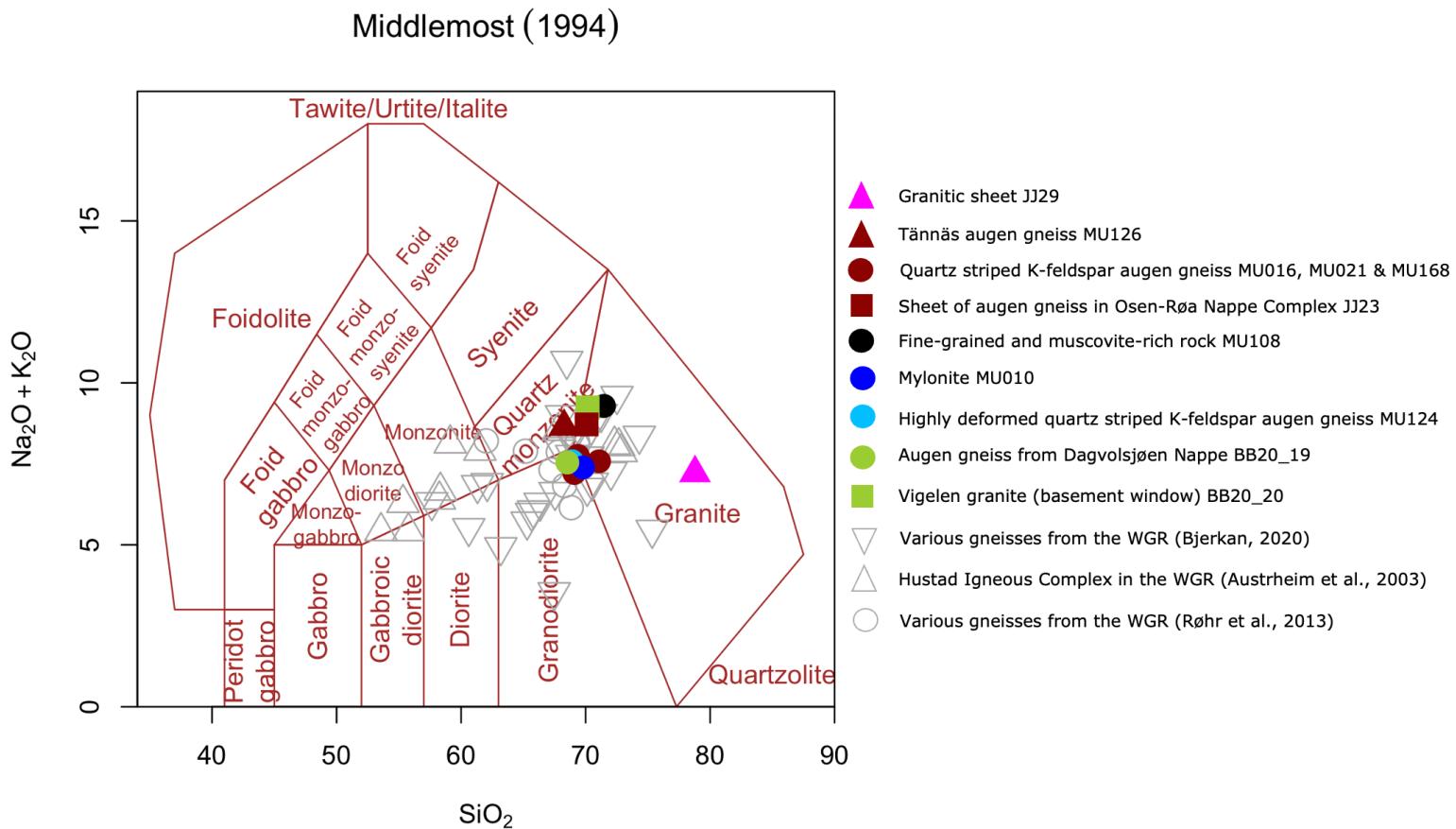


Figure 53. Classification of igneous rocks from Middlemost (1994) with $\text{Na}_2+\text{K}_2\text{O}$ on the y-axis and SiO_2 on the x-axis, known as the TAS diagram. The rocks from this study are clustered and plot in the granite, quartz monzonite and granodiorite fields. The rocks from the WGR are more scattered, and the rocks from Røhr et al. (2013) plot in the field of quartz monzonite and granodiorite, the rocks from Austrheim et al. (2003) plot in the granite, monzonite, monzodiorite and gabbroic diorite fields while the rocks from Bjerkan (2020) plot in the granite, quartz monzonite, granodiorite, monzonite and diorite fields.

Another classification of igneous rocks is given by Debon and Le Fort (1983) in Fig. 54. The Q-P diagram provides a classification of quartz saturated rocks with the two variables P and Q . The Q value is calculated as $Q = \text{Si}/3 - (\text{K} + \text{Na} + 2 \cdot \text{Ca}/3)$, representing the proportion of quartz present in the rock. The P value is determined by the ratio plagioclase/K-feldspar, calculated as $P = \text{K} - (\text{Na} + \text{Ca})$. The augen gneisses plot in the granite (BB20_20, MU010, MU168, and MU124) and the adamellite (BB20_19, MU016, MU021 and MU168) fields. JJ29, the granitic sheet, is rich in quartz and plots inside of the granodiorite field while MU108 (the fine-grained and muscovite-rich rock) plots to the right of the diagram. This is outside of the field of common magmatic granitoid rocks. The samples from the WGR (Bjerkan (2020), Austrheim et al. (2003) and Røhr et al. (2013)) are more distributed in the classification diagram, but appr. half of them plot around the samples from this study. One sample from Bjerkan (2020) plots in the tonalite field while others plot in the quartz syenite field and two from Austrheim et al. (2003) plot in the monzogabbro field. Eight samples from the three contributors plot in the quartz monzodiorite field.

Debon and Le Fort P – Q

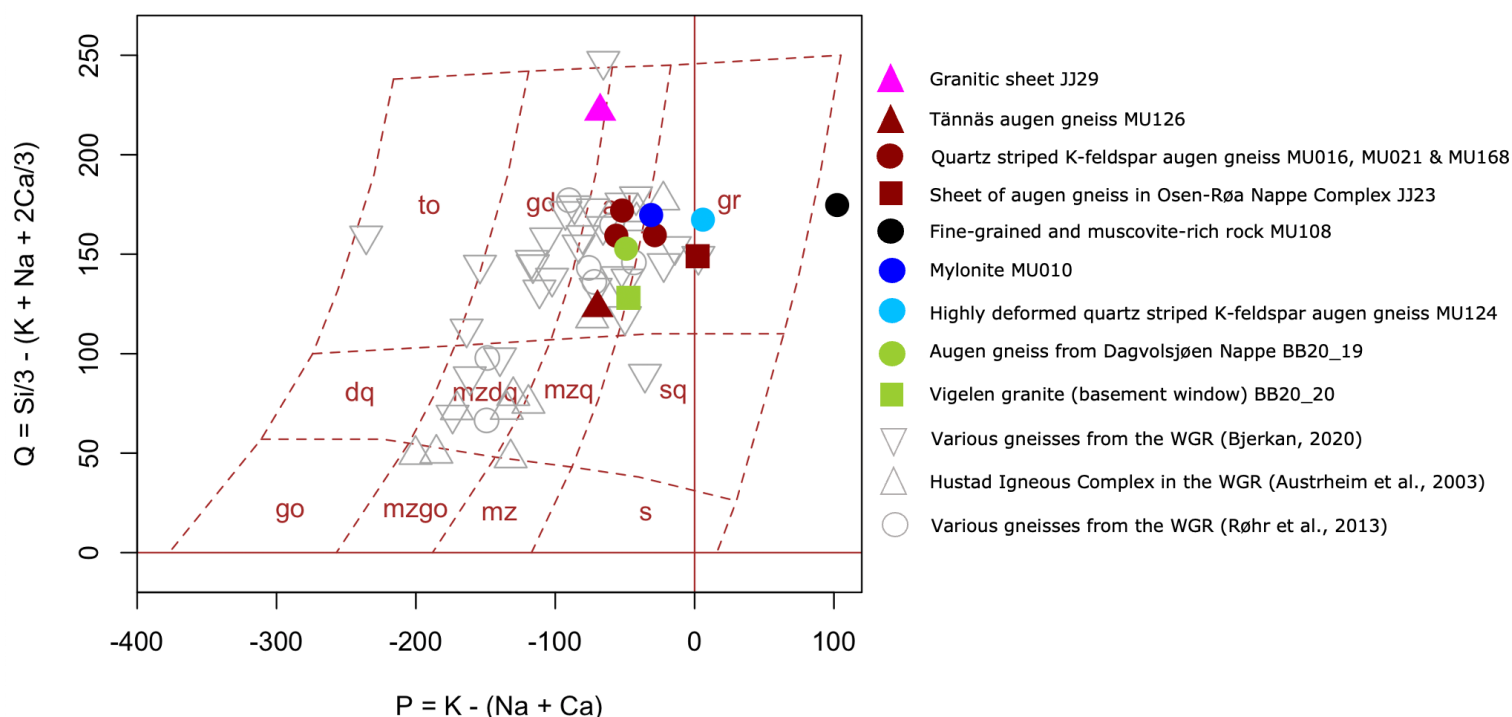


Figure 54. Classification of igneous rocks from Debon and Le Fort (1983) (the Q-P diagram). The augen gneisses and granites from this study plot in the granite (gr) and adamellite (ad) fields, except from JJ29 that plots in the granodiorite field and MU108 that plots outside of the field of common magmatic granitoid rocks. The samples from Bjerkan (2020), Austrheim et al. (2003) and Røhr et al. (2013) (from the WGR) are more distributed in the diagram, but half of these cluster around the rocks from this study.

The Alumina Saturation Index (ASI) diagram of Shand (1943) is in Fig. 55. This diagram plots the ratio A/CNK ($\text{Al}_2\text{O}_3/(\text{CaO}+\text{Na}_2+\text{K}_2\text{O})$) against A/NK ($\text{Al}_2\text{O}_3/(\text{Na}_2\text{O}+\text{K}_2\text{O})$) to discriminate between peraluminous, metaluminous and peralkaline rocks. Muscovite granitoid suits normally plot in the peraluminous field while biotite-amphibole granitoid suits generally plot in the metaluminous field and on the boundary between per- and metaluminous (Shand, 1943). Most samples from this study plot close to the boundary between the fields of peraluminous and metaluminous. The Vigelen basement granite (BB20_20), the granitic intrusion (JJ29) and the strongly quartz striped K-feldspar augen gneiss (MU126) plot in the metaluminous field. One of the quartz striped K-feldspar augen gneisses (MU016) plots on the boundary, while the other samples from this study plot in the peraluminous field. The fine-grained and muscovite-rich rock (MU108) plots in the middle of the peraluminous field. Most of the samples from the WGR plot in the metaluminous field and around the boundary.

A/CNK – A/NK plot (Shand 1943)

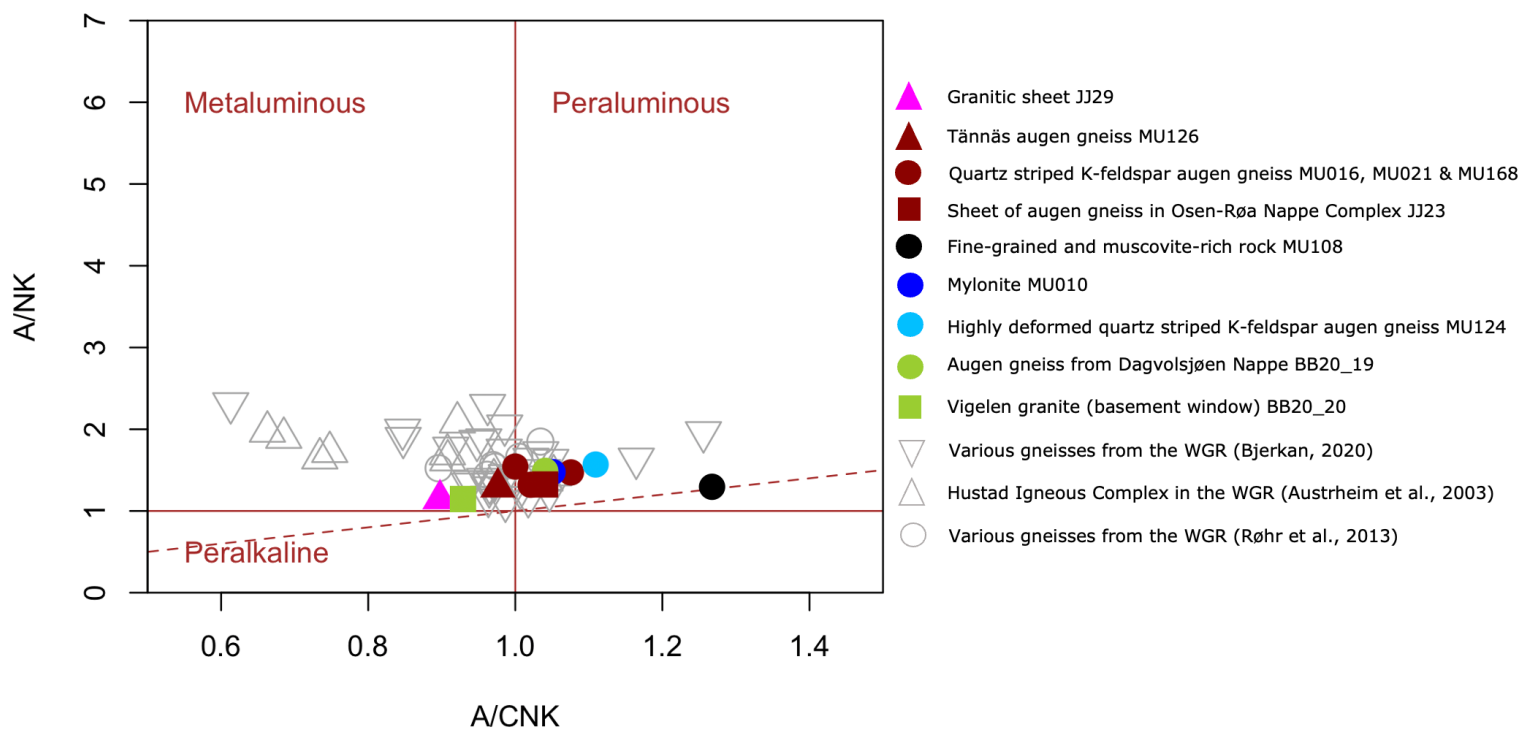


Figure 55. Classification of metaluminous, peraluminous and peralkaline rocks of Shand (1943) (A/CNK – A/NK diagram). Most of the samples are clustered around the boundary between metaluminous and peraluminous. BB20_20, JJ29 and MU126 plot in the metaluminous field. MU016 plots on the border between metaluminous and peraluminous while the other samples plot in the peraluminous field. MU108 plots in the middle of the peraluminous field. Most of the samples from Bjerkan (2020), Austrheim et al. (2003) and Røhr et al. (2013) from the WGR plot around the boundary between metaluminous and peraluminous, but in the metaluminous field.

To highlight rocks of trondhjemite and tonalite composition, the triangular An-Ab-Or diagram of O'Connor (1965) is useful. This diagram illustrates the ratio between normative anorthite (An), albite (Ab) and orthoclase (Or) in rocks with more than 10% quartz (O'Connor, 1965). Samples of this study plot in the granite (BB20_20, JJ29, MU021 and MU126) and quartz monozonite (MU016, BB20_19, MU010 and MU168) fields (Fig. 56). The fine-grained and muscovite-rich rock (MU108) plots much closer to the Or-

corner. The granite intrusion (JJ29) is closest to the trondhjemite field. The gneisses from Bjerkan (2020) plot in the fields of granite and granodiorite in addition to one sample just inside of the trondhjemite field. One sample from Austrheim et al. (2003) plots in the tonalite field, while the others plot in the granodiorite, the quartz monzonite and the granite fields. The samples from Røhr et al. (2013) are in the granodiorite and quartz monzonite fields.

Feldspar triangle (O'Connor 1965)

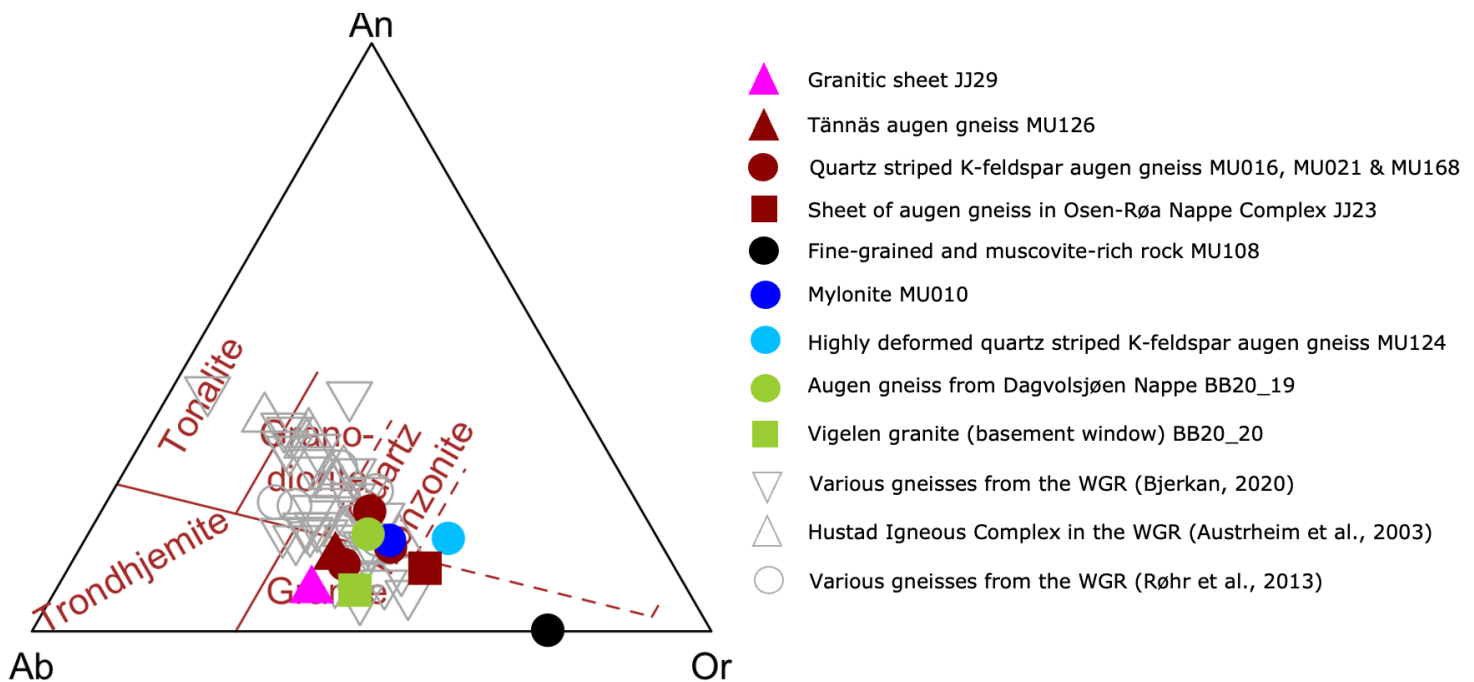


Figure 56. Feldspar triangle diagram with anorthite (An), albite (Ab) and orthoclase (Or) of O'Connor (1965). The samples from this thesis plot in the granite and quartz monzonite fields, except for MU124 and MU108. MU124 plots right outside of the granite and quartz monzonite fields while MU108 plots closer to the corner with Or. The gneisses from the WGR (Austrheim et al., 2003, Røhr et al., 2013, Bjerkan, 2020) plot mainly in the fields of granite, quartz monzonite and granodiorite. Two samples from Bjerkan (2020) plot in the trondhjemite and tonalite field and one sample from Austrheim et al. (2003) plots in the tonalite field.

Frost and Frost (2008) classifies felspathic igneous rocks using five geochemical variables: the Fe-index ($\text{FeO}/(\text{FeO}+\text{MgO})$), the modified alkali-lime-index ($\text{Na}_2+\text{K}_2\text{O}-\text{CaO}$ vs SiO_2), the feldspathoid silica-saturation index, the aluminum-saturation index ($\text{A}/\text{CNK} = \text{Al}_2\text{O}_3/\text{CaO}+\text{Na}_2\text{O}+\text{K}_2\text{O}$) and the alkalinity-index ($\text{Al}_2\text{O}_3/(\text{Na}_2\text{O}+\text{K}_2\text{O})$) (Frost et al., 2001, Frost and Frost, 2008). In Fig. 57a, the Fe-index is plotted against the SiO_2 content and most of the samples plot in the magnesian field. The fine-grained and muscovite-rich rock (MU108) plots in the ferroan field. The majority of the samples from the WGR plot in the magnesian field. In Fig. 57b, the modified alkali-lime-index is plotted against SiO_2 , and the samples are scattered. However, most of the samples border between the calc-alkalic and alkali-calcic fields. MU108 plots in the alkalic field. In these two diagrams, the intrusion JJ29 plots more to the right due to its high SiO_2 content. BB20_20, the Vigelen basement granite, has a higher Fe-index and modified alkali-lime-index than the augen gneisses from the Dagsvolsjøen and Tännäs nappes (Fig. 57a-b).

Granite tectonic discrimination – Frost and Frost (2008)

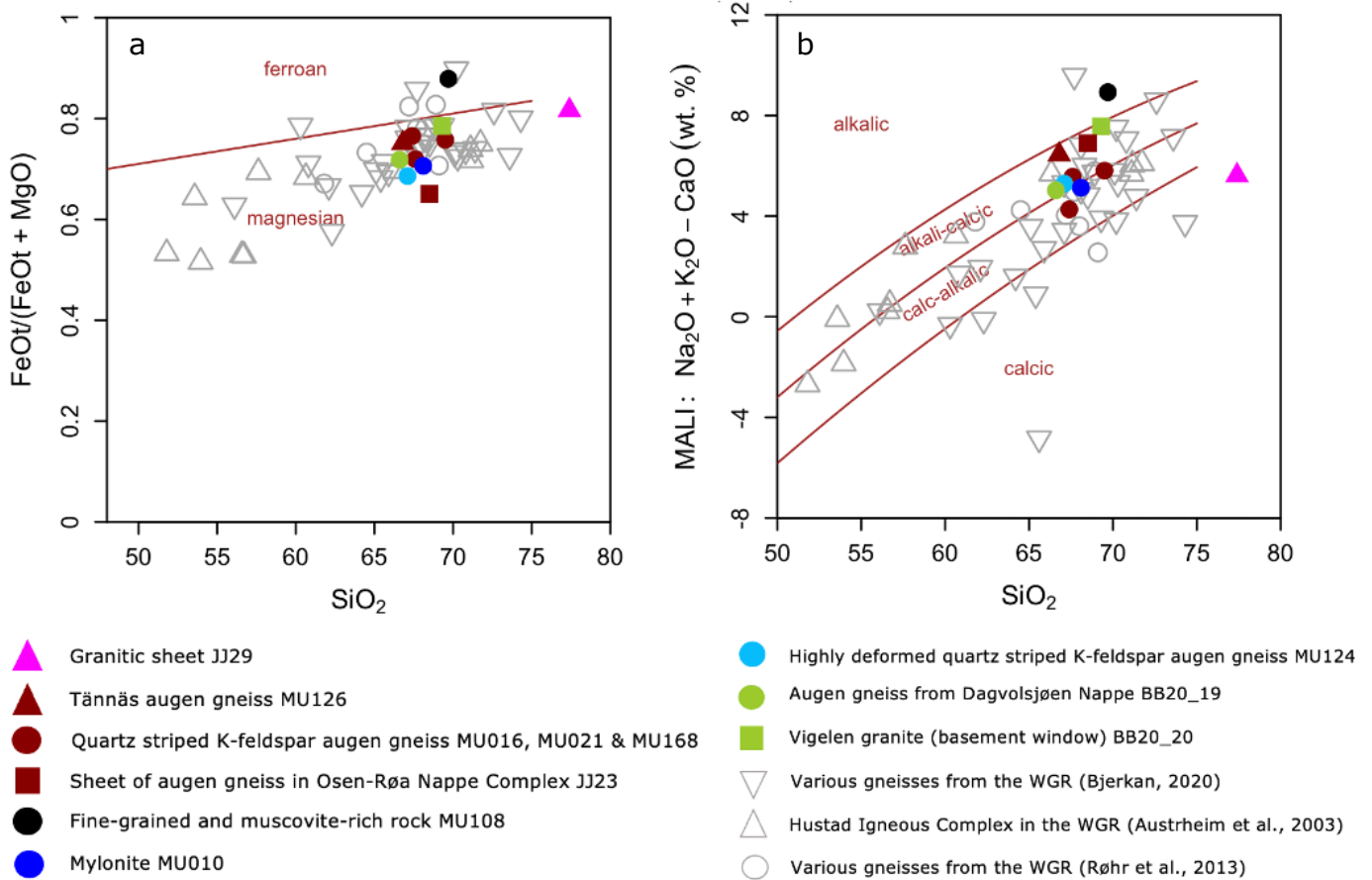


Figure 57. Tectonic discrimination diagrams for granite from Frost and Frost (2008). a) The diagram has SiO_2 on the x-axis and $\text{FeO}/(\text{FeO} + \text{MgO})$ (the Fe-index) on the y-axis. All samples except six (three from Bjerkan (2020), two from Røhr et al. (2013) and MU108) plot in the magnesian field. b) SiO_2 is plotted on the x-axis against modified alkali-lime-index on the y-axis. Most of the samples from this study and the WGR plot around the calc-alkaline and alkali-calcic border. MU108 plots in the alkalic field and JJ29 plots in the calcic field.

To distinguish between A-type granites and I- and S-type granites, the granite classification of Whalen et al. (1987) is used (Fig. 58). The diagrams have Ga/Al on the x-axis since I- and S-type granites are characterized by a low Ga/Al ratio, and this will distinguish them from A-type granites (Whalen et al., 1987). Ga/Al is plotted against major or trace elements, in this case Y (Fig. 578a) and Zr (Fig. 58b) to discriminate between A-type granites from the other two. In Fig. 58a, all the samples from this study and from the WGR from Bjerkan (2020), Austrheim et al. (2003) and Røhr et al. (2013) plot in the I- and S-type field. The Vigelen basement granite (BB20_20) plots on the border between A-type and I- and S-type granites. This is consistent with the diagram in Fig. 58b, except for the Vigelen granite (BB20_20) and one sample from Bjerkan (2020). These two plot in the A-type granite field.

Distinguish A-type granites – Whalen et al. (1987)

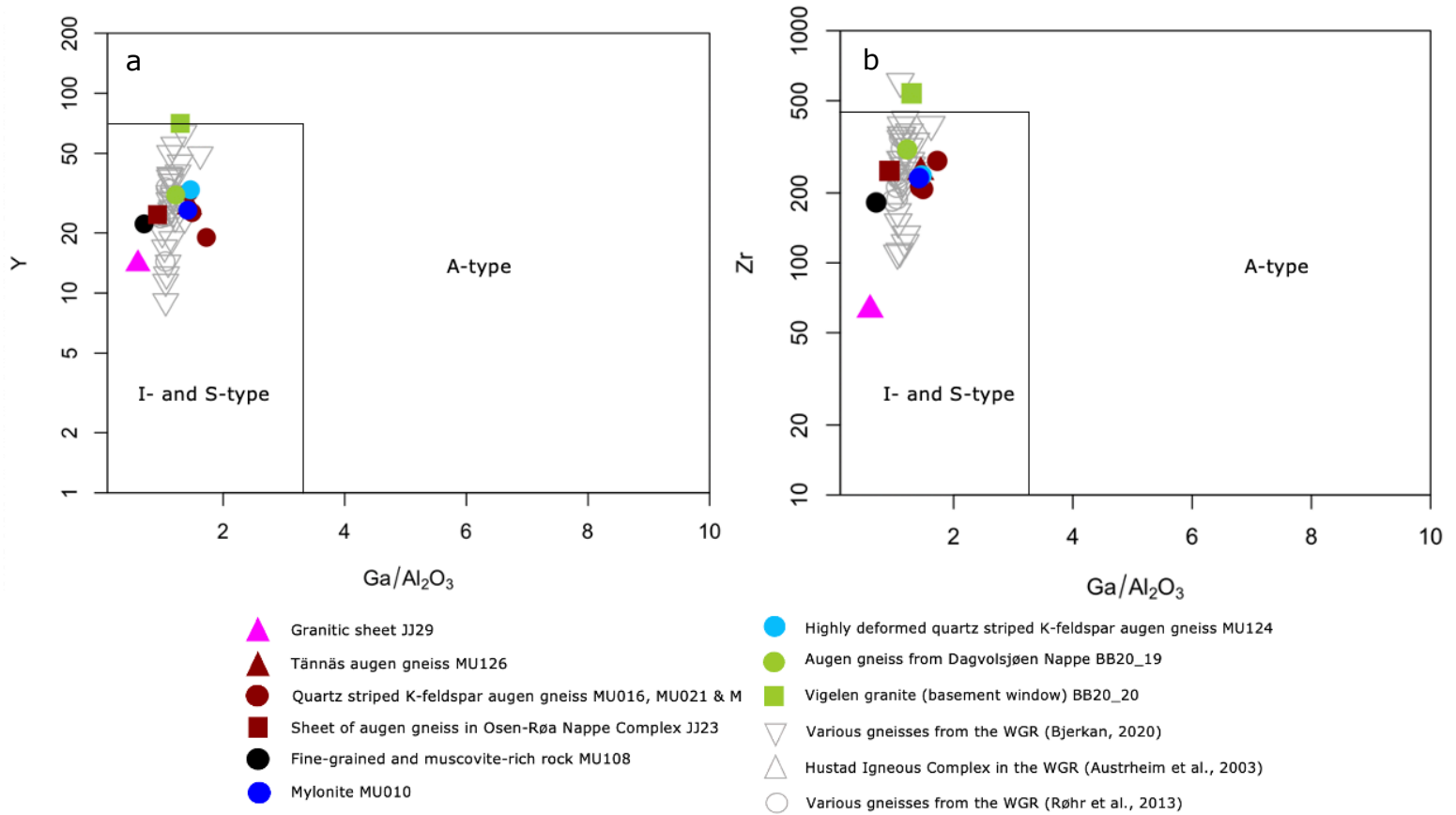
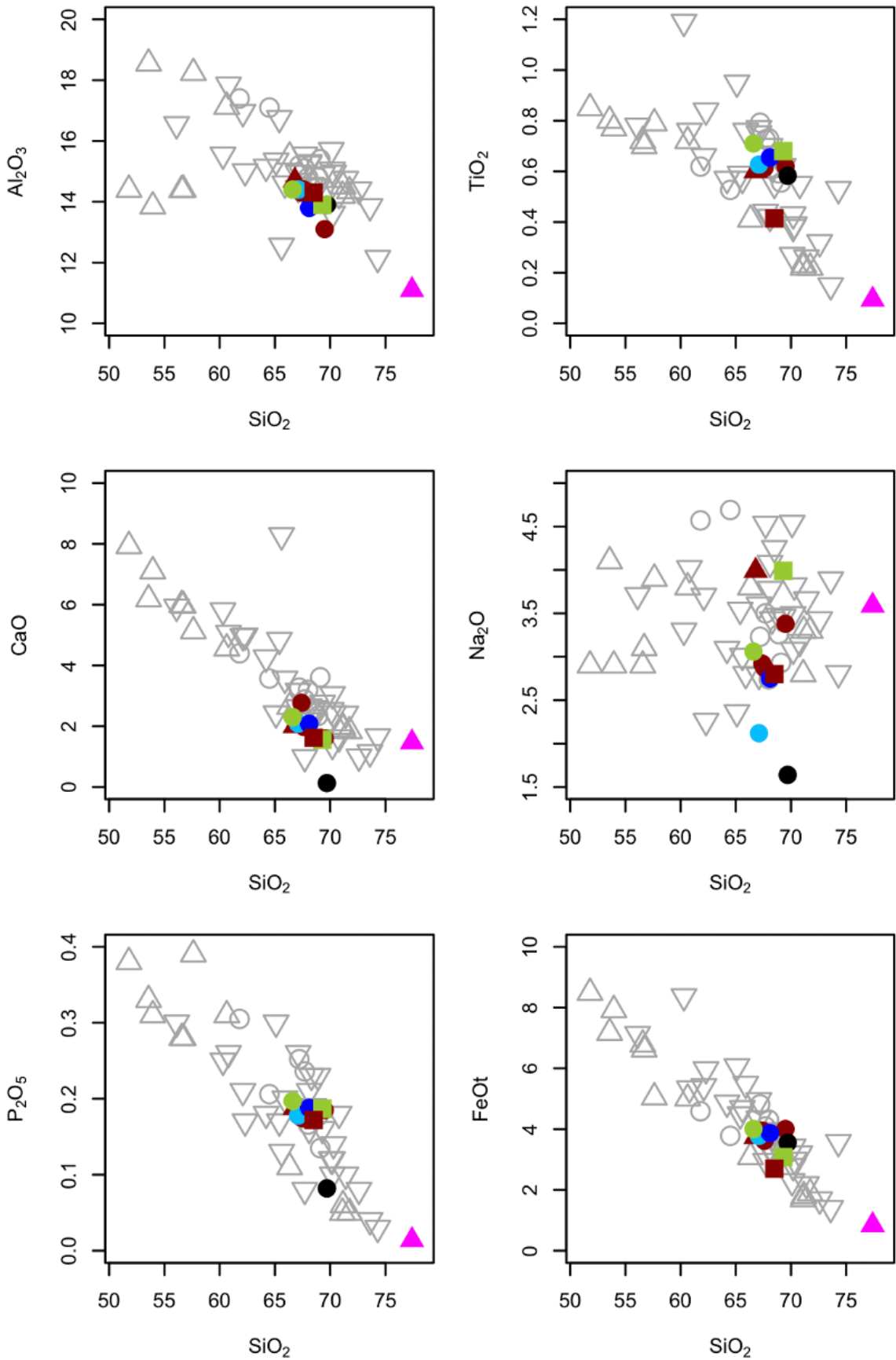


Figure 58. Classification of granites from Whalen et al. (1987) to distinguish between I- and S-type and A-type granites. a) Ga/Al plotted against Y. All samples from this study and from the WGR (Bjerkan, 2020, Austrheim et al., 2003, Røhr et al., 2013) plot in the I- and S-type granite field. The Vigelen basement granite (BB20_20) plots on the boundary between I- and S-type and A-type granite. b) Ga/Al plotted against Zr. The Vigelen basement granite (BB20_20) plots in the field of A-type granite. The other samples, both from this study and the WGR, plot in the I- and S-type granite field.

5.4.2 Major elements

Harker diagrams are shown in Fig. 59, and they are binary plots that visualize the trends of geochemical elements. The geochemical elements are relative to an index element, such as SiO₂. The plots in Fig. 59 show that Al₂O₃, TiO₂, CaO, P₂O₅, FeO and MgO have a negative trend relative to SiO₂ (both for the rocks of this study and the gneisses from the WGR). The plot with K₂O has a positive trend relative to SiO₂, and Na₂O is scattered and show no significant trend. The fine-grained and muscovite-rich rock (MU108) distinct from the other samples from this study in CaO, Na₂O, P₂O₅ and K₂O. In most of the plots, the samples from this study are clustered close to 70 wt.% SiO₂. This overlaps with the trend of the samples from Bjerkan (2020), Austrheim et al. (2003) and Røhr et al. (2013).

Multiple plot of SiO₂ vs. Al₂O₃, TiO₂, MgO, CaO, Na₂O, K₂O, P₂O₅, FeOt



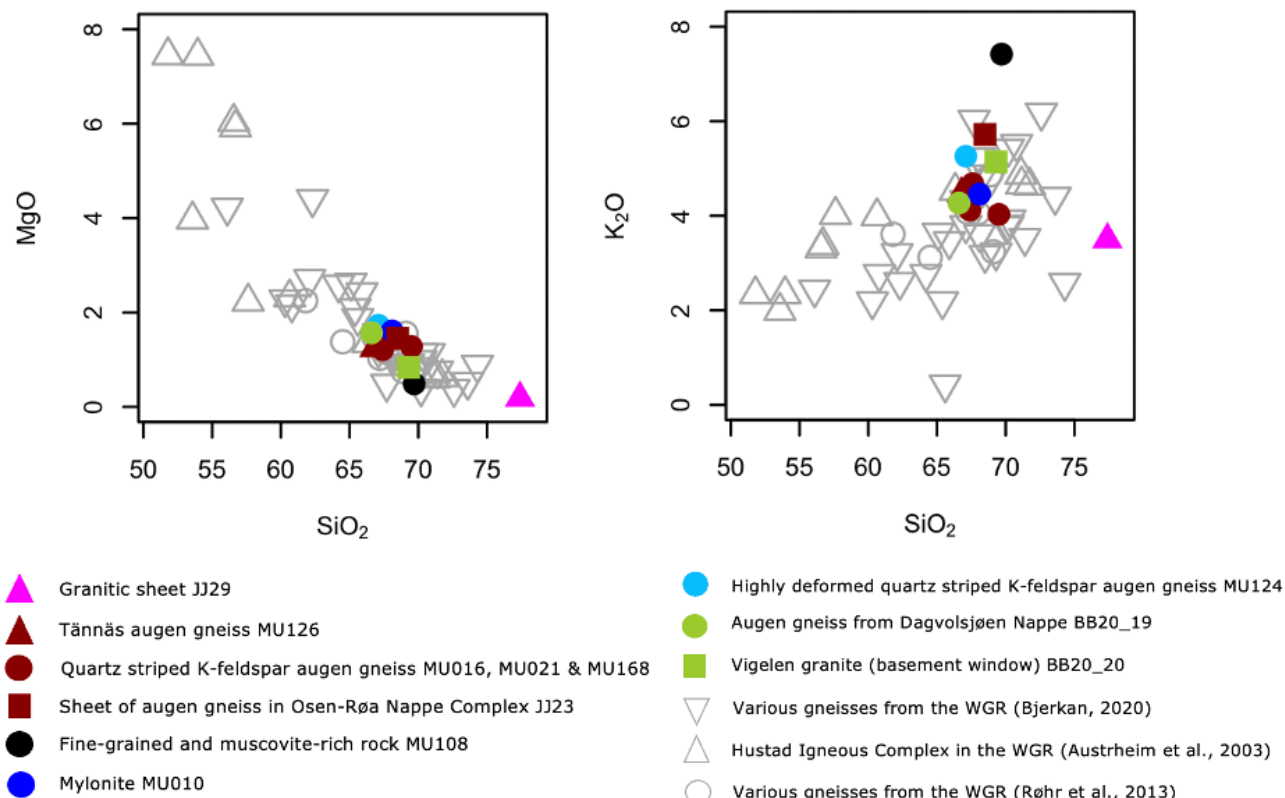


Figure 59. Harker diagrams with major elements expressed as oxides against SiO₂ on the x-axis. The plots with Al₂O₃, TiO₂, CaCO₃, P₂O₅, FeO and MgO have a negative trend relative to SiO₂. The plot with K₂O has a positive trend relative to SiO₂, while the plot with Na₂O is scattered.

5.4.3 Rare earth elements in spider diagrams

In Fig. 60, REE abundances are plotted using the chondrite reservoir of Boynton (1984). The samples from this study show a gentle enrichment towards the LREE and a flat abundance for HREE (Fig. 60a). The exception is the granitic intrusion (JJ29) that has a very gentle increase towards the end of the HREE. In addition, all the samples show a small, negative anomaly for Eu. There is also a negative Dy anomaly in the samples of this study analysed at NTNU that are not present in the samples analysed at NGU (BB20_19 and BB20_20). This is probably an analytical artefact, and it will not be discussed further. The samples from the WGR show the REE pattern (Fig. 60b).

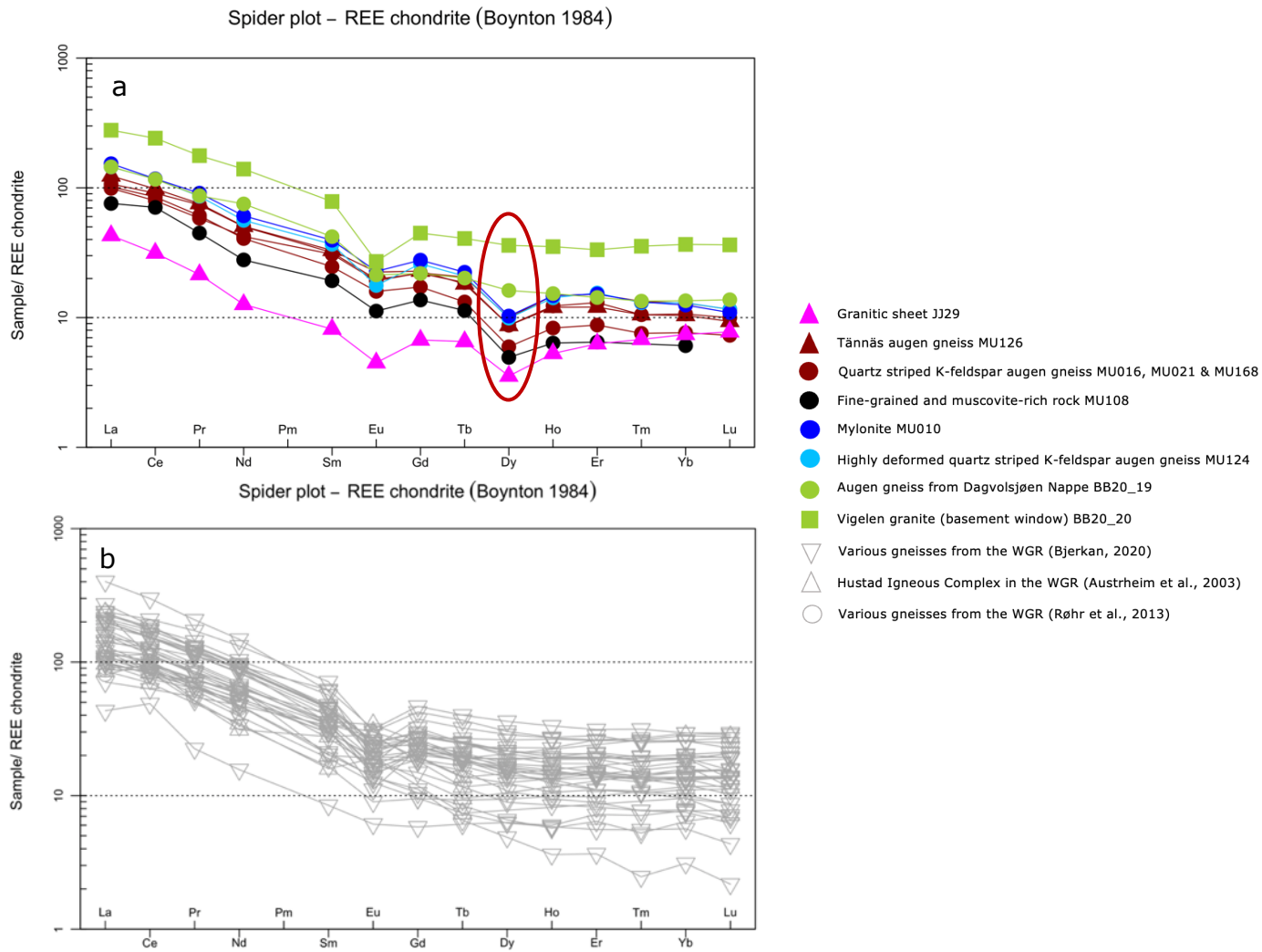


Figure 60. Chondrite-normalized trace element diagrams after Boynton (1984). All the plotted samples (both from this study and the WGR) show a gentle enrichment towards the LREE, in addition to a flat abundance for the HREE. There is a small, negative Eu anomaly. a) Spider diagram with the samples from this study. Some of the samples (analysed at NTNU) show a negative Dy anomaly while the samples analysed at NGU do not have this anomaly (marked with a red circle). It is probably an analytical artefact. b) Spider diagram of the samples from the WGR from Bjerkan (2020), Austrheim et al. (2003) and Røhr et al. (2013).

In Fig. 61, REE abundances are plotted normalised to NMORB (normal mid-ocean ridge basalts) of Sun and McDonough (1989). The values are based on average values from previous studies. The samples of this study show an enrichment in the LREE compared to the typical MORB-composition and the HREE (Fig. 61a). The granitic intrusion differs slightly from the other samples with its weak, positive trend towards the HREE. The spider diagram shows that there are negative anomalies for Nb, P and Ti and a positive anomaly for Pb. The Vigelen granite (BB20_20) has higher concentration of the HREE compared to the other samples from this study. The samples from the WGR show the same REE pattern (Fig. 61b).

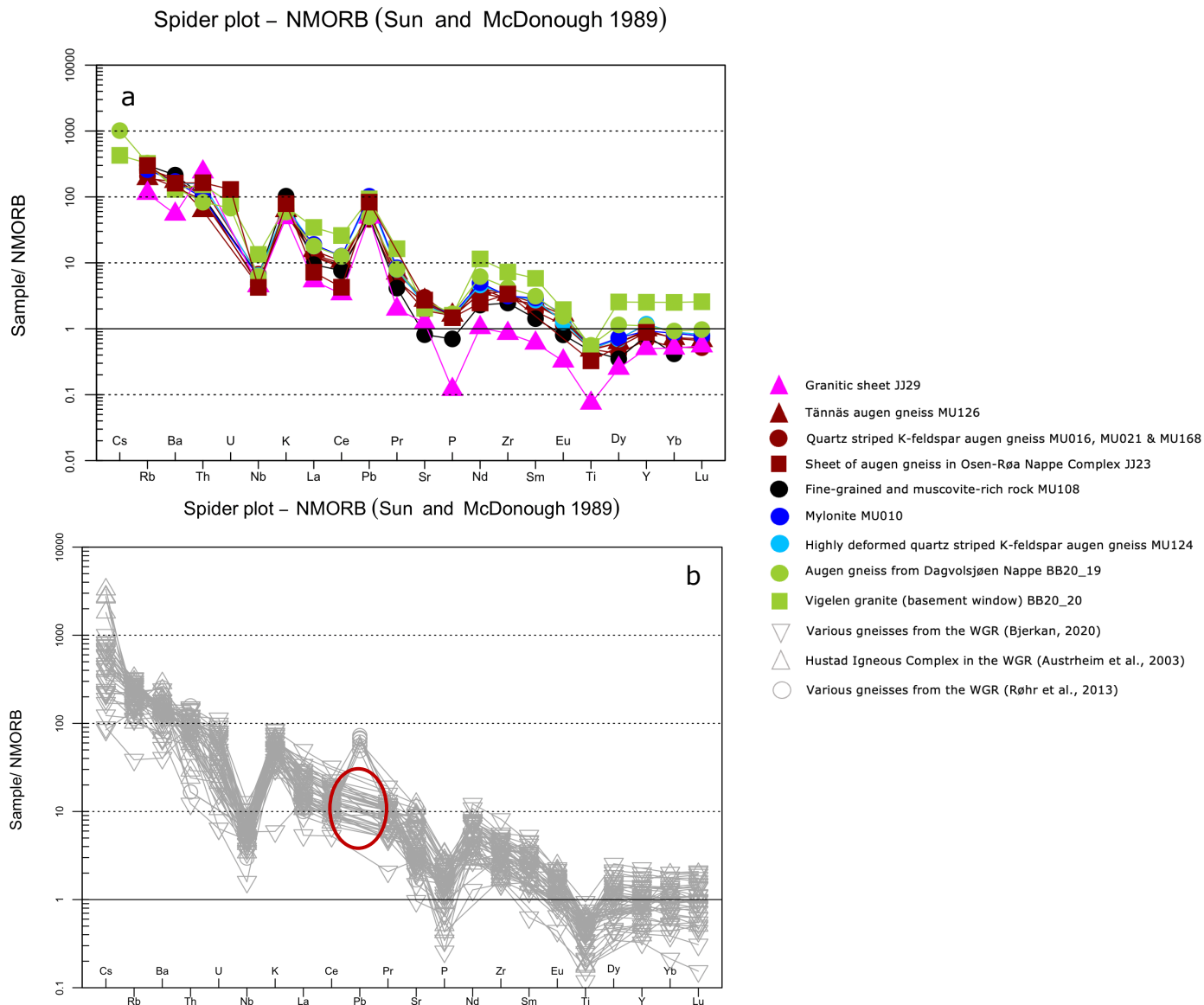


Figure 61. MORB-normalized trace element diagrams of Sun and McDonough (1989). The samples from this study and from the WGR (Austrheim et al., 2003, Røhr et al., 2013, Bjerkan, 2020) have an enrichment in LREE compared to the typical MORB-composition and HREE. There are negative anomalies for Nb, P and Ti, while Pb has a positive anomaly. a) Spider diagram of the samples from this study. b) Spider diagram of the samples from the WGR of Bjerkan (2020), Austrheim et al. (2003) and Røhr et al. (2013). The red circle signifies that there are no analysed Pb for most of the samples of Bjerkan (2020) and Austrheim et al. (2003).

5.4.4 Tectonic discrimination diagrams

In the granite tectonic discrimination diagrams from Pearce et al. (1984), Y+Nb is plotted against Rb (Fig. 62a) and Y is plotted against Nb (Fig. 62b). For granites, these immobile elements are likely to be the most effective elements for tectonic discrimination since they are stable during hydrothermal alteration and up to mid-amphibolite facies (Pearce et al., 1984, Winter, 2014, Rollinson and Pease, 2021). In Fig. 62, all the samples from this study and from the WGR from Bjerkan (2020), Austrheim et al. (2003) and Røhr et al. (2013) cluster. The majority of the samples are within the fields of volcanic arc, except the Vigelen granite (BB20_20) and eight of the gneisses from Bjerkan (2020). These plot in the within plate field.

Granite tectonic discrimination – Pearce et al. (1984)

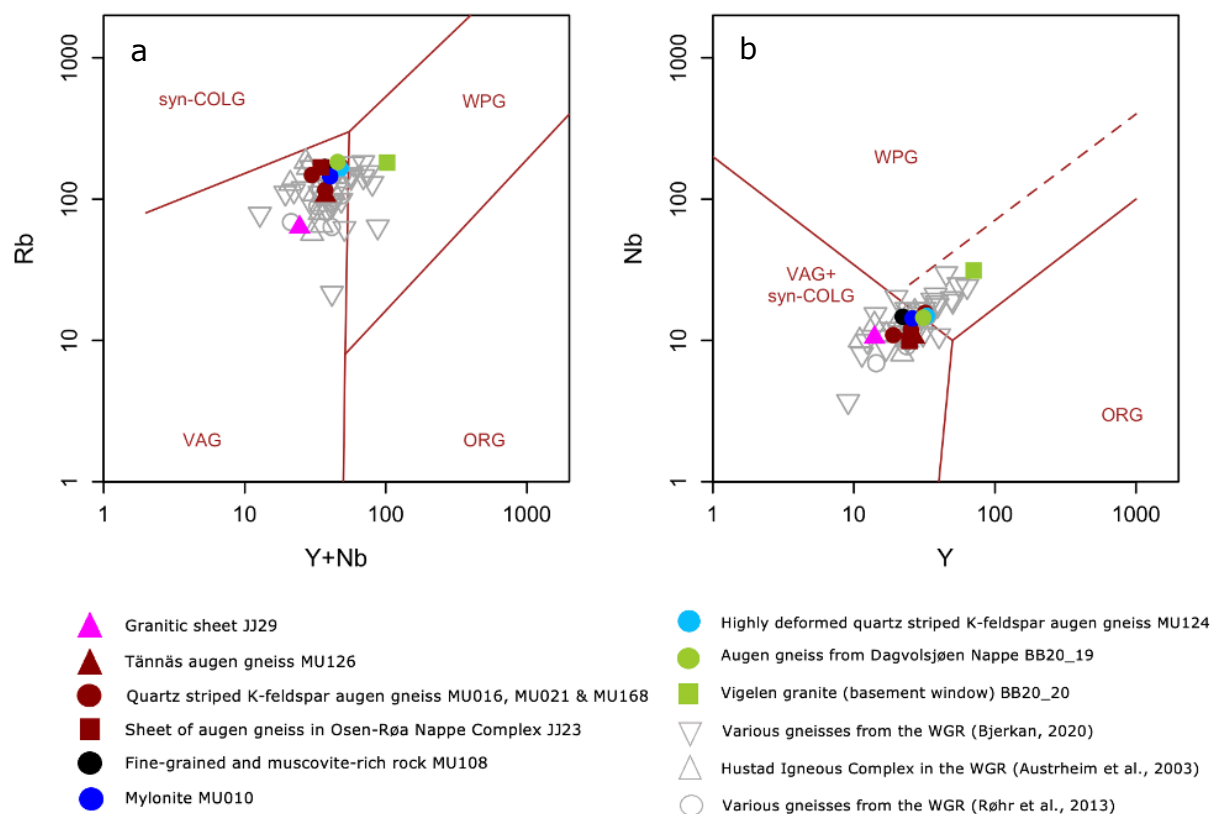


Figure 62. Tectonic discrimination diagrams for granites from Pearce et al. (1984). a) Y+Nb on the x-axis plotted against Rb on the y-axis. Most of the samples plot in the volcanic arc field (VAG) with the exception of BB20_20 and eight of the samples from Bjerkan (2020) since these plot in the within plate field (WPG). b) Y on the x-axis and Nb on the y-axis. BB20_20 and the eight samples from Bjerkan (2020) plot in the WPG field, while the others plot in the VAG+synCOLG fields.

6 Discussion

In the present study, the augen gneiss of the Dagvolsjøen Nappe in the central Norwegian Caledonides has been mapped and analysed. The following chapters will discuss and connect the findings of this study, and these findings will be discussed in a regional context. Furthermore, the pre-Caledonian history of the Dagvolsjøen Nappe will be discussed.

6.1 The Dagvolsjøen Nappe

Are there different variants of the Dagvolsjøen augen gneiss?

The field work revealed possibly three different variants of the augen gneiss assigned to the Dagvolsjøen Nappe. Even though there are noticeable differences in the matrix among the different variants, it is interpreted that all three variants are the Dagvolsjøen augen gneiss due to the mineralogy, texture and geochemical analyses. Additionally, based on the geochemical analysis, it is interpreted that the different variants originated from the same or similar protolith, providing further support for their classification as the Dagvolsjøen augen gneiss. The differences could be local variations and has not been further investigated in this study. However, the unstriped augen gneiss with fine-grained matrix has not been analysed for geochemistry and should therefore be analysed to confirm this. Furthermore, the analysed protomylonite (MU010) is interpreted to have originated from the same protolith as the Dagvolsjøen augen gneiss based on the geochemical analysis. The protomylonite clusters together with the augen gneiss of Dagvolsjøen Nappe in all the geochemical diagrams. In addition, all the mylonites have the pinkish augens of K-feldspar like the augen gneiss.

During the field work, the fine-grained and muscovite-rich sample (MU108) was assumed to be an augen gneiss. Further investigations revealed that it is the only sample examined in thin sections that does not have mineral segregation. Additionally, MU108 does not plot with the other samples in the geochemical classification diagrams in Figs. 53-57. In the classification of igneous rocks from Debon and Le Fort (1983) in Fig. 54, MU108 plots outside of the range for granitoid rocks, indicating it might not have an igneous protolith. The geochemical analysis and the texture may indicate that this sample is, although very similar in appearance in the field, is most likely not an augen gneiss, but a metasediment. It can be hard to distinguish the strongly deformed sedimentary meta-arkose and conglomerate of the underlying Rendalen Formation from the augen gneiss in the field. Consequently, the sample MU108 can have been misinterpreted in the field. Due to this, it can be a sheet of metasediment from the Rendalen Formation interlayered among the augen gneisses in the Dagvolsjøen Nappe. The major element classification of sediments after Herron (1988) has been used to classify MU108. In this diagram, it plots in the quartz arenite field (Fig. 63). Since MU108 was not analysed for geochronology, we cannot compare the U-Pb age distribution. If it is a metasedimentary rock, we would expect a wide range of detrital zircon ages.

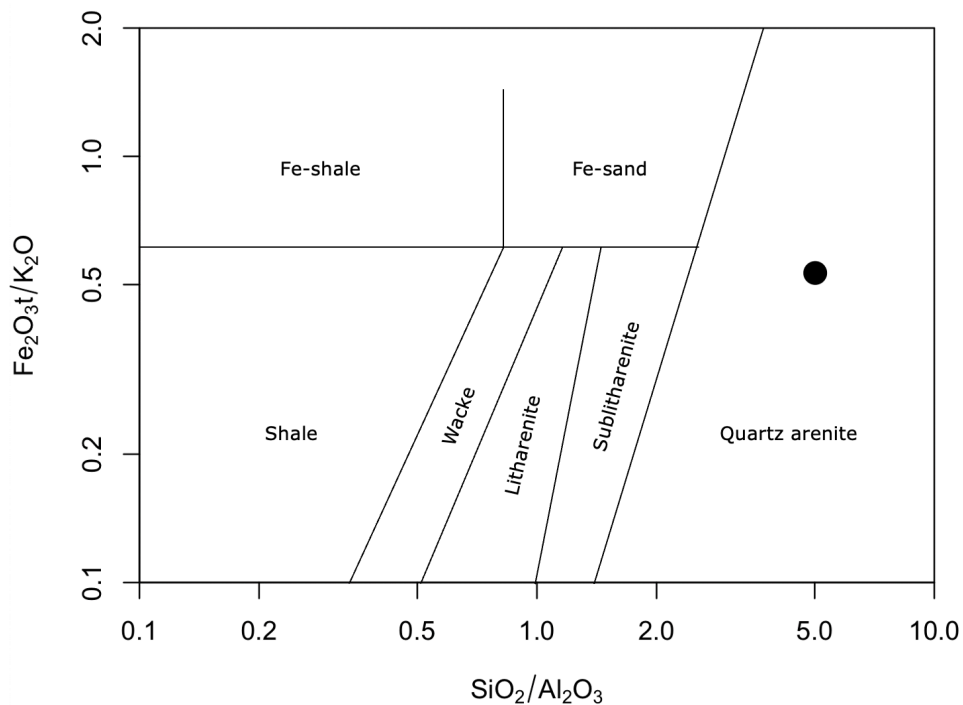


Figure 63. Major element classification of sediments after Herron (1988). The diagram is based on the chemical parameters: $\text{SiO}_2/\text{Al}_2\text{O}_3$ ratio and the $\text{Fe}_2\text{O}_3/\text{K}_2\text{O}$ ratio to distinguish between sandstones and shales (Herron, 1988). MU108 plots in the quartz arenite field.

Temperature conditions and kinematic indicators

Temperature estimates derived from deformation mechanisms observed in quartz and feldspar are in the range 400-600 °C, which corresponds to upper greenschist to lower amphibolite facies (Tullis, 2002). The lowest estimated temperature is in the protomylonite, which has top-to-the west sense of shear. Gee et al. (1994) interpreted the northwest movement to be a result of extension, which has overprinted an earlier top-to-the east shear fabric. This temperature estimate could therefore be interpreted to have occurred during the extensional tectonics along the Røragen detachment in Devonian times (Gee et al., 1994). Hence, the top-to-the east sense of shear recorded in the augen gneiss could be interpreted to have occurred prior to the extensional tectonics. Similar peak metamorphic temperature estimates of 500-540 °C have been recorded close to the study area, but at different structural levels (Jakob et al., 2022).

U-Pb geochronology analysis

Two samples of augen gneiss from the Dagvolsjøen Nappe yield zircon U-Pb ages of 1658 ± 5 Ma (MU021) and 1649 ± 5 Ma (BB20_19). The analyses are mainly concordant, but the sample MU021 has two analyses under the concordia line. These two analyses yield an age of 1698 ± 13 Ma, and the zircons are interpreted to be inherited. The source for these zircons remains unknown in this study. The concordant analyses are interpreted to record the intrusion of the granitic protolith to the augen gneiss (section 5.3 U-Pb geochronology). The ages of MU021 and BB20_19 are slightly overlapping at the 2 sigma uncertainty, and that could indicate that these two samples are coeval or originated from the same intrusion. Alternatively, they represent two intrusions that were emplaced closely in time. The sample collected in the upper part of the Osen-Røa Nappe Complex (JJ23) yields a $^{207}\text{Pb}/^{206}\text{Pb}$ age of 1659 ± 5 Ma with an equivalent concordia age. This sample could represent a thin sheet of augen gneiss from the Dagvolsjøen Nappe hosted

in the Osen-Røa Nappe Complex, or a sheet of basement of Skardøra antiform. The age of 1659 ± 5 Ma matches perfectly with the age of Dagvolsjøen Nappe and the basement of the Skardøra antiform. Since the rock has been interpreted to be an augen gneiss in the field and it plots together with the samples from the Dagvolsjøen Nappe in the geochemical diagrams, we interpret that sample JJ23 represents a thin sheet of augen gneiss of the Dagvolsjøen Nappe within the Osen-Røa Nappe Complex. Therefore, three samples of from the Dagvolsjøen Nappe were analysed for U-Pb geochronology (BB20_19, JJ23 and MU021). They have an average intrusion $^{207}\text{Pb}/^{206}\text{Pb}$ age of 1655 ± 5 Ma, thus protolith of the Dagvolsjøen augen gneiss is ~ 1655 Ma.

Geochemical analysis

The geochemical classifications indicate that the protolith of the augen gneiss is a granite, granodiorite, adamellite or quartz monzonite. Regardless, it is suggested that the protolith for the Dagvolsjøen augen gneiss is a granitoid, and granite is used for the protolith in this study. In the Harker diagrams in Fig. 59, the elements are well clustered, except for Na. This suggest that the metamorphism and tectonism were isochemical with the exception of Na. Thus, the geochemical data can be used with some confidence to document the geochemistry (Reverdatto et al., 2019) of the protolith of the augen gneiss.

The classification diagrams of Whalen et al. (1987) in Fig. 58 suggest the protolith of the Dagvolsjøen augen gneiss is an I- or S-type granite, and not an A-type granite. However, in the feldspathic igneous rocks' classification scheme from Frost et al. (2001) in Fig. 64, all the samples from this study plot in the field of S-type granites, but close to the I-type field (as defined by rocks from the Lachlan Fold Belt). In contrast, in the ASI diagram of Shand (1943) in Fig. 55, the samples plot on the boundary of the metaluminous and peraluminous fields, indicating there is not a sedimentary source for the protolith. If the protolith was a S-type granite, the samples would plot more in the peraluminous field. Additionally, I-type granites can also plot in the peraluminous field and be weakly peraluminous (Chappell et al., 2012, Winter, 2014), and this can explain why several of the samples plot around the boundary. Additional evidence for an I-type granite protolith for the augen gneiss is the decrease of P_2O_5 with increasing SiO_2 (Fig. 65). This negative correlation between these elements is a common feature of I-type granites (Gao et al., 2016, Yomeun et al., 2022). According to Wolf and London (1994), experimental studies indicate that apatite solubility is low in metaluminous and weakly peraluminous (I-type) melts, while it is an inverse trend in peraluminous (S-type) melts. Hence, the different behaviour of apatite can be used to distinguish I- and S-type granites. Consequently, we may discard that the protolith of the Dagvolsjøen augen gneiss is a S-type granite. Despite that the protolith may be an I-type granite, distinction between the different types of granites is not always easy (Chappell and White, 1992, Wu et al., 2003).

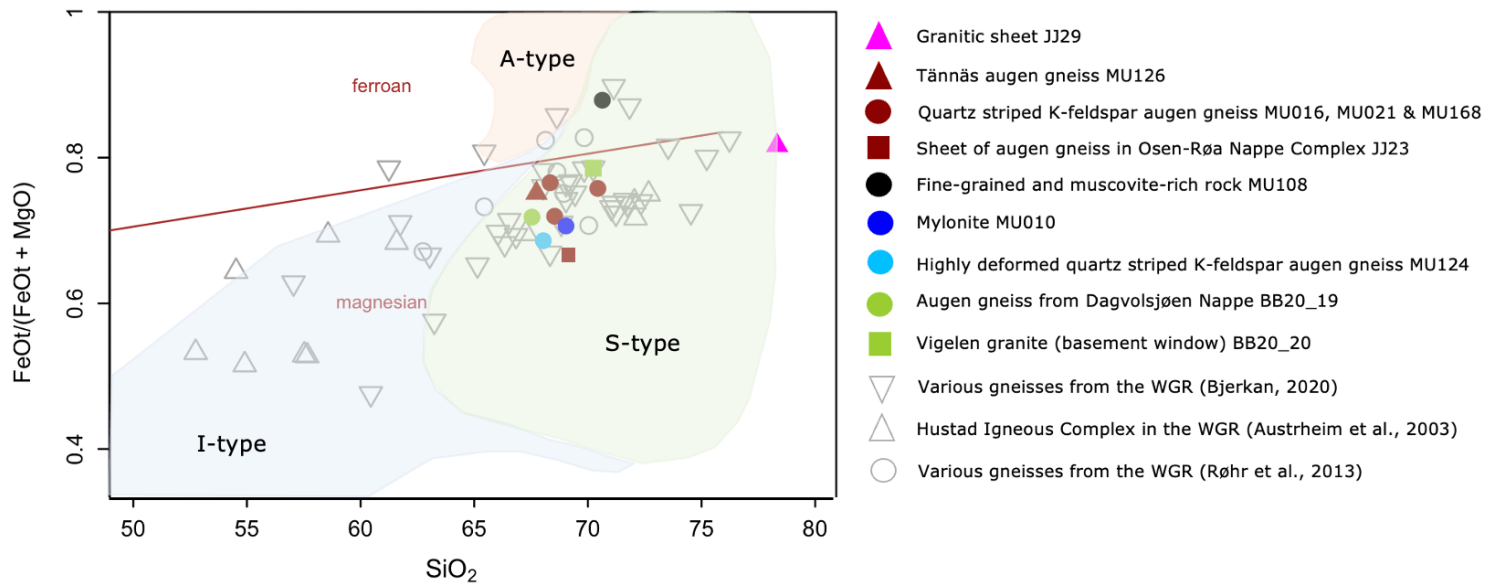


Figure 64. Feldspathic igneous rocks' classification scheme from Frost et al. (2001) with the composition range from of rocks from the Lachlan Fold Belt.

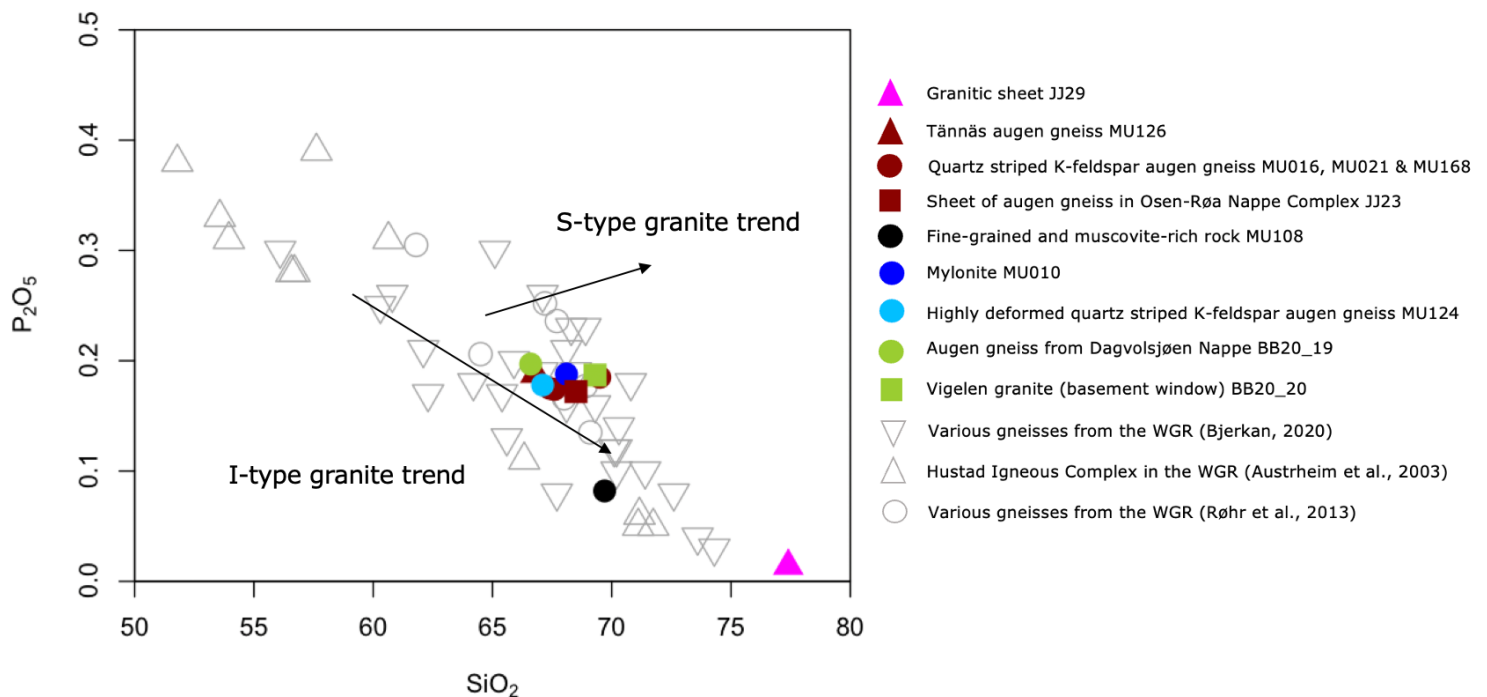


Figure 65. Trends of I- and S-type granites proposed by Chappell and White (1992) with inspiration from Wu et al. (2003) based on P_2O_5 vs SiO_2 . The plotted samples show a I-type granite trend.

In the chondrite normalized spider plot in Fig. 60, the REE pattern has an enrichment in LREE compared to HREE and looks like a right-dip seagull. This pattern has been reported in volcanic arc environments (Slagstad, 2003, Winter, 2014). In addition, the negative Nb, Sr and P anomalies and the positive Pb anomaly in the spider diagram in Fig. 61 are generally interpreted as a subduction related/derived magma or/and continental crust signature (Li et al., 2011, Singh et al., 2019). The depletion in Nb compared to the adjacent LILE could characterize crust assimilation prior to the emplacement. This

geochemical signature is assumed to be formed in a subduction related setting with country rock assimilation (Rezaei-Kahkhaei et al., 2010). Based on the REE patterns and the tectonic discrimination diagrams of Pearce et al. (1984) (Fig. 62), the geochemical composition of the protolith of the Dagvolsjøen augen gneiss suggests a volcanic arc setting with a continental component in a supra-subduction environment.

The depletion in Eu and Sr in Figs. 60 and 61 can indicate that plagioclase was stable in the source, and this suggests a low pressure of <8 kbar (Nagudi et al., 2003). Furthermore, the HREE patterns are relatively flat, indicating that there was no deep fractionation process, supporting the suggested low pressure. This is due the magma being produced outside of the stability of garnet. If garnet was left after the partial melting, there should be a positive slope to the HREE (Winter, 2014).

6.2 Correlation between the Dagvolsjøen Nappe and other tectonic units in the central Scandinavian Caledonides

There is a commonly accepted correlation between the augen gneisses within the different nappes in the central Caledonides in Norway and Sweden. In the following sections, these correlations will be discussed.

6.2.1 The Vigelen granite

U-Pb geochronological analysis

Concordant analyses of the Vigelen granite (the basement exposed in the Skardøra antiform, sample BB20_20) yield a $^{207}\text{Pb}/^{206}\text{Pb}$ age of 1657 ± 7 Ma, which overlaps in error with the age of the augen gneiss in the Dagvolsjøen Nappe. One analysis of BB20_20 is discordant and interpreted to be an inherited zircon with the age 1848 ± 23 Ma. This zircon could be inherited from an older source when the protolith intruded, but the source remains unknown in this study. However, the Vigelen granite has the same age as rocks from the TIB, both the inherited zircon and the zircons interpreted to represent the magmatic crystallization of the protolith. Several episodes of magmatism have been reported from the TIB, known as TIB0 (1.85-1.83 Ga), TIB1 (1.81-1.77 Ga), TIB2 (c. 1.7 Ga) and TIB3 (1.68-1.65 Ga) (Larson and Berglund, 1992, Ahl et al., 2001). The rocks of TIB are underlying the Scandinavian Caledonides (Fig. 5), and it reasonable to correlate the Vigelen granite in with the TIB, explicitly the TIB3 magmatism. If this is the case, the basement window(s) could be a continuation of the TIB underneath the Caledonian nappe stack.

Other granites in tectonic windows in southeast Norway have been dated to similar ages and are within error of the age of the Vigelen granite: A granite in the Atnsjøen window (sample JL-08-14) exhibit a concordia age of 1659 ± 5 Ma and a granite in the Tufsingdalen window (sample JL-07-11) exhibit a concordia age of 1655 ± 4 Ma (Fig. 66) (Lamminen et al., 2011). In addition, a low-strain domain remnant of the igneous protolith in the HIC in the WGR has been dated to 1654 ± 1 Ma (granite) and 1653 ± 2 Ma (monzodiorite) by Austrheim et al. (2003). The ages of c. 1650 of Handke et al. (1995) also corresponds, and they are from the basement in the WGR (NGU, 2013). Hence, the basement in the field area correlates within error in age with other basement windows in southeast Norway and the WGR.

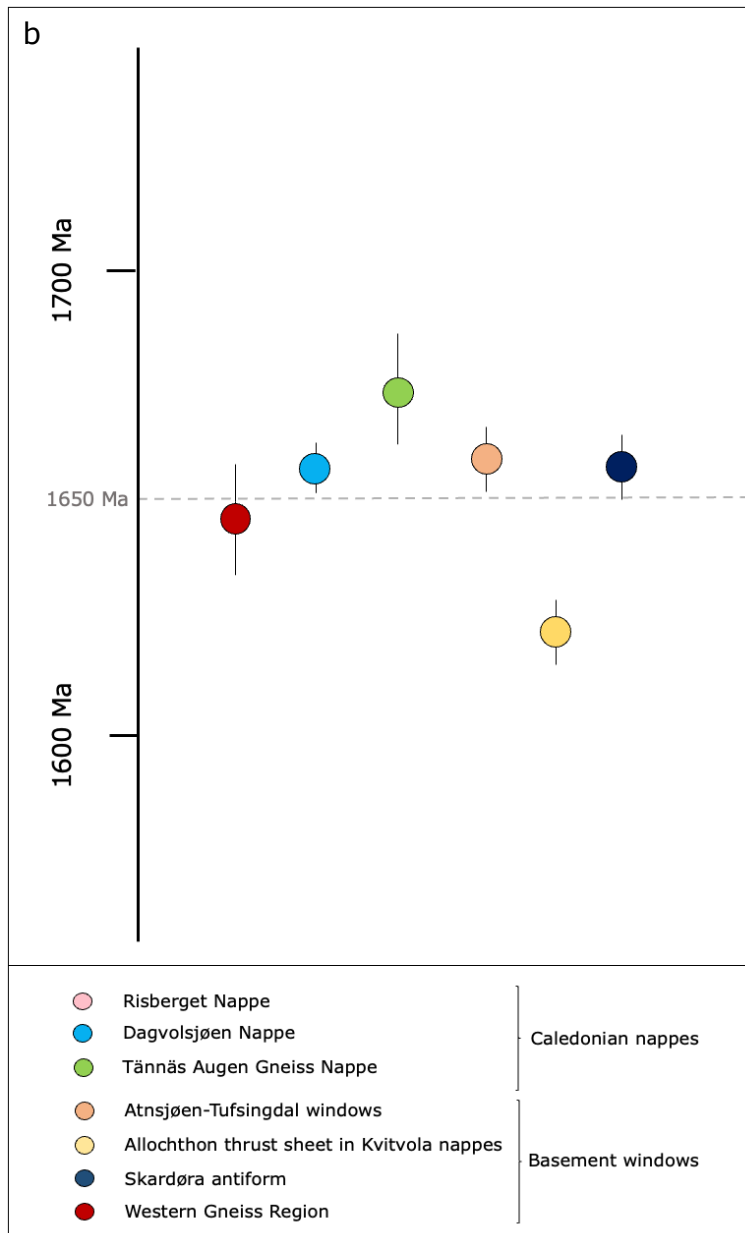
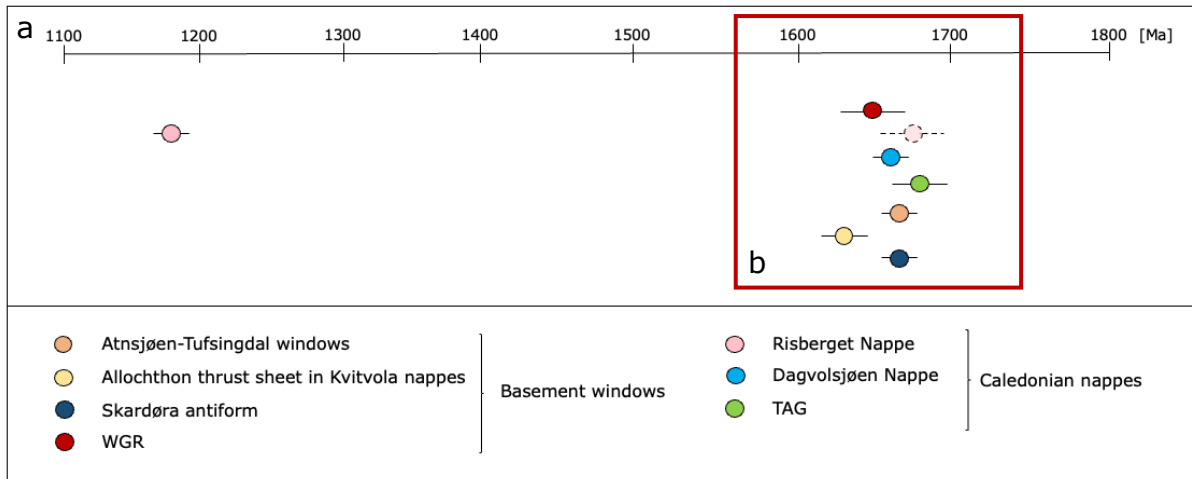


Figure 66. Age distribution of the magmatic crystallization age of igneous rocks and protoliths from the Risberget Nappe (pink, $n=5$, from Handke et al. (1995) and Lamminen et al. (2011)), the Dagvolsjøen Nappe (light blue, $n=3$, from this study), the TAG (green, $n=2$, from Claesson (1980)

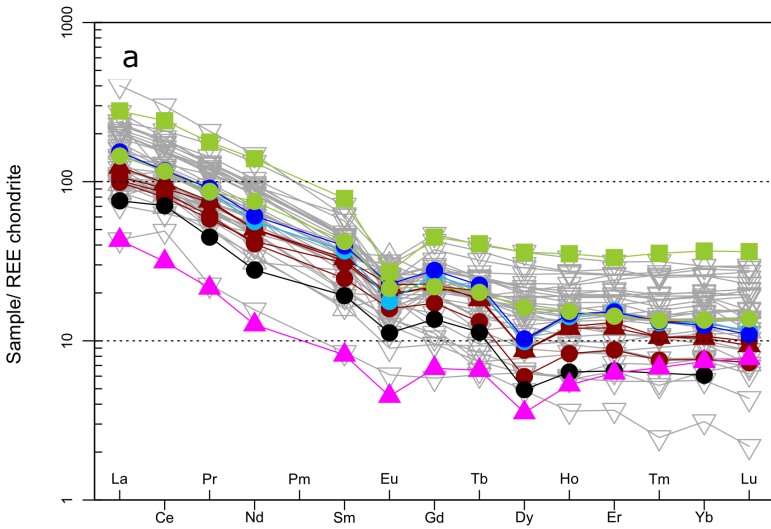
and this study), basement windows in the Osen-Røa Nappe Complex (orange, $n=3$, from Lamminen et al. (2011)), allochthon thrust sheet in the Kvitvola nappes (yellow, $n=1$, from Lamminen et al. (2015)), the Skardøra antiform (dark blue, $n=1$, from this study) and the WGR (red, $n=55$, from Bjerkan (2020), DesOrmeau et al. (2015), Røhr et al. (2013), Butler et al. (2018), Wang et al. (2021), Skår and Pedersen (2003), Kylander-Clark and Hacker (2014), Skår et al. (1994), Corfu et al. (2014b), Austrheim et al. (2003) and Krogh et al. (2011)). The ages are represented as median age, and the 2 sigma is represented in the black line (also median). One sample is maybe from the Risberget Nappe and is marked in light pink with stippled lines due to the uncertainty. It has the age 1649 ± 14 Ma (Røhr et al., 2013). b) Zoom-in of the red rectangle in a) without the sample that is uncertain from Røhr et al. (2013).

Geochemical analysis

In all the geochemical classification diagrams, the Vigelen basement granite does not plot far away from the samples from the Dagvolsjøen Nappe. However, the Vigelen basement granite is more metaluminous (Fig. 55) and more ferroan (Fig. 57) than the Dagvolsjøen augen gneiss. The spider diagrams also show that the basement is slightly more enriched in HREE compared to the augen gneiss, suggesting a different petrogenesis. In Fig. 58, the Vigelen granite plots in the A-type granite field. Based on these plots, the Vigelen basement granite has a more A-type signature compared to the augen gneiss of Dagvolsjøen Nappe, the TAG and the gneisses of WGR. According to Winter (2014) and Zhao and Zhou (2009), A-type granites can have an intraplate geotectonic signature and can be generated in extensional environments, such as back-arc rifts (Wang et al., 2020). In the Y-Nb-Rb tectonic discrimination diagram of Pearce et al. (1984), the Vigelen basement granite indeed plots in the within plate field. The fact that the Vigelen basement granite has a more A-type granite signature distinguishes it from the protolith of the augen gneiss that has an I-type granite and volcanic arc signature. In addition, the basement is an unfoliated granite while the augen gneiss is metamorphosed and was transported during the Caledonian thrusting. If the Vigelen basement granite in the field area had been the protolith, the granite should also have experienced metamorphism and it had to extend over a great distance. This can indicate no or little affinity between the Vigelen granite in the basement window exposed in the Skardøra antiform and the augen gneiss of the Dagvolsjøen Nappe.

If all the samples from this study and the studies from the WGR by Bjerkan (2020), Austrheim et al. (2003) and Røhr et al. (2013) are plotted together in spider diagrams, the Vigelen basement granite plots together with rocks from the WGR (Fig. 67). Based on the REE patterns, there could be affinity between the Vigelen granite and the gneisses in the WGR. However, the rocks from the WGR plot different in the tectonic discrimination diagrams, indicating that the petrogenesis is different and that there is no affinity. This is supported by the classification of granites of Whalen et al. (1987) in Fig. 58.

Spider plot – REE chondrite (Boynton 1984)



Spider plot – NMORB (Sun and McDonough 1989)

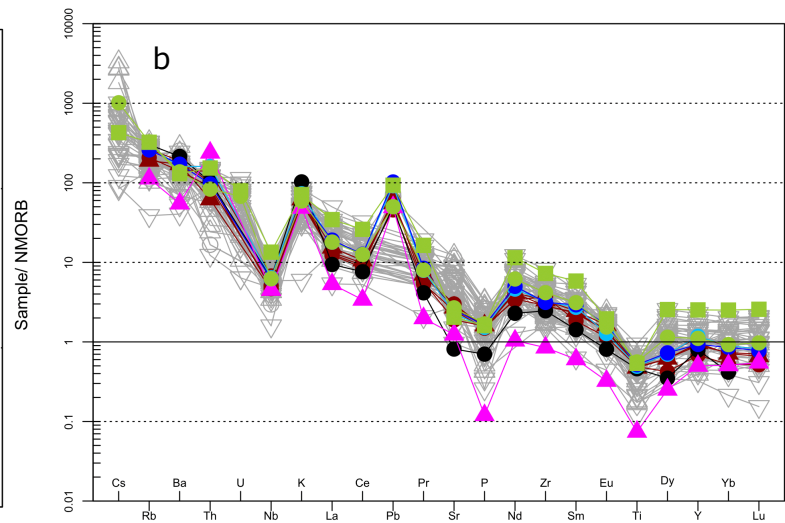


Figure 67. Spider diagrams. a) Chondrite-normalised trace diagram of Boynton (1984). See figure text for Fig. 60 for further explanation. b) NMORB-normalised trace element diagram of Sun and McDonough (1989). See figure text for Fig. 61 for further explanation.

6.2.2 The Tännäs Augen Gneiss Nappe

The TAG appears in the eastern part of the study area, on the eastern limb of the Skardøra antiform. By comparing the augen gneiss in the field and in thin section, the rocks of the Dagvolsjøen Nappe and the TAG are similar (Figs. 68 and 69). The TAG in Norway and has all three variants of the augen gneiss. However, just one locality (MU162) with the unstriped augen gneiss with fine-grained matrix was observed in the Norwegian part of the TAG. Additionally, only two outcrops were studied in the Swedish part of the TAG due to time restriction, and only the quartz striped K-feldspar variation was observed. Although, this does not mean that the two other variants do not exist in the TAG in Sweden, but further investigations are needed. Alternatively, could the unstriped augen gneiss be a feature of the Dagvolsjøen Nappe? Further investigations could provide the information to validate the statement or to discard it. The mineral content and the texture do not vary much between the samples collected in the Dagvolsjøen Nappe, the Norwegian part of the TAG and the Swedish part of TAG.

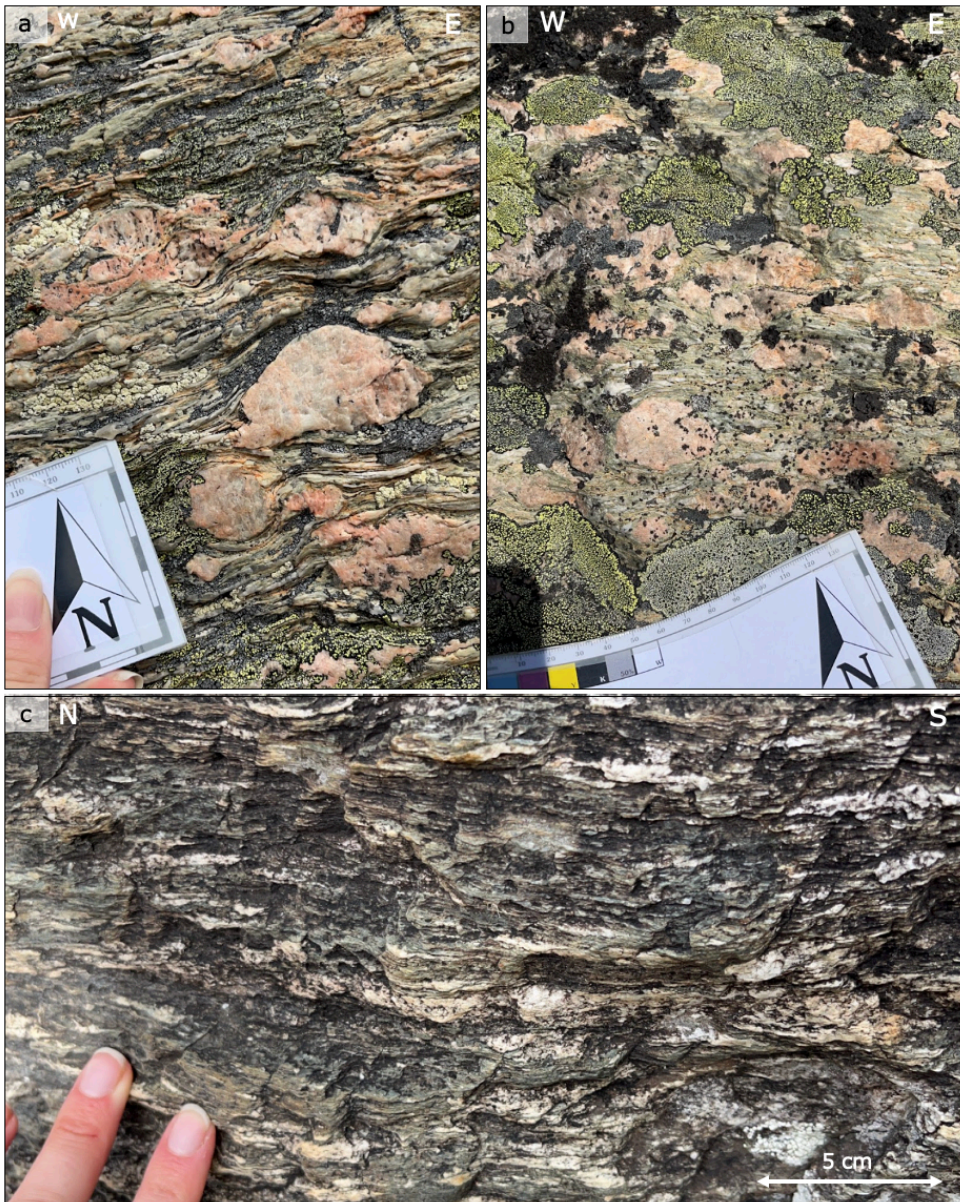


Figure 68. Field photos from the Dagvolsjøen Nappe and the TAG. a) The Dagvolsjøen augen gneiss from the western limb of the Skardøra antiform (MU021). b) The Tännäs augen gneiss from the eastern limb of the Skardøra antiform (MU168). c) The Tännäs augen gneiss from the Tännäs area, Sweden (MU125).

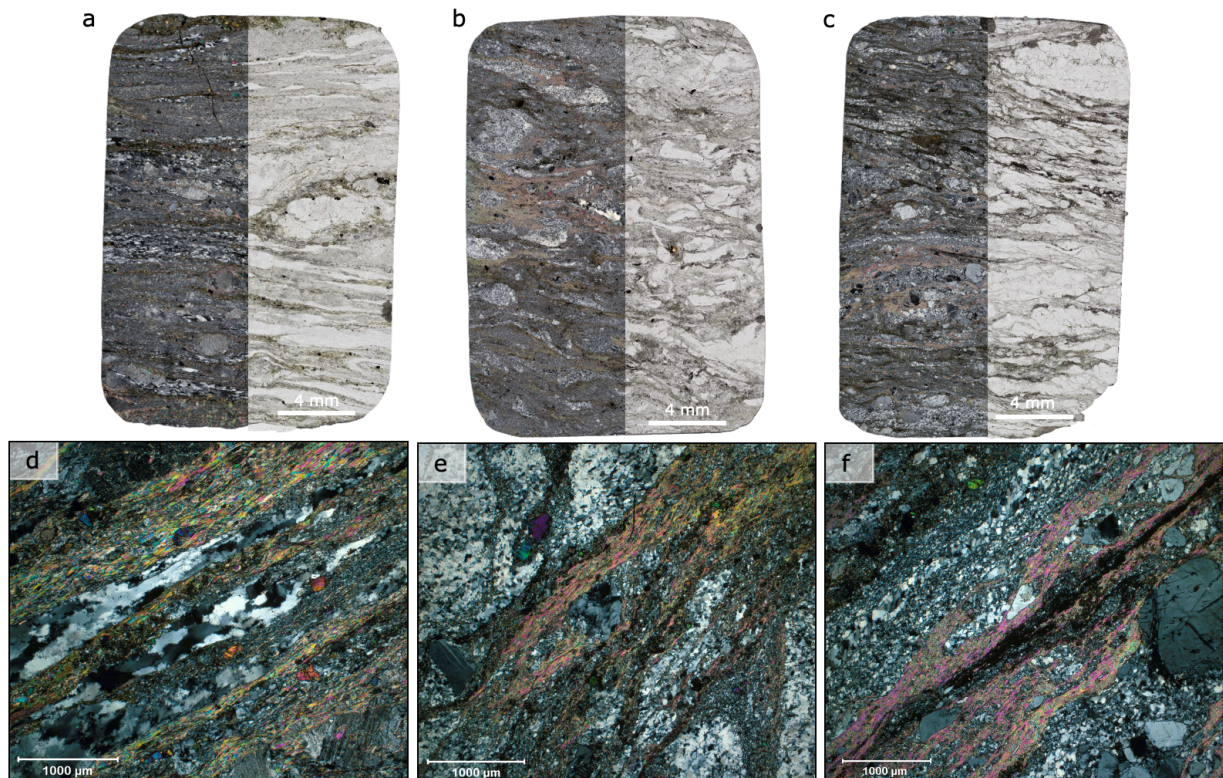


Figure 69. Micrographs of augen gneisses from the Dagvolsjøen Nappe and the TAG. a) Scan photo of a thin section from the western limb of the Skardøra antiform (Dagvolsjøen Nappe, MU021). To the left: PPL, to the right: XPL. Both with 5x magnification. b) Scan photo of a thin section from the eastern limb of the Skardøra antiform (TAG, MU168). To the left: PPL, to the right: XPL. Both with 5x magnification. c) Scan photo of a thin section from the Tännäs area (TAG, MU126). To the left: PPL, to the right: XPL. Both with 5x magnification. d) Thin section micrograph of MU021. See the Fig. 18 for details. e) Thin section micrograph of MU168. The observed minerals are quartz, K-feldspar, micas (biotite, muscovite and minor chlorite), epidote and plagioclase. f) Thin section micrograph of MU126. See the Fig. 24 for details.

The foliation of the augen gneiss of the Dagvolsjøen Nappe dip gently to the west, while the augen gneiss of the TAG in the eastern part of the mapping area is dipping gently to the east, consisting with the augen gneiss eroded in the centre of the Skardøra antiform. This implies that the augen gneiss is a single tectonostratigraphic unit despite being non-continuous in the field.

The U-Pb analysis gives similar ages for the TAG and the Dagvolsjøen Nappe that overlap within error. The Dagvolsjøen augen gneiss yields an average $^{207}\text{Pb}/^{206}\text{Pb}$ age of 1655 ± 5 Ma and the Tännäs augen gneiss yields a $^{207}\text{Pb}/^{206}\text{Pb}$ age of 1654 ± 5 Ma. Both ages are interpreted to be the age of the magmatic crystallization for the protolith. This suggests that the protolith of the augen gneiss was formed from the same or similar intrusion close in time. Geochemical analysis supports this since the augen gneiss from the Dagvolsjøen Nappe and the TAG cluster together in all the geochemical plots. This indicates that the Tännäs augen gneiss may also have originated from an I-type granite protolith. The Dagvolsjøen and Tännäs augen gneisses additionally have the same REE patterns and plot together in the tectonic discrimination diagrams, indicating a volcanic arc signature in a supra-subduction environment for the protolith. Consequently, based on the structural, geochronological and geochemical data, the Dagvolsjøen Nappe and the TAG can be correlated.

6.2.2.1 *The granitic intrusion*

Since the granitic sheet from the eastern limb of the Skardøra antiform is cutting the foliation of the augen gneiss, the intrusion and the augen gneiss have a different deformation history. However, they have a common deformation history after the emplacement. Both the intrusion and the augen gneiss have quartz with SGR as the main deformation mechanism. Because GBM is also observed in the augen gneiss, but not in the granitic sheet, the augen gneiss could have reached the peak metamorphism before the emplacement. The interpretation could therefore be that the temperature conditions for the SGR deformation and the overprinting BLG deformation happened after the emplacement of the intrusion. Therefore, the interpretation is that the augen gneiss and the intrusion experienced temperatures of appr. 500 °C during or after the emplacement. Since the contact between the augen gneiss and the intrusion is sharp, and does not have evidence of chilling against the wall rock, this can indicate that the wall rock was at high temperature at the time of intrusion (Size, 1979).

The intrusion reveals a Caledonian age with a lower intercept age of 436 ± 43 Ma to 351 ± 38 Ma. A Caledonian age is not precise enough to meet the aim to date the fabric forming event. Consequently, we can only say that the augen formation occurred between ~ 1655 Ma and the emplacement of the granitic sheet. The timing of the augen formation and the emplacement of the granitic intrusion can be discussed in the context of different tectonic models: (1) prior to the Caledonian thrusting, (2) during the Caledonian thrusting and (3) during the orogenic collapse. Regarding the first model, Nilsen et al. (2007) described arc-related intrusives with the ages of 437-431 Ma in the Trondheim Nappe Complex. For the second model, syn-thrusting dikes have been described, e.g. the Årdal dyke swarm and the Samnanger Complex. The Årdal dyke swarm intruded 427 Ma (Lundmark and Corfu, 2008) and the Samnanger Complex consists of granitoids that were emplaced 421 Ma (Jakob et al., 2017). The syn-extensional setting, model (3), is e.g. reflected by felsic dykes emplaced 402-401 Ma. The felsic dykes are interpreted to have been emplaced during the latest phase of exhumation (Nordgulen et al., 2002, Kendrick et al., 2004). Since the lower intercept age for the granitic sheet is not precise, the age of the emplacement overlaps with the three tectonic models described above. We can therefore not pinpoint the emplacement of the granitic intrusion and determine the tectonic setting. Consequently, we cannot conclude precisely when the augen formation occurred in this study.

The sheet of granite includes older, inherited zircons with the ages of 1711 ± 14 Ma and 1658 ± 6 Ma. The latter age matches the ages reported from the Dagvolsjøen and Tännäs nappes. A possibility is therefore that the zircons are inherited from the augen gneiss during the emplacement, however, there is no evidence of melting of the host rock. Another possibility is that the zircons are derived from the metasediments structurally underlain. Regardless, the source for the older zircons remains unknown in this study. The only certainty is that the source of the inherited zircons was structurally below the augen gneiss when the granite sheet was emplaced. For the other group of inherited zircons (1711 ± 14 Ma), an older component is the source. The age c. 1700 Ma is an uncommon age for the WGR, but Bjerkan (2020) reported the ages 1690 ± 49 Ma and 1691 ± 22 Ma for the protolith of the host gneisses. This age overlaps within error with the age of the inherited zircons. Due to this, it is not certain if the WGR is the source or not. The inherited zircons can have originated from any tectonostratigraphic structurally below the augen gneiss at the time of the emplacement of the granitic sheet.

6.2.3 The Risberget Nappe

The median age of the protolith of the augen gneiss assigned to the Risberget Nappe is 1189 ± 3 Ma (Fig. 66a) (Handke et al., 1995, Lamminen et al., 2011). This age is not reported in this study, even though the Dagvolsjøen Nappe and the Risberget Nappe are traditionally correlated. Røhr et al. (2013) dated a granodioritic augen gneiss of the Risberget Nappe to be 1676 ± 18 Ma, which is just within the error of the age reported in this study. However, it is limited structural control on the tectonic unit where the 1676 ± 18 Ma augen gneiss of Røhr et al. (2013) was sampled. Even though the reported age of 1190-1180 Ma for the protolith in the Risberget Nappe was not found in this study, only four samples from the Dagvolsjøen Nappe and the TAG were analysed for geochronology. Because of the possibility of two different ages reported in the Risberget Nappe (c. 1675 Ma and c. 1190-1180 Ma), further investigations are needed to determine the relationship between the two age groups and the Dagvolsjøen Nappe.

Due to the absence of geochemical data from the augen gneiss of the Risberget Nappe, a comprehensive comparison of the geochemical composition is not available. Consequently, a correlation or no correlation between the Dagvolsjøen and the Risberget Nappe is not established in this study.

6.2.4 The Western Gneiss Region

The reported ages from this study of the Dagvolsjøen Nappe and the TAG are within error with ages reported from the WGR (Fig. 66). The median age for the magmatic crystallisation of the protolith(s) for the rocks of the WGR is 1649 ± 9 Ma (Skår et al., 1994, Skår and Pedersen, 2003, Austrheim et al., 2003, Krogh et al., 2011, Røhr et al., 2013, Corfu et al., 2014b, Kylander-Clark and Hacker, 2014, DesOrmeau et al., 2015, Butler et al., 2018, Bjerkan, 2020, Wang et al., 2021).

In the geochemical diagrams in section 5.4 *Geochemistry*, the samples from this study and the samples from the WGR plot together even though the samples from the WGR are more scattered. There is a cluster of the samples of the WGR together with the cluster of the samples from this study. In addition, the samples from WGR and this study exhibit the same trends in the Harker diagrams and in the spider diagrams. Based on the geochronological and geochemical data, the Dagvolsjøen Nappe and the WGR could have affinity. Consequently, the augen gneiss of the Dagvolsjøen Nappe and the WGR may have the same protolith or they originated from different intrusions emplaced closely in time and in the same environment. Consequently, the protolith of Dagvolsjøen augen gneiss may have been part of the basement west of the WGR. Since the WGR is interpreted to be Baltican basement (Butler et al., 2018), the protolith of the Dagvolsjøen augen gneiss could therefore also be of Baltican derivation.

6.3 The pre-Caledonian history of the Dagvolsjøen Nappe

In the Wilson cycle, granites can occur in different tectonic settings: (1) rifting of the continental crust, (2) above subduction zones and (3) post-orogenic (Kinny et al., 2003, Wu et al., 2009). The data obtained in this study suggests a volcanic arc setting in a supra-subduction zone environment for the possible I-type granitic protolith, corresponding to (2). However, this study has not proved or disapproved that the protolith of the augen gneiss is of Baltican ancestry. Nevertheless, it is commonly considered that the lower part of the Caledonian nappe stack originated at the western part of the Baltoscandian margin (Roberts and Gee, 1985, Gee et al., 1985). In addition,

a possible correlation with the WGR supports that the protolith may be of Baltican derivation. If the protolith is from Baltica, paleogeographic reconstruction models can be used to demonstrate where the protolith might have originated. A palaeogeographic reconstruction model of Pisarevsky et al. (2014) shows a potential paleoposition of Baltica (Fig. 70). Pisarevsky et al. (2014) suggests that subduction and accretion occurred along the Baltican margin 1650 Ma. This is where the protolith of the Dagvolsjøen augen gneiss could have been formed, and the paleogeographic model suggests that the protolith was formed close to the equator (Fig. 70).

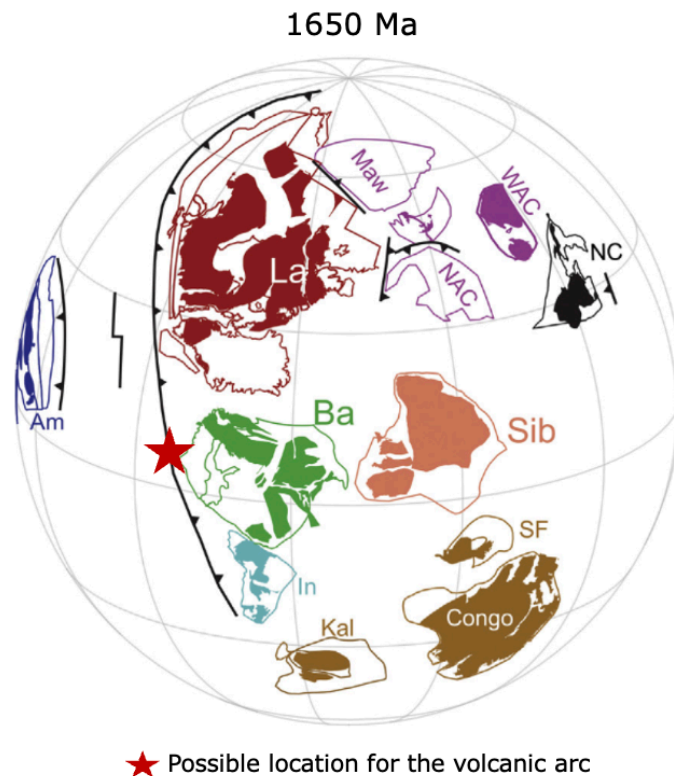


Figure 70. Global paleogeographic reconstruction at 1650 Ma according to Pisarevsky et al. (2014). Archean crust is represented by filled polygons. The continents are: La = Laurentia, NAC = North Australian craton, WAC = West Australian Craton, Maw = Mawson Craton, Sib = Siberia, SF = São Francisco, Kal = Kalahari, Am = Amazonia, and NC = North China. There is in this model subduction and accretion along the Baltican margin, and a possible location of the volcanic arc generating the protolith for the Dagvolsjøen augen gneiss is marked with a red star. The figure is from Pisarevsky et al. (2014).

Rapakivi magmatism?

Rapakivi magmatism is known from the southern part of Finland, and the plutonism occurred in two main pulses between 1650-1615 Ma and 1575-1540 Ma, where the Wiborg suite was formed 1.65-1.5 Ma (Åhäll et al., 2000, Heinonen et al., 2010). Krill (1980) described rapakivi textures in the Oppdal augen gneiss of the Risberget Nappe, which is dated to 1189 ± 1 Ma by Handke et al. (1995). Considering the reported ages of the Risberget Nappe are ~ 1190 Ma, is there a significant time gap of appr. 450 million years between the crystallization age of the Wiborg suite and the protolith for the Risberget Nappe. This implies an unlikely relationship between the two, and there is no reason to suggest a c. 1655 rapakivi domain outboard of the WGR. In addition, the Proterozoic rapakivi granites in Finland are interpreted to have formed in an anorogenic extensional regime (Haapala and Rämö, 1992). However, the rapakivi texture could be a

feature of the 1180-1190 Ma augen gneiss, without it being related to the Finnish rapakivi magmatism. Therefore, it is possible that the ~1655 Ma augen gneisses were intruded by rapakivi granites ~1190 Ma. It is therefore possible that a similar rapakivi suite once existed in the western part of Baltica (Fig. 71). Since there is no indication for the occurrence of rapakivi texture in the 1655 ± 5 Ma augen gneiss of the Dagsvolsjøen Nappe, it appears that the augen gneiss has more in common with the ~1650 gneisses of the WGR.

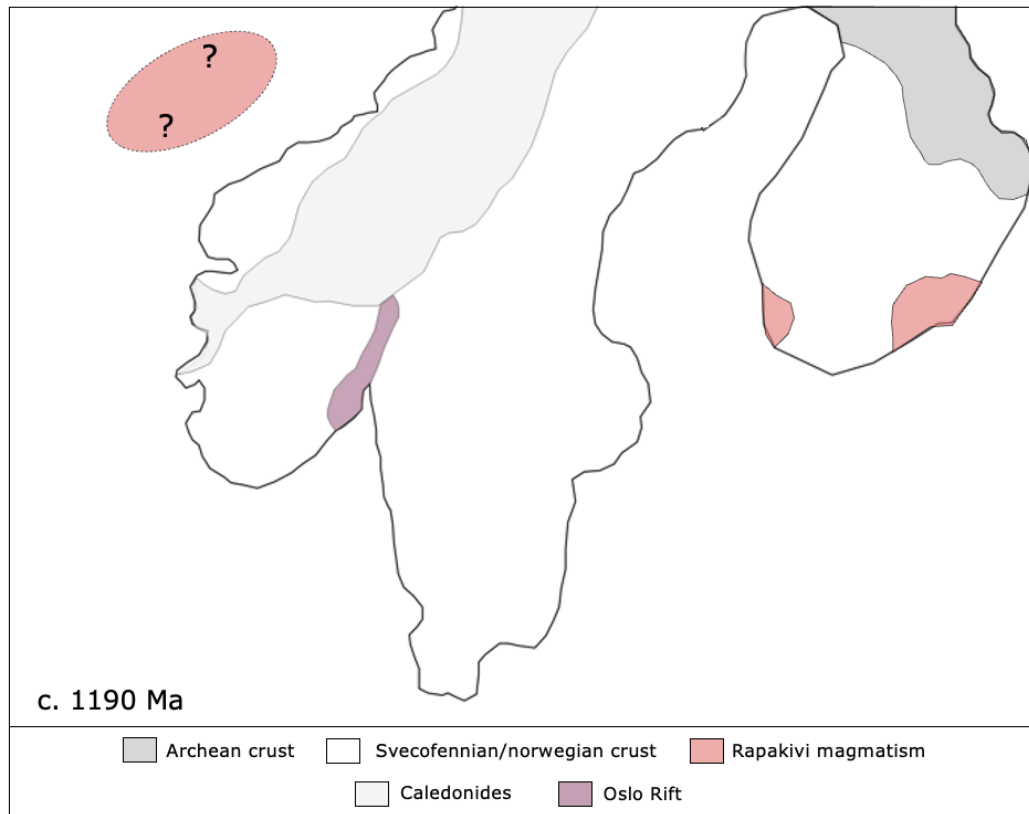


Figure 71. Simplified map over Fennoscandia after Bingen et al. (2008a), Andersson et al. (2007), Lamminen et al. (2011) and Lamminen et al. (2015). Rapakivi magmatism is known in the southern part of Finland with ages between 1650-1615 Ma and 1575-1540 Ma (Ahäll et al., 2000, Heinonen et al., 2010). The c. 1655 Ma augen gneiss could have been intruded by c. 1190 Ma rapakivi granite outboard of WGR. The Caledonides and the Oslo Rift occurred after the potential rapakivi magmatism, but are on the map for geographical context.

Volcanic arc complex?

If there is affinity between the WGR and the Dagsvolsjøen Nappe, it implies that the protolith(s) of the WGR, Dagsvolsjøen Nappe and TAG extended beyond the present-day geographic position of the WGR (Fig. 72). Since there are variable ages reported for the protolith of the gneisses of WGR, could there have been a volcanic arc complex? The arcs could have generated the magma for the protoliths at different times, and this can possibly explain the c. 1655 Ma for the Dagsvolsjøen and TAG and the range 1576-1713 Ma in the WGR (Skår et al., 1994, Skår and Pedersen, 2003, Austrheim et al., 2003, Krogh et al., 2011, Røhr et al., 2013, Corfu et al., 2014b, Kylander-Clark and Hacker, 2014, DesOrmeau et al., 2015, Butler et al., 2018, Bjerkan, 2020, Wang et al., 2021).

Since there is probably no affinity between the Dagsvolsjøen Nappe and the Vigelen granite exposed in the Skardøra antiform, there was another magma generating

environment for the Vigelen granite. The Vigelen granite could have been generated in an extensional geotectonic environment, such as a back-arc continental rift (Fig. 72b). However, the exact magma forming environment for the Vigelen granite is not thoroughly investigated in this study.

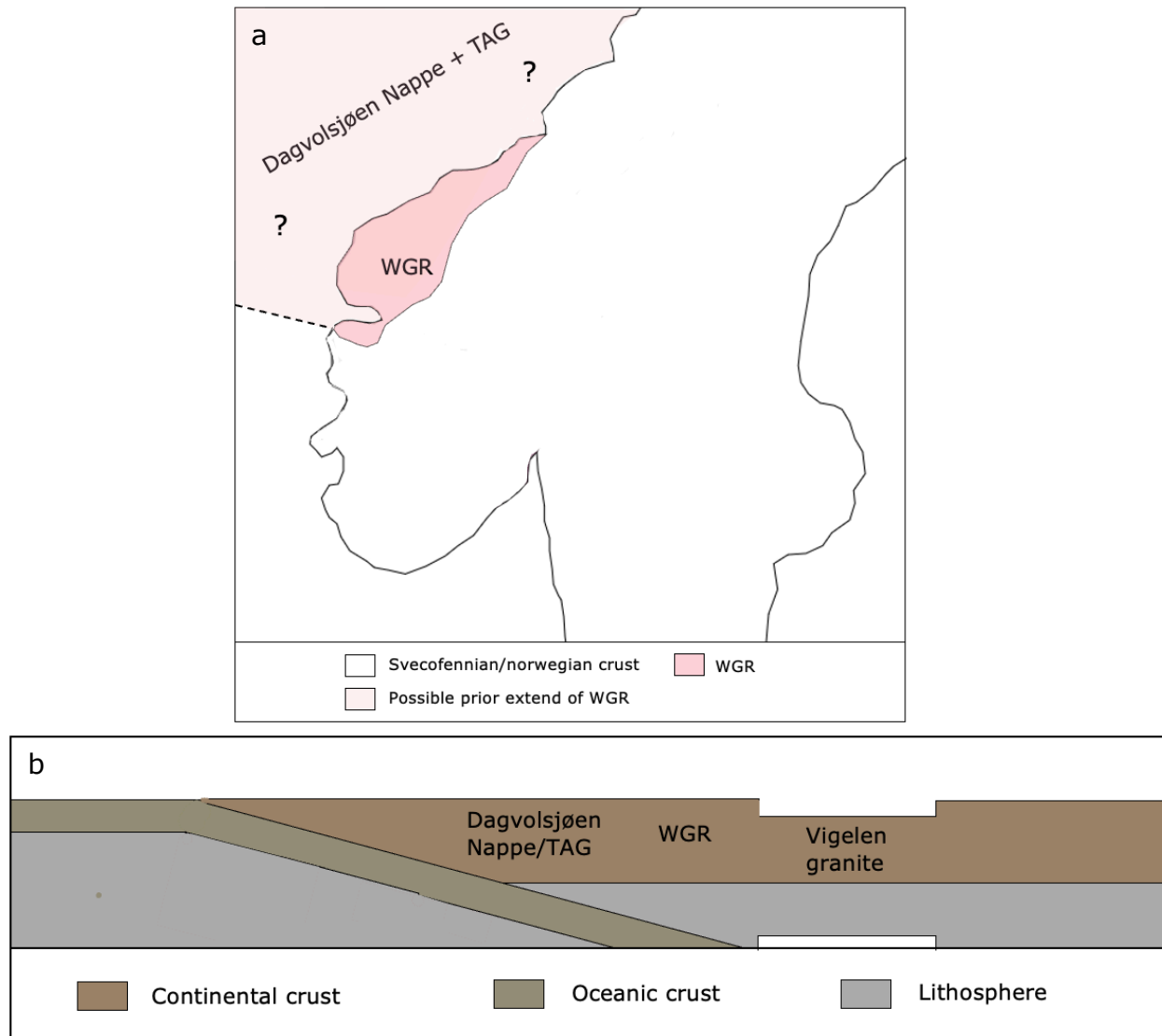


Figure 72. a) Simplified map over western part of Fennoscandinavia after Lamminen et al. (2011). The WGR is marked in pink, and the possible extended part is marked in light pink with stippled lines. b) A simplified and proposed cross-section. The protolith(s) for the Dagvolsjøen Nappe, the TAG and the WGR was probably an I-type granite that was emplaced c. 1655 Ma. What the granites intruded remains unknown. The Vigelen granite is an A-type granite, and A-type granites can occur in extensional regimes, such as back-arc continental rift. The figure is not to scale.

Displacement of the Dagvolsjøen Nappe

Nystuen (1983) estimated a southeastward displacement of 200-400 km for the Osen-Røa Nappe Complex, positioning the basin northwestward of the current Norwegian coast (Fig. 73). As the Dagvolsjøen augen gneiss is structurally above the rocks of the Osen-Røa Nappe Complex, it is commonly and traditionally inferred that the Dagvolsjøen Nappe experienced a longer transport distance. Consequently, it is suggested that the Dagvolsjøen Nappe originated more distal to Baltica compared to the Osen-Røa Nappe Complex. Likewise, the Dagvolsjøen Nappe had a shorter transport distance than the

overlying Hummelfjellet and Särvi nappes (Fig. 73). Previous estimates indicate that the Dagvolsjøen Nappe has been transported at least 200 km, although further investigations are required to establish a more precise displacement distance.

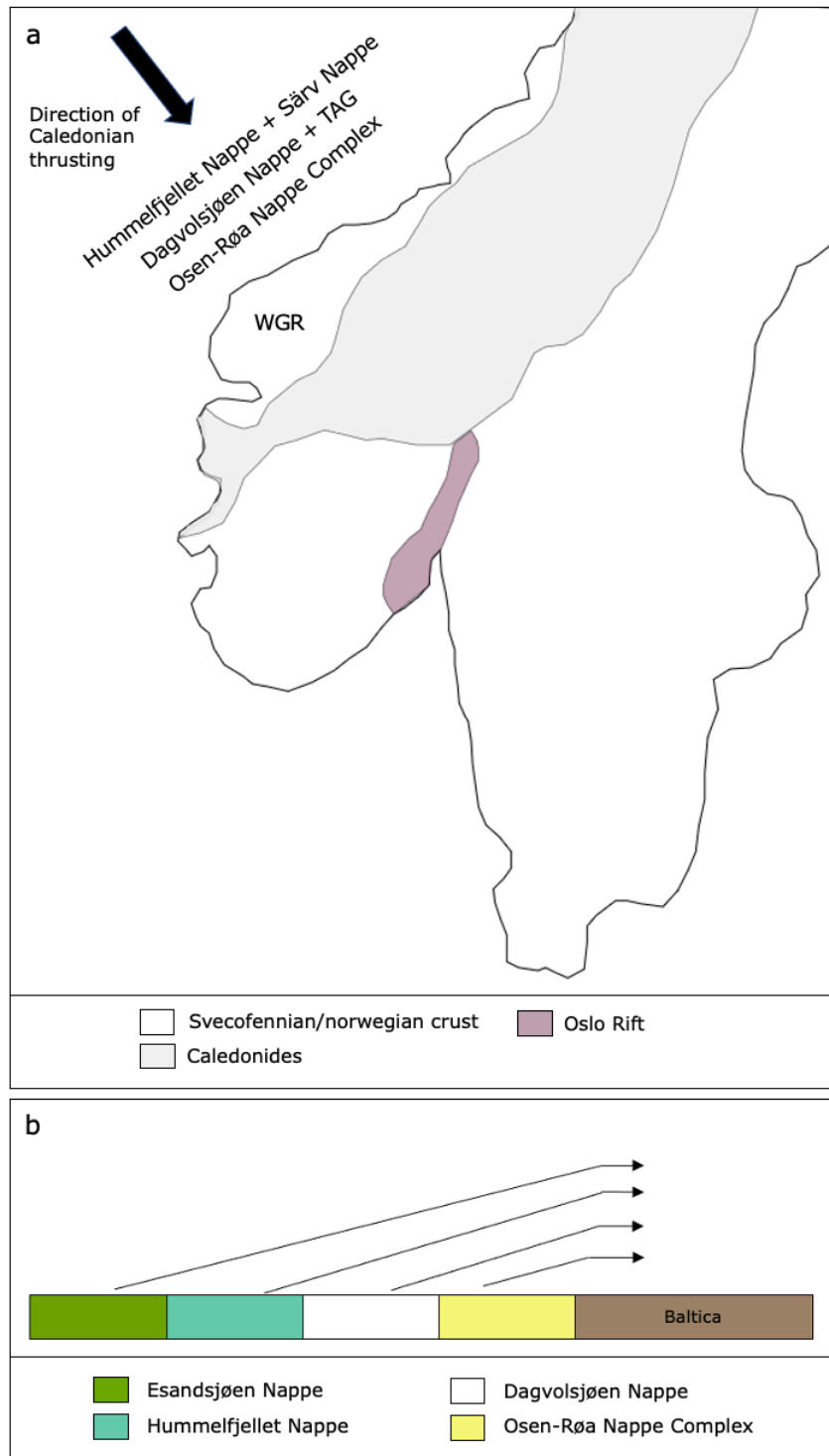


Figure 73. a) Simplified model for the western part of Baltica. a) The possible locations of the Osen-Røa Nappe Complex, the Dagvolsjøen Nappe, TAG, Hummelfjellet Nappe and the Särvi Nappe prior to the Caledonian orogeny. The figure is modified after Lamminen et al. (2011) and Roffeis and Corfu (2014). The Caledonides and the Oslo Rift are on the map for geographical context. b) Simplified cross-section of the Baltoscandian margin for the nappes in the field area before the Caledonian orogeny. The Osen-Røa Nappe Complex was most inboard relative to Baltica with Dagvolsjøen Nappe, Hummelfjellet Nappe and Esandsjøen Nappe increasingly more outboard. The figure is after Gee et al. (2013) and not to scale.

6.4 Further work

In order to obtain a deeper understanding of the augen gneiss assigned to the Dagvolsjøen Nappe and the correlated nappes, further research is required:

- Further investigations on the variants of the augen gneiss within the Dagvolsjøen Nappe, such as conducting geochemical analysis of the unstriped augen gneiss with fine-grained matrix and performing geochronological analysis of the strongly quartz striped K-feldspar augen gneiss and the unstriped augen gneiss with fine-grained matrix.
- U-Pb age dating of the conglomerate/meta-arkose of the Osen-Røa Nappe Complex and MU108. By dating MU108, a conclusive information about the rock type can be made.
- Additional geochronological analyses, e.g. $^{40}\text{Ar}/^{39}\text{Ar}$ dating, to determine the timing of the augen formation in the augen gneiss. These analyses would contribute to a more comprehensive understanding of the chronological evolution of Dagvolsjøen augen gneiss.
- Analyse Lu-Hf data of zircons from the augen gneiss. The Lu-Hf isotope system can give information about the source of the protolith. By examining the Lu-Hf signatures, valuable insights can be gained regarding the origin of the augen gneiss.
- Map and analyse geochronological and geochemical data for the augen gneiss of the Risberget Nappe. Previous studies provide limited lithological and geochemical descriptions/analyses of the augen gneiss of the Risberget Nappe. With a more comprehensive lithological description and geochemical analyses, a more certain correlation, or no correlation, between the Risberget and the Dagvolsjøen nappes can be established.

7 Conclusion

The aim of this study was to comprehensively map and obtain geochronological and geochemical data of the augen gneiss of the Dagvolsjøen Nappe in the central Norwegian Caledonides. As the Dagvolsjøen Nappe is commonly correlated with other nappes containing augen gneisses in the central Scandinavian Caledonides, a comparative analysis has been done.

Field investigations demonstrated that the augen gneiss of the Dagvolsjøen Nappe can possibly be divided into three variations based on the matrix: (1) quartz striped K-feldspar augen gneiss, (2) unstriped augen gneiss with fine-grained matrix and (3) strongly quartz striped K-feldspar augen gneiss. Based on the mineralogy, the texture and the geochemical analyses, they are all interpreted as the Dagvolsjøen augen gneiss. However, further investigations are necessary for the unstriped augen gneiss before a conclusion is made. All three variants are observed on both limbs of the Skardøra antiform, indicating their presence in both the Dagvolsjøen Nappe and the TAG. However, the unstriped augen gneiss with a fine-grained matrix is less abundant in the TAG in the field area. Despite the augen gneiss being non-continuous in the field, structural observations indicate that the augen gneiss is a single tectonostratigraphic unit.

This study provides an average $^{207}\text{Pb}/^{206}\text{Pb}$ age of 1655 ± 5 Ma for the augen gneiss of the Dagvolsjøen Nappe. The Tännäs augen gneiss yields a $^{207}\text{Pb}/^{206}\text{Pb}$ age of 1654 ± 5 Ma, which is within error of the Dagvolsjøen Nappe. The analyses are mostly concordant and interpreted to be the magmatic crystallisation age of the protolith of the augen gneiss. The Vigelen granite, exposed in the Skardøra antiform, yields a $^{207}\text{Pb}/^{206}\text{Pb}$ age of 1657 ± 6 Ma. A granitic sheet has been emplaced in the augen gneiss assigned to the TAG, and it has a lower intercept age of 436 ± 43 Ma to 351 ± 38 Ma. The host rock has not been affected by the emplacement. Hence, the formation of the augen in the augen gneiss occurred between ~ 1655 Ma and the emplacement of the granitic intrusion, but the exact timing remains uncertain. The age group of 1190-1180 Ma provided by Handke et al. (1995) and Lamminen et al. (2011) for the augen gneiss of the Risberget Nappe differs from the ages yielded from the Dagvolsjøen Nappe and the TAG.

The Dagvolsjøen Nappe can be correlated with the TAG in Sweden, and it is suggested that the nappes have a common protolith. Geochronological and geochemical data suggest that the protolith of the augen gneiss may have been an I-type granite that may have been generated in a volcanic arc setting in a supra-subduction environment c. 1655 Ma. There is a possible affinity between the Dagvolsjøen Nappe/TAG and the WGR. Hence, the protolith of the augen gneisses of the Dagvolsjøen and TAG nappes could be of Baltican derivation. There is no or little affinity between the Dagvolsjøen augen gneiss and the Vigelen granite, while the correlation between the Dagvolsjøen Nappe and the Risberget Nappe remains uncertain in this study.

References

- AHL, M., BERGMAN, S., BERGSTRÖM, U., ELIASSON, T., RIPA, M. & WEIHED, P. 2001. *Geochemical classification of plutonic rocks in central and northern Sweden*, Sveriges geologiska undersökning.
- ANDERSEN, T. 2002. Correction of common lead in U–Pb analyses that do not report ²⁰⁴Pb. *Chemical geology*, 192, 59-79.
- ANDERSSON, U. B., RUTANEN, H., JOHANSSON, Å., MANSFELD, J. & RIMŠA, A. 2007. Characterization of the Paleoproterozoic mantle beneath the Fennoscandian Shield: Geochemistry and isotope geology (Nd, Sr) of ~ 1.8 Ga mafic plutonic rocks from the Transscandinavian Igneous Belt in southeast Sweden. *International Geology Review*, 49, 587-625.
- ARNBOM, J.-O. 1980. Metamorphism of the Seve Nappes at Åreskutan, Swedish Caledonides. *Geologiska Föreningen i Stockholm Förhandlingar*, 102, 359-371.
- AUSTRHEIM, H., CORFU, F., BRYHNI, I. & ANDERSEN, T. B. 2003. The Proterozoic Hustad igneous complex: a low strain enclave with a key to the history of the Western Gneiss Region of Norway. *Precambrian Research*, 120, 149-175.
- BERGMAN, S., STEPHENS, M. B., ANDERSSON, J., KATHOL, B. & BERGMAN, T. 2012. *Bedrock map of Sweden, scale 1:1 million*, 1:1 million Sveriges geologiska undersökning
- BINGEN, B., ANDERSSON, J., SÖDERLUND, U. & MÖLLER, C. 2008a. The Mesoproterozoic in the Nordic countries. *Episodes Journal of International Geoscience*, 31, 29-34.
- BINGEN, B., GRIFFIN, W., TORSVIK, T. & SAEED, A. 2005. Timing of Late Neoproterozoic glaciation on Baltica constrained by detrital zircon geochronology in the Hedmark Group, south-east Norway. *Terra Nova*, 17, 250-258.
- BINGEN, B., NORDGULEN, O. & VIOLA, G. 2008b. A four-phase model for the Sveconorwegian orogeny, SW Scandinavia. *Norsk geologisk tidsskrift*, 88, 43.
- BINGEN, B., VIOLA, G., MÖLLER, C., VANDER AUWERA, J., LAURENT, A. & YI, K. 2021. The Sveconorwegian orogeny. *Gondwana Research*, 90, 273-313.
- BJERKAN, G. 2020. *Zircon U-Pb geochronology and whole-rock geochemistry of migmatitic gneisses reveal the late Paleoproterozoic through Devonian history of the Western Gneiss Region*. NTNU.
- BOURDON, B., TURNER, S., HENDERSON, G. M. & LUNDSTROM, C. C. 2003. Introduction to U-series geochemistry. *Reviews in mineralogy and geochemistry*, 52, 1-21.
- BOYNTON, W. V. 1984. Cosmochemistry of the rare earth elements: meteorite studies. *Developments in geochemistry*. Elsevier.
- BRAATHEN, A., NORDGULEN, Ø., OSMUNDSSEN, P.-T., ANDERSEN, T. B., SOLLI, A. & ROBERTS, D. 2000. Devonian, orogen-parallel, opposed extension in the Central Norwegian Caledonides. *Geology*, 28, 615-618.
- BUTLER, J., JAMIESON, R., DUNNING, G., PECHA, M., ROBINSON, P. & STEENKAMP, H. 2018. Timing of metamorphism and exhumation in the Nordøyane ultra-high-pressure domain, Western Gneiss Region, Norway: new constraints from complementary CA-ID-TIMS and LA-MC-ICP-MS geochronology. *Lithos*, 310, 153-170.
- CHAPPELL, B. W., BRYANT, C. J. & WYBORN, D. 2012. Peraluminous I-type granites. *Lithos*, 153, 142-153.
- CHAPPELL, B. W. & WHITE, A. 1992. I- and S-type granites in the Lachlan Fold Belt. *Earth and Environmental Science Transactions of the Royal Society of Edinburgh*, 83, 1-26.
- CHERNIAK, D. 2010. Diffusion in accessory minerals: zircon, titanite, apatite, monazite and xenotime. *Reviews in mineralogy and geochemistry*, 72, 827-869.
- CLAESSON, S. 1980. A Rb-Sr isotope study of granitoids and related mylonites in the Tännäs Augen Gneiss Nappe, southern Swedish Caledonides. *Geologiska Föreningen i Stockholm Förhandlingar*, 102, 403-420.

- COCKS, L. R. M. & TORSVIK, T. H. 2005. Baltica from the late Precambrian to mid-Palaeozoic times: the gain and loss of a terrane's identity. *Earth-Science Reviews*, 72, 39-66.
- CORFU, F. 2013. A century of U-Pb geochronology: The long quest towards concordance. *Bulletin*, 125, 33-47.
- CORFU, F., ANDERSEN, T. & GASSER, D. 2014a. The Scandinavian Caledonides: main features, conceptual advances and critical questions. *Geological Society, London, Special Publications*, 390, 9-43.
- CORFU, F., AUSTRHEIM, H. & GANZHORN, A.-C. 2014b. Localized granulite and eclogite facies metamorphism at Flatraket and Kråkeneset, Western Gneiss Region: U-Pb data and tectonic implications. *Geological Society, London, Special Publications*, 390, 425-442.
- CORFU, F., HANCHAR, J. M., HOSKIN, P. W. & KINNY, P. 2003. Atlas of zircon textures. *Reviews in mineralogy and geochemistry*, 53, 469-500.
- DEBON, F. & LE FORT, P. 1983. A chemical-mineralogical classification of common plutonic rocks and associations. *Earth and Environmental Science Transactions of the Royal Society of Edinburgh*, 73, 135-149.
- DESORMEAU, J. W., GORDON, S. M., KYLANDER-CLARK, A. R., HACKER, B. R., BOWRING, S. A., SCHOENE, B. & SAMPERTON, K. M. 2015. Insights into (U) HP metamorphism of the Western Gneiss Region, Norway: A high-spatial resolution and high-precision zircon study. *Chemical Geology*, 414, 138-155.
- DEWEY, J. F. & BURKE, K. 1974. Hot spots and continental break-up: implications for collisional orogeny. *Geology*, 2, 57-60.
- DICKIN, A. P. 2005. *Radiogenic isotope geology*, Cambridge university press.
- FOSSEN, H. 1992. The role of extensional tectonics in the Caledonides of south Norway. *Journal of structural geology*, 14, 1033-1046.
- FOSSEN, H. & HURICH, C. A. 2005. The Hardangerfjord Shear Zone in SW Norway and the North Sea: a large-scale low-angle shear zone in the Caledonian crust. *Journal of the Geological Society*, 162, 675-687.
- FROST, B. R., BARNES, C. G., COLLINS, W. J., ARCULUS, R. J., ELLIS, D. J. & FROST, C. D. 2001. A geochemical classification for granitic rocks. *Journal of petrology*, 42, 2033-2048.
- FROST, B. R. & FROST, C. D. 2008. A geochemical classification for feldspathic igneous rocks. *Journal of Petrology*, 49, 1955-1969.
- GANZHORN, A.-C., LABROUSSE, L., PROUTEAU, G., LEROY, C., VRIJMOED, J., ANDERSEN, T. B. & ARBARET, L. 2014. Structural, petrological and chemical analysis of syn-kinematic migmatites: Insights from the Western Gneiss Region, Norway. *Journal of Metamorphic Geology*, 32, 647-673.
- GAO, P., ZHENG, Y.-F. & ZHAO, Z.-F. 2016. Distinction between S-type and peraluminous I-type granites: Zircon versus whole-rock geochemistry. *Lithos*, 258, 77-91.
- GEE, D. G., FOSSEN, H., HENRIKSEN, N. & HIGGINS, A. K. 2008. From the early Paleozoic platforms of Baltica and Laurentia to the Caledonide Orogen of Scandinavia and Greenland. *Episodes Journal of International Geoscience*, 31, 44-51.
- GEE, D. G., GUEZOU, J.-C., ROBERTS, D. & WOLFF, F. C. 1985. The central-southern part of the Scandinavian Caledonides., The Caledonide Orogen - Scandinavia and related areas. Vol. 1, 109-133.
- GEE, D. G., JANÁK, M., MAJKA, J., ROBINSON, P. & VAN ROERMUND, H. 2013. Subduction along and within the Baltoscandian margin during closing of the Iapetus Ocean and Baltica-Laurentia collision. *Lithosphere*, 5, 169-178.
- GEE, D. G., JUHLIN, C., PASCAL, C. & ROBINSON, P. 2010. Collisional orogeny in the Scandinavian Caledonides (COSC). *Gff*, 132, 29-44.
- GEE, D. G., KLONOWSKA, I., ANDRÉASSON, P.-G. & STEPHENS, M. B. 2020. Middle thrust sheets in the Caledonide orogen, Sweden: the outer margin of Baltica, the continent-ocean transition zone and late Cambrian-Ordovician subduction-accretion. *Geological Society, London, Memoirs*, 50, 517-548.

- GEE, D. G., LADENBERGER, A., DAHLQVIST, P., MAJKA, J., BE'ERI-SHLEVIN, Y., FREI, D. & THOMSEN, T. 2014. The Baltoscandian margin detrital zircon signatures of the central Scandes. *Geological Society, London, Special Publications*, 390, 131-155.
- GEE, D. G., LOBKOWICZ, M. & SINGH, S. 1994. Late Caledonian extension in the Scandinavian Caledonides—the Røragen detachment revisited. *Tectonophysics*, 231, 139-155.
- GEE, D. G. & STEPHENS, M. B. 2020. Chapter 20 Lower thrust sheets in the Caledonide orogen, Sweden: Cryogenian–Silurian sedimentary successions and underlying, imbricated, crystalline basement. *Geological Society, London, Memoirs*, 50, 495-515.
- GEHRELS, G. 2011. Detrital zircon U-Pb geochronology: Current methods and new opportunities. *Tectonics of sedimentary basins: Recent advances*, 45-62.
- GORBATSCHEV, R. 2004. The transscandinavian igneous belt-introduction and background. *Special paper-Geological survey of Finland*, 37, 9.
- GRANSETH, A., SLAGSTAD, T., COINT, N., ROBERTS, N. M., RØHR, T. S. & SØRENSEN, B. E. 2020. Tectonomagmatic evolution of the Sveconorwegian orogen recorded in the chemical and isotopic compositions of 1070–920 Ma granitoids. *Precambrian research*, 340, 105527.
- GRENNÉ, T., IHLEN, P. & VOKES, F. 1999. Scandinavian Caledonide metallogeny in a plate tectonic perspective. *Mineralium Deposita*, 34, 422-471.
- GULESIDER. 2022. Kart [Online]. Available: <https://kart.gulesider.no/s%C3%B8k/sverige> [Accessed 10.10.2022].
- HANDKE, M., TUCKER, R. & ROBINSON, P. Contrasting U-Pb Ages for the Risberget Augen Gneiss in the Norwegian Caledonides: Getting to the root of the problem. *Geological Society of America Abstracts with Programs*, 1995. 226.
- HEINONEN, A., ANDERSEN, T. & RÄMÖ, O. 2010. Re-evaluation of rapakivi petrogenesis: Source constraints from the Hf isotope composition of zircon in the rapakivi granites and associated mafic rocks of southern Finland. *Journal of Petrology*, 51, 1687-1709.
- HERRON, M. M. 1988. Geochemical classification of terrigenous sands and shales from core or log data. *Journal of Sedimentary Research*, 58, 820-829.
- HOLMQUIST, P. 1894. Om diabasen på Ottfjället i Jemtland. *Geologiska Föreningen i Stockholm Förhandlingar*, 16, 175-192.
- HOLMSEN, P. 1963. On the tectonic relations of the Devonian complex of the Røragen area, East Central Norway.
- HURICH, C. & ROBERTS, D. 2018. The concealed Kopperå fault: A half-graben bounding structure located along the eastern flank of the Trøndelag depression, mid-Norway.
- HÖGDAHL, K., ANDERSSON, U. B. & EKLUND, O. 2004. *The Transscandinavian Igneous Belt (TIB) in Sweden: a review of its character and evolution*, Geological survey of Finland Espoo.
- HAAPALA, I. & RÄMÖ, O. T. 1992. Tectonic setting and origin of the Proterozoic rapakivi granites of southeastern Fennoscandia. *Earth and Environmental Science Transactions of the Royal Society of Edinburgh*, 83, 165-171.
- JACKSON, S. E., PEARSON, N. J., GRIFFIN, W. L. & BELOUSOVA, E. A. 2004. The application of laser ablation-inductively coupled plasma-mass spectrometry to in situ U–Pb zircon geochronology. *Chemical geology*, 211, 47-69.
- JAKOB, J., ALSAIF, M., CORFU, F. & ANDERSEN, T. B. 2017. Age and origin of thin discontinuous gneiss sheets in the distal domain of the magma-poor hyperextended pre-Caledonian margin of Baltica, southern Norway. *Journal of the Geological Society*, 174, 557-571.
- JAKOB, J., ANDERSEN, T. B., MOHN, G., KJØLL, H. J. & BEYSSAC, O. 2022. A Revised Tectono-Stratigraphic Scheme for the Scandinavian Caledonides and Its Implications for Our Understanding of the Scandian Orogeny. *Geol. Soc. Am. Spec. Paper. In New Developments in the Appalachian-Caledonian-Variscan Orogen*.

- JANOŠEK, V., FARROW, C. M. & ERBAN, V. 2006. Interpretation of whole-rock geochemical data in igneous geochemistry: introducing Geochemical Data Toolkit (GCDkit). *Journal of Petrology*, 47, 1255-1259.
- KARTVERKET. 2022. <https://www.norgeskart.no/#!?project=norgeskart&layers=1002&zoom=3&lat=71.97864.00&lon=396722.00>. [Accessed 10.10.2022 2022].
- KENDRICK, M., EIDE, E., ROBERTS, D. & OSMUNDSEN, P. 2004. The Middle to Late Devonian Høybakken detachment, central Norway: 40Ar–39Ar evidence for prolonged late/post-Scandian extension and uplift. *Geological Magazine*, 141, 329-344.
- KINNY, P., STRACHAN, R., KOCKS, H. & FRIEND, C. 2003. U–Pb geochronology of late Neoproterozoic augen granites in the Moine Supergroup, NW Scotland: dating of rift-related, felsic magmatism during supercontinent break-up? *Journal of the Geological Society*, 160, 925-934.
- KRILL, A. G. 1980. Tectonics of the Oppdal area, central Norway. *Geologiska Föreningen i Stockholm Förhandlingar*, 102, 523-530.
- KROGH, T. E., KAMO, S. L., ROBINSON, P., TERRY, M. P. & KWOK, K. 2011. U–Pb zircon geochronology of eclogites from the Scandian Orogen, northern Western Gneiss Region, Norway: 14–20 million years between eclogite crystallization and return to amphibolite-facies conditions. *Canadian Journal of Earth Sciences*, 48, 441-472.
- KUMPULAINEN, R. A., HAMILTON, M., SÖDERLUND, U. & NYSTUEN, J. P. 2021. U-Pb baddeleyite age for the Ottfjället Dyke Swarm, central Scandinavian Caledonides: new constraints on Ediacaran opening of the Iapetus Ocean and glaciations on Baltica. *GFF*, 143, 40-54.
- KYLANDER-CLARK, A. R. & HACKER, B. R. 2014. Age and significance of felsic dikes from the UHP western gneiss region. *Tectonics*, 33, 2342-2360.
- LAMMINEN, J., ANDERSEN, T. & NYSTUEN, J. P. 2011. Zircon U-Pb ages and Lu-Hf isotopes from basement rocks associated with Neoproterozoic sedimentary successions in the Sparagmite Region and adjacent areas, South Norway: the crustal architecture of western Baltica. *Norwegian Journal of Geology/Norsk Geologisk Forening*, 91.
- LAMMINEN, J., ANDERSEN, T. & NYSTUEN, J. P. 2015. Provenance and rift basin architecture of the Neoproterozoic Hedmark Basin, South Norway inferred from U–Pb ages and Lu–Hf isotopes of conglomerate clasts and detrital zircons. *Geological Magazine*, 152, 80-105.
- LARSON, S. Å. & BERGLUND, J. 1992. A chronological subdivision of the Transscandinavian Igneous Belt—three magmatic episodes? *Geologiska Föreningen i Stockholm Förhandlingar*, 114, 459-461.
- LI, B., MASSONNE, H.-J. & ZHANG, J. 2020. Evolution of a gneiss in the Seve nappe complex of central Sweden—Hints at an early Caledonian, medium-pressure metamorphism. *Lithos*, 376, 105746.
- LI, L.-M., SUN, M., WANG, Y., XING, G., ZHAO, G., CAI, K. & ZHANG, Y. 2011. Geochronological and Geochemical study of Palaeoproterozoic gneissic granites and clinopyroxenite xenoliths from NW Fujian, SE China: Implications for the crustal evolution of the Cathaysia Block. *Journal of Asian Earth Sciences*, 41, 204-212.
- LI, Z.-X., BOGDANOVA, S., COLLINS, A., DAVIDSON, A., DE WAELE, B., ERNST, R., FITZSIMONS, I., FUCK, R., GLADKOCHUB, D. & JACOBS, J. 2008. Assembly, configuration, and break-up history of Rodinia: a synthesis. *Precambrian research*, 160, 179-210.
- LUDWIG, K. R. 1998. On the treatment of concordant uranium-lead ages. *Geochimica et Cosmochimica Acta*, 62, 665-676.
- LUNDMARK, A. M. & CORFU, F. 2008. Emplacement of a Silurian granitic dyke swarm during nappe translation in the Scandinavian Caledonides. *Journal of Structural Geology*, 30, 918-928.
- MCCLELLAN, E. A. 2004. Metamorphic conditions across the Seve-Köli Nappe boundary, southeastern Trondheim region, Norwegian Caledonides: Comparison of garnet-

- biotite thermometry and amphibole chemistry. *Norwegian Journal of Geology/Norsk Geologisk Forening*, 84.
- MCKERROW, W., MAC NIOCAILL, C. & DEWEY, J. 2000. The Caledonian orogeny redefined. *Journal of the Geological society*, 157, 1149-1154.
- MCLENNAN, S. M. & ROSS TAYLOR, S. 2011. Geology, Geochemistry and Natural Abundances. *Encyclopedia of Inorganic and Bioinorganic Chemistry*.
- MEZGER, K. & KROGSTAD, E. 1997. Interpretation of discordant U-Pb zircon ages: An evaluation. *Journal of metamorphic Geology*, 15, 127-140.
- MIDDLEMOST, E. A. 1994. Naming materials in the magma/igneous rock system. *Earth-science reviews*, 37, 215-224.
- NAGUDI, B., KOEBERL, C. & KURAT, G. 2003. Petrography and geochemistry of the Singo granite, Uganda, and implications for its origin. *Journal of African Earth Sciences*, 36, 73-87.
- NGU. 2022a. 1:1.350.000 Bedrock map [Online]. NGU. Available: https://geo.ngu.no/kart/berggrunn_mobil/ [Accessed 26.09.2022].
- NGU. 2022b. 1:250.000 Bedrock map [Online]. NGU. Available: https://geo.ngu.no/kart/berggrunn_mobil/ [Accessed 26.09.2022].
- NGU 2023. Berggrunn - Nasjonal berggrunnsdatabase NGU: NGU.
- NGU, D. G. 2013. Geochronological database of magnetic events in Norway and related areas: update 2013. NGU.
- NILSEN, O., CORFU, F. & ROBERTS, D. 2007. Silurian gabbro-diorite-trondhjemite plutons in the Trondheim Nappe Complex, Caledonides, Norway: petrology and U-Pb geochronology. *NORSK GEOLOGISK TIDSSKRIFT*, 87, 329.
- NILSEN, O. & WOLFF, F. C. 1989. Røros og Sveg. Berggrunnskart Røros og Sveg M 1:250 000.
- NORDGULEN, O., BRAATHEN, A., CORFU, F., OSMUNDTSEN, P. T. & HUSMO, T. 2002. Polyphase kinematics and geochronology of the late-Caledonian Kollstraumen detachment, north-central Norway. *Norsk geologisk tidsskrift*, 82, 299-316.
- NORTON, M. G., MCCLAY, K. R. & WAY, N. A. 1987. Tectonic evolution of Devonian basins in northern Scotland and southern Norway. *Norsk Geologisk Tidsskrift*, 67, 323.
- NYSTUEN, J. P. 1982. Late Proterozoic basin evolution on the Baltoscandian craton: the Hedmark Group, southern Norway. *Bulletin-Norges geologiske undersøkelse*.
- NYSTUEN, J. P. 1983. Nappe and thrust structures in the Sparagmite region, southern Norway.
- O'CONNOR, J. 1965. A classification for quartz-rich igneous rocks based on feldspar ratios. *US Geological Survey, Professional Papers 525B*, B79-B84.
- OSMUNDTSEN, P. T., BRAATHEN, A., SOMMARUGA, A., SKILBREI, J. R., NORDGULEN, Ø., ROBERTS, D., ANDERSEN, T. B., OLESEN, O. & MOSAR, J. 2005. Metamorphic core complexes and gneiss-cored culminations along the Mid-Norwegian margin: an overview and some current ideas. *Norwegian Petroleum Society Special Publications*, 12, 29-41.
- PASSCHIER, C. W. & TROUW, R. A. 2005. *Microtectonics*, Springer Science & Business Media.
- PEARCE, J. A. 2014. Immobile element fingerprinting of ophiolites. *Elements*, 10, 101-108.
- PEARCE, J. A., HARRIS, N. B. & TINDLE, A. G. 1984. Trace element discrimination diagrams for the tectonic interpretation of granitic rocks. *Journal of petrology*, 25, 956-983.
- PETRUS, J. A. & KAMBER, B. S. 2012. VizualAge: A novel approach to laser ablation ICP-MS U-Pb geochronology data reduction. *Geostandards and Geoanalytical Research*, 36, 247-270.
- PIRKLE, F. & PODMEYER, D. 1993. Zircon: origin and uses. *Transactions*, 292, 1-20.
- PISAREVSKY, S. A., ELMING, S.-Å., PESONEN, L. J. & LI, Z.-X. 2014. Mesoproterozoic paleogeography: Supercontinent and beyond. *Precambrian Research*, 244, 207-225.

- POWELL, C. M., LI, Z.-X., MCELHINNY, M., MEERT, J. & PARK, J. 1993. Paleomagnetic constraints on timing of the Neoproterozoic breakup of Rodinia and the Cambrian formation of Gondwana. *Geology*, 21, 889-892.
- REVERDATTO, V. V., LIKHANOV, I. I., POLYANSKY, O. P., SHEPLEV, V. S. & KOLOBOV, V. Y. 2019. *The nature and models of metamorphism*, Springer.
- REZAEI-KAHKHAEI, M., KANANIAN, A., ESMAEILI, D. & ASIABANHA, A. 2010. Geochemistry of the Zargoli granite: Implications for development of the Sistan Suture Zone, southeastern Iran. *Island Arc*, 19, 259-276.
- ROBERT, B., DOMEIER, M. & JAKOB, J. 2021. On the origins of the Iapetus ocean. *Earth-Science Reviews*, 221, 103791.
- ROBERTS, D. 2003. The Scandinavian Caledonides: event chronology, palaeogeographic settings and likely modern analogues. *Tectonophysics*, 365, 283-299.
- ROBERTS, D. & GEE, D. G. 1985. An introduction to the structure of the Scandinavian Caledonides. *The Caledonide orogen-Scandinavia and related areas*, 1, 55-68.
- ROBERTS, D. & WOLFF, F. C. 1981. Tectonostratigraphic development of the Trondheim region Caledonides, central Norway. *Journal of Structural Geology*, 3, 487-494.
- ROBINSON, P. 1995. Extension of Trollheimen tectono-stratigraphic sequence in deep synclines near Molde and Bratvåg, Western Gneiss Region, southern Norway. *Norsk Geologisk Tidsskrift*, 75, 181-197.
- ROCK, N. M. S. 1987. The need for standardization of normalized multi-element diagrams in geochemistry: a comment. *Geochemical Journal*, 21, 75-84.
- ROFFEIS, C. & CORFU, F. 2014. Caledonian nappes of southern Norway and their correlation with Sveconorwegian basement domains. *Geological Society, London, Special Publications*, 390, 193-221.
- ROLLINSON, H. & PEASE, V. 2021. *Using geochemical data: To understand geological processes*, Cambridge University Press.
- ROLLINSON, H. R., ROLLINSON, H. & PEASE, V. 2021. *Using geochemical data: To understand geological processes*, Cambridge University Press.
- ROOT, D. & CORFU, F. 2012. U-Pb geochronology of two discrete Ordovician high-pressure metamorphic events in the Seve Nappe Complex, Scandinavian Caledonides. *Contributions to Mineralogy and Petrology*, 163, 769-788.
- RØHR, T. S., BINGEN, B., ROBINSON, P. & REDDY, S. M. 2013. Geochronology of Paleoproterozoic augen gneisses in the Western Gneiss Region, Norway: evidence for Sveconorwegian zircon neocrystallization and Caledonian zircon deformation. *The Journal of Geology*, 121, 105-128.
- RÖSHOFF, K. 1978. Structures of the Tännäs Augen Gneiss Nappe and its relation to the under- and overlying units in the central Scandinavian Caledonides.
- SCHALTEGGER, U., SCHMITT, A. & HORSTWOOD, M. 2015. U-Th-Pb zircon geochronology by ID-TIMS, SIMS, and laser ablation ICP-MS: recipes, interpretations, and opportunities. *Chemical Geology*, 402, 89-110.
- SCHOENE, B. 2014. 4.10-U-Th-Pb Geochronology. *Treatise on geochemistry*, 4, 341-378.
- SHAND, S. 1943. Classic A/CNK vs A/NK plot for discriminating metaluminous, peraluminous and peralkaline compositions. Hafner Publishing Co.: New York, NY, USA.
- SINGH, P. K., VERMA, S. K., SINGH, V. K., MORENO, J. A., OLIVEIRA, E. P. & MEHTA, P. 2019. Geochemistry and petrogenesis of sanukitoids and high-K anatectic granites from the Bundelkhand Craton, India: Implications for late-Archean crustal evolution. *Journal of Asian Earth Sciences*, 174, 263-282.
- SIZE, W. B. 1979. Petrology, geochemistry and genesis of the type area trondhemite in the Trondheim Region, Central Norwegian Caledonides.
- SKÅR, Ø., FURNES, H. & CLAEISSON, S. 1994. Proterozoic orogenic magmatism within the Western Gneiss region, Sunnfjord, Norway. *Norsk Geologisk Tidsskrift*, 74, 114-126.
- SKÅR, Ø. & PEDERSEN, R. B. 2003. Relations between granitoid magmatism and migmatization: U-Pb geochronological evidence from the Western Gneiss Complex, Norway. *Journal of the Geological Society*, 160, 935-946.

- SLAGSTAD, T. 2003. Geochemistry of trondhjemites and mafic rocks in the Bymarka ophiolite fragment, Trondheim, Norway: petrogenesis and tectonic implications. *Norwegian Journal of Geology*, 83, 167-185.
- SLAGSTAD, T., ROBERTS, N. M., MARKER, M., RØHR, T. S. & SCHIELLERUP, H. 2013. A non-collisional, accretionary Sveconorwegian orogen. *Terra Nova*, 25, 30-37.
- SLÁMA, J., KOŠLER, J., CONDON, D. J., CROWLEY, J. L., GERDES, A., HANCHAR, J. M., HORSTWOOD, M. S., MORRIS, G. A., NASDALA, L. & NORBERG, N. 2008. Plešovice zircon—a new natural reference material for U–Pb and Hf isotopic microanalysis. *Chemical Geology*, 249, 1-35.
- STEPHENS, M., GUSTAVSON, M., RAMBERG, I. & ZACHRISSON, E. 1985. The Caledonides of central-north Scandinavia—a tectonostratigraphic overview. *The Caledonide orogen—Scandinavia and related areas*, 135-162.
- STRÖMBERG, A. G. 1961. *On the tectonics of the Caledonides in the south-western part of the county of Jämtland, Sweden*, Almquist & Wiksells.
- SUESS, E. 1906. The Face of the Earth, vol. 2. *F. Tempsky, Vienna*.
- SUN, S.-S. & MCDONOUGH, W. F. 1989. Chemical and isotopic systematics of oceanic basalts: implications for mantle composition and processes. *Geological Society, London, Special Publications*, 42, 313-345.
- SVERJENSKY, D. A. 1984. Europium redox equilibria in aqueous solution. *Earth and Planetary Science Letters*, 67, 70-78.
- TORSVIK, T., SMETHURST, M., MEERT, J. G., VAN DER VOO, R., MCKERROW, W., BRASIER, M., STURT, B. & WALDERHAUG, H. 1996. Continental break-up and collision in the Neoproterozoic and Palaeozoic—a tale of Baltica and Laurentia. *Earth-Science Reviews*, 40, 229-258.
- TORSVIK, T. H. & COCKS, L. R. M. 2005. Norway in space and time: a centennial cavalcade. *Norwegian Journal of Geology/Norsk Geologisk Forening*, 85.
- TUCKER, R. D., ROBINSON, P., SOLLI, A., GEE, D. G., THORSNES, T., KROGH, T. E., NORDGULEN, Ø. & BICKFORD, M. 2004. Thrusting and extension in the Scandian hinterland, Norway: New U–Pb ages and tectonostratigraphic evidence. *American Journal of Science*, 304, 477-532.
- TULLIS, J. 2002. Deformation of granitic rocks: experimental studies and natural examples. *Reviews in Mineralogy and Geochemistry*, 51, 51-95.
- TÖRNEBOHM, A. 1888. Om fjällproblemet. *Geologiska Föreningen i Stockholm Förhandlingar*, 10, 328-336.
- VAN GOSEN, B. S., VERPLANCK, P. L., SEAL II, R. R., LONG, K. R. & GAMBOGI, J. 2017. Rare-earth elements. US Geological Survey.
- VERMEESCH, P. 2018. IsoplotR: A free and open toolbox for geochronology. *Geoscience Frontiers*, 9, 1479-1493.
- VERMEESCH, P. 2020. Unifying the U–Pb and Th–Pb methods: joint isochron regression and common Pb correction. *Geochronology*, 2, 119-131.
- VILLA, I. M. & HANCHAR, J. M. 2017. Age discordance and mineralogy. *American Mineralogist*, 102, 2422-2439.
- VONCKEN, J. H. L. 2016. *The rare earth elements: an introduction*, Springer.
- WALSH, E. & HACKER, B. 2004. The fate of subducted continental margins: Two-stage exhumation of the high-pressure to ultrahigh-pressure Western Gneiss Region, Norway. *Journal of metamorphic Geology*, 22, 671-687.
- WANG, C.-C., WIEST, J. D., JACOBS, J., BINGEN, B., WHITEHOUSE, M. J., ELBURG, M. A., SØRSTRAND, T. S., MIKKELSEN, L. & HESTNES, Å. 2021. Tracing the Sveconorwegian orogen into the Caledonides of West Norway: Geochronological and isotopic studies on magmatism and migmatization. *Precambrian Research*, 362, 106301.
- WANG, X., OH, C. W., PENG, P., ZHAI, M., WANG, X. & LEE, B. Y. 2020. Distribution pattern of age and geochemistry of 2.18–2.14 Ga I- and A-type granites and their implication for the tectonics of the Liao-Ji belt in the North China Craton. *Lithos*, 364, 105518.

- WARVIK, K., RINGSTAD, H. B., AUGLAND, L. E., CORFU, F. & GABRIELSEN, R. H. 2022. The Revsegg and Kvitenuit allochthons, Scandinavian Caledonides: origins and evolution in the Caledonian Wilson cycle. *Journal of the Geological Society*, 179.
- WETHERILL, G. W. 1956. Discordant uranium-lead ages, I. *Eos, Transactions American Geophysical Union*, 37, 320-326.
- WHALEN, J. B., CURRIE, K. L. & CHAPPELL, B. W. 1987. A-type granites: geochemical characteristics, discrimination and petrogenesis. *Contributions to mineralogy and petrology*, 95, 407-419.
- WHITE, W. M. 2014. *Isotope geochemistry*, John Wiley & Sons.
- WIEDENBECK, M., ALLE, P., CORFU, F., GRIFFIN, W., MEIER, M., OBERLI, F. V., QUADT, A. V., RODDICK, J. & SPIEGEL, W. 1995. Three natural zircon standards for U-Th-Pb, Lu-Hf, trace element and REE analyses. *Geostandards newsletter*, 19, 1-23.
- WILSON, J. T. 1966. Did the Atlantic close and then re-open?
- WILSON, R. W., HOUSEMAN, G. A., BUITER, S., MCCAFFREY, K. J. & DORÉ, A. G. 2019. Fifty years of the Wilson Cycle concept in plate tectonics: an overview. *Geological Society, London, Special Publications*, 470, 1-17.
- WINTER, J. 2014. Principles of igneous and metamorphic petrology (p. 739). Harlow, UK: Pearson education.
- WOLF, M. B. & LONDON, D. 1994. Apatite dissolution into peraluminous haplogranitic melts: an experimental study of solubilities and mechanisms. *Geochimica et cosmochimica acta*, 58, 4127-4145.
- WOLFF, F. C. 1979. BESKRIVELSE TIL DE BERGGRUNNSGEOLOGISKE KART TRONDHEIM OG OESTERSUND 1: 250000 (MED FARGETRYKE KART).
- WU, C., YANG, J., ROBINSON, P. T., WOODEN, J. L., MAZDAB, F. K., GAO, Y., WU, S. & CHEN, Q. 2009. Geochemistry, age and tectonic significance of granitic rocks in north Altun, northwest China. *Lithos*, 113, 423-436.
- WU, F.-Y., JAHN, B.-M., WILDE, S. A., LO, C.-H., YUI, T.-F., LIN, Q., GE, W.-C. & SUN, D.-Y. 2003. Highly fractionated I-type granites in NE China (I): geochronology and petrogenesis. *Lithos*, 66, 241-273.
- YOMEUN, B. S., WANG, W., TCHOUANKOUE, J. P., KAMANI, M. S. K., NDONFACK, K. I. A., HUANG, S.-F., BASUA, E. A. A., LU, G.-M. & XUE, E.-K. 2022. Petrogenesis and tectonic implication of Neoproterozoic I-type granitoids and orthogneisses in the Goa-Mandja area, Central African Fold Belt (Cameroon). *Lithos*, 420, 106700.
- ZHAO, T.-P. & ZHOU, M.-F. 2009. Geochemical constraints on the tectonic setting of Paleoproterozoic A-type granites in the southern margin of the North China Craton. *Journal of Asian Earth Sciences*, 36, 183-195.
- AHALL, K.-I., CONNELLY, J. N. & BREWER, T. S. 2000. Episodic rapakivi magmatism due to distal orogenesis?: Correlation of 1.69–1.50 Ga orogenic and inboard, "anorogenic" events in the Baltic Shield. *Geology*, 28, 823-826.

Appendices

Appendix A – Observations points/field localities

EUREF89 Zone 32				EUREF89 Zone 32				EUREF89 Zone 32			
Locality	E	N	Rock	Locality	E	N	Rock	Locality	E	N	Rock
mu001	648020,323	6943816,51	Quart	mu065	653874,129	6951588,01	Un	mu138	657521,956	6952432,99	QS
mu002	653531,768	6950439,43	QS	mu066	653844,449	6951621,72	Un	mu139	657540,733	6952016,82	QS
mu075	653672,822	6950820,94	Un	mu067	653852,567	6951501,33	Un	mu140	657697,223	6951999,41	QS
mu044	653839,023	6951150,46	Un	mu068	653767,774	6951471,07	Do	mu141	657793,695	6951914,67	QS
mu003	653738,371	6951957,05	Un	mu069	653754,015	6951475,10	FM	mu141	657899,262	6951883,72	QS
mu005	653738,195	6952030,91	QS	mu070	653802,836	6951419,77	My	mu142	658085,418	6951950,49	QS
mu045	653712,338	6952355,84	DQS	mu071	653812,951	6951286,01	Do	mu143	658086,510	6952017,42	QS
mu006	653462,445	6953430,62	Un	mu072	653856,199	6951269,60	Un	mu144	658047,738	6952205,81	QS
mu007	653600,936	6954142,13	QS	mu073	653887,744	6951232,96	Un	mu145	657992,712	6952296,43	DQS
mu008	653463,349	6953587,98	QS	mu074	653798,657	6951212,24	Do	mu146	657994,465	6952396,78	DQS
mu009	653452,740	6953608,63	QS	mu076	653616,914	6950697,43	Un	mu147	658009,564	6952597,81	QS
mu010	653498,152	6953960,60	My	mu077	653506,136	6950511,67	Un	mu148	658017,923	6952630,44	DQS
mu011	653579,041	6953882,56	QS	mu079	653346,081	6949940,06	Un	mu149	658041,727	6952693,29	QS
mu012	653707,083	6954019,68	QS	mu080	653203,919	6949855,43	My	mu150	657474,765	6952643,95	QS
mu013	653750,425	6954194,52	QS	mu081	653124,552	6949840,93	Un	mu151	657559,749	6952467,35	QS
mu014	653818,890	6954329,96	QS	mu082	653086,735	6949790,20	Un	mu152	657551,874	6952411,33	DQS
mu015	653837,847	6954354,39	QS	mu083	653032,381	6949703,23	Un	mu152	657132,733	6952481,97	DQS
mu016	653849,287	6954393,57	QS	mu084	652853,391	6949740,50	Un	mu153	656978,177	6952498,68	QS
mu017	653779,512	6954463,23	QS	mu085	652684,066	6950002,27	Un	JJ29	656898,412	6952559,89	Gr
mu018	653677,803	6954444,34	QS	mu086	652417,784	6950078,99	Un	mu155	656947,409	6952836,00	QS
mu019	653637,752	6954184,16	QS	mu087	652424,068	6950182,94	Un	mu156	656923,772	6952868,20	QS
mu020	653694,396	6954126,95	My	mu087	652497,779	6950639,14	Un	mu157	656872,261	6952923,23	QS
mu022	653685,961	6950764,44	QS	mu088	652710,474	6950712,06	QS	mu158	656827,836	6953168,91	QS
mu021	653735,561	6950910,37	QS	mu089	652775,899	6950477,67	Un	mu159	656828,203	6953189,85	QS
mu023	653523,278	6950566,15	QS	mu090	653011,365	6950550,15	Un	mu160	656757,069	6953232,11	QS
mu024	653533,980	6950577,84	My	mu093	653144,105	6950561,38	QS	mu161	656690,385	6953282,03	QS
mu025	653744,980	6950859,00	My	mu094	653224,729	6950541,92	QS	mu162	656541,341	6953413,74	Un
mu026	653744,671	6950988,48	Un	mu095	653370,354	6950530,63	QS	mu163	656478,877	6953448,95	QS
mu026	653812,610	6951115,44	QS	mu096	653422,814	6950450,75	QS	mu164	656385,085	6953487,14	QS
mu026	653520,299	6952866,17	Un	mu097	653368,584	6950363,67	Un	mu165	656275,478	6953476,07	QS
mu027	653467,387	6953117,31	My	mu098	653338,756	6950125,86	Un	mu166	656188,566	6953389,16	My
mu028	653425,398	6953347,97	My	mu099	653243,873	6949994,27	QS	mu167	656255,954	6953344,66	QS
mu029	653346,956	6953785,14	QS	mu100	653152,210	6950017,65	Un	mu168	656365,788	6953251,22	QS
mu030	653529,684	6954003,43	QS	mu101	652965,044	6950036,50	Un	mu169	656347,057	6953189,43	My
mu031	653576,384	6954023,89	QS	mu102	653584,192	6950133,06	My	mu170	656592,390	6953008,69	QS
mu032	653900,959	6954632,15	DQS	mu103	653622,731	6950160,90	Un	mu171	656726,012	6952828,75	QS
mu033	653964,110	6954740,28	QS	mu104	653714,949	6950449,97	Un	mu172	656777,871	6952239,92	QS
mu034	654020,493	6954928,59	QS	mu105	653900,863	6950491,00	Un	mu174	656860,583	6952057,09	My
mu035	654101,944	6954976,00	My	mu106	653752,144	6950724,65	Un	mu175	656982,288	6951874,69	QS
mu036	653876,515	6954652,53	QS	mu107	653701,384	6950829,74	Un	mu176	657051,560	6951921,16	QS
mu037	653885,155	6954619,80	DQS	mu108	653661,134	6950769,65	FS	mu177	656730,251	6952144,32	My
mu038	653876,277	6954578,74	DQS	mu109	653569,084	6950711,96	Un	mu178	653686,289	6950795,84	Un
mu039	653476,491	6953027,67	My	mu110	653497,936	6950685,17	QS	mu179	653827,425	6950853,19	My
mu040	653576,061	6952771,74	QS	mu111	653425,029	6950681,48	Un	mu180	653955,581	6951126,06	Un
mu041	653778,961	6952070,26	Un	mu112	653309,457	6950727,45	Un	mu182	653593,734	6951971,75	MA
mu042	653764,108	6951940,60	Un	mu113	653286,419	6950739,43	QS	mu183	653791,558	6952250,57	DQS
mu043	653850,436	6951398,07	Un	mu114	653488,049	6949845,89	QS	mu184	653684,815	6952564,17	DQS
mu181	653777,741	6951710,29	Do	mu115	653463,303	6949781,77	DQS	mu185	653684,991	6952587,21	QS
mu046	653687,248	6952338,27	Un	mu116	653380,567	6949716,46	DQS	mu186	653557,347	6952640,41	My
mu047	653718,652	6952312,33	QS	mu117	653337,470	6949652,35	DQS	mu187	653440,679	6953317,67	Un
mu048	653721,280	6952250,70	Un	mu118	653199,011	6949615,63	QS	mu188	653420,057	6953354,75	Un
mu049	653858,513	6952096,45	Un	mu119	653108,369	6949571,42	QS	mu189	653341,552	6953431,20	QS
mu050	654193,890	6952130,60	QS	mu120	653294,577	6949551,41	QS	mu190	653291,849	6953525,12	QS
mu051	654201,843	6952151,36	DQS	mu121	648851,071	6948596,16	K	mu191	653214,942	6953746,84	QS
mu052	653794,744	6952107,36	Un	mu122	648903,386	6948381,62	QS	mu192	653205,870	6953798,31	Un
mu053	653774,427	6951991,77	Un	mu123	657322,361	6950369,84	DQS	mu193	653240,676	6953860,83	QS
mu054	653752,038	6951926,45	Do	mu124	657356,506	6950363,85	DQS	mu194	653148,301	6953959,71	QS
mu055	653742,567	6951909,07	Un	mu128	656631,059	6952344,75	QS	mu195	653140,448	6954061,42	QS
mu056	653786,202	6951862,28	Un	mu129	656636,018	6952352,77	My	mu196	653283,434	6954060,05	Un
mu057	653739,669	6951744,90	Un	mu130	656675,524	6952388,00	QS	mu197	653515,942	6952922,68	My
mu058	653775,296	6951729,12	Do	mu131	656743,576	6952371,80	QS	mu198	653611,488	6952525,55	Un
mu059	653821,245	6951701,67	Un	mu132	656812,497	6952393,44	QS	mu199	653654,473	6952419,36	QS
mu060	653875,828	6951707,11	Un	mu133	656896,829	6952372,16	QS	mu200	653715,544	6952332,93	Un
mu061	654016,074	6951657,01	QS	mu134	657119,832	6952391,88	QS	mu201	653761,299	6951761,30	Do
mu062	654053,257	6951655,60	QS	mu135	657175,201	6952366,55	QS	mu202	653629,528	6950653,17	Un
mu063	654069,562	6951663,70	QS	mu136	657310,350	6952439,21	My	mu125	679123,126	6933529,11	TQS
mu064	654028,356	6951538,39	QS	mu137	657344,673	6952427,79	QS	mu126	679193,521	6933537,12	TQS

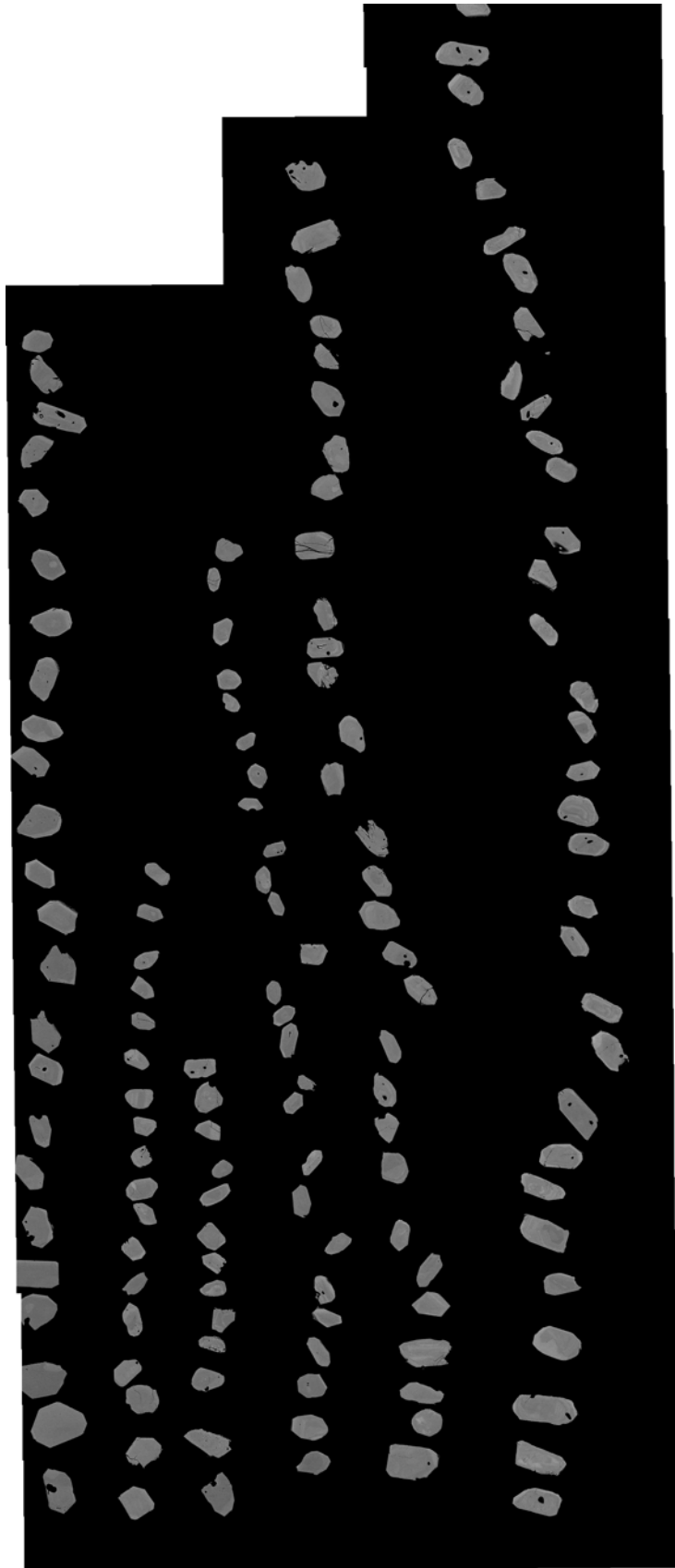
QS-quartz striped K-feldspar augen gneiss, Un-unstriped augen gneiss with fine-grained matrix, DQS-strongly quartz striped K-feldspar augen gneiss, TQS-Tännäs augen gneiss, My-mylonite, Gr-granite (intrusion), FS-fine-grained and muscovite-rich rock, Ma-meta-arkose, K-cataclastite (not in the field area), Quart-quartzite (not in the field area)

Appendix B – Geochronology

Sample	Pb207/Pb206 age	2SE	Pb206/U238 age	2SE	Pb207/U235	2SE	Pb206/U238	2SE	ρ 206Pb/238U v 207Pb/235U	U/Th
BB20_20										
BB20_20-1	1664,1	15,5	1665,7	40,2	4,1499	0,1264	0,2951	0,0081	-0,0267	0,7186
BB20_20-2	1642,2	45,2	1699,9	104,5	4,2674	0,3368	0,3046	0,0216	-0,0688	0,8381
BB20_20-3	1652,8	12,8	1628,0	41,4	4,0123	0,1256	0,2874	0,0083	0,0154	0,6959
BB20_20-4	1656,8	22,3	1665,1	57,0	4,1110	0,1675	0,2946	0,0113	-0,0115	0,5552
BB20_20-5	1655,7	14,3	1648,5	40,3	4,0891	0,1233	0,2916	0,0081	0,0243	0,5066
BB20_20-6	1660,6	20,4	1692,7	48,7	4,2028	0,1465	0,3000	0,0096	0,0428	0,7594
BB20_20-7	1645,4	10,9	1656,6	37,7	4,0702	0,1159	0,2931	0,0076	0,0653	1,3998
BB20_20-8	1848,8	23,4	1272,3	34,4	3,3918	0,1189	0,2183	0,0065	-0,1011	1,2563
BB20_20-9	1650,7	14,4	1715,1	46,6	4,2530	0,1433	0,3045	0,0092	-0,1023	0,9397
BB20_20-10	1657,6	16,7	1653,0	43,6	4,1023	0,1325	0,2927	0,0088	0,1606	0,7544
BB20_20-11	1661,2	10,8	1668,8	39,6	4,1618	0,1224	0,2956	0,0080	0,0533	0,6000
BB20_20-12	1651,5	11,5	1631,8	37,6	4,0362	0,1170	0,2882	0,0075	-0,0335	0,4908
BB20_20-13	1660,0	14,0	1661,7	40,3	4,1456	0,1257	0,2943	0,0081	0,0405	0,7645
BB20_20-14	1651,9	13,3	1661,5	39,7	4,1340	0,1247	0,2942	0,0080	0,0068	1,4789
BB20_20-15	1656,1	8,3	1661,4	38,0	4,1413	0,1183	0,2941	0,0076	-0,0474	2,2005
BB20_20-16	1653,2	11,4	1596,9	37,1	3,9456	0,1131	0,2812	0,0074	0,1238	2,1542
BB20_20-17	1662,6	9,8	1643,5	38,1	4,1071	0,1177	0,2905	0,0076	0,0893	0,8599
BB20_20-18	1654,9	10,3	1656,0	39,5	4,1333	0,1228	0,2931	0,0079	0,0305	0,5705
BB20_19										
BB20_19-1	1654,8	6,1	1634,6	35,9	4,0611	0,1103	0,2887	0,0072	0,1222	0,6371
BB20_19-2	1650,6	6,9	1635,5	36,3	4,0521	0,1117	0,2889	0,0073	-0,0505	0,8523
BB20_19-3	1651,8	6,2	1651,8	36,6	4,1023	0,1133	0,2921	0,0074	-0,0357	0,7422
BB20_19-4	1655,2	14,0	1677,3	48,9	4,1782	0,1501	0,2974	0,0098	-0,0079	1,4789
BB20_19-5	1634,0	8,6	1630,5	36,3	4,0058	0,1118	0,2879	0,0072	-0,0945	1,4291
BB20_19-6	1648,2	7,5	1652,4	36,7	4,0957	0,1137	0,2923	0,0074	0,0091	0,8848
BB20_19-7	1649,5	7,7	1651,5	36,4	4,0890	0,1123	0,2921	0,0073	0,0646	1,5956
BB20_19-8	1639,8	8,4	1656,8	38,3	4,0707	0,1160	0,2928	0,0074	-0,2859	1,2753
BB20_19-9	1651,7	6,0	1649,7	36,5	4,0692	0,1110	0,2917	0,0073	0,0911	1,1819
BB20_19-10	1655,7	5,8	1642,8	36,4	4,0529	0,1109	0,2903	0,0073	0,0589	0,9132
BB20_19-11	1653,0	10,1	1657,7	38,1	4,1026	0,1185	0,2933	0,0077	0,0680	0,8232
BB20_19-12	1649,0	6,3	1648,8	36,3	4,0629	0,1108	0,2915	0,0073	0,0545	1,3392
BB20_19-13	1642,6	12,7	1695,9	40,3	4,1884	0,1223	0,3011	0,0081	0,2071	1,0746
BB20_19-14	1645,8	6,7	1517,7	34,0	3,6890	0,1008	0,2655	0,0067	0,0647	2,1807
BB20_19-15	1652,0	9,8	1624,8	38,0	4,0047	0,1151	0,2868	0,0076	0,0613	1,0905
BB20_19-16	1646,5	9,2	1616,5	37,0	3,9775	0,1125	0,2851	0,0074	0,0787	1,1059
JJ29										
JJ29-1	1667,0	9,8	1587,2	36,3	3,9393	0,1129	0,2793	0,0072	0,0360	1,5552
JJ29-2	1644,3	7,5	1587,4	35,5	3,8900	0,1075	0,2793	0,0070	0,0082	0,8818
JJ29-3	1645,6	6,7	1554,0	35,1	3,8031	0,1061	0,2727	0,0069	-0,0782	1,2858
JJ29-4	1489,6	11,1	975,1	30,1	2,0941	0,0728	0,1633	0,0054	0,1226	4,8086
JJ29-5	1642,3	5,8	1528,2	34,8	3,7220	0,1043	0,2676	0,0069	-0,0552	1,3348
JJ29-6	1654,8	7,4	1770,1	39,5	4,4327	0,1241	0,3161	0,0081	0,0466	1,0106
JJ29-7	1657,2	6,0	1652,4	36,7	4,1301	0,1139	0,2922	0,0074	-0,0410	0,3542
JJ29-8	1657,4	8,6	1683,1	38,3	4,2201	0,1200	0,2984	0,0077	-0,0047	0,8479
JJ29-9	1685,8	13,4	1640,9	39,4	4,1689	0,1260	0,2899	0,0079	-0,0345	0,7851
JJ29-10	1692,9	8,8	1634,5	36,6	4,1596	0,1154	0,2887	0,0073	0,0955	0,8823
JJ29-11	1651,1	8,2	1634,2	37,7	4,0715	0,1167	0,2886	0,0075	0,0746	1,2728
JJ29-12	1670,8	7,1	1423,8	36,2	3,5198	0,1074	0,2472	0,0070	0,0310	0,5487
JJ29-13	1654,9	6,5	1618,9	36,8	4,0235	0,1126	0,2856	0,0073	0,0737	1,1301
JJ29-14	1714,6	14,3	1570,6	42,3	4,0112	0,1347	0,2760	0,0083	-0,1312	0,9750
JJ29-15	1655,2	7,0	1631,6	36,7	4,0539	0,1130	0,2881	0,0073	0,0821	0,9113
JJ29-16	1657,5	10,1	1598,3	37,5	3,9724	0,1188	0,2814	0,0075	-0,3356	0,9672

Sample	Pb207/Pb206 age	2SE	Pb206/U238 age	2SE	Pb207/U235	2SE	Pb206/U238	2SE	rho 206Pb/238U v 207Pb/235U	U/Th
JJ23										
JJ23-1	1655,2	10,9	1652,4	38,0	4,1073	0,1172	0,2923	0,0076	0,0895	0,9283
JJ23-2	1653,4	7,0	1628,5	35,9	4,0304	0,1105	0,2875	0,0072	-0,0557	0,8817
JJ23-3	1646,7	12,2	1643,4	38,5	4,0600	0,1190	0,2905	0,0077	0,0432	0,6651
JJ23-4	1659,0	8,8	1656,7	37,6	4,1147	0,1159	0,2932	0,0075	0,0278	0,7662
JJ23-5	1657,4	10,1	1612,9	38,7	3,9794	0,1168	0,2844	0,0077	0,1472	0,5640
JJ23-6	1659,8	11,0	1682,0	38,3	4,1752	0,1202	0,2982	0,0077	-0,0264	0,8603
JJ23-7	1652,7	10,6	1712,1	38,8	4,2539	0,1207	0,3043	0,0078	0,0861	0,6306
JJ23-8	1655,9	8,2	1657,7	37,7	4,1056	0,1161	0,2934	0,0076	0,0125	0,9111
JJ23-9	1661,9	5,6	1646,3	36,5	4,0888	0,1113	0,2910	0,0073	0,0019	0,4488
JJ23-10	1655,6	9,8	1645,1	37,4	4,0652	0,1158	0,2908	0,0075	0,0522	0,5408
JJ23-11	1647,6	12,7	1663,9	39,3	4,1104	0,1226	0,2946	0,0079	-0,1046	0,6778
JJ23-12	1655,2	8,2	1625,7	37,1	4,0249	0,1135	0,2869	0,0074	0,0598	0,5185
JJ23-13	1663,0	9,8	1635,5	36,9	4,0612	0,1130	0,2889	0,0074	0,1314	0,7049
JJ23-14	1657,5	7,8	1647,8	36,8	4,0912	0,1140	0,2914	0,0074	-0,0687	0,9546
JJ23-15	1656,8	9,4	1656,3	37,9	4,1136	0,1177	0,2931	0,0076	-0,0450	0,9493
JJ23-16	1665,7	5,6	1634,7	36,4	4,0861	0,1124	0,2887	0,0073	0,0634	0,9042
JJ23-17	1663,7	7,5	1670,1	37,7	4,1832	0,1173	0,2958	0,0076	0,0035	0,3774
JJ23-18	1667,5	8,2	1640,9	37,7	4,1149	0,1172	0,2900	0,0075	-0,0060	0,8527
MU126										
MU126-1	1647,0	7,9	1628,0	36,5	4,0224	0,1117	0,2874	0,0073	-0,0438	0,8493
MU126-2	1645,2	9,2	1635,8	37,6	4,0360	0,1162	0,2889	0,0075	0,0198	1,0781
MU126-3	1656,9	9,9	1640,1	36,7	4,0869	0,1127	0,2898	0,0074	0,2489	1,1549
MU126-4	1643,1	9,0	1634,2	39,3	4,0376	0,1190	0,2886	0,0079	0,0994	1,1714
MU126-5	1652,4	6,6	1627,5	36,1	4,0430	0,1105	0,2873	0,0072	0,1543	0,8703
MU126-6	1646,9	8,0	1631,0	35,8	4,0494	0,1113	0,2880	0,0072	-0,0151	1,0477
MU126-7	1655,2	7,6	1650,9	36,9	4,1067	0,1134	0,2920	0,0074	0,1421	0,9116
MU126-8	1650,7	7,1	1637,9	36,5	4,0550	0,1121	0,2894	0,0073	0,0217	2,6952
MU126-9	1657,1	9,0	1674,0	37,6	4,1630	0,1166	0,2966	0,0076	0,0478	1,4433
MU126-10	1646,2	7,2	1625,2	36,1	3,9912	0,1109	0,2868	0,0072	-0,1663	1,6767
MU126-11	1653,5	6,6	1675,1	37,7	4,1404	0,1153	0,2968	0,0076	0,0631	1,2160
MU126-12	1641,8	12,8	1675,4	41,1	4,1202	0,1264	0,2971	0,0083	0,0523	0,6713
MU126-13	1652,5	6,0	1608,4	35,8	3,9765	0,1092	0,2835	0,0071	0,0408	1,0754
MU126-14	1657,4	9,7	1656,7	37,3	4,1187	0,1144	0,2931	0,0075	0,1706	1,4856
MU126-15	1644,8	8,7	1647,0	37,9	4,0708	0,1134	0,2908	0,0073	0,0593	1,2992
MU126-16	1656,3	10,5	1644,4	37,3	4,0942	0,1171	0,2907	0,0075	-0,1107	1,1282
MU126-17	1654,6	9,0	1630,1	37,2	4,0483	0,1154	0,2878	0,0074	-0,0618	1,4338
MU126-18	1653,9	8,3	1642,5	37,2	4,0797	0,1163	0,2903	0,0075	-0,1982	1,3603
MU021										
MU021-1	1658,4	5,7	1625,5	38,3	4,0344	0,1164	0,2869	0,0076	0,0169	1,0199
MU021-2	1638,1	20,8	1676,4	49,2	4,1472	0,1527	0,2973	0,0099	0,0279	1,0357
MU021-3	1659,0	7,5	1628,9	38,0	4,0472	0,1165	0,2876	0,0076	0,0112	1,0819
MU021-4	1654,0	8,0	1646,4	36,5	4,0941	0,1129	0,2911	0,0073	-0,0122	1,1669
MU021-5	1656,6	6,7	1648,0	37,7	4,0907	0,1124	0,2910	0,0073	0,0995	1,2988
MU021-6	1718,6	10,9	1641,2	39,7	4,1899	0,1283	0,2900	0,0079	-0,2452	1,0679
MU021-7	1645,4	11,7	1640,1	37,6	4,0283	0,1171	0,2898	0,0075	-0,1352	1,3146
MU021-8	1700,4	10,5	1610,9	44,1	4,0554	0,1325	0,2840	0,0088	0,1701	1,3918
MU021-9	1666,8	11,8	1687,6	39,0	4,2080	0,1214	0,2993	0,0079	0,0707	1,4127
MU021-10	1658,5	14,9	1688,6	38,0	4,1920	0,1194	0,2995	0,0077	0,1518	0,9573
MU021-11	1660,5	6,9	1626,5	41,0	4,0133	0,1252	0,2871	0,0082	-0,2553	1,0703
MU021-12	1700,6	20,4	1801,4	48,0	4,6106	0,1564	0,3225	0,0098	0,0483	1,3622
MU021-13	1658,8	6,8	1655,9	36,4	4,0996	0,1125	0,2930	0,0073	0,0328	1,5327
MU021-14	1662,3	5,6	1685,2	37,4	4,1932	0,1156	0,2988	0,0075	-0,1189	1,0080
MU021-15	1667,4	10,3	1662,6	37,0	4,1481	0,1156	0,2943	0,0074	0,0303	2,7895
MU021-16	1656,6	7,3	1645,1	36,8	4,0914	0,1144	0,2908	0,0074	-0,0918	1,3440
MU021-17	1653,9	7,9	1662,6	36,6	4,1297	0,1127	0,2943	0,0073	0,1569	0,9856
MU021-18	1664,1	7,5	1617,9	38,7	4,0184	0,1194	0,2853	0,0077	-0,1615	1,0306

Appendix C – BSE image



Appendix D – Geochemistry (this study)

Method for the different elements and samples

NGU_ID	119103	119104	119105	119108	119109	119110	119111	119112	94551	94552	113957
Sample	MU010	MU016	MU021	MU108	MU124	MU126	MU168	JJ29	BB20_19	BB20_20	JJ23
SiO2	XRF	XRF	XRF	XRF	XRF	XRF	XRF	XRF	XRF	XRF	XRF
Al2O3	XRF	XRF	XRF	XRF	XRF	XRF	XRF	XRF	XRF	XRF	XRF
Fe2O3t	XRF	XRF	XRF	XRF	XRF	XRF	XRF	XRF	XRF	XRF	XRF
TiO2	XRF	XRF	XRF	XRF	XRF	XRF	XRF	XRF	XRF	XRF	XRF
MgO	XRF	XRF	XRF	XRF	XRF	XRF	XRF	XRF	XRF	XRF	XRF
CaO	XRF	XRF	XRF	XRF	XRF	XRF	XRF	XRF	XRF	XRF	XRF
Na2O	XRF	XRF	XRF	XRF	XRF	XRF	XRF	XRF	XRF	XRF	XRF
K2O	XRF	XRF	XRF	XRF	XRF	XRF	XRF	XRF	XRF	XRF	XRF
MnO	XRF	XRF	XRF	XRF	XRF	XRF	XRF	XRF	XRF	XRF	XRF
P2O5	XRF	XRF	XRF	XRF	XRF	XRF	XRF	XRF	XRF	XRF	XRF
H2O+	XRF	XRF	XRF	XRF	XRF	XRF	XRF	XRF	XRF	XRF	XRF
Co	XRF	XRF	XRF	XRF	XRF	XRF	XRF	XRF	XRF	XRF	XRF
Cr	XRF	XRF	XRF	XRF	XRF	XRF	XRF	XRF	XRF	XRF	XRF
Cu	XRF	XRF	XRF	XRF	XRF	XRF	XRF	XRF	XRF	XRF	XRF
Ga	XRF	XRF	XRF	XRF	XRF	XRF	XRF	XRF	XRF	XRF	XRF
Ni	XRF	XRF	XRF	XRF	XRF	XRF	XRF	XRF	XRF	XRF	XRF
Pb	XRF	XRF	XRF	XRF	XRF	XRF	XRF	XRF	XRF	XRF	XRF
Sc	XRF	XRF	XRF	XRF	XRF	XRF	XRF	XRF	XRF	XRF	XRF
V	XRF	XRF	XRF	XRF	XRF	XRF	XRF	XRF	XRF	XRF	XRF
Zn	XRF	XRF	XRF	XRF	XRF	XRF	XRF	XRF	XRF	XRF	XRF
Rb	ICP(borat)	ICP(borat)	ICP(borat)	ICP(borat)	ICP(borat)	ICP(borat)	ICP(borat)	ICP(borat)	LA-ICP-MS	LA-ICP-MS	XRF
Sr	ICP(borat)	ICP(borat)	ICP(borat)	ICP(borat)	ICP(borat)	ICP(borat)	ICP(borat)	ICP(borat)	LA-ICP-MS	LA-ICP-MS	XRF
Y	ICP(borat)	ICP(borat)	ICP(borat)	ICP(borat)	ICP(borat)	ICP(borat)	ICP(borat)	ICP(borat)	LA-ICP-MS	LA-ICP-MS	XRF
Zr	ICP(borat)	ICP(borat)	ICP(borat)	ICP(borat)	ICP(borat)	ICP(borat)	ICP(borat)	ICP(borat)	LA-ICP-MS	LA-ICP-MS	XRF
Nb	ICP(borat)	ICP(borat)	ICP(borat)	ICP(borat)	ICP(borat)	ICP(borat)	ICP(borat)	ICP(borat)	LA-ICP-MS	LA-ICP-MS	XRF
Sn									LA-ICP-MS	LA-ICP-MS	XRF
Cs									LA-ICP-MS	LA-ICP-MS	
Ba	ICP(borat)	ICP(borat)	ICP(borat)	ICP(borat)	ICP(borat)	ICP(borat)	ICP(borat)	ICP(borat)	LA-ICP-MS	LA-ICP-MS	XRF
La	ICP(HNO3)	ICP(HNO3)	ICP(HNO3)	ICP(HNO3)	ICP(HNO3)	ICP(HNO3)	ICP(HNO3)	ICP(HNO3)	LA-ICP-MS	LA-ICP-MS	XRF
Ce	ICP(HNO3)	ICP(HNO3)	ICP(HNO3)	ICP(HNO3)	ICP(HNO3)	ICP(HNO3)	ICP(HNO3)	ICP(HNO3)	LA-ICP-MS	LA-ICP-MS	XRF
Pr	ICP(HNO3)	ICP(HNO3)	ICP(HNO3)	ICP(HNO3)	ICP(HNO3)	ICP(HNO3)	ICP(HNO3)	ICP(HNO3)	LA-ICP-MS	LA-ICP-MS	XRF
Nd	ICP(HNO3)	ICP(HNO3)	ICP(HNO3)	ICP(HNO3)	ICP(HNO3)	ICP(HNO3)	ICP(HNO3)	ICP(HNO3)	LA-ICP-MS	LA-ICP-MS	XRF
Sm	ICP(HNO3)	ICP(HNO3)	ICP(HNO3)	ICP(HNO3)	ICP(HNO3)	ICP(HNO3)	ICP(HNO3)	ICP(HNO3)	LA-ICP-MS	LA-ICP-MS	
Eu	ICP(HNO3)	ICP(HNO3)	ICP(HNO3)	ICP(HNO3)	ICP(HNO3)	ICP(HNO3)	ICP(HNO3)	ICP(HNO3)	LA-ICP-MS	LA-ICP-MS	
Gd	ICP(HNO3)	ICP(HNO3)	ICP(HNO3)	ICP(HNO3)	ICP(HNO3)	ICP(HNO3)	ICP(HNO3)	ICP(HNO3)	LA-ICP-MS	LA-ICP-MS	
Tb	ICP(HNO3)	ICP(HNO3)	ICP(HNO3)	ICP(HNO3)	ICP(HNO3)	ICP(HNO3)	ICP(HNO3)	ICP(HNO3)	LA-ICP-MS	LA-ICP-MS	
Dy	ICP(HNO3)	ICP(HNO3)	ICP(HNO3)	ICP(HNO3)	ICP(HNO3)	ICP(HNO3)	ICP(HNO3)	ICP(HNO3)	LA-ICP-MS	LA-ICP-MS	
Ho	ICP(HNO3)	ICP(HNO3)	ICP(HNO3)	ICP(HNO3)	ICP(HNO3)	ICP(HNO3)	ICP(HNO3)	ICP(HNO3)	LA-ICP-MS	LA-ICP-MS	
Er	ICP(HNO3)	ICP(HNO3)	ICP(HNO3)	ICP(HNO3)	ICP(HNO3)	ICP(HNO3)	ICP(HNO3)	ICP(HNO3)	LA-ICP-MS	LA-ICP-MS	
Tm	ICP(borat)	ICP(borat)	ICP(borat)	ICP(borat)	ICP(borat)	ICP(borat)	ICP(borat)	ICP(borat)	LA-ICP-MS	LA-ICP-MS	
Yb	ICP(borat)	ICP(borat)	ICP(borat)	ICP(borat)	ICP(borat)	ICP(borat)	ICP(borat)	ICP(borat)	LA-ICP-MS	LA-ICP-MS	
Lu	ICP(HNO3)	ICP(HNO3)	ICP(HNO3)	ICP(HNO3)	ICP(HNO3)	ICP(HNO3)	ICP(HNO3)	ICP(HNO3)	LA-ICP-MS	LA-ICP-MS	
Hf	ICP(borat)	ICP(borat)	ICP(borat)	ICP(borat)	ICP(borat)	ICP(borat)	ICP(borat)	ICP(borat)	LA-ICP-MS	LA-ICP-MS	XRF
Ta									LA-ICP-MS	LA-ICP-MS	XRF
W									LA-ICP-MS	LA-ICP-MS	XRF
Bi									LA-ICP-MS	LA-ICP-MS	XRF
Th	ICP(borat)	ICP(borat)	ICP(borat)	ICP(borat)	ICP(borat)	ICP(borat)	ICP(borat)	ICP(borat)	LA-ICP-MS	LA-ICP-MS	XRF
U									LA-ICP-MS	LA-ICP-MS	XRF

NGU_ID	Sample	SiO2	Al2O3	Fe2O3r	TiO2	MgO	CaO	Na2O	K2O	MnO	P2O5	H2O+	Co	Cr	Cu
119103	MU010	68,1	13,8	4,30	0,655	1,61	2,08	2,75	4,46	0,079	0,188	1,130	8,4	18,3	12,1
119104	MU016	67,4	14,3	4,39	0,611	1,21	2,77	2,92	4,12	0,094	0,175	1,160	6,5	16,5	8,3
119105	MU021	69,5	13,1	4,45	0,620	1,28	1,60	3,38	4,03	0,079	0,185	0,964	8,1	26,1	5,2
119108	MU108	69,7	13,9	3,95	0,583	0,49	0,13	1,64	7,42	0,021	0,082	1,070	6,2	24,1	<5
119109	MU124	67,1	14,4	4,20	0,627	1,73	2,09	2,12	5,26	0,090	0,178	1,330	9,4	19,2	21,6
119110	MU126	66,8	14,7	4,16	0,601	1,24	2,01	3,99	4,47	0,102	0,188	0,874	8,3	37,0	18
119111	MU168	67,6	14,4	4,02	0,614	1,41	1,98	2,87	4,68	0,086	0,174	1,270	5,7	23,3	6,4
119112	JJ29	77,4	11,1	0,94	0,094	0,19	1,47	3,59	3,50	0,038	0,014	1,030	<4	19,1	<5
94551	BR20_19	66,6	14,4	4,45	0,710	1,57	2,30	3,06	4,27	0,073	0,197	1,110	11,1	19,1	23,3
94552	BR20_20	69,3	13,9	3,42	0,680	0,84	1,56	3,99	5,14	0,094	0,187	0,395	<4	26,1	<5
113957	JJ23	68,5	14,3	3	0,414	1,45	1,62	2,8	5,72	0,07	0,172	1,02	<30	<50	<20

	Ga	Ni	Pb	Sc	V	Zn	Be	Rb	Sr	Y	Zr	Nb	Sn	Cs	Ba	La	Ce	Pr	Nd
16,5	14,2	30,7	8,4	64,1	71,6	145	228	26,0	232	14,3	1080	47,6	94,8	11,1	36,5				
17,8	12,8	18,1	9,7	67,4	54,9	116	270	25,3	208	11,9	888	33,2	73,5	9,03	30,1				
16,0	12,4	18,1	7,8	61,0	67,6	148	170	19,0	275	10,9	1190	31,6	68,7	7,45	24,4				
13,9	11,8	15,0	7,8	68,0	16,1	169	73,2	22,2	182	14,7	1350	23,5	57,1	5,47	16,7				
17,3	14,2	27,6	9	61,6	66,0	165	205	32,9	238	14,9	1000	44,9	94,2	10,5	33,7				
17,3	13,6	16,5	6,9	63,4	80,2	106	243	26,9	246	10,5	1080	38,3	79,3	9,23	30,3				
11,2	12,8	13,7	9,8	58,0	61,5	171	222	32,0	212	15,7	896	30,7	64,3	7,11	25,3				
17,0	5,5	14,8	<5	8,7	7,1	63,3	111	14,0	62,8	10,5	345	13,3	25,4	2,62	7,58				
17,4	13,3	15,0	10,7	76,3	57,0	183	241	31,0	308	14,5	2,600	7,10	86,5	45,0	94				
18,7	6,9	28,0	8,4	31,3	65,7	181	184	70,7	537	31,3	3,800	2,99	820	86,2	195				
<20	<50	6,2	37	168	245	249	9,9	<5	1020	18	32	18	21,6	83,7					

Sn	Cs	Ba	La	Ce	Pr	Nd	Sm	Eu	Gd	Tb	Dy	Ho	Er	Tm	Yb	Lu	Hf	Ta	W	Bi	Th	U
1080		47,6	94,8	11,1	36,5	7,70	1,67	7,18	1,06	3,31	1,06	3,19	0,428	2,61	0,352	7,17					11,6	
888		33,2	73,5	9,03	30,1	6,19	1,45	5,67	0,883	2,81	0,883	2,74	0,341	2,23	0,321	6,29					10,7	
1190		31,6	68,7	7,45	24,4	4,81	1,17	4,46	0,636	1,92	0,597	1,84	0,245	1,60	0,235	8,21					12,1	
1350		23,5	57,1	5,47	16,7	3,75	0,825	3,54	0,537	1,59	0,457	1,36	< 0,2	1,27	< 0,2	5,71					12,4	
1000		44,9	94,2	10,5	33,7	7,16	1,30	6,72	0,990	3,19	1,02	3,25	0,421	2,72	0,372	7,29					19,3	
1080		38,3	79,3	9,23	30,3	6,43	1,65	5,91	0,862	2,80	0,862	2,53	0,341	2,17	0,301	6,61					7,43	
896		30,7	64,3	7,11	25,3	6,01	1,41	5,73	0,972	3,22	1,06	3,18	0,432	2,70	0,373	6,77					16,8	
345		13,3	25,4	2,62	7,58	1,59	0,330	1,74	0,310	1,14	0,380	1,32	0,220	1,55	0,250	2,36					28,7	
2,600	7,10	865	45,0	94	10,6	45,1	1,57	5,67	0,956	5,21	1,100	3,00	0,434	2,82	0,442	7,65		0,837	0,82	0,220	10,0	3,18
3,800	2,99	820	86,2	195	21,6	83,7	1,99	11,60	1,930	11,60	2,530	7,00	1,150	7,66	1,170	12,60		1,810	0,38	0,110	18,4	3,75
18	32		18										<5		19,7	6,1		13,2				

Appendix E – Geochemistry from Bjerkan (2020)

Sample	SiO2	Al2O3	Fe2O3t	TiO2	MgO	CaO	Na2O	K2O	MnO	P2O5	H2O+	Co	Cr	Cu
197551	70,3	14,95	3,32	0,39	1,14	2,42	3,82	3,92	0,08	0,14	0,36		10	
197556	70,2	13,6	3,8	0,43	0,39	1,38	3,49	5,42	0,1	0,1	0,29		10	
197569	67,1	14,45	4,83	0,77	1,21	2,62	3,6	4,33	0,11	0,26	0,72		10	
197590	68,1	15,25	3,72	0,42	1,16	2,65	4,08	3,61	0,09	0,16	0,41		20	
200962	70,1	15,7	2,54	0,27	0,84	2,53	4,54	3,78	0,07	0,12	0,45		10	
200963	65,6	12,55	5,21	0,57	1,88	8,28	3,01	0,43	0,08	0,13	1,52		70	
200965	68,5	14,5	4,4	0,55	1,31	2,59	4,25	3,17	0,12	0,19	0,67		10	
200966	72,6	14,4	1,87	0,32	0,38	1	3,43	6,18	0,04	0,08	0,65		10	
200981	68,1	15,3	3,79	0,7	1,05	2,19	3,78	5,23	0,08	0,21	0,56		10	
200985	62,3	15	6,63	0,84	4,4	4,98	2,26	2,6	0,08	0,17	1,5		130	
200986	70,8	14,25	3,55	0,55	1,14	1,63	3,17	5,52	0,06	0,18	0,46		20	
200992	67,7	15,55	3,28	0,44	0,49	0,98	4,53	6,03	0,1	0,08	0,29		10	
200994	68,9	14,5	4,29	0,67	1,06	2,52	3,47	4,87	0,09	0,23	0,41		10	
200996	68,3	14,55	4,13	0,61	1,13	2,29	3,43	4,87	0,08	0,23	0,6		10	
201000	73,6	13,85	1,56	0,15	0,53	1,14	3,89	4,4	0,04	0,04	0,34		<10	
127866M	64,2	15,15	5,41	0,57	2,59	4,26	3,09	2,77	0,1	0,18	0,81		130	
127868M	62,1	16,95	6,01	0,66	2,71	4,96	3,7	3,21	0,1	0,21	0,58		10	
127876M	60,8	17,85	5,93	0,76	2,17	5,07	4,02	2,77	0,12	0,26	0,62		10	
127877M	65,1	15,35	6,74	0,95	2,63	2,42	2,36	3,64	0,09	0,3	1,11		50	
127878M	69,3	14,9	3,75	0,62	0,92	2,77	3,46	3,22	0,1	0,16	0,46		<10	
127879M	65,9	14,6	6,1	0,76	2,43	3,56	2,8	3,46	0,13	0,2	0,96		60	
127882M	74,3	12,15	3,97	0,53	0,89	1,66	2,81	2,58	0,09	0,03	0,89		30	
127884M	60,3	15,55	9,3	1,19	2,28	5,81	3,3	2,19	0,24	0,25	0,52		<10	
127885M	65,4	16,75	4,98	0,59	2,09	4,84	3,54	2,19	0,1	0,17	0,68		10	
127886M	70,2	15,05	3,09	0,38	0,99	3,05	3,08	3,81	0,07	0,12	0,37		<10	
127891M	67,1	14,95	5,5	0,75	1,56	3,16	2,79	3,8	0,09	0,19	0,37		10	
127894M	56,1	16,55	7,92	0,78	4,22	5,93	3,71	2,44	0,16	0,3	0,99		70	
127895M	71,4	14,75	2,43	0,26	0,77	2,41	3,66	3,53	0,05	0,1	0,46		20	

NI	Pb	Sc	V	Rb	Sr	Y	Zr	Nb	Sn	Cs	Ba	La	Ce	Pr	Nd
37	150	307	26	233	14,3	2	5,74	931	49,4	91,7	10,35	36,4			
17	182	135	49,4	394	19,8	3	2,86	722	70,3	145	17,5	62,2			
53	143	246	39,1	392	17,7	2	4,58	950	62,4	122	14,6	55			
43	158	320	29,4	262	16,5	3	7,05	813	54,7	101	11,5	40,5			
27	114,5	772	12,4	150	9,9	1	2,88	1150	37,6	68,2	7,81	28,3			
67	21,6	617	27,8	317	13,7	2	0,63	255	33,1	68,3	8,48	32,4			
51	154	176,5	45,1	263	29,8	4	5,84	417	32,8	80,9	8,56	31,9			
18	165,5	189	20	245	20,2	2	2,15	653	33,3	76,1	6,31	20,2			
46	129,5	357	55,3	415	24,9	3	3,07	1530	73,9	169	21	79,3			
142	84,6	230	26,7	224	11,7	2	5,31	332	30,1	60,3	7,78	30,8			
44	178	219	37,9	343	21	2	5,41	910	61,5	125	14,4	52,8			
10	98,4	86,6	31,6	604	16,7	1	4	596	124,5	242	25,3	88,9			
49	149	250	38,6	355	18,5	2	4,93	1040	73,6	140,5	15,75	57,2			
52	147	294	36,1	279	19,3	2	3,12	985	62,4	125	14,95	53,8			
11	167,5	253	14,2	112	15,3	2	4,18	873	13,4	39,5	2,74	9,4			
86	88	485	18,6	211	12	2	1,33	1035	84,4	152,5	15,55	53,1			
120	119	597	16,9	242	8,8	1	1,68	985	51,4	98,1	10,35	36,3			
99	95,8	609	29,1	279	12,5	2	2,06	736	64,1	131,5	14,95	54			
99	128	567	23,6	334	16,6	3	1,5	909	66	139,5	16,05	58,4			
44	144,5	222	50,2	356	19	3	3,31	664	34,4	92,4	10,05	37,8			
85	117,5	303	30	276	14,5	2	1,56	883	58,1	124	13,95	50,2			
41	62,2	278	40,1	366	10,8	3	1,6	741	44,9	98,1	11	38,9			
164	63,7	280	63,5	250	24,1	3	0,86	437	43,5	104,5	13,5	55,8			
79	91,8	466	30,9	122	11,1	2	1,19	433	22	50,9	6,69	28,4			
42	110,5	378	11,4	166	8	1	2,39	758	31,1	66,2	7,01	23,6			
85	137,5	262	25,1	332	11,5	2	4,12	930	62,1	123,5	13,7	49,7			
161	110	806	23,9	133	10	1	4,76	832	30,8	65,8	7,9	30,7			
26	78,3	516	9,1	110	3,7	1	0,59	1140	40,7	77,7	8,4	28,6			

Sm	Eu	Gd	Tb	Dy	Ho	Er	Tm	Yb	Lu	Hf	Ta	Th	U	Ga
5,95	1,09	4,82	0,79	4,4	0,95	2,85	0,41	2,86	0,44	6,6	0,9	13,1	4,3	17
11,05	1,7	9,69	1,52	9,25	1,94	5,49	0,83	5,43	0,87	9,9	1,3	17,4	3,72	22,1
8,96	1,84	7,74	1,2	6,99	1,4	4,1	0,59	4,01	0,63	9,5	1	12,75	3,36	16,2
6,64	1,18	5,24	0,87	5,08	1,03	3,2	0,45	3,17	0,51	7,4	1	14,5	5,32	17,7
3,97	1,02	2,71	0,4	2,12	0,41	1,35	0,17	1,34	0,23	4,4	0,6	10,7	4,66	16,8
5,74	1,15	5,51	0,85	4,94	1,01	3,08	0,43	2,73	0,44	8,3	0,7	10,25	3,23	15,8
6,24	0,82	5,75	1,1	7,39	1,63	5,5	0,87	6,14	0,95	8,1	3,1	18,2	4,66	18,8
3,22	0,66	2,46	0,44	3,03	0,71	2,06	0,35	2,44	0,38	6,5	1,5	14,7	1,36	14,4
13,9	2,21	10,95	1,74	9,75	1,96	5,92	0,81	5,32	0,8	9,6	1,3	12,45	2,72	18,2
5,77	1,44	5,57	0,86	5,28	1,07	3,02	0,44	2,89	0,45	6,6	0,7	10,6	3,07	17,3
8,82	1,41	7,2	1,18	6,97	1,4	4,41	0,63	4,26	0,68	9,1	1,3	14,6	2,71	15,9
11,85	1,26	8,34	1,18	6,33	1,25	3,65	0,47	3,12	0,5	13,4	0,6	11,3	3,8	17,2
9,3	1,85	7,53	1,16	6,96	1,48	4,32	0,59	3,91	0,67	8,9	1	14,35	3,56	16,5
8,94	1,53	7,16	1,16	6,62	1,34	3,94	0,53	3,76	0,61	7,6	1,1	13,35	3,38	16,6
1,65	0,45	1,51	0,29	2,03	0,43	1,52	0,23	1,61	0,25	3,5	0,7	10,5	1,76	15,2
6,86	1,39	4,67	0,73	3,49	0,68	1,86	0,25	1,57	0,2	5,4	0,4	11,3	1,56	17,5
5,24	1,23	3,86	0,55	2,87	0,61	1,73	0,25	1,63	0,22	6,5	0,2	8,37	0,87	17,6
8,69	1,91	6,77	0,96	5,2	1,08	2,93	0,44	2,81	0,43	7,3	0,6	11,5	1,54	19,8
8,98	1,74	6,96	0,9	4,9	0,89	2,32	0,34	1,99	0,28	8,9	0,6	16,9	0,75	21
7,92	1,62	7,03	1,27	8,41	1,9	5,42	0,84	5,36	0,73	9,1	1,5	11,1	2,36	16,7
8,39	1,64	6,36	0,99	5,57	1,19	3,13	0,45	2,8	0,36	7,5	0,6	17,4	2,18	18,7
6,98	1,04	5,54	0,93	5,94	1,39	4,08	0,64	4,2	0,62	9	0,7	18,25	1,38	15,3
12,1	2,31	12,1	1,9	11,6	2,39	6,57	1,02	6,16	0,92	6,4	1,5	6,69	0,87	21,1
6,53	1,24	5,88	0,92	5,46	1,11	2,91	0,43	2,51	0,33	3,3	0,4	1,47	0,3	19,9
3,71	0,92	2,48	0,35	2,01	0,42	1,17	0,18	1,18	0,14	4,6	0,5	9,14	1,83	15,9
7,73	1,73	6,19	0,87	4,6	0,95	2,33	0,35	2,1	0,28	9,2	0,5	18,15	1,76	17,6
5,81	1,42	5,09	0,66	3,99	0,76	2,32	0,34	2,31	0,36	3,7	0,7	9,91	2,94	20,1
4,13	1,01	2,89	0,31	1,57	0,26	0,77	0,08	0,65	0,07	2,8	<0,1	7,35	0,3	15,6

Appendix F – Geochemistry from Austrheim et al. (2003)

Sample	SiO ₂	Al ₂ O ₃	Fe ₂ O _{3t}	TiO ₂	MgO	CaO	Na ₂ O	K ₂ O	MnO	P ₂ O ₅	H ₂ O ⁺	Co	Cr	Cu
FAR3	71,11	14,2	1,89	0,22	0,6	1,99	2,8	4,87	0,06	0,05	0,5	3,2	140	<5
FAR5	71,16	14,51	2,00	0,23	0,71	1,91	3,3	4,66	0,06	0,06	0,47	3,9	162	<5
FAR20	71,74	14,35	2,10	0,22	0,63	1,84	3,3	4,64	0,07	0,05	0,3		98	<5
FAR35C	66,33	15,49	3,43	0,41	1,35	2,64	3,8	4,53	0,07	0,11	0,45		115	22
FAR23	57,62	18,24	5,61	0,79	2,23	5,13	3,9	4,02	0,09	0,39	0,71		104	129
FAR31	56,7	14,4	7,36	0,7	5,92	5,97	3,1	3,38	0,12	0,28	0,85	28,3	402	84
FAR33	56,57	14,39	7,54	0,72	6,04	5,99	2,9	3,31	0,12	0,28	0,78		398	112
FAR15	51,79	14,4	9,43	0,85	7,45	7,93	2,9	2,34	0,16	0,38	1,37		446	150
FAR19	53,95	13,85	8,80	0,77	7,44	7,1	2,9	2,34	0,15	0,31	1,17	33,1	508	168
FAR21	53,57	18,55	7,97	0,8	3,97	6,18	4,1	1,99	0,15	0,33	1,68	23,3	123	10
DRA1	60,64	17,13	5,57	0,72	2,32	4,56	3,8	3,99	0,1	0,31	0,7	14,9	112	81

NI	Pb	Sc	V	Rb	Sr	Y	Zr	Nb	Sn	Cs	Ba	La	Ce	Pr	Nd
7		2,9	28	129	366	11	122	10		2,9	915	26,6	56,3		20,8
7		4,1	29	167	340	17	133	11		4,1	900	30,1	67,1		37,4
6			26	184	313	14	126	13			824				
11			55	153	519	24	232	15			938				
31			148	92	1100	21	161	14			1800				
129		18,8	180	106	776	22	195	13		18,8	1200	72,7	88,4		39,7
27			173	100	773	24	194	15			1000				
143			231	65	975	24	149	11			1500				
147		23,2	200	80	790	24	169	10		23,2	1100	38	77,6		
40		19,3	169	57	832	22	181	8		19,3	492	34,9	67,5		18,7
28		12,7	128	111	770	27	221	16		12,7	1200	47,4	110,1		

Sm	Eu	Gd	Tb	Dy	Ho	Er	Tm	Yb	Lu	Hf	Ta	Th	U	Ga
3,1	1,4		0,35					2	0,23	3	0,5	7	0,5	
3,9	1,4		0,45					3,3	0,49	3,6	0,7	10,4	2,1	
6,7	2,2		0,9					5,9	0,89	3,5	0,7	5,4	1,8	
6,7	2		0,65					4	0,5	3,9	0,5	3,5	1,3	
5,4	2,1		0,55					3,5	0,37	4,6	0,4	2,9	1	
7	2,5		0,9					4	0,43	5,3	0,9	7	1,6	

Appendix G – Geochemistry from Røhr et al. (2013)

Sample	SiO ₂	Al ₂ O ₃	Fe ₂ O _{3t}	TiO ₂	MgO	CaO	Na ₂ O	K ₂ O	MnO	P ₂ O ₅	H ₂ O+	Co	Cr	Cu
1 (PR-412)	61,8	17,4	5,1	0,619	2,25	4,4	4,57	3,61	0,099	0,305	0,466	13	33,1	<2
2 (PR-866)	64,5	17,1	4,2	0,527	1,38	3,57	4,69	3,12	0,102	0,206	0,412	7,9	18,6	18,5
3 (PR-D)	67,7	15,1	4,54	0,726	1,15	2,88	3,5	4,35	0,114	0,236	0,396	8,5	11,1	15,6
4 (PR-944x)	67,2	15,2	5,35	0,792	1,03	3,27	3,23	4,08	0,096	0,252	0,293	8	15,2	7
6 (PR-A)	68,9	14,8	3,98	0,592	0,747	2,34	3,26	4,87	0,091	0,177	0,278	5,1	5,9	4,8
7 (PR-B)	69,1	15,4	4,18	0,556	1,56	3,61	2,93	3,24	0,078	0,135	0,074	11,3	15,6	17,1
8 (PR-C)	68	14,8	4,79	0,73	1,43	3,2	2,74	4,06	0,106	0,166	-0,03	9,7	26,3	18,7

NI	Pb	Sc	V	Rb	Sr	Y	Zr	Nb	Sn	Cs	Ba	La	Ce	Pr	Nd
20,2	18,4	12	82,9	119	1020	24	212	10,5			1600	38	92		35
4,7	16,8	6,9	57,7	89,2	580	23,7	185	9,1			1360	34	74		25
8,6	20,2	7,5	51,4	148	281	33,8	233	15,3			1030	27	71		30
5	14,7	11,8	42,7	63,5	194	26,2	349	15,1			1370	28	75		28
3,6	20,5	7,7	28,5	106	151	33,2	311	14,8			1050	25	79		35
14,3	20	9,2	57,9	68,8	294	14,4	189	6,9			837	36	83		27
15,6	21,8	7,7	72,2	81,3	258	24,6	240	13,2			1040	72	148		56

Sm	Eu	Gd	Tb	Dy	Ho	Er	Tm	Yb	Lu	Hf	Ta	Th	U	Ga
												8,9		18,2
												6,8		16,6
												9,5		16
												<4		16,7
												<4		16,7
												11,1		16,2
												19		15,5



 **NTNU**

Norwegian University of
Science and Technology